

Integral Reactor Containment Condensation Model and Experimental Validation

**Reactor Concepts
Research Development and Demonstration**

Qiao Wu
Oregon State University

In collaboration with:
University of Wisconsin, Madison

Brian Robinson, Federal POC
Mitchell Farmer, Technical POC

INTEGRAL REACTOR CONTAINMENT CONDENSATION MODEL AND EXPERIMENTAL VALIDATION

Final Report

Prepared by:

Qiao Wu (PI), Dongyoung Lee, Etienne Mullin, Bradyn Wuth, Benjamin Bristol

Department of Nuclear Engineering and Radiation Health Physics
Oregon State University

Qiao.Wu@Oregonstate.edu

Michael L. Corradini (Co-PI) and Dhongik Yoon;

Department of Engineering Physics
University of Wisconsin-Madison

December, 2015



TABLE OF CONTENTS

LIST OF FIGURES	3
LIST OF TABLES.....	11
NOMENCLATURE	12
SUMMARY	14
1 Introduction	16
2 Background.....	17
2.1 Significance	17
2.2 Contributions to the NEUP Program	18
3 Literature Survey.....	19
3.1 Small Modular Reactors.....	19
3.2 Condensation Phenomena.....	20
3.3 Film Condensation and Film Flow Dynamics.....	22
3.3.1 Condensation Heat Transfer Modeling.....	22
3.3.2 Wave Dynamics of Film Flow	28
4 Test Facility and Modification	31
4.1 Reactor Pressure Vessel	33
4.2 High Pressure Containment.....	33
4.3 Heat Transfer Plate.....	35
4.4 Cooling Pool Vessel.....	36
4.5 Steam Supply System.....	36
4.6 Facility P&ID	36
4.7 Facility Limitations.....	38
5 Film Condensation Scaling Analysis	39
5.1 Scaling Based on Empirical Correlation	39
5.2 Scaling Based Diffusion Layer Model.....	40
5.2.1 Film Condensation Heat Transfer Coefficient.....	43
5.2.2 Gas/Steam Heat Transfer Coefficient	43
5.2.3 Film Condensation and Gas/Steam Heat Transfer Coefficient	44
5.3 Scaling Based on Local Heat Transfer Model	44
5.4 Scaling Analysis Results	48
6 Experimental Investigation	50
6.1 Test Matrix and Procedure.....	50
6.1.1 Test Set 1	50

6.1.2	Test Set 2	51
6.2	Test Overview	52
6.3	Data Processing and Analysis Methods	56
6.3.1	Transient Data Processing	56
6.3.2	Quasi-Steady State Data Processing	60
6.4	Test Results	67
6.4.1	Mass Balance	67
6.4.2	Energy Balance	73
6.4.3	Condensation Rates vs. System Pressure	81
6.4.4	Condensation Rates vs. Non-condensable Gas Inventory	83
6.5	Error Analysis for Measured Conduction Heat Flux	85
6.5.1	Edge Effects	85
6.5.2	Spatial Error on Thermocouple Measurements	88
6.5.3	Temperature Field Distortion	88
6.5.4	Challenges with Surface Temperature Measurement	89
6.6	Correction for HTP Temperatures	89
6.7	Uncertainty Quantification	92
6.8	Test Result Conclusion	96
7	Modeling of the Tests Using MELCOR	100
7.1	Simplifications/Assumptions	101
7.2	Model Constituents	102
7.3	Nodalization	103
7.4	Initial Conditions	105
7.5	Results	105
7.6	MELCOR Model Conclusion	113
8	Summary and Conclusions	114
	References	116
	Appendix A – COMPLETE SIMULATION RESULTS	119
	Appendix B – FULL INPUT FOR MELCOR	177

LIST OF FIGURES

Figure 3-1,	Map of global SMR technology development [Reprinted with permission from (IAEA, “Advances in SMR Technology Development 19
Figure 3-2,	Condensation types [14] 21
Figure 4-1,	The MASLWR test facility and modifications for the proposed investigation 31
Figure 4-2,	RPV internal components of MASLWR test facility [56]..... 33
Figure 4-3,	Cross-sectional view of the HPC (left) and CPV (right), joined by the HTP. 34
Figure 4-4,	Diagram of HTP embedded thermocouples..... 34
Figure 4-5,	Six sets of thermocouples in HTP..... 35
Figure 4-6,	P&ID of relevant instruments of the OSU MASLWR test facility. 37
Figure 5-1,	Illustrative outline and thermal resistance network of the diffusion layer model... 40
Figure 5-2,	One-dimensional film flow model. 45
Figure 5-3,	Flow chart for solving steady-state condensing film flow [58]. 46
Figure 5-4,	Velocity profiles along a condensation plate 47
Figure 5-5,	Film thickness profiles along a condensation plate. 47
Figure 5-6,	Comparison of film thickness between suggested models and previous work in turbulent film flow regime 48
Figure 5-7,	Total heat transfer rate ratio with respect to length scaling factor..... 49
Figure 6-1,	HPC pressure for Test Set 1 (low flow rates) 53
Figure 6-2,	HPC pressure for Test Set 1 (high flow rates) 53
Figure 6-3,	HPC pressure for Test Set 2 (near vacuum I.C.)..... 55
Figure 6-4,	HPC pressure for Test Set 2 (atmospheric I.C.)..... 55
Figure 6-5,	Discretized nodes of the heat transfer plate for numerical modeling 56
Figure 6-6,	Flow chart for inverse heat transfer analysis 58
Figure 6-7,	Heat transfer plate surface heat flux estimation in a blow-down transient..... 59

Figure 6-8, HPC mass balance, Test 1.1	69
Figure 6-9, HPC mass balance, Test 1.6.....	69
Figure 6-10, HPC mass balance, Test 2.1	70
Figure 6-11, HPC mass balance, Test 2.7	70
Figure 6-12, Integral mass error for Test Set 1 (low flow rates).....	71
Figure 6-13, Integral mass error for Test Set 1 (high flow rates)	71
Figure 6-14, Integral mass error for Test Set 2	72
Figure 6-15, Energy balance across HTP, Test 1.1	75
Figure 6-16, Energy balance across HTP, Test 1.6.....	76
Figure 6-17, Energy balance across HTP, Test 2.1	76
Figure 6-18, Energy balance across HTP, Test 2.7.....	77
Figure 6-19, Integral CPV energy error for Test Set 1 (low flow rates).....	77
Figure 6-20, Integral CPV energy error for Test Set 1 (high flow rates).....	78
Figure 6-21, Integral CPV energy error for Test Set 2	78
Figure 6-22, Integral HTP energy error for Test Set 1 (low flow rates)	79
Figure 6-23, Integral HTP energy error for Test Set 1 (high flow rates)	79
Figure 6-24, Integral HTP energy error for Test Set 2.....	80
Figure 6-25, Average heat flux from HTP measurements for Test Set 1	81
Figure 6-26, Average heat flux from HTP measurements for Test Set 2	82
Figure 6-27, Average heat transfer coefficient from HTP measurements for Test Set 1.....	82
Figure 6-28, Average heat transfer coefficient from HTP measurements for Test Set 2.....	83
Figure 6-29, Conduction heat flux measured at six axial levels on the HTP.....	83
Figure 6-30, Conduction heat flux as measured on the HTP after terminating steam supply	84
Figure 6-31, Thermocouple placement for investigating edge effect	85
Figure 6-32, Quadratic temperature profile interpolated across width of the heat transfer plate	87

Figure 6-33,	Diagram of embedded thermocouple placement.....	89
Figure 6-34,	Condensation heat flux calculated from alternate method vs. system pressure ..	91
Figure 6-35,	Heat transfer coefficients calculated from alternate method vs. system pressure	91
Figure 6-36,	Uncertainty of heat flux from HTP measurements (Test 2.1).....	92
Figure 6-37,	Uncertainty of heat transfer coefficient from HTP measured (Test 2.1)	92
Figure 6-38,	Uncertainty of heat flux with corrected surface temperatures	93
Figure 6-39,	Uncertainty of heat transfer coefficient with corrected surface temperatures	93
Figure 6-40,	Condensation heat transfer coefficient predictions from popular models.....	97
Figure 6-41,	Diagram of the theorized fin effect	98
Figure 7-1	Heat Structure in a Control Volume.....	101
Figure 7-2	Nodalization of the Containment and Cooling system	104
Figure 7-3	Containment Pressure for Test 2.4	106
Figure 7-4	Containment Temperature for Test 2.4	106
Figure 7-5	Heat flux at location 6 for Test 2.4	108
Figure 7-6	Direct and digressing heat flow.....	109
Figure 7-7	Containment Pressure for Test 2.7	110
Figure 7-8	Containment Temperature for Test 2.7	110
Figure 7-9	Heat Flux at location 6 for Test 2.7.....	111
Figure 7-10	Experimental Steady State Heat Flux of all CCT's at Location 6	111
Figure 7-11	Simulation Film Thickness during Steady State for Test 2.4 and 2.7.....	112
Figure A-1	Containment Pressure for Test 1.1	120
Figure A-2	Containment Temperature for Test 1.1	120
Figure A-3	CPV Temperature for Test 1.1	121
Figure A-4	Heat Flux at Location 6 for Test 1.1	121
Figure A-5	Heat Flux at Location 5 for Test 1.1	122

Figure A-6 Heat Flux at Location 4 for Test 1.1	122
Figure A-7 Heat Flux at Location 3 for Test 1.1	123
Figure A-8 Heat Flux at Location 2 for Test 1.1	123
Figure A-9 Containment Pressure for Test 1.2	124
Figure A-10 Containment Temperature for Test 1.2	124
Figure A-11 CPV Temperature for Test 1.2	125
Figure A-12 Heat Flux at Location 6 for Test 1.2	125
Figure A-13 Heat Flux at Location 5 for Test 1.2	126
Figure A-14 Heat Flux at Location 4 for Test 1.2	126
Figure A-15 Heat Flux at Location 3 for Test 1.2	127
Figure A-16 Heat Flux at Location 2 for Test 1.2	127
Figure A-17 Containment Pressure for Test 1.3	128
Figure A-18 Containment Temperature for Test 1.3	128
Figure A-19 CPV Temperature for Test 1.3	129
Figure A-20 Heat Flux at Location 6 for Test 1.3	129
Figure A-21 Heat Flux at Location 5 for Test 1.3	130
Figure A-22 Heat Flux at Location 4 for Test 1.3	130
Figure A-23 Heat Flux at Location 3 for Test 1.3	131
Figure A-24 Heat Flux at Location 2 for Test 1.3	131
Figure A-25 Containment Pressure for Test 1.4	132
Figure A-26 Containment Temperature for Test 1.4	132
Figure A-27 CPV Temperature for Test 1.4	133
Figure A-28 Heat Flux at Location 6 for Test 1.4	133
Figure A-29 Heat Flux at Location 5 for Test 1.4	134
Figure A-30 Heat Flux at Location 4 for Test 1.4	134

Figure A-31 Heat Flux at Location 3 for Test 1.4	135
Figure A-32 Heat Flux at Location 2 for Test 1.4	135
Figure A-33 Containment Pressure for Test 1.5	136
Figure A-34 Containment Temperature for Test 1.5	136
Figure A-35 CPV Temperature for Test 1.5	137
Figure A-36 Heat Flux at Location 6 for Test 1.5	137
Figure A-37 Heat Flux at Location 5 for Test 1.5	138
Figure A-38 Heat Flux at Location 4 for Test 1.5	138
Figure A-39 Heat Flux at Location 3 for Test 1.5	139
Figure A-40 Heat Flux at Location 2 for Test 1.5	139
Figure A-41 Containment Pressure for Test 1.6	140
Figure A-42 Containment Temperature for Test 1.6	140
Figure A-43 CPV Temperature for Test 1.6	141
Figure A-44 Heat Flux at Location 6 for Test 1.6	141
Figure A-45 Heat Flux at Location 5 for Test 1.6	142
Figure A-46 Heat Flux at Location 4 for Test 1.6	142
Figure A-47 Heat Flux at Location 3 for Test 1.6	143
Figure A-48 Heat Flux at Location 2 for Test 1.6	143
Figure A-49 Containment Pressure for Test 2.1	145
Figure A-50 Containment Temperature for Test 2.1	146
Figure A-51 CPV Temperature for Test 2.1	146
Figure A-52 Heat Flux at Location 6 for Test 2.1	147
Figure A-53 Heat Flux at Location 5 for Test 2.1	147
Figure A-54 Heat Flux at Location 4 for Test 2.1	148
Figure A-55 Heat Flux at Location 3 for Test 2.1	148

Figure A-56 Heat Flux at Location 2 for Test 2.1	149
Figure A-57 Steady State Film Thickness for Test 2.1	149
Figure A-58 Containment Pressure for Test 2.2	150
Figure A-59 Containment Temperature for Test 2.2	150
Figure A-60 CPV Temperature for Test 2.2	151
Figure A-61 Heat Flux at Location 6 for Test 2.2	151
Figure A-62 Heat Flux at Location 5 for Test 2.2	152
Figure A-63 Heat Flux at Location 4 for Test 2.2	152
Figure A-64 Heat Flux at Location 3 for Test 2.2	153
Figure A-65 Heat Flux at Location 2 for Test 2.2	153
Figure A-66 Steady State Film Thickness for Test 2.2	154
Figure A-67 Containment Pressure for Test 2.3	154
Figure A-68 Containment Temperature for Test 2.3	155
Figure A-69 CPV Temperature for Test 2.3	155
Figure A-70 Heat Flux at Location 6 for Test 2.3	156
Figure A-71 Heat Flux at Location 5 for Test 2.3	156
Figure A-72 Heat Flux at Location 4 for Test 2.3	157
Figure A-73 Heat Flux at Location 3 for Test 2.3	157
Figure A-74 Heat Flux at Location 2 for Test 2.3	158
Figure A-75 Steady State Film Thickness for Test 2.3	158
Figure A-76 Containment Pressure for Test 2.4	159
Figure A-77 Containment Temperature for Test 2.4	159
Figure A-78 CPV Temperature for Test 2.4	160
Figure A-79 Heat Flux at Location 6 for Test 2.4	160
Figure A-80 Heat Flux at Location 5 for Test 2.4	161

Figure A-81 Heat Flux at Location 4 for Test 2.4	161
Figure A-82 Heat Flux at Location 3 for Test 2.4	162
Figure A-83 Heat Flux at Location 2 for Test 2.4	162
Figure A-84 Steady State Film Thickness for Test 2.4.....	163
Figure A-85 Containment Pressure for Test 2.5	163
Figure A-86 Containment Temperature for Test 2.5	164
Figure A-87 CPV Temperature for Test 2.5	164
Figure A-88 Heat Flux at Location 6 for Test 2.5	165
Figure A-89 Heat Flux at Location 5 for Test 2.5	165
Figure A-90 Heat Flux at Location 4 for Test 2.5	166
Figure A-91 Heat Flux at Location 3 for Test 2.5	166
Figure A-92 Heat Flux at Location 2 for Test 2.5	167
Figure A-93 Steady State Film Thickness for Test 2.5.....	167
Figure A-94 Containment Pressure for Test 2.6	168
Figure A-95 Containment Temperature for Test 2.6	168
Figure A-96 CPV Temperature for Test 2.6	169
Figure A-97 Heat Flux at Location 6 for Test 2.6	169
Figure A-98 Heat Flux at Location 5 for Test 2.6	170
Figure A-99 Heat Flux at Location 4 for Test 2.6	170
Figure A-100 Heat Flux at Location 3 for Test 2.6	171
Figure A-101 Heat Flux at Location 2 for Test 2.6	171
Figure A-102 Steady State Film Thickness for Test 2.6.....	172
Figure A-103 Containment Pressure for Test 2.7	172
Figure A-104 Containment Temperature for Test 2.7	173
Figure A-105 CPV Temperature for Test 2.7	173

Figure A-106 Heat Flux at Location 6 for Test 2.7	174
Figure A-107 Heat Flux at Location 5 for Test 2.7	174
Figure A-108 Heat Flux at Location 4 for Test 2.7	175
Figure A-109 Heat Flux at Location 3 for Test 2.7	175
Figure A-110 Heat Flux at Location 2 for Test 2.7	176
Figure A-111 Steady State Film Thickness for Test 2.7.....	176

LIST OF TABLES

Table 3-1,	Falling film flow regimes by Reynolds number [16].....	22
Table 3-2	Classification of condensation computer codes	28
Table 3-3	Falling liquid film flow regimes by wave types	29
Table 3-4,	Film thickness correlations for vertical downward film flow	30
Table 4-1,	OSU MASLWR test facility scaling [56]	31
Table 4-2,	Elevation of relevant facility thermocouples	36
Table 6-1,	Test matrix for first set of condensation tests	50
Table 6-2,	Test matrix for second set of condensation tests	51
Table 6-3,	Description of the first set of tests	52
Table 6-4,	Quasi steady pressures reached in the second set of tests.....	54
Table 6-5,	Test facility instrument channels employed in the analysis.....	61
Table 6-6,	Input parameters employed in the analysis	62
Table 6-7,	Left and right bounds of the regions of interest selected for detailed analysis	67
Table 6-8,	Mass error and error percent	72
Table 6-9,	Energy errors and percent errors.....	80
Table 6-10,	Measurements involved in evaluating the edge effect	86
Table 6-11,	Average heat flux after accounting for the edge effects.....	87
Table 6-12,	Average heat flux accounting for spatial error.....	88
Table 6-13,	Relevant Instrument Uncertainties	94
Table 7-1	Nodalization detail.....	104
Table 7-2	Initial conditions for simulation	105
Table 7-3	Thermal Conductivity of SS304.....	107
Table B-1	MELCOR files and descriptions.....	178
Table B-2	Necessary changes in input between different tests.....	178

NOMENCLATURE

English

A	Area, or parameter defined in Equation (5-8)	$[m^2]$
C	Specific heat capacity or constant	$[kJ/kg/K]$
CPV	Cooling Pool Vessel	
E	Internal energy	$[J]$
D	Diffusion coefficient	$[m^2/s]$
Fo	Defined in Equation (6-5)	
g	Gravitational acceleration	$[m/s^2]$
Gr	Grashof number	
h	Heat transfer coefficient	$[w/m^2K]$
h, H	Enthalpy	$[kJ/kg]$
HPC	High Pressure Containment	
k	Thermal conductivity	$[w/m^2K]$
Ka	Karlovitz number	
L	Length or height	$[m]$
\dot{m}	Mass Flux	$[kg/m^2s]$
Nu	Nusselt Number	
p	Pressure	$[N/m^2]$
Pr	Prandtl number	
q''	Heat flux	$[w/m^2]$
R	Gas constant	$[kJ/kg/K]$
Re	Reynolds Number	
Sc	Schmidt number	
Sh		
T	Temperature	$[K]$
t	Time	$[s]$
u	Velocity	$[m/s]$
V	Volume	$[m^3]$
w	Width	$[m]$
W	Mass Fraction	
x	film flow direction coordinate	$[m]$
X	Logarithmic mean mass fraction	
y	coordinate perpendicular to the wall	$[m]$

Greek Symbols

δ	Film thickness	(m)
λ	Wave length	(m)
ρ	density	$[kg/m^3]$
ν	dynamic viscosity	$[Ns/m^2]$
Θ	Parameter defined in Equation (5-15)	

Ψ Parameter defined in Equation (5-17)

Subscripts

A	<i>Total</i>
b	Bulk fluid
$cond$	Condensation
$conv$	Convection
f	Fluid
fg	vapor-liquid property difference
g	non-condensable gas
i	film-vapor interface
$n/c, nc$	Non-condensable
p	constant pressure
R	Ratio
s	film without wave, or steam
v	vapor
w	Wall
x	function of film flow direction coordinate

SUMMARY

This NEUP funded project, NEUP 12-3630, is for experimental, numerical and analytical studies on high-pressure steam condensation phenomena in a steel containment vessel connected to a water cooling tank, carried out at Oregon State University (OrSU) and the University of Wisconsin at Madison (UW-Madison). In the three years of investigation duration, following the original proposal, the planned tasks have been completed:

- (1) Performed a scaling study for the full pressure test facility applicable to the reference design for the condensation heat transfer process during design basis accidents (DBAs), modified the existing test facility to route the steady-state secondary steam flow into the high pressure containment for controllable condensation tests, and extended the operations at negative gage pressure conditions (OrSU).
- (2) Conducted a series of DBA and quasi-steady experiments using the full pressure test facility to provide a reliable high pressure condensation database (OrSU).
- (3) Analyzed experimental data and evaluated condensation model for the experimental conditions, and predicted the prototypic containment performance under accidental conditions (UW-Madison).

A film flow model was developed for the scaling analysis, and the results suggest that the 1/3 scaled test facility covers large portion of laminar film flow, leading to a lower average heat transfer coefficient comparing to the prototypic value. Although it is conservative in reactor safety analysis, the significant reduction of heat transfer coefficient (50%) could under estimate the prototypic condensation heat transfer rate, resulting in inaccurate prediction of the decay heat removal capability. Further investigation is thus needed to quantify the scaling distortion for safety analysis code validation.

Experimental investigations were performed in the existing MASLWR test facility at OrST with minor modifications. A total of 13 containment condensation tests were conducted for pressure ranging from 4 to 21 bar with three different static inventories of non-condensable gas. Condensation and heat transfer rates were evaluated employing several methods, notably from measured temperature gradients in the HTP as well as measured condensate formation rates. A detailed mass and energy accounting was used to assess the various measurement methods and to support simplifying assumptions required for the analysis. Condensation heat fluxes and heat transfer coefficients are calculated and presented as a function of pressure to satisfy the objectives of this investigation. The major conclusions for those tests are summarized below:

- (1) In the steam blow-down tests, the initial condensation heat transfer process involves the heating-up of the containment heat transfer plate. An inverse heat conduction model was developed to capture the rapid transient transfer characteristics, and the analysis method is applicable to SMR safety analysis.
- (2) The average condensation heat transfer coefficients for different pressure conditions and non-condensable gas mass fractions were obtained from the integral test facility, through the measurements of the heat conduction rate across the containment heat transfer plate, and from the water condensation rates measurement based on the total energy balance equation.

- (3) The test results using the measured HTP wall temperatures are considerably lower than popular condensation models would predict mainly due to the side wall conduction effects in the existing MASLWR integral test facility. The data revealed the detailed heat transfer characteristics of the model containment, important to the SMR safety analysis and the validation of associated evaluation model. However this approach, unlike separate effect tests, cannot isolate the condensation heat transfer coefficient over the containment wall, and therefore is not suitable for the assessment of the condensation heat transfer coefficient against system pressure and non-condensable gas mass fraction.
- (4) The average condensation heat transfer coefficients measured from the water condensation rates through energy balance analysis are appropriate, however, with considerable uncertainties due to the heat loss and temperature distribution on the containment wall. With the consideration of the side wall conduction effects, the results indicate that the measured heat transfer coefficients in the tests is about 20% lower than the prediction of Dehbi's correlation, mainly due to the side wall conduction effects. The investigation also indicates an increase in the condensation heat transfer coefficient at high containment pressure conditions, but the uncertainties invoked with this method appear to be substantial.
- (5) Non-condensable gas in the tests has little effects on the condensation heat transfer at high elevation measurement ports. It does affect the bottom measurements near the water level position. The results suggest that the heavier non-condensable gas is accumulated in the lower portion of the containment due to stratification in the narrow containment space. The overall effects of the non-condensable gas on the heat transfer process should thus be negligible for tall containments of narrow condensation spaces in most SMR designs. Therefore, the previous correlations with non-condensable gas effects are not appropriate to those small SMR containments due to the very poor mixing of steam and non-condensable gas.

The MELCOR simulation results agree with the experimental data reasonably well. However, it is observed that the MELCOR overpredicts the heat flux for all analyzed tests. The MELCOR predicts that the heat fluxes for CCT's approximately range from 30 to 45 kW/m² whereas the experimental data (averaged) ranges from about 25 to 40 kW/m². This may be due to the limited availability of liquid film models included in MELCOR. Also, it is believed that due to complex test geometry, measured temperature gradients across the heat transfer plate may have been underestimated and thus the heat flux had been underestimated.

The MELCOR model predicts a film thickness on the order of 100 microns, which agrees very well with film flow model developed in this study for scaling analysis. However, the expected differences in film thicknesses for near vacuum and near atmospheric test conditions are not significant. Further study on the behavior of condensate film is expected to refine the simulation results. Possible refinements include but are not limited to, the followings: CFD simulation focusing on the liquid film behavior and benchmarking with experimental analyses for simpler geometries.

1 INTRODUCTION

This NEUP funded project, NEUP 12-3630, is for experimental, numerical and analytical studies on high-pressure steam condensation phenomena in a steel containment vessel connected to a water cooling tank, carried out at Oregon State University (OrSU) and the University of Wisconsin at Madison (UW-Madison). The experimental results are employed to validate the containment condensation model in reactor containment system safety analysis code for integral SMRs. Such a containment condensation model is important to demonstrate the adequate cooling. In the three years of investigation, following the original proposal, the following planned tasks have been completed:

- (1) Performed a scaling study for the full pressure test facility applicable to the reference design for the condensation heat transfer process during design basis accidents (DBAs), modified the existing test facility to route the steady-state secondary steam flow into the high pressure containment for controllable condensation tests, and extended the operations at negative gage pressure conditions (OrSU).
- (2) Conducted a series of DBA and quasi-steady experiments using the full pressure test facility to provide a reliable high pressure condensation database (OrSU).
- (3) Analyzed experimental data and evaluated condensation model for the experimental conditions, and predicted the prototypic containment performance under accidental conditions (UW-Madison).

The results are applicable to integral Small Modular Reactor (SMR) designs, including NuScale, mPower, Westinghouse SMR, Holtec-160 and other integral reactors with small containments of relatively high pressures under accidental conditions. Testing has been conducted at the OrSU laboratory in the existing MASLWR (Multi-Application Small Light Water Reactor) integral test facility sponsored by the US Department of Energy. Its high-pressure stainless steel containment model (~2 MPa) is scaled to the NuScale SMR currently under development at NuScale Power, Inc.. Minor modifications to the model containment have been made to control the non-condensable gas fraction and to utilize the secondary loop stable steam flow for condensation testing. UW-Madison has developed a containment condensation model, which leveraged previous validated containment heat transfer work carried out at UW-Madison, and extended the range of applicability of the model to integral SMR designs that utilize containment vessels of high heat transfer efficiencies.

In this final report, the research background and literature survey are presented in Chapter 2 and 3, respectively. The test facility description and modifications are summarized in Chapter 4, and the scaling analysis is introduced in Chapter 5. The tests description, procedures, and data analysis are presented in Chapter 6, while the numerical modeling is presented in Chapter 7, followed by a conclusion section in Chapter 8.

2 BACKGROUND

After passive engineering features were proposed to accomplish advanced reactor safety functions in the middle of the late eighties, most of the novel reactor designs incorporated passive containment cooling systems (PCCS) to remove decay heat from the containment, including SMRs in recent years. Those features are of great significance particularly after the recent core meltdown accidents at Fukushima Daiichi Nuclear Power Stations after a devastating 8.9 Richter scale earthquake followed by a catastrophic Tsunami. In those advanced designs, steam condensation plays a vital role in removing decay heat from the containment atmosphere under accident conditions. Especially for integral SMRs proposed or under development, they utilize relatively small volume steel containment vessels, initially operating under ambient pressure or a vacuum with external air or water-cooling that serves as the containment heat sink. During accident transients, high-pressure cooling water leaves the primary circuit and enters the containment where it flashes into steam. This steam is then condensed on the containment vessel wall, with the peak pressure and temperature in the containment strongly dependent on the containment environment conditions including the amount of non-condensable gases present and the bulk steam flow induced convection effects. Lack of high-pressure (over 0.5 MPa) containment condensation data, the existing condensation models or correlations were not properly validated for possible applications under those SMR accidental conditions, which motivated this collaborative investigation between OrSU and UW-Madison.

2.1 Significance

Previous theoretical and experimental studies have primarily focused on large reactor plant containment buildings without significant containment pressurization, and few studies have been conducted on high-pressure steel containment vessels that rely on passive cooling to condense steam in the containment.

In early 1980s most of the accident analysis codes dealing with containment thermal-hydraulics, such as CONTEMP-4, used empirical correlations to estimate heat transfer from the gaseous bulk to the containment surfaces. The most commonly utilized correlations for condensation were based on the data in a pressure range from 0.1 to 0.28 MPa by Uchida et al. [1]. The next generation of codes like CONTAIN 1.1 took a step forward by implementing more mechanistic representations of the phenomena. This provided an increase in the confidence of their results along with a deeper understanding of the processes involved in the scenario.

Mechanistic condensation modeling has been traditionally addressed through two different approaches: solution of conservation equations in the boundary layer and the application of the heat/mass transfer analogy. According to Herr and Kadambi [2], the boundary layer solutions, although insightful from a theoretical point of view, are not very practical for containment analysis due to their complexity and expense; conversely, the analogy based models can be easily implemented into the nodal system codes used in containment accident analysis and they provide an insight of phenomenon with a non-time consuming feature.

The analogy models have made use of correlations of mass transfer obtained by the Chilton–Colburn analogy (Collier and Thome, [3]) and assume closure laws concerning heat transfer across the film. Fundamentals of this modeling approach are given by Kim et al. [4] who derived expressions for forced and natural convection condensation in the

presence of a non-condensable gas and analyzed the potential impact of film waviness. Later in 1993 Peterson et al. [5] used the Clapeyron equation to develop a more compact expression of condensation heat transfer, in which the condensation driving force, based on concentration differences, was formulated as a function of temperature differences, which is much more convenient in heat transfer problems. In 1998, Herranz et al. [6] proposed an improved model of condensation heat transfer on surfaces based on Peterson's approach, extending the model to deal with large gas-wall temperature differences, high mass fluxes, and the wavy structure of the condensate. Particular attention has been paid to the definition of key variables such as the Grashof number and the steam diffusion coefficient through non-condensable binary mixtures. The model has been validated against the database of Anderson et al. [7] in a pressure range of 0.1 to 0.3 MPa. Comparisons to Dehbi's database [9] in a pressure range of 0.15 to 0.45 MPa have also been conducted with an acceptable accuracy. Nevertheless, the lack of high pressure condensation test data presents challenges to the condensation model evaluation at high pressure conditions. This project aims at establishing a high pressure steam condensation database relevant to the development of SMRs, and validating the existing correlation/models.

2.2 Contributions to the NEUP Program

In this study, the modeling efforts follows the work of Herranz et al. [8] due to its maturity, simplicity and relevance to SMR designs. To validate or improve its applicability to SMR containment condensation at relatively high pressure conditions, testing have conducted at OrSU's laboratory in the existing DOE sponsored integral test facility, the MASLWR test facility, with a high-pressure stainless steel containment model (2~5 MPa), scaled to NuScale SMR design under development. Minor modifications to the model containment have been made to control the non-condensable gas fraction to quantify the non-condensable effects. Also, the secondary loop steam line was re-routed to the containment for parametric studies. The researchers at UW-Madison developed a containment condensation model, which leveraged previous validated containment heat transfer work done at UW-Madison, and extended the range of applicability of the model to integral SMR designs that utilize high heat transfer efficiency containment vessels.

This study advances the body of knowledge regarding condensation in containment vessels under accident conditions in three major ways. First, the existing database of experimental containment condensation data has been significantly expanded by providing data collected at a full design pressure and temperature under representative transient accident scenario. Second, the containment heat transfer model has been updated, implemented in MELCOR, and validated. This implementation provides a more fundamental model within a currently used containment system code, addressing some limitations of currently employed models. Finally, the model has been evaluated against the database of containment condensation data and correlations currently used in safety analyses by the NRC and design agents. This evaluation assess the model predictive performance relative to these correlations while extending the model validation to the new integral SMR containment systems. This work contributes to the objectives of the DOE SMR campaign to advance commercial nuclear reactor concepts for near-term deployment. It could support both design and design validation of small volume containment vessels in SMR applications by improving the modeling of postulated accident scenario containment condensation in system level containment codes.

3 LITERATURE SURVEY

3.1 Small Modular Reactors

Many countries are interested in SMRs as an option for future power and energy security. Eleven countries are participating in the development of more than 45 SMR designs by late 2014 according to the International Atomic Energy Agency (IAEA) as shown in Figure 3.1 [10]. Advanced SMRs have four unique features compared with 2nd and 3rd generation reactors, which includes an enhancement of safety performance, small size, integral design and modularization.

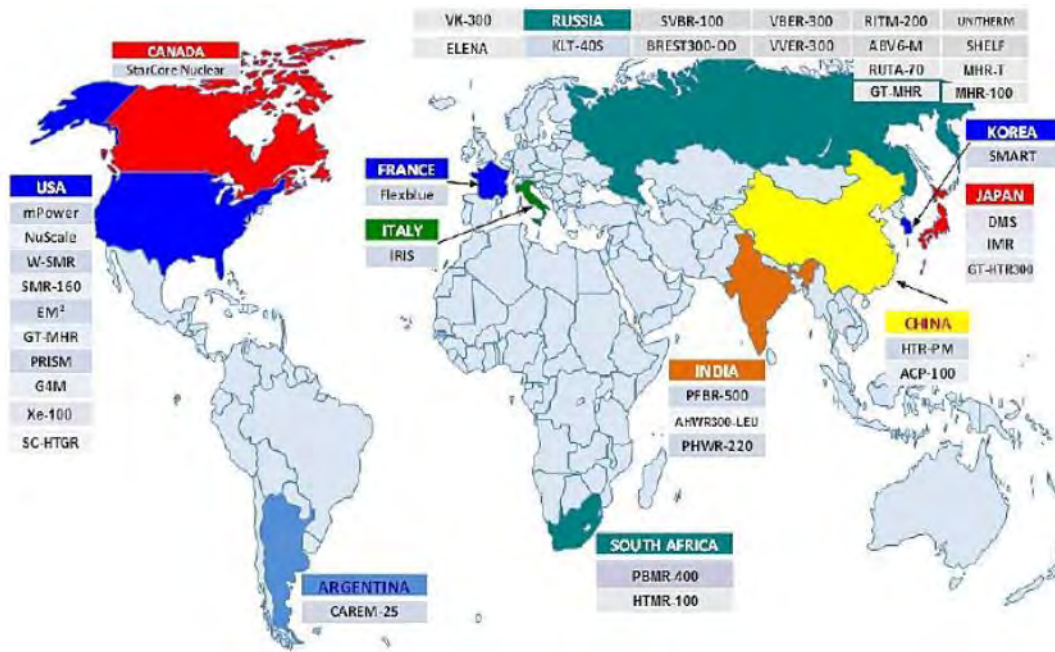


Figure 3-1, Map of global SMR technology development [Reprinted with permission from (IAEA, “Advances in SMR Technology Development

Most advanced SMRs use different approaches compared with current operating reactors. The SMRs utilize natural driving forces of gravity, natural circulation and passive safety systems, which allows for independence from AC or DC power sources during accidents. These inherent safety features make the possibilities of severe accidents significantly lower and provide their systems a high level of reliability. Moreover, human errors, one of the contributing factors to accidents, can be eliminated by SMRs passive systems, even under severe accident conditions. All the SMR designs would be safely shutdown automatically for more than 72 hours, which is the minimum coping time for the 3rd generation reactors regulated by the US Nuclear Regulatory Commission (NRC) without on-site and off-site power [11].

Due to their small size, SMRs have low power density and site flexibility. The potential consequences of an accident relative to a large power plant are thus limited. SMR's can be sited in areas near centers of demand with relatively high population densities, which

are now served by fossil-fueled plants. SMRs can also support seawater desalination processes to supply water and energy to coastal sites.

One of the innovative features of advanced SMRs is the integral design. The major components of the reactor, which include core, reactor cooling pumps, steam generator, and pressurizer, are all accommodated in the same Reactor Pressure Vessel (RPV). The integral reactor design contributes significantly to reduce the possibilities of potential large-break LOCA or small-break LOCA by eliminating large-loop piping and reducing the flow area of the coolant. The other revolutionary part of the advanced SMRs is the modular type. Several submodules of a SMR, which can be fabricated, tested and inspected at off-site facilities, could be transported and assembled on-site. The shipping of shop-fabricated structures is dependent on the maximum size envelope for current equipped transportation system, and the method of shipping can be altered to suit each particular site. Due to the modularization of the SMRs, the construction schedule and cost for SMRs can be significantly reduced. Moreover, as the demand for local power increases, some of the SMRs could be deployed as multiple-modules to add additional power conversion [12].

Even though many Research and Development (R&D) activities are under way for the design of advanced SMRs, further steps remain to be completed to the feasibility of the SMRs deployments. Licensing process, legal/regulatory framework, and validation and verification processes are the main issues remaining for the deployments of the SMRs. For further validation and verification of the most proposed SMRs, the distinct concept of operations, such as natural circulation, passive systems, containment condensation, etc., should be demonstrated in SMR test facilities [10]. There are several SMRs on the front line of development using water as a coolant: they are CAREM, SMART, mPower, IRIS and NuScale.

Several integral SMRs proposed or under development utilize relatively small volume steel containment vessels under ambient pressure or a vacuum with external air or water-cooling that serves as the containment heat sink. During accident transients, high-pressure cooling water leaves the primary circuit and enters the containment where it flashes into steam. This steam is then condensed on the containment vessel wall, with the peak pressure and temperature in the containment strongly dependent on the containment environment conditions including the amount of non-condensable gases present and the bulk steam flow induced convection effects. Lack of high-pressure (over 0.5 MPa) containment condensation data, the existing condensation models or correlations were not properly validated for possible applications under those SMR accidental conditions, which motivated this collaborative investigation.

3.2 Condensation Phenomena

Modes of condensation are classified by the homogenous and heterogeneous condensation. Homogeneous condensation occurs entirely within a supercooled vapor. The liquid droplet is surrounded by superheated pure vapor and is not attached to a lower temperature wall. Figure 3-2 shows three different possible cases of homogeneous condensation.

There are two idealized heterogeneous condensation processes depending on the condition of the cooling surface: film-wise and dropwise condensations. In dropwise condensation, liquid drops form at particular nucleation sites on a solid surface, and the drops remain separate during their growth phase until they are carried away by gravity or

vapor shear forces [13]. In film-wise condensation, the drops quickly coalesce to form a continuous liquid film on the cooling surface shown in Figure 3-1. Consequently, the steam no longer condenses directly on the cooling wall completely covered by liquid film, and the condensation process occurs on the film-vapor interface.

The heat transfer coefficients that can be achieved by dropwise condensation are an order of magnitude greater than those of a film condensation. Therefore, it is desirable to take advantage of dropwise condensation in applications. However, dropwise condensation eventually will develop into film flow in practical containment cooling applications, film-wise heat transfer coefficients are commonly adopted for engineering design purposes with conservative approach [13].

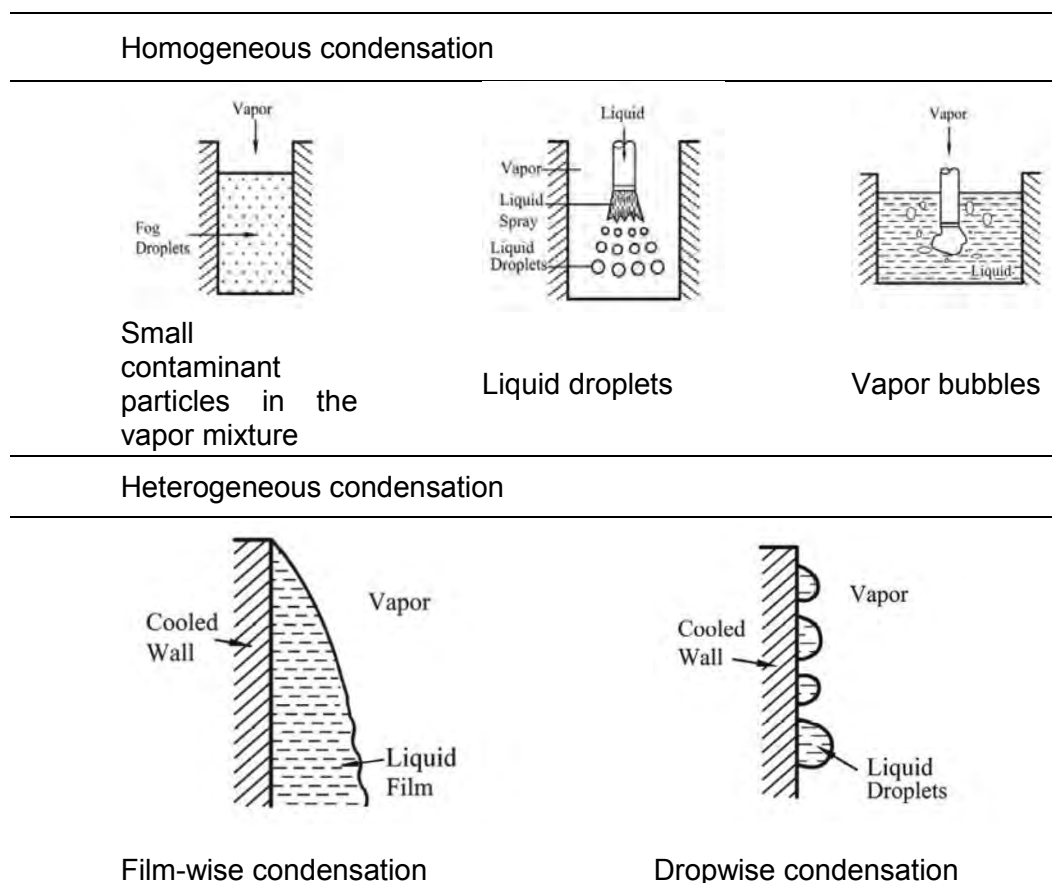


Figure 3-2, Condensation types [14]

In containment heat transfer analysis, dropwise condensation usually changes quickly into film condensation during the initial period of condensation, which has limited effect on the final containment pressure-temperature responses [15]. Therefore, this investigation primarily deals with film-wise condensation, which is generally classified as laminar, wavy and turbulent film condensations based on the film flow Reynolds number. At a low film Reynolds numbers near the top of the cooling surface, the condensate flow is laminar and wave-free. At some point down the vertical wall where waves form on the condensate film, due to instabilities at the vapor-liquid interface, leading to the so-called wavy film flow. At a much higher Reynolds number a transition from stable wavy-laminar flow to turbulent flow occurs. It is not well understood regarding the critical Reynolds number for the film

flow transition to wavy and turbulent regimes. Table 3-1 summarizes the falling film flow regimes that have been postulated with their Reynolds number by different researchers.

In this research, we are interested in the heat transfer coefficient and the corresponding Nusselt number under film-wise condensation. Heat transfer coefficients according to each of the regimes will be discussed.

Table 3-1, Falling film flow regimes by Reynolds number [16]

Flow regime	Kutateladze (1963)	Ishigai et al. (1974)	Brauner (1989)	Morioka et al. (1993)
Laminar flow	$Re \leq 30$	$Re \leq 1.88 Ka^{0.3}$		$Re \leq 16$
First transition		$1.88 Ka^{0.3} \leq Re \leq 8.8 Ka^{0.3}$		$16 < Re \leq 60$
Stable wavy-laminar	$30 < Re < 1800$	$8.8 Ka^{0.3} \leq Re < 300$	$Re < 1000$	$60 \leq Re < 300$
Second transition		$300 \leq Re \leq 1600$		$300 \leq Re \leq 1600$
Fully turbulent	$Re \geq 1800$	$Re \geq 1600$	$1000 \leq Re$	

3.3 Film Condensation and Film Flow Dynamics

To serve the research project, the following literature reviews focus on the heat transfer coefficients, film wavy regimes, and film thickness of vertical condensation falling film, based on experimental and theoretical approaches.

3.3.1 Condensation Heat Transfer Modeling

The theoretical works on the condensation heat transfer have been addressed by two separate methods: a solution of conservation equations in the boundary layer and an application of heat and mass transfer analogy in the closure relations. Both methods start from Nusselt's theoretical work of 1916 [17]. Nusselt presented the first analytical solution that dealt with the heat transfer coefficient of filmwise condensate flow. In his pioneering work, he considered the ideal situation with the following assumptions:

- The flow of condensate in the film is laminar.
- The fluid properties are constant.
- Subcooling of the condensate may be neglected.
- Momentum convective change through the film is negligible.
- The vapor is stationary and exerts no drag on the downward motion of the condensate.
- Heat transfer through the film is by conduction only

The mean value of the heat transfer coefficient by Nusselt's theory over the whole surface was given by

$$\bar{h}_{film} = 0.943 \left[\frac{\rho_f (\rho_f - \rho_{v,b}) g h'_{fg} k_f^3}{4 \mu_f L (T_b - T_w)} \right]^{1/4} \quad (3-1)$$

(A) Boundary Layer Model

One of the most important parameters in determining the heat transfer coefficient of film condensation is the amount of non-condensable gas. The presence of even a small quantity of non-condensable gas in the steam can reduce the heat transfer coefficients significantly. Based on the importance of non-condensable gas, the boundary layer model is to solve the mass, momentum and energy conservation equations, for both liquid film and gaseous boundary mixture layer. The non-condensable gas fraction at the interface between liquid film and a binary mixture is higher than its value in the ambient.

Minkowycz and Sparrow (1966) [18] were some of the first researchers to solve the boundary layer equations for laminar forced and free convective condensation on an isothermal plate. Their solution was achieved using stream functions and similarity transformation. Their study included the effects of interfacial resistance, superheating, thermal diffusion and property variation in the condensate film.

Fillo (1985) [19] proposed a model for vapor condensation with non-condensable gas, based upon a turbulent gas-vapor boundary layer. His method is viable for both forced and natural convection since the bulk velocity remains unspecified. Unfortunately, the equations are only listed and not solved for comparisons with experimental data.

Dehbi et al. (1991) [9] solved the boundary layer equations for the case of turbulent free convection condensation in the presence of non-condensable gases over vertical surfaces. Turbulence was treated using the Turbulent Kinetic Energy (TKE) method and empirical constants from experiments in pure air were employed. They reduced the partial differential equations into ordinary differential equations by using the independent variable transformation suggested by Minkowycz and Sparrow. Their solution showed excellent agreement with experimental data.

Oh and Revankar (2005) [20] performed the filmwise condensation analysis in a vertical tube with non-condensable gases using the boundary layer method. The transport quantities, such as interfacial friction factor, heat transfer Nusselt number and mass transfer Sherwood number, were calculated by the numerical method and compared with various condensation correlations. For the turbulent model in the gas mixture region, various simple algebraic models were used and the results were compared with experimental data. Results showed that Prandtl mixing length type model is better than any other turbulent model.

One of the major challenges with this type of solution is the complexity involved in numerically solving the differential equations, and as a result some of the physical intuition is lost in computational solutions. The other problem is the implementation of these solutions in computer codes used to model accident scenarios, causing a large amount of time for convergence. According to Herr and Kadambi (1993) [2], the boundary layer solutions, although insightful from a theoretical point of view, are not applicable to containment analysis with complex flow regimes and interface conditions.

(B) Heat and Mass Transfer Analogy

An alternative theoretical approach for condensation modeling has been addressed by the application of the heat and mass transfer analogy. The thermal resistances in the condensate film and gas/vapor boundary layer are estimated by correlations along with heat and mass transfer analogy.

The heat and mass transfer analogy was first introduced by Colburn and Hougen in 1934 [22]. They described the heat transfer process as controlled by the mass concentration gradient through the non-condensable layer, as the sum of sensible heat and latent heat flows. Since then, this analogy has been used to obtain solutions for several condensing systems. Kim and Corradini (1990) [23] summarized the use of this approach with forced and natural convection condensation in the presence of a non-condensable gas, and analyzed the potential impact of the film waviness.

Peterson et al. (1993) [5][24] introduced a diffusion layer model, a more straight forward expression of the condensation heat transfer coefficient. They described the total gas heat flux, partitioned into condensing and convective components:

$$q'' = q''_{cond} + q''_{conv} = h_{cond}(T_b - T_i) + h_{conv}(T_b - T_i) = -h_{fg} C \dot{m}_v v_i + k_v \frac{\partial T}{\partial y} \quad (3-2)$$

By using the diffusion theory and a modified Clausius-Clapeyron equation, where the difference between vapor and liquid specific volumes (v_{fg}) was approximated as its mean value in the boundary layer, Peterson et al. were able to obtain a condensation velocity defined as:

$$v_i = \frac{D_0 \bar{h}_{fg} \dot{m}_v X_{v,avg}}{RT_{avg}^2 X_{g,avg} \delta_g} (T_i - T_b), \quad (3-3)$$

where $X_{v,avg}$ and $X_{g,avg}$ are the logarithmic average mass fractions of vapor and non-condensable gas, respectively, D_0 denotes the diffusion coefficient, and δ_g is the effective thickness of the diffusion layer. From this equation Peterson et al. derived the following condensation heat transfer coefficient:

$$h_{cond} = \frac{D \bar{h}_{fg} C \dot{m}_v X_{v,avg}}{P T_{avg} v_{fg} X_{g,avg}} \quad (3-4)$$

In 1998, Herranz et al. [8] proposed an improved version of the condensation heat transfer model at the surface based on Peterson's approach, and extended the model to conditions with large gas-wall temperature differences, high mass fluxes, and the wavy structure of the condensate. Particular attention was paid to the definition of the key variables such as the Grashof number, and steam diffusion coefficient in non-condensable binary mixtures. The model has been validated using the database of Herranz et al. [6] in a pressure range of 0.1 to 0.3 MPa. Herr and Kadambi (1993) [2] argued that the analogy based models could be easily implemented into the nodal system codes for containment analysis, and they provide an insight to the phenomena without a time-consuming numerical simulation.

(C) Empirical Approach

The most used heat transfer correlations for condensation in containment were derived from experimental results, due to the complexity of the condensation heat transfer phenomena. The empirical approach is based on correlation from experimental data, leading to two groups of empirical heat transfer correlations: one for film condensation only and the other for the total heat transfer process.

Rohsenow (1956) [26] improved Nusselt's analysis for filmwise laminar flows by allowing for a non-linear temperature distribution through the film due to convective effects. The results indicated that the latent heat of vaporization (h'_{fg}) in Eq. (3-1) should be replaced by:

$$h'_{fg} = h_{fg} \left[1 + 0.68 \frac{C_{p,f}(T_i - T_w)}{h_{fg}} \right] \quad (3-5)$$

For wavy and turbulent film condensation process, it is difficult to derive the heat transfer coefficient following the approach for laminar film flows. The practical engineering approach relies heavily on empirical correlations. The typical approach can be demonstrated by the correlation of Kutateladze (1982) [27] for the mean condensation heat transfer coefficient on a vertical plate with interfacial wave effects:

$$\bar{h} = \frac{k_f}{(v_f^2 / g)^{1/3}} \frac{\text{Re}_\delta}{1.08 \text{Re}_\delta^{1.22} - 5.2}, \quad 30 \leq \text{Re}_\delta \leq 1800 \quad (3-6)$$

For turbulent flow on a vertical plate, Labuntsov (1957) [28] recommended the following experimental correlation for the local condensation heat transfer coefficient:

$$h_x = 0.023 k_f \left[\frac{\rho_f (\rho_f - \rho_v) g}{\mu_f^2} \right]^{1/3} \text{Re}_\delta^{0.25} \text{Pr}_f^{-0.5} \quad (3-7)$$

Chun and Seban (1971) [29] obtained the following empirical correlation for evaporation of water from the vertical wall, which is applicable for condensation:

$$h_x = 3.8 \times 10^{-3} \frac{k_f}{(v_f^2 / g)^{1/3}} \text{Re}_\delta^{0.4} \text{Pr}_f^{-0.65} \quad (3-8)$$

Butterworth (1983) [30] obtained the average heat transfer coefficient for film condensation that includes laminar, wavy laminar, and turbulent flow by Equation (3-1), (3-6) and (3-7) in the following form:

$$\bar{h} = \frac{k_f}{(v_f^2 / g)^{1/3}} \frac{\text{Re}_\delta}{8750 + 58 \text{Pr}_f^{-0.5} (\text{Re}_\delta^{0.75} - 253)} \quad (3-9)$$

The practical total heat transfer coefficients used for containment vessel design and equipment qualification were obtained by Uchida (1964) [1] and Tagami (1965) [32] directly from test data close to prototypic conditions. Uchida's experiments were

performed with a 140 mm by 300 mm vertical plate in a closed vessel filled with steam and non-condensable gas. The air-steam mixture experiment was tested in the range of 0.1 to 0.28 MPa, resulting in a simple correlation for the total heat transfer coefficient given by:

$$h_{Uchida} = 380 \left(\frac{W_{n/c}}{1 - W_{n/c}} \right)^{-0.7}, \quad (3-10)$$

where $W_{n/c}$ represents the non-condensable air mass fractions. This correlation, which depends only on the ratio of mass fractions, is one of the correlations implemented in GOTHIC code.

Tagami conducted experiments using two different conditions: a forced convection and a natural convection. The forced convection was to simulate the initial stages of a large break LOCA, and the suggested the total heat transfer coefficient for the transient is given by

$$h_{TOT} = h_{TOT_max} \left(\frac{t}{t_A} \right)^{0.5}, \text{ where } h_{TOT_max} = 426 \left(\frac{E_A}{t_A V_c} \right)^{0.6}, \quad (3-11)$$

where E_A is a dimensional grouping of the energy added, V_c is the containment volume and t_A is the total time for the addition. For natural convection dominated quiescent conditions, Tagami proposed the following total heat transfer coefficient similar to Uchida's correlation:

$$h_{Tagami} = 11.4 + 284 \left(\frac{1 - W_{n/c}}{W_{n/c}} \right) \quad (3-12)$$

Uchida and Tagami's results indicated that the total condensation heat transfer coefficient for natural convection depended on only the mass fraction of non-condensable gas. Their conclusion was confirmed by Kataoka et al. (1992) [33], who obtained a correlation from experiments along a flat vertical plate between two pools of different temperatures.

$$h_{Kataoka} = 430 \left(\frac{W_{n/c}}{1 - W_{n/c}} \right)^{-0.8} \quad (3-13)$$

However, Dehbi et al. (1991) [9] conducted their experiments in a pressure range from 0.15 to 0.45 MPa, and concluded that the total heat transfer coefficient also depends on other containment variables, such as the containment pressure, temperature difference between the bulk steam and the wall, and the length of the condensation plate, as presented in the following correlation:

$$h_{Dehbi} = \frac{L^{0.05} \left[(3.7 + 28.7P) - (2438 + 458.3P) \log W_{n/c} \right]}{T_b - T_w}, \quad (3-14)$$

where L is total length of condensation wall, P represents the containment pressure, and $T_b - T_w$ denotes the temperature difference between bulk steam and condensation wall.

The dependence on other containment parameters was also reported by Green et al. (1994) [34] and Liu et al. (2000) [35]. Green's correlation was obtained from a realistic full-height test facility:

$$h_{Green} = 316 \left(\frac{W_{n/c}}{1 - W_{n/c}} \right)^{-0.86} \Delta T^{-0.15} \quad (3-15)$$

The correlation developed by Liu et al. is given by:

$$h_{Liu} = C X_s^{2.344} P^{0.252} \Delta T^{0.307} \quad (3-16)$$

where C is the constant coefficient, equal to 55.635 W/m², X_s is the steam mole fraction. This correlation is valid for the pressure range: 0.26 < P < 0.46 MPa.

In general, the values given by theoretical correlations are lower than the empirical heat transfer measurements in natural convection. Green and Almenas (1996) [36] proposed three mechanisms to account for such behavior:

- Theoretical models impose bulk velocities that usually are much lower than reality.
- Formation of mist in the gas-vapor boundary layer under saturated conditions may increase the sensible heat transfer from the atmosphere to the walls.
- The rippled nature of the condensate film also enhances the heat transfer process.

According to Peterson (1996) [37], those experimental condensation correlations are applicable if the boundary conditions are similar to those in the tests (pressure value, gas velocities, wall length, etc.). Otherwise, the correlation tends to under predict the results.

(D) Numerical Approach

Significant developments of computational power allow a numerical approach to validate and verify condensation models derived from experiments and analytical methods. There are great number of codes that can model and analyze condensation in containment for various nuclear systems shown in Table 3-2.

In nuclear system analysis, large, complex structures have to be represented by averaged "lumped" parameters. Recently, modelling of water vapor condensation in the presence of non-condensable gases has been conducted using commercial Computational Fluid Dynamics (CFD) [38]. The advantages of using CFD include the ability of predicting water vapor condensation in complex geometries with fewer assumptions in modelling the mass and heat transfer involved. These commercially available CFD codes generally do not have built-in steam condensation models. Consequently, it is necessary to implement steam condensation model via user-defined subroutines.

Sharma et al. (2012) [39] first applied the CFD-based generalized analysis for condensation modeling of containment wall surfaces. They suggested a generalized heat transfer coefficient based on a curve fitting of most of the reported semi-empirical condensation models. Their CFD simulation has been validated against the limited experiment data reported.

With respect to the condensation model, the nuclear numerical code can have either an empirical model, a boundary layer model, or a model that makes use of the heat and mass

transfer analogy. The nuclear reactor system computational codes have been validated extensively using many experiments. However, the validation performed in an Integrated Effect Test (IET) facility could call capability of the nuclear code into question due to the complexity of condensation phenomenon [40].

Table 3-2 Classification of condensation computer codes

Code	Type of code	Nature of the code	Condensation model
GOTHIC	Nuclear	Lumped	Uchida & Tagami or Boundary layer
RELAP5/MOD3.3	Nuclear	Lumped	Uchida or Heat & Mass analogy
FLUENT	Commercial	Field equations	User defined
CONTAIN	Nuclear	Lumped	Heat & Mass analogy
MELCOR	Nuclear	Lumped	Heat & Mass analogy
COMPACT	Nuclear	Lumped	Uchida & Tagami

3.3.2 Wave Dynamics of Film Flow

Through the review of the different correlations and models for film condensation heat transfer processes, we believe that the film flow dynamics should be of significant impact on the accurate prediction of the heat transfer coefficient. For instance, a vertical film flow always starts from droplets agglomeration, and gradually develops into laminar and then turbulent film flow depending on length of the cooling plate. For a test plate length mainly covered by a laminar film flow, its average heat transfer coefficient should be different from that of a prototypic condensation surface with large area covered by turbulent film flow. To address this scaling effect, the understanding of the film flow dynamics could shed light on the interpretation of the correlations based test data obtained on relatively short condensation plates. In nuclear engineering, unfortunately, the liquid film flows were more extensively examined from the interfacial heat/mass transfer perspective, than film flow itself [41].

On the other hand, wave dynamics of a thin liquid falling film has been the subject of intensive research for several decades in chemical engineering, where research focuses on film flow stability, different film types, measuring film thickness, and wavy film behaviors. Those investigations should be combined with the film condensation research, particularly for the scaling effects of experimental data. Generally, a falling film can be treated as open channel flow hydrodynamic systems in many aspects and features except wave natures of the instabilities [42].

Many researchers have performed studies on the flow dynamics of falling films following Kapitza's (1949) [46] pioneering work. Kapitza predicted that if the Reynolds number was greater than a specific value, the onset of waves would be examined by theoretical and experimental methods.

Table 3-3 Falling liquid film flow regimes by wave types

Author (Years)	Re # range	Flow regime	Features	Methods
Zadrazil et al. (2014) [43]	n/a	Ripple wave		Experiment
	n/a ~ 613	Dual wave	$\delta_w > \delta_s, \lambda_w < \lambda_s$	
	613 ~ 1,226	Thick ripple	$\delta_w \sim \delta_s, \lambda_w \sim \lambda_s$	
	1,226 ~ n/a	Disturbance wave	$\delta_w \gg \delta_s, \lambda_w < \lambda_s$	
Chang (1994) [44]	$\ll 1$	Low flow rate	Intermolecular force	Theory Experiment
	1 ~300	Intermediate region	Interfacial wave	
	300 ~ 1,000	Moderate region	Gevity-capillary instabilities begin	
	1000 <	Very large flow rate	Shear-wave	
Morioka et al. (1993) [45]	~ 16	Laminar		Experiment
	16 ~ 60	Frist transition	Experimentally examined failing film flowed outside of a pipe of 28 mm diameter and 1.4 m length.	
	60 ~300	Stable wavy-laminar		
	300 ~ 1600	Second transition		
	1600 <	Fully turbulent		

In case of a pipe flow, it is obvious that the flow transition from laminar to turbulent occurs around a critical Reynolds number. Similarly, as suggested by several researchers [13], [45], [47], the transition from laminar to turbulent falling film flow can occur at a critical Reynolds number from 1,600 to 1,800. A condensation falling film transforms to different types of waves dependent on its Reynolds number as shown in Table 3-3 [43]-[45].

Recently, Zadrazil et al. (2014) [43] experimentally examined the characteristics of falling film flow using a laser-based measurement technique. They classified the film flow regime according to the Reynolds number with wave features such as length of wave subtract (λ_s), wave length (λ_w), film thickness of wave (δ_w), and film thickness subtract (δ_s).

Nusselt (1916) [17] first derived a laminar film thickness based on the assumptions of viscous flow where no shear or wave motion exist at the liquid interface. This theory showed that the liquid film mass flow rate increases as a cubic power of film thickness. After Nusselt's work, much theoretical and experimental research for the film thickness has been conducted and tabulated at Table 3-4.

Brauner (1987) [48] developed a numerical study of turbulent wavy films by prescribing a geometric shape for large waves. He derived film thickness from energy and mass balances of laminar and turbulent wavy flow.

Table 3-4, Film thickness correlations for vertical downward film flow

Authors	Year	Geometry	Reynolds # Flow regime	Film thickness	Methods
Nusselt [17]	1916	Flat plate	Laminar	$\delta = (3\nu^2 \text{Re}/g)^{1/3}$	Theory
Kapitza [49]	1949	Flat plate	< 100	$\delta = (2.4\nu^2 \text{Re}/g)^{1/3}$	Theory Experiment
Brauer [50]	1956	Cylinder	20~1,800	$\delta = 0.302(3\nu^2/g)^{1/3} \text{Re}^{8/15}$	Experiment
Takahama & Kato [51]	1980	Cylinder	150~2,000	$\delta = 0.473(\nu^2/g)^{1/3} \text{Re}^{0.526}$	Experiment
Brauner [48]	1987	Flat plate	Laminar Turbulent	$\delta = (3/8\nu^2 \text{Re}/g)^{1/3}$ $\delta = 0.104(\nu^2/g)^{1/3} \text{Re}^{7/12}$	Theory Experiment
Karapantsios et al. [52]	1989	Cylinder	126~3,275	$\delta = 0.451(\nu^2/g)^{1/3} \text{Re}^{0.538}$	Experiment

4 TEST FACILITY AND MODIFICATION

To assess the system pressure effects on containment wall condensation heat transfer, the experimental investigation of this study has been performed on an existing test facility, the MASLWR test facility. It is a 1:3 height, 1:255 volume, and 1:1 time scaled model of the Multi-Application Small Light Water Reactor (MASLWR) proposed by INL, OSU and NEXANT in 2003 [55], which is the original model of the NuScale SMR under development. The facility is able to perform scaled tests for the natural circulation process in the primary loop, reactor system depressurization during accidental blowdowns, and the associated containment responses.

Figure 4-1 shows the schematics of the original test facility, which include an integral reactor model, a separate containment linked to the core through pipes that simulate vents and breaks, and a containment cooling pool. The summary of the scaling parameters are given in Table 4-1.

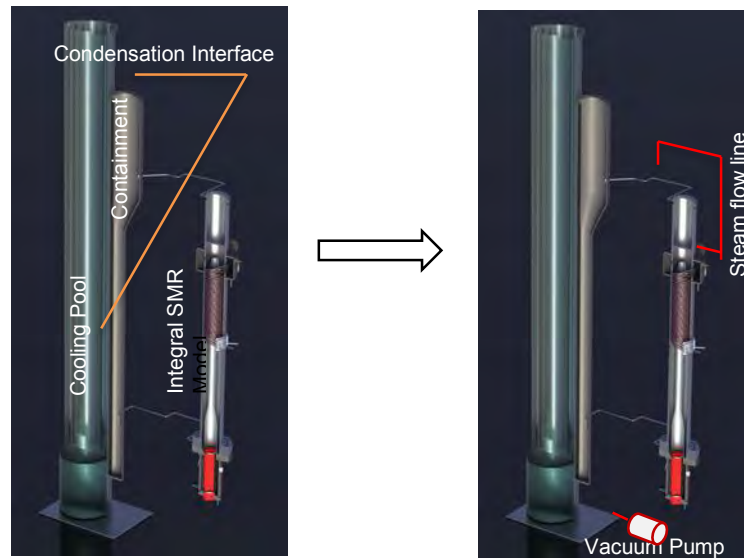


Figure 4-1, The MASLWR test facility and modifications for the proposed investigation

Table 4-1, OSU MASLWR test facility scaling [56]

Geometric Parameters	Scaling Ratio
Area	1:82.2
Length	1:3.1
Volume	1:254.7
Operating Parameters	
Temperature	1:1
Pressure	1:1
Time	1:1
Power	1:254.7
Mass Flow Rate	1:254.7
Fluid Velocity	1:3.1

A heat transfer plate lies between the cooling pool and the containment considering the difference in surface and volume scaling ratios. The high-pressure containment is a 5.75 m tall SS304 vessel consisting of three sections: a 3.87 m high lower cylindrical section of 0.27 m ID, a 1.21 m high upper cylindrical section of 0.508 m ID, and an eccentric cone section that connects the other two sections, as shown in Figure 4-1. Between the cooling pool and the containment, a 0.0381 m thick, 0.168 m wide, SA240 TP304 SS heat transfer plate runs 5.59 m vertical length. The containment and the cooling pool are insulated from atmosphere. The integral reactor model is capable of providing steam flow at a power of 398 kW with a maximum primary system pressure of 11.4 MPa at 590 K, sufficient to perform the proposed quasi-steady and transient containment condensation tests. In the steam vent line on the top of the integral reactor model, a vortex flow meter measures the steam flow rate controlled by an adjustable valve.

There were three planned minor modifications to the system for this investigation. However, due to the difficulty in accessing the containment inside, only two modifications have been completed. First, a vacuum pump has been added to the containment for the purpose of controlling the non-condensable gas fraction, an important parameter affecting the condensation rate. The vacuum pump, Model 8925a of Welch Vacuum - Thomas Ind., has 1.5 hp, is sufficient to draw a vacuum in the containment up to 1 Psia. The second modification has been done by connecting a ½" pipe line from the secondary loop steam outlet to the containment for controllable quasi-steady state condensation tests. In this way, a metered steady steam flow can be introduced in the containment from the secondary loop for better condensation heat transfer measurements.

In the original plan, a modification to the steam outlet nozzle in the containment was planned. Due to the difficulty in accessing the containment inside, this modification couldn't be performed. The intention was to add a diffusive, multidirectional steam injection nozzle in the containment to minimize the forced convection effects, isolating the other condensation mechanisms for a near "quiescent" condition. The impact of excluding this modification on this project is limited since the "quiescent" flow condition may not be established in the narrow space of the containment. The current vertical downward opening configuration may disturb the steam natural circulation in the containment, but should not affect the film flow on the containment wall. Nevertheless, the proposed "quiescent" tests will not be included in the investigation thereafter.

Relevant adjustments to the instrumentation, control system, and data acquisition systems have also been made. A three-way solenoid valve has been installed in the steam line, rerouting the steam flow to the containment while shutting-off the normal releasing path. Several thermocouples were installed to monitor the containment steam temperature and the water pool temperature. More importantly, the secondary loop system was upgraded, raising the pressure limit to 400 Psig from the original 250 Psig, enabling a maximum containment of 300 Psig in the tests. Flow meters, pipes and connections in the secondary loop were all replaced for the higher pressure rating, which was a more costing and time consuming than expected.

To meet the NQA-1 requirements, parallel to the test program of the NuScale Power using the same test facility, an independent OSU QA program was upgraded thoroughly, covering 18 elements of the nuclear qualify control requirements. Graduate students were trained as the QA manager, document control officer, and operators. Several internal surveillances and two external audits were conducted to identify the possible improvements of the QA program. Meanwhile, instruments were regularly calibrated to

assure the accuracy and performance, and appropriate procedures were developed for operation, maintenance, calibration, and training.

4.1 Reactor Pressure Vessel

The Reactor Pressure Vessel (RPV) contains a core heated by electrical power ($<400\text{kW}$), a riser section, pressurizer, helical coil steam generator, and down-comer. The primary loop simulates the prototypic natural circulation without coolant pump, as shown schematically in

Inside the RPV fluid enters the core and is heated so that it has buoyancy force. Then, coolant moves up through the riser and descends through the down-comer located between outer wall of the riser and the inner wall of the reactor vessel by losing its energy to helical coil shaped Steam Generator (SG). Once fluid gets to the shroud connected to the riser entrance, it reenters the core by natural circulation flow.

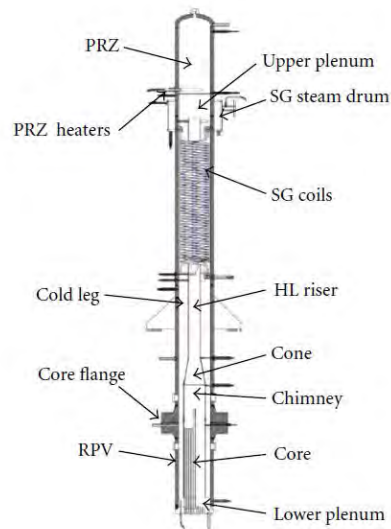


Figure 4-2, RPV internal components of MASLWR test facility [56].

4.2 High Pressure Containment

The MASLWR facility containment vessel, termed the High Pressure Containment (HPC), is a tall and narrow stainless steel vessel standing at a height of 5.75 meters with a lower and upper diameter of 27 cm and 51 cm respectively. The vessel was constructed in three shells with a conical frustum joining the lower and upper segments. A lower flat plate and upper torispherical head seal the ends of the vessel. Due to the scaling requirements of the containment, only a portion of the vessel's external surface may conduct heat to the cooling pool. A flat surface subtends the otherwise circular cross section along the entire height of the containment to accommodate mating between the vessels with the scaled heat transfer plate (Figure 4-3). The other surfaces of the HPC maintain a near-adiabatic condition with 10 cm of calcium silicate insulation and the optional use of three banks of strip heaters to maintain saturation conditions on the wall.

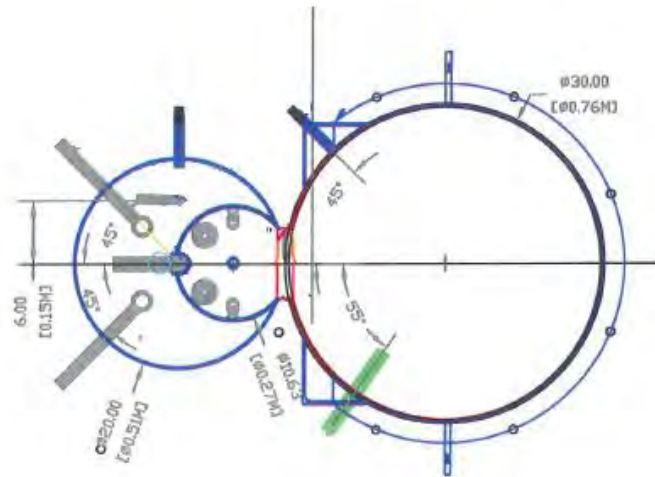


Figure 4-3, Cross-sectional view of the HPC (left) and CPV (right), joined by the HTP.

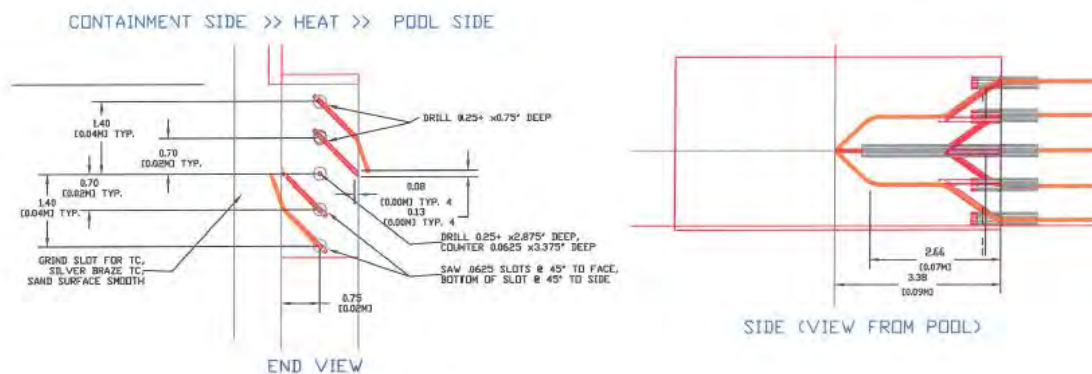


Figure 4-4, Diagram of HTP embedded thermocouples

Thermocouples are available in various locations within the HPC to provide information on the temperature distribution within the containment. As shown in Figure 4-4, these include a measurement for the steam bulk at the top of the containment (TF802) and a measurement for the condensate pool temperature (TF804). Thermocouples placed just off the surface of the heat transfer plate measure temperatures within the condensation boundary layers (TF821 through TF861). Several thermocouples measure the HPC vessel surface on the insulated sides of the containment (TW892 through TW894) and on the containment strip heaters (TH892-TH894).

System pressure is measured at the top of the containment relative to ambient pressure (PT801). The liquid level of the condensate is measured with a level differential pressure meter (LDP801). The level is based on a pressure differential between the top and bottom of the containment, equating to the hydrostatic head of the condensate pool. A standard density of water is used to convert to a length scale [56].

4.3 Heat Transfer Plate

The heat transfer plate (HTP) mates the HPC and cooling pool which, as scaled, represents the entire outside surface area of the prototypic MASLWR containments. As per the scaling requirements, the heat transfer plate in the MASLWR facility shares many parameters of the prototypic vessel. The balance between the convective and conductive heat transfer resistances must be maintained to replicate the spatial temperature response of the containment wall. Additionally, the thermal capacitance (tendency to absorb heat) must be conserved. As such, the HTP was designed with the same material and thickness of the prototypic containment wall [55], made of stainless steel type 316L. The HTP is 3.81 cm thick, 16.84 cm wide, and 5.65 meters tall, spanning all but the upper head of the containment vessel.

The heat flux on the condensation plate is the vital parameter to calculating the condensation heat transfer rate, which can be obtained via a temperature gradient measured from an array of embedded thermocouples (Figure 4-5 and Figure 4-4). Six sets of thermocouples are installed on the heat transfer plate at six elevations ($i=1$ through 6). In each elevation, there are 5 thermocouples equipped across the Heat Transfer Plate, with TW8i1 in the condensation film, TW8i2 in the plate near the HPC, TW8i3 located in the plate midline, TW8i4 in the plate close to the CPV side, and TW8i5 in the water pool.

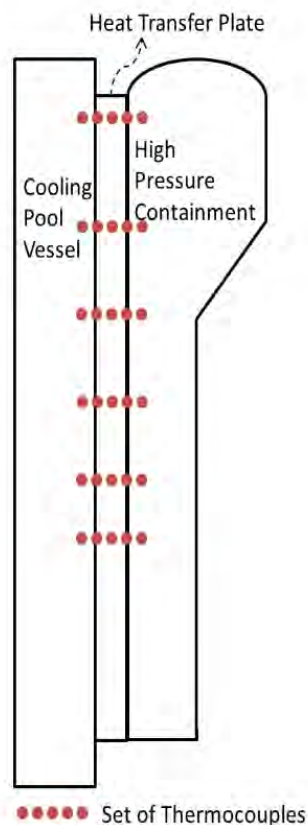


Figure 4-5, Six sets of thermocouples in HTP.

4.4 Cooling Pool Vessel

Across the HTP from the containment lies the cooling pool vessel (CPV), modeling the open pool in which the prototypic MASLWR containment is submerged. The CPV is taller than the HPC at 7.37 meters with an outside diameter of 76.84 cm and thickness of 0.635 cm. The CPV is insulated with 5 cm of calcium silicate. Thermocouples are employed to measure bulk temperature in the upper regions of the cooling pool (TF901 through TF903). A level differential pressure meter measures the liquid level (LDP901). [23]

4.5 Steam Supply System

To support this investigation, a modification was made to the steam supply system of the MASLWR test facility. For these tests, the primary side of the MASLWR facility was operated at reduced power to produce steam with the steam generator. The steam outlet piping, which normally exhausts to the environment, was modified to tap into the Automatic Depressurization System (ADS) penetrations on the containment. A set of remotely controlled valves allows the redirection of flow on command. The rate of steam supply was controlled by managing the feed flow pump as well as the core power.

The secondary circuit is pressurized throughout the tests. Choking of the flow between the steam generator and the containment occurs at the pressure regulating valve upstream of the modified steam piping. The inlet steam pressure is assumed to be at the HPC pressure (PT801) and the steam temperature is measured in the ADS penetration (TF873A). The flow rate is quantified with a magnetic flow meter in the feed flow line (FMM501).

4.6 Facility P&ID

The P&ID diagram shown in Figure 4-6 describes the placement of instruments in the HPC, HTP, and CPV. Table 4-2 contains the elevations of important thermocouple measurements relative to the bottom of the HPC.

Table 4-2, Elevation of relevant facility thermocouples

Instrument	Elevation (m)	Location
TF873A	4.68	Steam inlet
TF802	~5.60	Upper steam bulk
TF804	~0.50	Condensate pool
TW/TF81X	1.00	HTP
TW/TF82X	2.50	HTP
TW/TF83X	3.20	HTP
TW/TF84X	4.10	HTP
TW/TF85X	5.10	HTP
TW/TF86X	5.60	HTP
TW/TH891	3.27	HPC insulated surface
TW/TH892	4.13	HPC insulated surface
TW/TH893	5.15	HPC insulated surface
TW/TH894	5.66	HPC insulated surface
TF901	5.60	CPV bulk
TF902	4.10	CPV bulk
TF903	2.50	CPV bulk

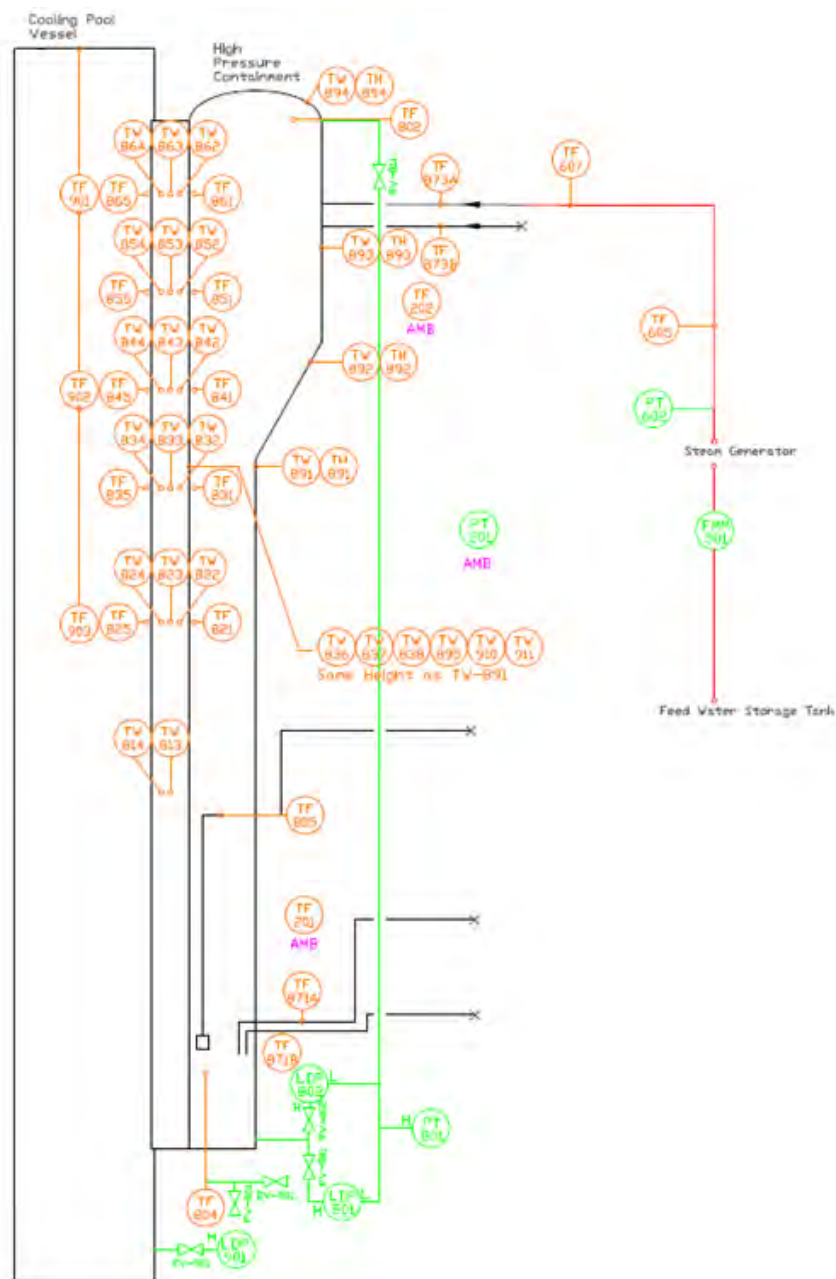


Figure 4-6, P&ID of relevant instruments of the OSU MASLWR test facility.

4.7 Facility Limitations

The MASLWR test facility provides a unique opportunity to evaluate condensation rates in an SMR containment configuration. However, experimental research into containment condensation has generally been performed with specifically designed separate effects facilities. These facilities allow for the purposeful placement of instrumentation and precise control of boundary conditions that cannot be accomplished with the MASLWR integral test facility. This facility was developed to broadly demonstrate the feasibility of the MASLWR concept. Since the conclusion of the original scope of work, use of the facility has been extended into testing it was not specifically designed for.

Since the construction of the MASLWR test facility, NuScale has adopted two design changes with relevance to this investigation. One of these changes is the adoption of a 'dry' containment. The containment of the original MASLWR concept is partially filled with water during operation. When the ECCS is actuated, the primary coolant from the RPV is vented into the pool to provide pressure suppression. In the present NuScale design, the containment is maintained at a deep vacuum. This removes the need for insulation and provides other operational benefits, however the peak pressures expected following an ECCS actuation are much higher.

Since the design change, MASLWR testing has generally been performed with a dry containment. While the facility can adequately function in this manner, the arrangement of instrumentation in the HPC is well suited to characterizing condensation occurring on the lower half of the plate as this region was intended on being submerged (i.e. lesser temperature resolution). Furthermore, the sole HTP thermocouple measuring the lower CPV surface temperature has since been damaged and is inoperative (TW812).

The second design change is a significant increase in the primary coolant operating pressure. In addition to the dry containment, these two changes increase peak containment pressure several-fold over the MASLWR concept. While the test facility was scaled to operate at the prototypic temperatures and pressures of the original concept, the facility is not designed to handle the increased pressure of the present NuScale design. As such, this investigation is limited to evaluating condensation at relatively moderate pressures (~21 bar). The same tests will ultimately be performed with the renovated facility across the full range of prototypic pressures.

Other limitations of the facility include a lack of bulk temperature measurements along the height of the containment. These temperature measurements are necessary for quantifying local non-condensable gas concentrations. Without these measurements, assumptions must be made as to the mixing of the gases as well as to the thermodynamic state of the steam (i.e. superheated vs. saturated).

A final pair of limitations make it difficult to maintain steady state conditions in the containment. Over the course of a test, the temperature of the cooling pool heat sink increases substantially. Additionally, the available condensation area on the heat transfer plate continuously decreases as the condensate level rises. Both of these limitations tend to reduce overall heat transfer rates over the course of the tests which leads to continuously increasing system pressure if the steam supply rate is kept constant.

5 FILM CONDENSATION SCALING ANALYSIS

The MASLWR test facility is a 1:3 height, 1:255 volume and 1:1 time scaled full pressure model of the Multi-Application Small Light Water Reactor. The original scaling analysis was carried out by Reyes [56] in 2002, following the Hierarchical Two-Tiered Scaling (H2TS) methodology [57]. For this NEUP project, no plan was proposed to change the global scaling of the MASLWR test facility, and the integral test data can be interpreted for the prototypic MASWLR conditions using the original scaling ratios.

However, for the shorter condensation plate in the scaled down test facility, the condensate film thickness is thinner and the film flow regimes may not fully represent the same film flow conditions as in the prototype, resulting in possible distortions in the film heat transfer coefficient. The shorter film flow length corresponds to a thinner film thickness, corresponding to a different average conductive heat transfer rate from that on a longer prototypic condensation plate. This might be considered to be a non-conservative distortion in reactor safety analysis. On the other hand, the average flow velocity of a thin film should be lower than that of a thick film, possibly leading to a weaker convective heat transfer rate, which could be viewed as a conservative distortion. These conflicting conclusions of the simple qualitative assessments require a scaling analysis to quantify the scaling distortion. In this study, the scaling analysis focuses on the water film flow heat transfer process through a so-called bottom-up scaling approach of the H2TS scaling methodology.

The bottom-up scaling along with the top-down scaling constitutes the Hierarchical, Two-Tiered Scaling methodology; ensuring the key prototypic processes and phenomena to be preserved in the model system. Generally, the first step is to identify the important transfer processes and potentially dominant mechanisms. In our case, the bottom event of concern is the film condensation process associated with film conduction, convection and condensation phenomena. The most important mechanisms, based on our prognosis, are the balance of condensation and convection. To capture the scaling effects of the two major mechanisms, the following three analyses have been performed.

5.1 Scaling Based on Empirical Correlation

The simplest film condensation heat transfer model is the empirical correlation of Dehbi et al. [9], which correlates the overall condensation film heat transfer with the bulk vapor temperature T_b , wall surface temperature T_w , system pressure P , non-condensable gas mass fraction W , and the condensation plate length L . Accordingly, the heat transfer coefficient scaling ratio of the model to the prototypic system is simply given by:

$$h_{Dehbi,R} = \frac{(h_{Dehbi})_{model}}{(h_{Dehbi})_{prototype}} = \left(\frac{L^{0.05} [(3.7 + 28.7P) - (2438 + 458.3P) \log W]}{T_b - T_w} \right)_{model} = \gamma^{0.05}, \quad (5-1)$$

where γ represents the length ratio of the condensation plate. Since the exponent of the length is merely 0.05, it is expected that the heat transfer coefficient ratio between the model and the prototypic system is very close to unity. In other words, as long as the model system pressure, temperature and non-condensable gas mass fraction remain the

same as in the prototypic system, the total film condensation heat transfer coefficient in the model system should be a good representation of the prototypic system.

5.2 Scaling Based Diffusion Layer Model

The second scaling consideration is based on the diffusion layer model, a lumped approach for the film heat transfer rate estimation over the length of the heat transfer plate, mostly applicable to turbulent film flows. With the presence of non-condensable gas, the diffusion layer model gives a useful approach to predict the condensation rate. Non-condensable gas accumulates at the liquid-vapor interface when the condensate liquid film forms near the cold wall. The condensate film and heat/mass transfer rates in gas/vapor mixtures are calculated separately in the diffusion layer model. Figure 5-1 illustrates the schematic for the thermal resistance of the model.

Under steady-state condition, the heat fluxes on the film surface and on the cooling wall remain the same. The condensate heat transfer is driven by the temperature difference between the cooling wall and the interface ($T_i - T_w$). Both latent and sensible heat are transferred through the interface, and the gas/vapor mixture regions.

$$q'' = h_{film}(T_i - T_w) = h_{cond}(T_b - T_i) + h_{conv}(T_b - T_i) = h_T(T_b - T_w) \quad (5-2)$$

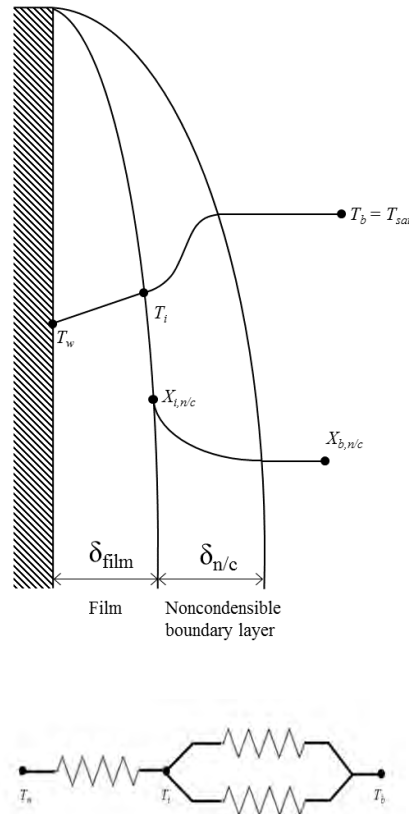


Figure 5-1, Illustrative outline and thermal resistance network of the diffusion layer model

By rearranging Eq. (5-1), the total heat transfer coefficient is readily given by:

$$h_T = \frac{h_{film}(h_{conv} + h_{cond})}{h_{film} + h_{conv} + h_{cond}} \quad (5-3)$$

The local film heat transfer coefficient (h_{film}) is from a modified Nusselt's equation [17]:

$$h_{film} = \left[\frac{\rho_f(\rho_f - \rho_{v,b})gh'_{fg}k_f^3}{4\mu_f x(T_i - T_w)} \right]^{1/4} \Psi, \quad (5-4)$$

where (h'_{fg}) accounts for condensate subcooling and temperature change across the film,

$$h'_{fg} = h_{fg} \left[1 + 0.68 \frac{C_{p,f}(T_i - T_w)}{h_{fg}} \right], \quad (5-5)$$

and Ψ takes into account the enhancement in heat transfer caused by the rippled surface of the film (waviness effect).

$$\Psi = \text{Re}_l^{0.04} \quad (5-6)$$

Kutateladze [27] recommended the following modified Reynolds number, averaged over the containment length, in the laminar wavy region:

$$\text{Re}_l = \left[\frac{3.7k_f L(T_i - T_w)}{\mu_f h'_{fg} (v_f^2/g)^{1/3}} + 4.8 \right]^{0.82} = [A \cdot L + 4.8]^{0.82}, \quad (5-7)$$

where A is a combination of properties and fluid conditions such that

$$A = \frac{3.7k_f (T_i - T_w)}{\mu_f h'_{fg} (v_f^2/g)^{1/3}} \quad (5-8)$$

The average film condensation coefficient for the entire length is therefore given by:

$$\bar{h}_{film} = \frac{1}{L} \int_0^L h_{film}(x) dx = 0.943 \left[\frac{\rho_l(\rho_l - \rho_{v,b})gh'_{fg}k_l^3}{4\mu_l L(T_i - T_w)} \right]^{1/4} \text{Re}_l^{0.04} \quad (5-9)$$

Using the heat and mass transfer analogy and the Clapeyron equation, the parallel coupling of convective and condensation heat transfers can be expressed as:

$$h_{con} = h_{conv} + h_{cond} = \frac{Sh}{L} k_{eff} \quad (5-10)$$

where Sh is the suction corrected Sherwood number, and k_{eff} is an effective thermal conductivity of the condensation and convection term:

$$Sh = 0.13Gr^{1/3}Sc^{1/3}\Theta, \quad (5-11)$$

$$k_{eff} = k_{cond} + \left(\frac{Pr}{Sc}\right)^{1/3} k_g, \quad (5-12)$$

where the Grashof number and the Schmidt number are defined bellow, respectively:

$$Gr = \frac{g\beta(T_w - T_i)L^3}{\nu^2} \quad (5-13)$$

$$Sc = \frac{\nu}{D} \quad (5-14)$$

Herranz et al. [25] suggested a suction factor to improve the Sherwood number:

$$\Theta = \frac{X_{nc}^i}{X_{nc}^{avg}} \quad (5-15)$$

Peterson et al. [24] integrated the Clapeyron equation over a temperature range and derived the following condensation thermal conductivity (k_{cond}) formula:

$$k_{cond} = \frac{C\dot{m}_v \bar{h}_{fg}^2 D}{R_v T_i T_b} \Phi, \quad (5-16)$$

where Φ is the ratio between the average molar fractions of steam and non-condensable gas in the boundary layer.

$$\Phi = \frac{\chi_{v,avg}}{\chi_{g,avg}} \quad (5-17)$$

Using the diffusion layer model, the ratio of the total heat transfer coefficients, ($h_{T,R}$) is examined by comparing the scaled-down test facility with the prototype facility.

$$h_{T,R} = \frac{(h_T)_{model}}{(h_T)_{prototype}} = \left[\frac{(\bar{h}_{film})_{model}}{(\bar{h}_{film})_{prototype}} \right] \left[\frac{(h_{con})_{model}}{(h_{con})_{prototype}} \right] \left[\frac{(\bar{h}_{film} + h_{con})_{model}}{(\bar{h}_{film} + h_{con})_{prototype}} \right]^{-1} \quad (5-18)$$

Finally, the total heat transfer coefficient ratio ($h_{T,R}$) can be examined separately in the following form:

$$h_{T,R} = \frac{(h_T)_{model}}{(h_T)_{prototype}} = (\bar{h}_{film,R}) \cdot (h_{con,R}) \cdot (\bar{h}_{film} + h_{con})_R^{-1} \quad (5-19)$$

5.2.1 Film Condensation Heat Transfer Coefficient

The MASLWR facility scaling report [56] showed the scaled-down facility was constructed to preserve the isochronicity of the two systems (experimental and prototypical) and established a thermodynamic similitude. The ratio of the film condensation heat transfer coefficient, the first term of Eq. (5-19), can be expressed as follows using Eq. (5-9).

$$\bar{h}_{film,R} = \frac{(\bar{h}_{film})_{model}}{(\bar{h}_{film})_{prototype}} = \frac{\left(\frac{3}{4} h_{film}(L) \text{Re}_l^{0.04}\right)_{model}}{\left(\frac{3}{4} h_{film}(L) \text{Re}_l^{0.04}\right)_{prototype}} = \left(\frac{1}{\gamma}\right)^{1/4} \left(\frac{(\text{Re}_l^{0.04})_{model}}{(\text{Re}_l^{0.04})_{prototype}}\right) \quad (5-20)$$

According to Eqs. (5-7) and (5-8), the ratio of the Reynolds number is a function of geometry, subcooling (ΔT) and fluid properties as follows

$$\text{Re}_{f,R} = \left[\frac{(L + 4.8/A)_{model}}{(L + 4.8/A)_{prototype}} \right]^{0.82} \quad (5-21)$$

Combining Eqs. (5-21) and (5-22) yields the ratio of the film condensation heat transfer coefficient:

$$\bar{h}_{film,R} = \gamma^{-1/4} \left[\frac{(L + 4.8/A)_{model}}{(L + 4.8/A)_{prototype}} \right]^{0.0328} \quad (5-22)$$

5.2.2 Gas/Steam Heat Transfer Coefficient

The ratio of the parallel coupling resistance, h_{con} ($=h_{cond}+h_{conv}$), composed of the length scaling factor (γ), the ratio of the Sherwood number and effective conductivity (k_{eff}) is as follows:

$$h_{con,R} = \frac{(h_{con,R})_{model}}{(h_{con,R})_{prototype}} = \frac{\left(\frac{Sh}{L} k_{eff}\right)_{model}}{\left(\frac{Sh}{L} k_{eff}\right)_{prototype}} = \frac{1}{\gamma} \left[\frac{(Sh)_{model}}{(Sh)_{prototype}} \right] \left[\frac{(k_{eff})_{model}}{(k_{eff})_{prototype}} \right] \quad (5-23)$$

Using definitions of the Sherwood number and the Grashof number, the Sh_R is given by,

$$Sh_R = \frac{(0.13Gr^{1/3}Sc^{1/3}\theta)_{model}}{(0.13Gr^{1/3}Sc^{1/3}\theta)_{prototype}} = \gamma \quad (5-24)$$

Consequently, the ratio of k_{eff} is one, since all thermodynamic properties are the same within the two systems.

$$k_{eff,R} = \frac{\left(k_{cond} + \left(\frac{Pr}{Sc} \right)^{1/3} k_g \right)_{model}}{\left(k_{cond} + \left(\frac{Pr}{Sc} \right)^{1/3} k_g \right)_{prototype}} = 1 \quad (5-25)$$

From Eqs. (5-24), (5-25) and (5-26), the ratio of parallel coupling resistance equals one.

$$h_{con,R} = 1 \quad (5-26)$$

5.2.3 Film Condensation and Gas/Steam Heat Transfer Coefficient

The last term of Eq. (5-19), $(h_{film} + h_{con})_R$, can be divided by $(\bar{h}_{film})_{prototype}$ in both numerator and denominator, leading to

$$(\bar{h}_{film} + h_{con})_R = \left[\frac{(\bar{h}_{film} + h_{con})_{model}}{(\bar{h}_{film} + h_{con})_{prototype}} \right] = \left[\frac{\bar{h}_{film,R} + (h_{con}/\bar{h}_{film})_R}{1 + (h_{con}/\bar{h}_{film})_{prototype}} \right] \quad (5-27)$$

Using Eqs. (5-23), (5-27), and (5-28), the total heat transfer coefficient ratio between two systems is readily given by

$$h_{T,R} = \left[\gamma^{-1/4} \left[\frac{(L + 4.8/A)_{model}}{(L + 4.8/A)_{prototype}} \right]^{0.0328} \right] \left[\frac{\bar{h}_{film,R} + (h_{con}/\bar{h}_{film})_R}{1 + (h_{con}/\bar{h}_{film})_{prototype}} \right]^{-1} \quad (5-28)$$

The numerical results, compared with the empirical correlation of Dehbi et al. will be discussed in section 5.5.

5.3 Scaling Based on Local Heat Transfer Model

The local heat transfer model is based on a one-dimensional film flow modeling using balance equations. Local heat transfer coefficient will be applied depending on local film thickness, film velocity, and laminar/turbulent flow regime. With the assumptions of

- Constant properties (ρ, μ),
- One-dimensional incompressible flow,
- Gravity force dominated film flow,
- Negligible shear stress at interface;
- Saturated film flow for simplicity of the hydro-dynamic behavior;
- Constant condensation rate per unit area (\dot{m}_{cond})

As demonstrated in Figure 5-2, the one-dimensional film flow governing mass and momentum equations are given by:

$$\frac{\partial \delta}{\partial t} + \frac{\partial (u\delta)}{\partial x} = \frac{\dot{m}_{cond}}{\rho} \quad (5-29)$$

$$\frac{\partial (u\delta)}{\partial t} + \frac{\partial (u^2\delta)}{\partial x} = g\delta - \frac{\tau_w}{\rho} \quad (5-30)$$

Since the falling film gradually transits from laminar to turbulence, the friction factor should depend on the Reynolds number. The wall shear stress is given by:

$$\tau_w = C_f \frac{1}{2} \rho u^2 \quad (5-31)$$

Laminar film flow [47]: $C_{f,L} = \frac{6}{Re}$ (5-32)

Turbulent Flow [50]: $C_{f,T} = \frac{0.408}{Re^{8/15}}$ (5-33)

The reported transition from laminar flow to turbulent flow occurs at $Re=1600$, which can also be confirmed using a perturbation analysis on the proposed model (Lee, 2015 [58]).

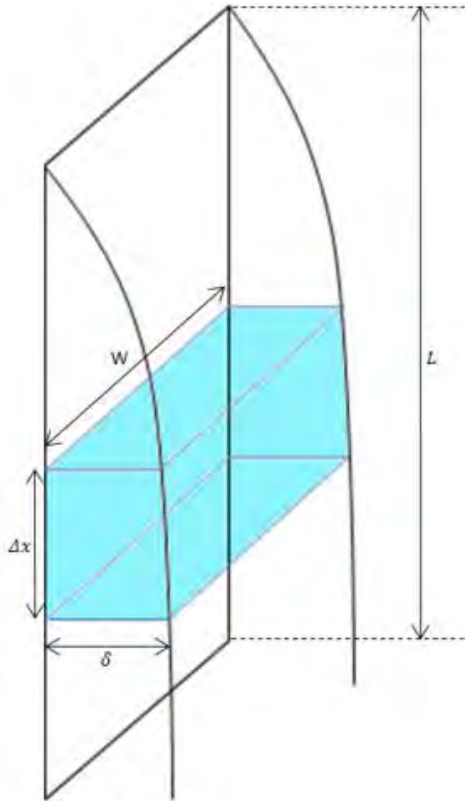


Figure 5-2, One-dimensional film flow model.

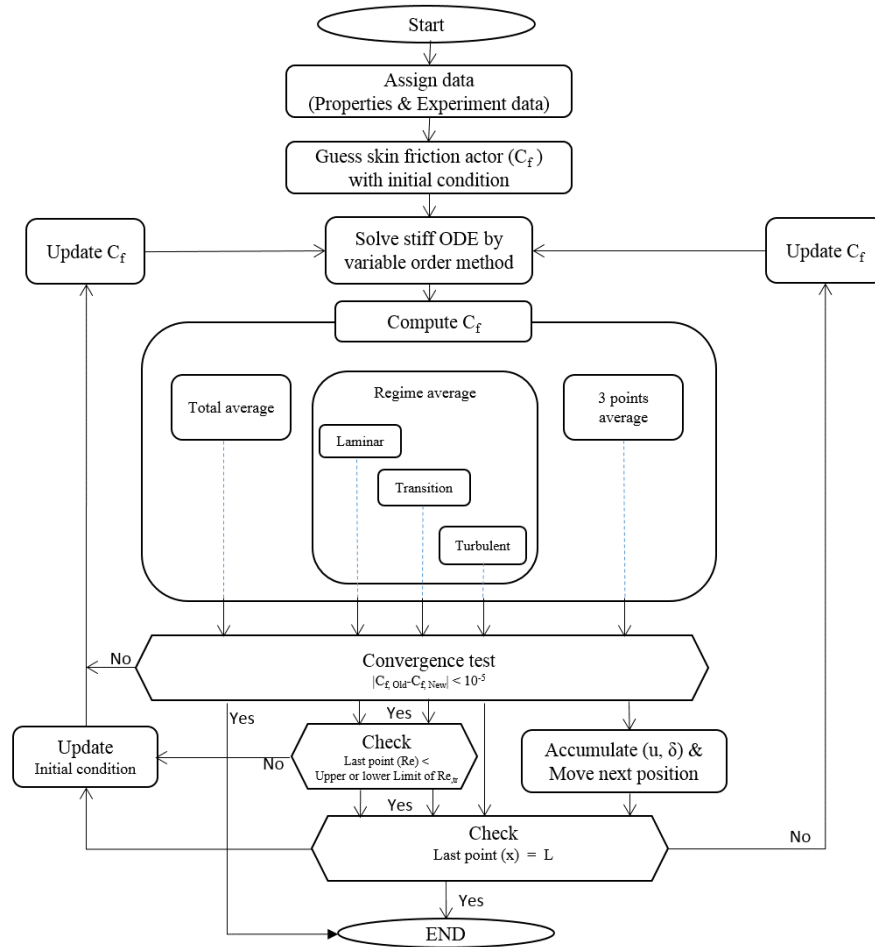


Figure 5-3, Flow chart for solving steady-state condensing film flow [58].

Using MATLAB code, Eqs. (5-29) and (5-30) can be solved numerically following the flow chart shown in Figure 5-3, and quasi-steady film velocity and the film thickness distributions for condensation rates at different time in a blow down test are presented in Figure 5-4 and Figure 5-5.

In a typical blow-down test, as the experimental time increased, the condensate rate decreased. For a specific time period, the film flow is considered to be approximately steady with a constant condensation rate. These solutions suggest that the film flow on the condensation plate will experience laminar to turbulent transition at certain location depending on the condensation rate. For high condensation flow rate, equivalent to the blow-down period around 800 s, the flow regime transition occurs at around 3 meter down the condensation plate which covers roughly 3/5 of the MASLWR high pressure containment height. For a prototypic MASLWR reactor with an 18 m tall containment, the laminar flow region only occupies 1/6 of the true condensation length. Therefore, the model system is dominated by laminar film flow, whereas the prototypic system by turbulent film flow. As the blow-down process progresses, the transition point shifts downstream corresponding to lower condensation rate, and the difference of flow regime becomes more substantial.

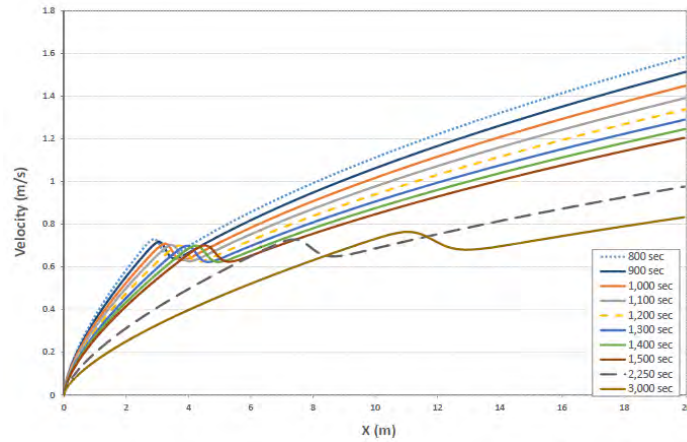


Figure 5-4, Velocity profiles along a condensation plate

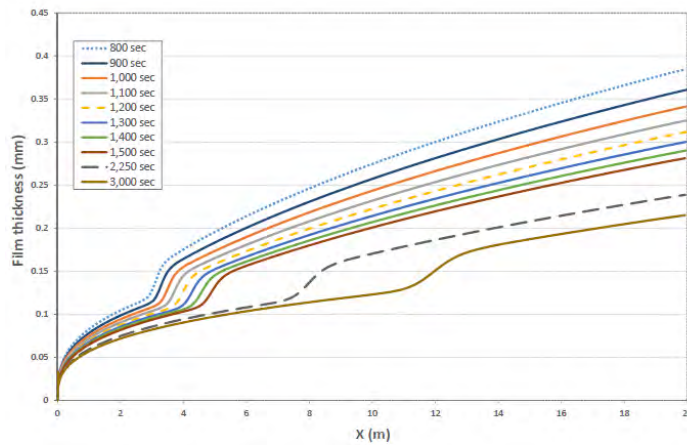


Figure 5-5, Film thickness profiles along a condensation plate.

Comparing the film thickness solutions of the flow model with previous work in turbulent film flow regime, the results are presented in Figure 5-6. The total average model considers the smooth transition region using average friction coefficient from laminar and turbulent flows with a weighting function proposed by Yen [60]. The 3-point average model takes the average value of the laminar and turbulent flow friction factors within the range of $Re=1600\pm200$.

The film model predicted film thickness agrees well with Brauner's (1987) experimental results [48]. Due to curvature effects for condensation on cylindrical surfaces, the film thickness predictions of Karapantsios et al. (1989) [52], Takahama & Kato (1980) [51], and Brauer's (1956) [50] are generally greater than the prediction of the current flat plate film flow model.

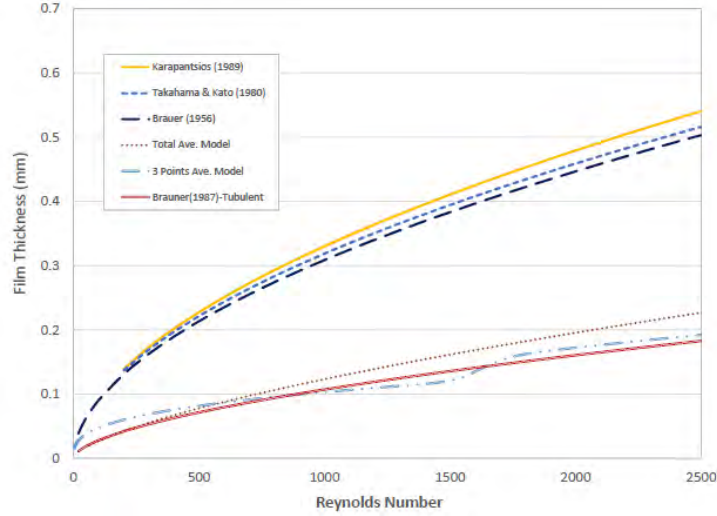


Figure 5-6, Comparison of film thickness between suggested models and previous work in turbulent film flow regime

For different flow regimes, the condensation heat transfer coefficients are different, and thus the average heat transfer coefficient will be obtained through the flow film model for the purpose of identifying the scaling ratio. In this study the following local correlations for each regime are employed:

Laminar (Nusselt, 1916, [17]):
$$h_x = \left[\frac{\rho_f (\rho_f - \rho_{v,b}) g h'_{fg} k_f^3}{4 \mu_f x (T_b - T_w)} \right]^{1/4} \quad (5-34)$$

Turbulent (Labuntsov, 1966, [59]):
$$h_x = 3.8 \times 10^{-3} \frac{k_f}{(v_f^2 / g)^{1/3}} \text{Re}^{0.4} \text{Pr}_f^{-0.65} \quad (5-35)$$

5.4 Scaling Analysis Results

Using those three approaches, i.e., empirical correlation, diffusion layer model and the local film flow model developed in this study, the total heat transfer rate ratio between the model system and the prototypic system can be readily computed against the geometrical length-scaling ratio (length scale). The scaling results are presented in Figure 5-7, with the system pressure around 2 bar at about 1000 s of the blow-down transient.

From the diffusion layer model, the length-scaling factor doesn't apparently affect the total heat transfer rate. It suggests that the model system's total heat transfer coefficient can be directly applicable to the prototypic system without much distortion, because it inherently assumed that the convection is turbulent natural circulations in the containment. The ratio of total heat transfer rate from Dehbi's correlation decreases slightly as the length scaling factor decreases. Therefore, the total heat transfer coefficient in the test facility should be slightly lower than that of the prototypic system (about 5% drop for a 1/3 height scaled test condensation plate). For safety design assessment, such a distortion is acceptable, and can be considered as a conservative distortion.

Calculations based on the developed one-dimensional film flow model suggests that the scaled down facility might substantially underestimate the condensation heat transfer rate as shown in Figure 5-7. With the assumption that m'' (condensation rate per unit area) is same between a test facility and the prototype, results showed that a 1/3 length scale test facility might underestimate the heat transfer rate by 50 % of the prototype value. The reason for underestimation is that the condensation heat transfer rate depends on the flow regime that is associated with the local film Reynolds number, which can be different along the length of a vertical structure. When the test plate length is reduced below $\sim 1/7$ of the prototypic length, it covers only laminar film flow, and the total heat transfer coefficient ratio remains constant.

In conclusion, the test facility is scaled to 1/3 of the prototypic length, mostly covering large portion of laminar film flow, leading to lower heat transfer coefficient. Although it is conservative in reactor safety analysis, the significant difference could under estimate the prototypic condensation heat transfer rate, resulting in inaccurate prediction of the decay heat removal capability. Further investigation is thus needed to quantify the scaling distortion for safety analysis code validation.

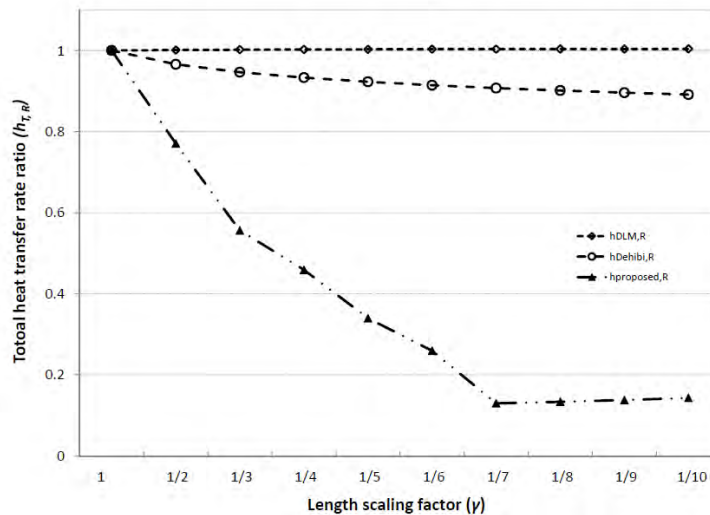


Figure 5-7, Total heat transfer rate ratio with respect to length scaling factor.

6 EXPERIMENTAL INVESTIGATION

The test investigation includes test matrix and procedure, test overview, data processing and analysis methods, test results and error analysis.

6.1 Test Matrix and Procedure

A series of tests were devised to characterize the condensation rates in the MASLWR containment. The objective of these tests was to achieve, in a controlled manner, high steam pressure in the containment vessel while measuring the condensation rate occurring along the heat transfer plate.

6.1.1 Test Set 1

Table 6-1, Test matrix for first set of condensation tests

<i>Air Pressure:</i>	<i>0.07 bar</i>	<i>0.5 bar</i>	<i>1.0 bar</i>
<i>40 kW</i>	Test 1.1	Test 1.3	Test 1.5
<i>80 kW</i>	Test 1.2	Test 1.4	Test 1.6

Steam for these tests was produced in the steam generator while operating the MASLWR facility at steady-state. The startup procedure involved slowly raising the RPV pressure and temperature with use of the pressurizer and core heaters. For the first round of testing, the core power was raised to either 10% or 20% of nominal operating power, 40 kW and 80 kW respectively. Secondary flow through the steam generator was initiated during the heat-up to promote natural circulation in the primary loop. The secondary flow was eventually increased until it was removing the entirety of the heat being supplied with the heaters. Appropriate control of the secondary was important for safely reaching operating conditions and was performed with the feed flow pump and the steam pressure regulating valve. The primary system was allowed to reach steady state as indicated by stable flow rates and fluid temperatures along the primary loop. Steam being generated at this stage was exhausted to the environment.

Prior to introducing steam into the containment, the desired initial air inventory in the containment was achieved with use of a vacuum pump. For the first round of tests, the containment was evacuated to either a 'near-vacuum' condition, 'half-vacuum' condition, or left at atmospheric pressure. At 1 Psia or 0.07 bar, the near vacuum condition was the lowest pressure that could be achieved with the containment vacuum pump.

For the first set of tests, it was decided that preheat would be used to mitigate the thermal inertia of the HPC surface. After evacuating the containment to the desired pressure, the three banks of heaters were set achieve a wall temperature of approximately 160°C, corresponding to a saturation pressure of about 6 bar. The heaters were turned off at the initiation of the tests to avoid energy balance complications.

Once the pre-test checklist had been completed, the tests were initiated by directing steam into the modified steam piping which taps into the containment. For the first round of tests, the steam pressure was maintained at approximately 21 bar in the secondary. Strip heating was employed to maintain saturation conditions along the length of the piping to prevent condensation upstream of the containment.

The first round of tests involved introducing a constant rate of steam into the containment until either the containment approached its design pressure of almost 21 bar or a predetermined time of 90 minutes had elapsed. The rate of steam being supplied to the containment was equal to the rate of steam being generated in the secondary, equivalent to either 40 kW or 80 kW of core power depending on the test. Once the termination conditions for the tests were met, the steam supply was directed back to the normal steam path and the containment was allowed to depressurize naturally from condensation. For the first two tests performed (Test 1.1 and Test 1.2), steam was redirected back into the containment for a second trial after 10 minutes of natural depressurization. However, for consistency, only the first of the two trials is considered in the analysis. When testing was complete for the day, the RPV was depressurized and allowed to cool down.

6.1.2 Test Set 2

Table 6-2, Test matrix for second set of condensation tests

	<i>Initial Pressure</i>	<i>Steam Drum Pressure</i>	<i>Ramp-Up Time</i>	<i>Reduced Power</i>	<i>Reduced Feed Flow (kg/s)</i>
<i>Test 2.1</i>	Near-Vacuum	5.17 bar	4 minutes	44 kW	0.0139
<i>Test 2.2</i>	Near-Vacuum	10.34 bar	6 minutes	52 kW	0.0164
<i>Test 2.3</i>	Near-Vacuum	17.24 bar	8 minutes	60 kW	0.0189
<i>Test 2.4</i>	Near-Vacuum	20.68 bar	10 minutes	68 kW	0.0215
<i>Test 2.5</i>	Atmospheric	10.34 bar	3 minutes	40 kW	0.0126
<i>Test 2.6</i>	Atmospheric	13.79 bar	5 minutes	48 kW	0.0151
<i>Test 2.7</i>	Atmospheric	20.68 bar	7 minutes	56 kW	0.0177

The first tests were performed such that the containment pressure and temperature were continually increasing throughout the testing period which may have introduced transient effects that cannot easily be accounted for. The MASLWR facility was not designed to support the type of steady state containment conditions that would be desirable for these containment condensation experiments. Nevertheless, a second set of tests were devised to mitigate transient effects and generally improve test conditions. The objective for these tests was to achieve a period of stable or even slightly decreasing containment pressure. The results would help determine if the continuously increasing temperatures and pressures from the first tests were influencing the observed trends in condensation rates.

The second set of tests were conducted by quickly ramping up the containment pressure and then reducing the flow rate of steam into the vessel so as to roughly match the rate of condensation on the heat transfer plate. Each test was designed to achieve and maintain (for a short period of time) a unique steam pressure. To ramp-up pressure in the containment at the beginning of each test, the core power was set to 120 kW with an appropriate feed flow rate. Calculations were made beforehand for each test to determine a 'ramp-up time' as well as a reduced core power and feed flow rate estimated to roughly match the condensation rate on the heat transfer plate. Containment pressure eventually began to increase again. This is because, as the tests progressed, the exposed condensation surface area decreased and the heat sink warmed up. These tests were terminated after 30 minutes had elapsed since the initial steam injection. Containment strip heating was not employed with these tests to simplify energy accounting.

While performing a scoping run of these tests, it was found that flow instabilities occurred once the steam flow rate was reduced. The instability was determined to be related to regulating a large pressure drop (i.e. choked flow) with a low mass flow rate (below critical flow rates). To avoid this, the steam drum pressures were reduced such that they were less than twice the target containment pressure to avoid critical flow.

6.2 Test Overview

The first set of tests saw pressure rise in the containment until either the pressure approached operating limits or a predetermined amount of time had elapsed. The cases with the lower steam flow (Test 1.1, Test 1.3, and Test 1.5) pressurized rather slowly as the condensation rate followed closely behind the rate of steam addition to the containment. Each of these tests was terminated after 90 minutes of testing had elapsed while the containment pressure remained well below design limits. The cases which used a higher power and steam flow (Test 1.2, Test 1.4, and Test 1.6) pressurized relatively rapidly as the condensation rate was outpaced by the rate of steam addition. These high power tests were terminated between 18 and 35 minutes once the containment design pressure was reached.

Table 6-3, Description of the first set of tests

	<i>Applied Power</i>	<i>Steam Rate</i>	<i>Flow</i>	<i>Initial Pressure</i>	<i>Final Pressure</i>	<i>Final NCG Fraction</i>	<i>Duration</i>
<i>Test 1.1</i>	40 kW	~0.0133 kg/s		0.07 bar	8.73 bar	0.017	90 min
<i>Test 1.2</i>	80 kW	~0.0264 kg/s		0.07 bar	20.59 bar	0.007	34 min
<i>Test 1.3</i>	40 kW	~0.0133 kg/s		.52 bar	10.94 bar	0.096	90 min
<i>Test 1.4</i>	80 kW	~0.0264 kg/s		.52 bar	20.59 bar	0.052	24 min
<i>Test 1.5</i>	40 kW	~0.0133 kg/s		1.31 bar	14.42 bar	0.186	90 min
<i>Test 1.6</i>	80 kW	~0.0264 kg/s		1.32 bar	20.60 bar	0.124	18 min

Figure 6-1 and Figure 6-2 show the containment pressures through the duration of each test with markings for the left and right bounds of the regions of interest. The low steam flow rates lead to a relatively unsteady pressurization in the containment, as can be seen in Figure 6-1. This appears to be due to regulating a large pressure drop (i.e. choked flow) with a low mass flow rate (below critical flow rates). A region of interest of 4000 seconds was selected for the low flow rate tests to avoid the more transient moments of the tests (e.g. thermal inertia effects). For the high flow rate tests, a shorter region of 500 seconds was required to avoid the more transient periods.

The temperature of the cooling pool was inconsistent between the first set of tests. The low steam flow rate tests lasted far longer than the high flow rate tests, and as a result significantly more energy was imparted into the system. Additionally, the initial temperature of the pool varied between tests. Tests 1.1 and 1.5 were conducted with initial average CPV temperatures of 26°C and 19°C respectively while the average of the other four tests was about 9°C. The inconsistent pool temperatures significantly impacted the heat fluxes measured in the tests but the heat transfer coefficients were largely unaffected.

The second round of tests aimed to improve testing conditions and provide a second data set for the analysis of containment condensation. An attempt was made to isolate the

pressure effect from the transient influence of continuously increasing pressures and temperatures by performing a series of quasi steady state tests. Each was devised to reach and maintain a unique pressure.

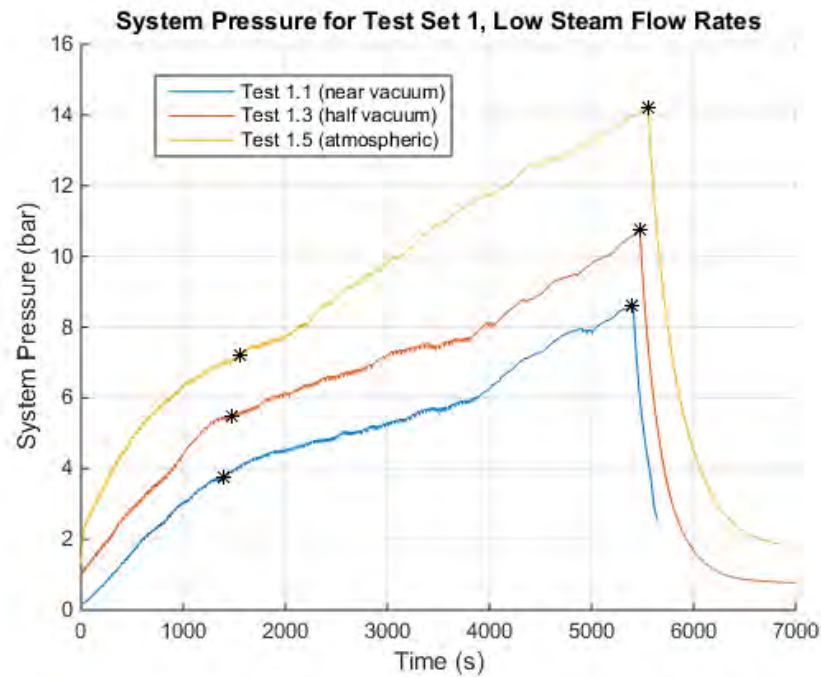


Figure 6-1, HPC pressure for Test Set 1 (low flow rates)

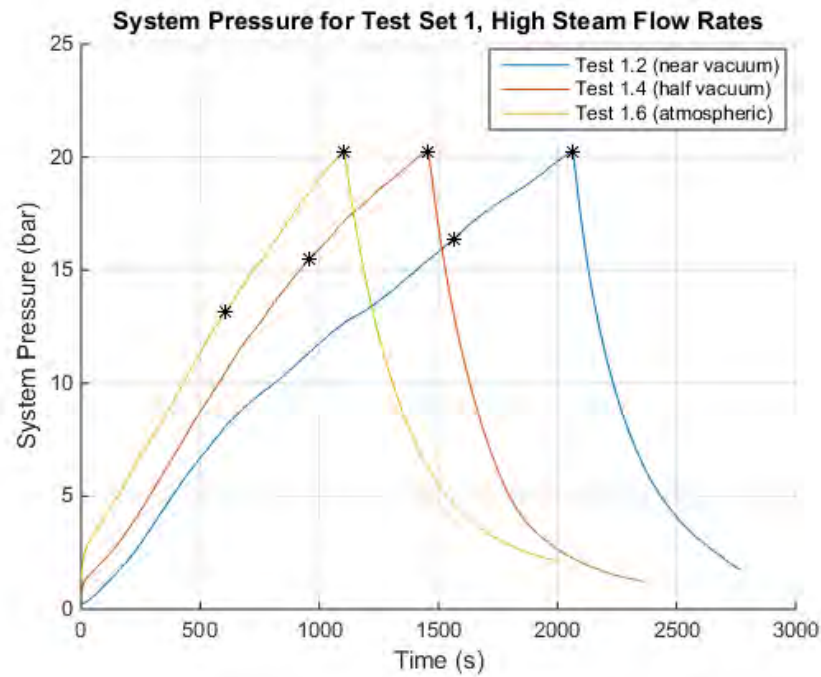


Figure 6-2, HPC pressure for Test Set 1 (high flow rates)

The temperature of the cooling pool was inconsistent between the first set of tests. The low steam flow rate tests lasted far longer than the high flow rate tests, and as a result significantly more energy was imparted into the system. Additionally, the initial temperature of the pool varied between tests. Tests 1.1 and 1.5 were conducted with initial average CPV temperatures of 26°C and 19°C respectively while the average of the other four tests was about 9°C. The inconsistent pool temperatures significantly impacted the heat fluxes measured in the tests but the heat transfer coefficients were largely unaffected.

The second round of tests aimed to improve testing conditions and provide a second data set for the analysis of containment condensation. An attempt was made to isolate the pressure effect from the transient influence of continuously increasing pressures and temperatures by performing a series of quasi steady state tests. Each was devised to reach and maintain a unique pressure.

Table 6-4, Quasi steady pressures reached in the second set of tests

	<i>Average NCG Fraction</i>	<i>Pressure Plateau</i>
<i>Test 2.1</i>	0.025	4-6 bar
<i>Test 2.2</i>	0.017	7-9 bar
<i>Test 2.3</i>	0.012	11-13 bar
<i>Test 2.4</i>	0.009	15-17 bar
<i>Test 2.5</i>	0.278	7-9 bar
<i>Test 2.6</i>	0.203	11-13 bar
<i>Test 2.7</i>	0.156	15-17 bar

While containment pressure was not maintained exceptionally steady during each quasi-steady period, the result, as shown in Figure 6-3 and Figure 6-4, was satisfactory. In fact, the aim and expectation for each test was to see the HPC pressure initially decrease following the transition to the reduced steam flow before gradually increasing again. Figure 6-3 and Figure 6-4 below show the containment pressure for the quasi-steady tests performed with the near-vacuum and atmospheric initial conditions in the containment.

This second round of testing was performed with more consistency in initial and boundary conditions, facilitating comparisons between tests. One important improvement was that the tests were shorter and each lasted the same amount of time (with exception of Test 2.2), reducing the differences in cooling pool temperature between each test.

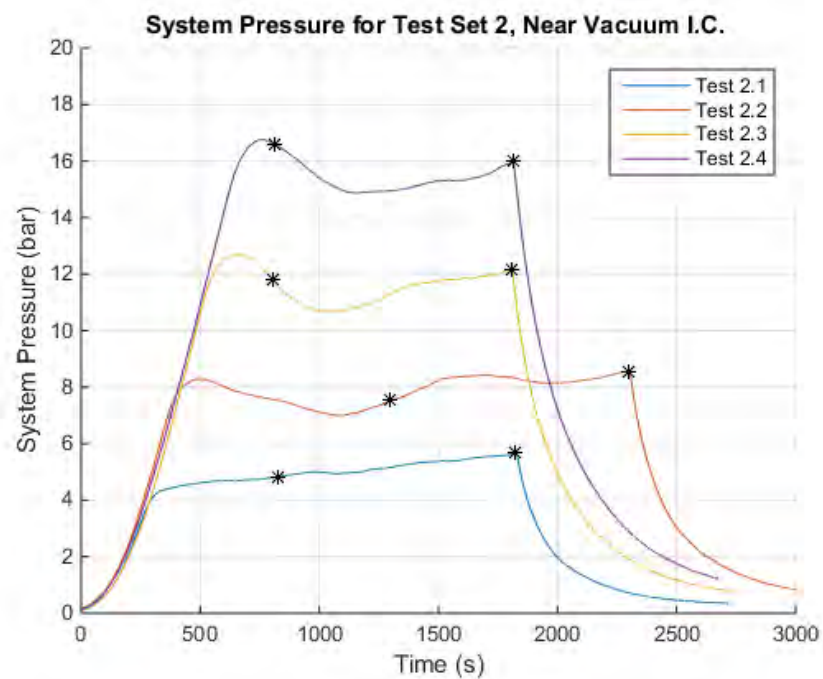


Figure 6-3, HPC pressure for Test Set 2 (near vacuum I.C.)

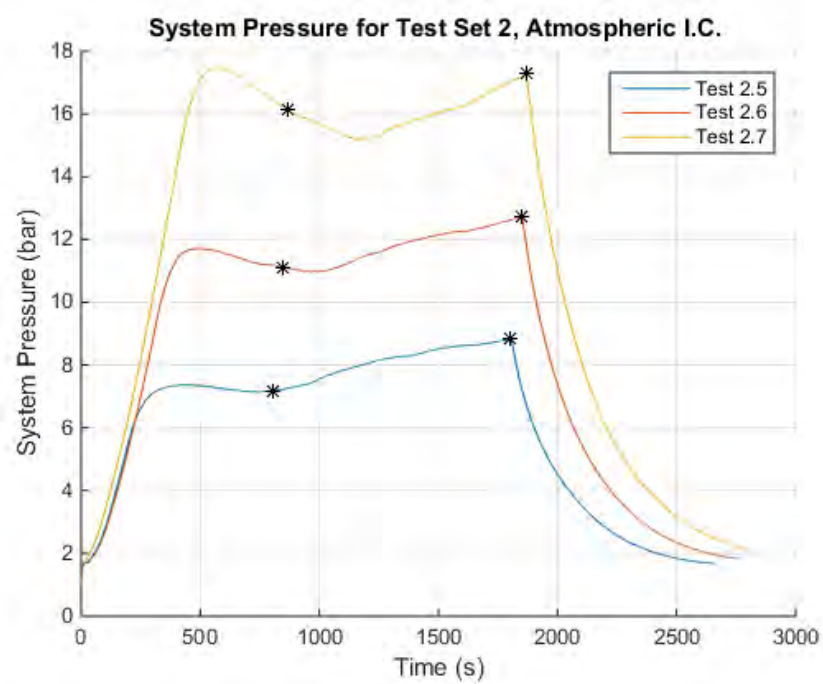


Figure 6-4, HPC pressure for Test Set 2 (atmospheric I.C.)

6.3 Data Processing and Analysis Methods

The data analysis presented in this report comprises the necessary calculations to quantify condensation rates, condensation heat fluxes, and heat transfer coefficients in the HPC for the 13 tests listed above. A mass and energy balance is included to evaluate the quantification methods employed. The data collected from the tests was imported and organized into EXCEL spreadsheets and read into the MATLAB coding environment where the calculations were performed.

6.3.1 Transient Data Processing

The first challenge of data processing is to accurately quantify the heat flux on the condensation wall, particularly for the proposed blow-down tests when the temperature of the condensation wall varies. To account for the plate heat capacity in the computation of the wall surface heat flux, an inverse heat transfer analysis has been performed in the first year.

The condensation plate conducts heat between the high-pressure containment and the cooling pool. The plate has six sets of five thermocouples at different elevations, measuring the temperature distribution from the containment side to the cooling pool. At each elevation, two of the five thermocouples measure the fluid temperature (air, water, or steam) adjacent to the heat transfer plate surface (one each inside), another two are embedded in the heat transfer plate near the two surfaces, and the fifth one is embedded at the midpoint of the plate (Figure 4-4). The holes drilled in the heat transfer plate for the thermocouples are filled with boron nitride heat conducting spray to minimize the difference between the actual heat transfer plate temperature and the temperature sensed by the embedded thermocouples.

To accurately calculate the heat flux on the plate surface for the quantification of the heat transfer coefficient, transient data can be employed through the inverse heat transfer analysis. A simplified geometry for the heat transfer plate has been adapted as shown in Figure 6-5. Assuming adiabatic boundary conditions at top and bottom sides, the lateral conductive heat transfer process dominates energy balance at the elevation of each set of thermocouples equipped. It is anticipated that if the temperature profile matches the three measurement values at each time step, the wall heat flux can be obtained from the temperature gradient on the surface, a better representation than using the three measurements alone with the steady-state assumption. When the process truly becomes steady state, the temperature profile should linear and the three temperature measurements are sufficient for the surface heat flux computation.

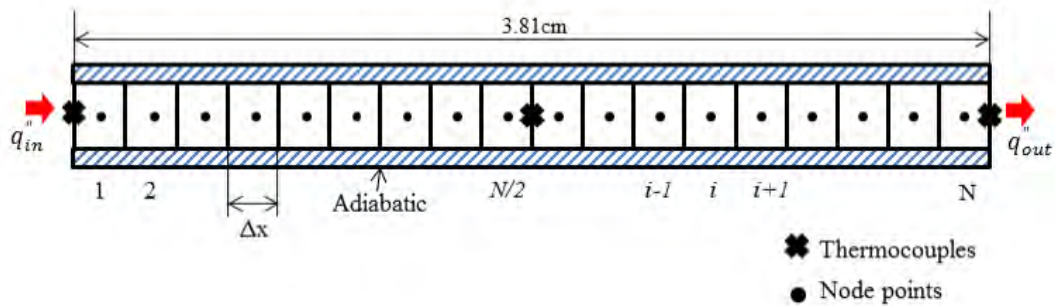


Figure 6-5, Discretized nodes of the heat transfer plate for numerical modeling

The time dependent, one dimensional conduction heat transfer equation with constant properties is given by:

$$\frac{1}{\alpha} \frac{\partial T}{\partial t} = \frac{\partial^2 T}{\partial x^2} \text{ where } \alpha = \frac{k}{\rho C_p} \quad (6-1)$$

This partial differential equation can be solved with one initial and two boundary conditions:

Initial condition: $T(x, 0) = T_i$ (6-2)

Left boundary condition: $q_{in}'' = k \frac{\partial T}{\partial x} \Big|_{x=0}$ (6-3)

Right boundary condition: $q_{out}'' = k \frac{\partial T}{\partial x} \Big|_{x=L}$ (6-4)

The backward Euler method for time and the central difference method for space were utilized to numerically solve the one-dimensional conduction problem. The discretized nodes (Figure 5) were created for the numerical calculation of temperature profiles in the heat transfer plate. Each node can be expressed by:

$$\begin{aligned} \text{Left boundary:} \quad & (1 + Fo)T_1^{p+1} - FoT_2^{p+1} = T_1^p + q_{in}'' \left(Fo \frac{\Delta x}{k} \right) \\ \text{Interior nodes:} \quad & -FoT_{i-1}^{p+1} + (1 + 2Fo)T_i^{p+1} - FoT_{i+1}^{p+1} = T_i^p \\ \text{Right boundary:} \quad & -FoT_{N-1}^{p+1} + (1 + Fo)T_N^{p+1} = T_N^p - q_{out}'' \left(Fo \frac{\Delta x}{k} \right) \end{aligned}$$

Here, Fo is a finite difference form of Fourier number:

$$Fo = \frac{\alpha \Delta t}{\Delta x^2} \quad (6-5)$$

The temperature profile can thus be computed by directly solving the following equation:

$$\begin{bmatrix} (1+Fo) & -Fo & 0 & 0 & 0 & 0 & 0 & 0 & 0 & 0 \\ -Fo & (1+2Fo) & -Fo & 0 & 0 & 0 & 0 & 0 & 0 & 0 \\ 0 & -Fo & (1+2Fo) & -Fo & 0 & 0 & 0 & 0 & 0 & 0 \\ 0 & 0 & -Fo & (1+2Fo) & -Fo & 0 & 0 & 0 & 0 & 0 \\ 0 & 0 & 0 & -Fo & (1+2Fo) & -Fo & 0 & 0 & 0 & 0 \\ 0 & 0 & 0 & 0 & -Fo & (1+2Fo) & -Fo & 0 & 0 & 0 \\ 0 & 0 & 0 & 0 & 0 & -Fo & (1+2Fo) & -Fo & 0 & 0 \\ 0 & 0 & 0 & 0 & 0 & 0 & -Fo & (1+2Fo) & -Fo & 0 \\ 0 & 0 & 0 & 0 & 0 & 0 & 0 & -Fo & (1+2Fo) & -Fo \\ 0 & 0 & 0 & 0 & 0 & 0 & 0 & 0 & -Fo & (1+Fo) \end{bmatrix} \begin{bmatrix} T_1^{p+1} \\ T_2^{p+1} \\ \vdots \\ T_{N/2}^{p+1} \\ \vdots \\ T_N^{p+1} \end{bmatrix} = \begin{bmatrix} T_1^p + q_{in}'' (Fo \Delta x / k) \\ T_2^p \\ \vdots \\ T_{N/2}^p \\ \vdots \\ T_N^p - q_{out}'' (Fo \Delta x / k) \end{bmatrix} \quad (6-6)$$

After solving for the temperature profile, the variance can be obtained by comparing calculated and measured temperatures in the heat transfer plate:

$$S(t_i) = \frac{1}{N} \sum_{i=1}^N (Y_i - T_i)^2 \quad (6-7)$$

Using the least square method to minimize the variance at each time step, by varying the surface heat flux, the transient solution of the temperature profile across the plate can be obtained through iterations. From the temperature profile at each time step, the surface heat fluxes on the both sides of the plate are readily computed. The procedure for computation convergence is demonstrated in Figure 6-6.

Starting with an initial guess of inlet and outlet heat fluxes, a temperature profile at a time step can be calculated from Equation (31). Then the differences of the predicted temperatures and the three measurement points are obtained for the variance quantification. By applying the least square method, the minimum variance can be achieved by varying the surface heat fluxes. This iteration process identifies a temperature profile corresponding to the minimum variance, leading to the solutions of the surface heat fluxes for condensation analysis.

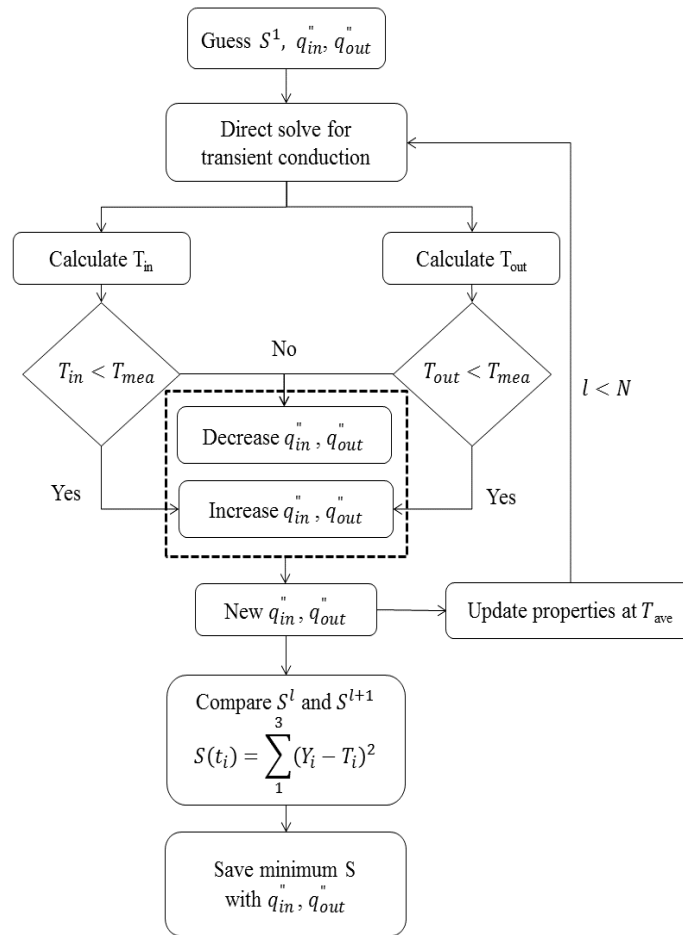


Figure 6-6. Flow chart for inverse heat transfer analysis

For the application of the inverse heat transfer analysis to quantify the surface heat fluxes, one data set of the MASLWR blow-down test was used. The test simulates a loss of feed water accident, resulting in the activation of the automatic depressurization of the reactor vessel. Initially, the reactor core was brought to a steady state at 75% core power and 1250 Psig system pressure. The accident was triggered by shutting-off the main feed water pump in the secondary flow system, losing the reactor heat sink. The core pressure rose rapidly, causing the core power trip to the decay heat mode. At the meantime, the automatic depressurization valve was actuated, releasing steam into the containment.

Normally, the steam blow-down process would persist until the containment pressure reaches equilibrium with the reactor vessel pressure. In this test, because the containment pressure limit is only 300 Psig, the containment relief valve was triggered when the pressure reached 250 Psig and the blow-down process paused to prevent excessive core water inventory loss. After the containment pressure fell back to 200 Psig, the relief valve shut off and the blow-down process resumed. This blow-down process was thus in a cycling mode, resulting in a cycling transit condensation process on the condensation plate, which is a good case for the application of the inverse heat transfer analysis.

The estimated inlet/outlet heat fluxes on the heat transfer plate at an elevation of 4.17m are shown in Figure 6-7. Right after the blow-down, the inlet heat flux (on the condensation surface) suddenly increased up to $73\text{ kW/m}^2\cdot\text{K}$. Afterwards, it quickly fell back and fluctuated as the containment relief valve cycled until the containment pressure remained below 250 Psig. The outlet heat flux (on the surface in contact with the cooling pool) rose rapidly and then entered the oscillating mode with a phase shift. After the cycling mode ended, the two heat fluxes converge, suggesting that a linear temperature profile was reached.

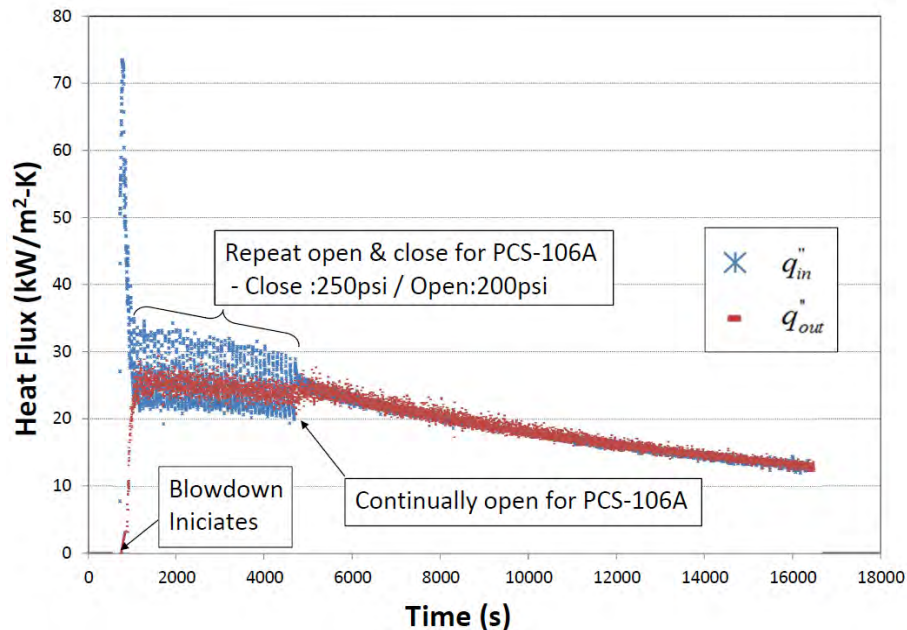


Figure 6-7, Heat transfer plate surface heat flux estimation in a blow-down transient

6.3.2 Quasi-Steady State Data Processing

For the quasi-steady state data processing, the following assumptions were made to permit meaningful analysis of the test data:

- The HPC and CPV are well insulated and environmental heat losses are assumed to be negligible. This assumption is justified from the results of the energy balance in section 6.4.2 of this report.
- Steam entering the containment is assumed to be superheated at the containment pressure (PT801) and the temperature measured in the ADS line (TF873A). If the flow is choked, it is occurring at the steam pressure regulating valve, well upstream of the containment and ADS line.
- The steam bulk in the HPC is assumed to be at saturation conditions during the course of the tests. This assumption is corroborated with wall temperature measurements at various locations. The non-condensable gases are assumed to be at the same temperature as the vapor. After termination of the steam flow into the containment, the ensuing depressurization leads to significant superheat (in regions not adjacent to the HTP) which is sustained in part by the thermal inertia of the structures.
- Non-condensable gases and steam do not mix and are assumed to segregate completely within the HPC. This formidable assumption was developed in review of the test results and is justified in the section 6.4.4. Complete segregation between the gasses may not be entirely realistic, however the test results clearly indicate strong stratification with non-condensable gases concentrated at the bottom of the containment. This simplifying assumption implies that the partial pressures of steam and air are both equal to the system pressure in the regions of the HPC that they respectively occupy.
- The temperature of the condensate pool at the bottom of the containment is measured with TF804. This thermocouple is elevated roughly half a meter from the bottom of the containment. During the initial period of each test, this thermocouple is measuring gas and vapor temperatures until becoming submerged in the condensate pool. To account for this, the condensate temperature and thermal properties are evaluated at saturation unless TF804 reads subcooled temperatures.
- Due to a lack of temperature instrumentation in the bottom portion of the CPV, the bulk temperature along the entire height of the pool is extrapolated from three temperature measurements available in the top half of the vessel (TF903, TF902, and TF901). A linear least-squares fit is employed for this purpose. The result of this extrapolation is discussed in section 6.4.2 of this report.
- The heat flux through the HTP is evaluated using Fourier's Law. This involves an assumption of steady state (i.e. negligible heat capacitance) and 1-D conduction. The validity these assumptions are addressed in section 6.4.2 of this report.
- Material and thermal properties for air and the SS316 HTP are assumed constant and independent of changing temperature and pressure.

6.3.2.1 Data Channels

The following instrument data channels were employed in the data analysis. Test facility data was collected at 1 second intervals. The data channels are identified with the same alphanumeric label in all of the calculations presented and throughout this thesis.

Table 6-5, Test facility instrument channels employed in the analysis

Channel	Description	Unit
High Pressure Containment		
FMM501	Steam flow rate	lbm/min
PT801	HPC gauge pressure (relative to ambient pressure)	psig
LDP801	HPC liquid level	in
TF802	HPC upper dome temperature	°F
TF804	HPC condensate pool temperature	°F
TF873A	HPC steam inlet temperature	°F
Heat Transfer Plate		
TW813	Centerline HTP temperature	°F
TW814	CPV side HTP surface temperature	°F
TW822	HPC side HTP surface temperature	°F
TW823	Centerline HTP temperature	°F
TW824	CPV side HTP surface temperature	°F
TW832	HPC side HTP surface temperature	°F
TW833	Centerline HTP temperature	°F
TW834	CPV side HTP surface temperature	°F
TW842	HPC side HTP surface temperature	°F
TW843	Centerline HTP temperature	°F
TW844	CPV side HTP surface temperature	°F
TW852	HPC side HTP surface temperature	°F
TW853	Centerline HTP temperature	°F
TW854	CPV side HTP surface temperature	°F
TW862	HPC side HTP surface temperature	°F
TW863	Centerline HTP temperature	°F
TW864	CPV side HTP surface temperature	°F
Cooling Pool Vessel		
LDP901	CPV liquid level	in
TF901	CPV temperature	°F
TF902	CPV temperature	°F
TF903	CPV temperature	°F

6.3.2.2 Input Parameters

In addition to the instrument data channels, the following input parameters were used for the data analysis.

Table 6-6, Input parameters employed in the analysis

Parameter	Value	Variable
High Pressure Containment		
Cross sectional area of lower HPC	0.0539 m ²	A_{HPC}
Total volume of HPC	0.5174 m ³	V_{HPC}
Heat Transfer Plate		
Width of HTP	0.1682 m	W_{HTP}
Thickness of HTP	0.0381 m	Th_{HTP}
Height of HTP	5.645 m	H_{HTP}
HTP elevation of 81X (relative to bottom of HTP)	1.00 m	--
HTP height for 81X	1.75 m	H_{81X}
HTP elevation of 82X	2.50 m	--
HTP height for 82X	1.10 m	H_{82X}
HTP elevation of 83X	3.20 m	--
HTP height for 83X	0.80 m	H_{83X}
HTP elevation of 84X	4.10 m	--
HTP height for 84X	0.95 m	H_{84X}
HTP elevation of 85X	5.10 m	--
HTP height for 85X	0.75 m	H_{85X}
HTP elevation of 86X	5.60 m	--
HTP height for 86X	0.295 m	H_{86X}
Cooling Pool Vessel		
Cross sectional area of CPV	0.4410 m ²	A_{CPV}
CPV elevation of TF903 (relative to bottom of CPV)	3.21 m	El_{903}
CPV elevation of TF902	4.81 m	El_{904}
CPV elevation of TF901	6.31 m	El_{905}
Average CPV pressure	1.3 bar	P_{CPV}
Material and Thermal Properties		
c_p for air (assumed constant, evaluated @120°C)	1.013 kJ/(kg-K)	Cp_{air}
c_p for HTP (SS316, assumed constant)	0.50 kJ/(kg-K)	Cp_{HTP}
k-thermal conductivity for HTP (assumed constant)	16.3 W/(m-K)	k_{HTP}
Density of HTP	8000 kg/m ³	ρ_{HTP}
Standard temperature for LDP measurements	4°C	T_{STD}
Standard pressure for LDP measurements	1.01325 bar	P_{STD}

6.3.2.3 Data Processing

This section presents the data manipulations required to form the quantities used in the calculations of the mass and energy balance, as well as the condensation characterization.

MATLAB based XSteam functions were employed to evaluate steam and liquid water properties as a function of pressure and temperature at each data point throughout the

tests. The properties evaluated are saturation temperatures, densities, and specific enthalpies and internal energies. For superheated steam or subcooled liquid, properties are evaluated as a function of pressure and enthalpy. When the fluid is saturated, the phase is specified (either / or v) along with the pressure. Saturation temperature does not require a phase specification.

The data imported into the MATLAB environment was converted to S.I. units. Units were chosen for compatibility with the XSteam steam table script. Pressures were converted to bar, temperatures were converted to °C, levels were converted to meters, and the steam flow rate was converted to kg/s.

The HPC liquid level measurement, LDP801 is based off of a pressure differential measured between the top and bottom of the containment equivalent to the hydrostatic head of the condensate pool (the hydrostatic head of the vapor component is neglected). The data acquisition system internally converts this pressure measurement to a liquid level assuming a liquid density at standard conditions of 4°C and 1.10325 bar. When importing the instrument data into MATLAB, the value for LDP801 was adjusted for the appropriate liquid density based on the temperature of TF804. Additionally, an adjustment to the channel was required to output a positively increasing value starting at 0 meters whereas the original channel output a negative value which tended toward 0 as the liquid level increased.

$$LDP801_{adjusted}(:) = \frac{[LDP801_{raw}(:) - LDP801_{raw}(1)]\rho(P_{STD}, T_{STD})}{\max[\rho(PT801, TF804), \rho_{sat,l}(PT801)]} \quad (6-8)$$

TF804 initially measures gas and vapor temperatures in the containment until becoming submerged in the condensate pool. To avoid occasionally calculating steam densities (TF804 will hang around the saturation line until submerged), the saturated liquid density is used unless the measured temperature is subcooled (Assumption □).

The HPC pressure measurement, PT801, was adjusted to provide absolute pressure as opposed to gauge pressure.

$$PT801_{adjusted} = PT801_{raw} + P_{STD} \quad (6-9)$$

These adjustments were performed after converting to S.I. units.

6.3.2.4 Condensate Pool Quantities

Volume of condensate pool:

$$V_{liq} = LDP801 \cdot A_{HPC} \quad (6-10)$$

Mass of condensate pool:

$$m_{liq} = V_{liq} \cdot \max[\rho(PT801, TF804), \rho_{sat,l}(PT801)] \quad (6-11)$$

TF804 initially measures gas and vapor temperatures in the containment until becoming submerged in the condensate pool. To avoid occasionally calculating steam densities (TF804 will ride the saturation line until submerged), the saturated liquid density is used unless the measured temperature is subcooled.

Internal energy of condensate pool:

$$E_{liq} = m_{liq} \cdot \min[u(PT801, TF804), u_{sat,l}(PT801)] \quad (6-12)$$

The same reasoning applies as the above comment for employing the minimum of the two specific energies.

6.3.2.5 Non-condensable Gas Quantities

Mass of non-condensable gas:

$$m_{NCG} = \frac{PT801_{initial} \cdot V_{HPC} \cdot MW_{air}}{\bar{R} \cdot (TF802 + TF804)_{initial} / 2} \quad (6-13)$$

The total mass of non-condensable gas in the containment remains unchanged along the course of each test. The mass is calculated using ideal gas relations. The containment pressure and average temperature used in the calculation are measured prior to preheating of the containment (in units of Pa and K respectively).

Volume of non-condensable gas:

$$V_{NCG} = \frac{m_{NCG} \cdot \bar{R} \cdot T_{sat}(PT801)}{PT801 \cdot MW_{air}} \quad (6-14)$$

As per Assumption □, the non-condensable gas and vapor are assumed to occupy distinct spaces in the containment with the non-condensable gas concentrated at the bottom. Pressure and temperature are evaluated in units of Pa and K respectively.

Internal energy of non-condensable gas:

$$E_{NCG} = m_{NCG} \cdot C_{p_{air}} \cdot T_{sat}(PT801) \quad (6-15)$$

6.3.2.6 Vapor Quantities

Volume of vapor:

$$V_{vap} = V_{HPC} - V_{liq} - V_{NCG} \quad (6-16)$$

The volume of vapor in the containment is taken as the entire volume of the HPC less the space occupied by the condensate and non-condensable gas (see Assumption □).

Mass of vapor:

$$m_{vap} = \rho_{sat,v}(PT801) \cdot V_{vap} \quad (6-17)$$

Internal energy of vapor:

$$E_{vap} = m_{vap} \cdot h_{sat,v}(PT801) \quad (6-18)$$

6.3.2.7 Steam Flow and Phase Change Quantities

Integral steam mass flow into HPC:

$$m_{stm,in} = \sum_{i=LB}^{RB} FMM501(i) \cdot dt \quad (6-19)$$

The integrated steam flow at any time along the course of the test is the cumulative sum of the flow rate times the data collection frequency. The frequency, dt , is equal to 1 second for all of the calculations. The terms LB and RB refer to the left and right bounds of the period of interest for each test.

Steam enthalpy flow rate into HPC:

$$\dot{H}_{stm,in} = FMM501 \cdot h(PT801, TF873A) \quad (6-20)$$

Integral enthalpy flow into HPC:

$$H_{stm,in} = \sum_{i=LB}^{RB} \dot{H}_{stm,in}(i) \cdot dt \quad (6-21)$$

Heat removed from inlet steam to become subcooled condensate (primarily latent heat):

$$E_{phase} = m_{liq} \cdot (h(PT801, TF873A) - \min[h(PT801, TF804), h_{sat,l}(PT801)]) \quad (6-22)$$

This calculation also incorporates the sensible heat removed from the superheated steam and the heat removed to subcooled the condensate.

Sensible heat removed from inlet steam to become bulk saturated vapor:

$$E_{sens} = m_{vap} \cdot (h(PT801, TF873A) - h_{sat,v}(PT801)) \quad (6-23)$$

As per Assumption □, the vapor and non-condensable gas in the containment is assumed to be at saturation temperature. The sensible heat removed from the superheated inlet vapor must be accounted for in the energy balance.

6.3.2.8 Heat Transfer Plate Quantities

Mass of the HTP:

$$m_{HTP} = \rho_{HTP} \cdot W_{HTP} \cdot Th_{HTP} \cdot H_{HTP} \quad (6-24)$$

Average temperature of the HTP:

$$Tavg_{HTP} = \sum_{i=1}^6 [TW8i3 \cdot \frac{H_{8iX}}{H_{HTP}}] \quad (6-25)$$

The centerline HTP temperatures are used to evaluate the average temperate of the plate. The plate is discretized into 6 sections centered on the 6 HTP thermocouple sets. The temperatures are weighted by the height of the sections they represent.

Internal energy of the HTP:

$$E_{HTP} = m_{HTP} \cdot Cp_{HTP} \cdot Tavg_{HTP} \quad (6-26)$$

Conductive heat flux through the lower HTP:

$$\dot{Q}''_{81X} = k_{HTP} \cdot \frac{(TW813 - TW814)}{Th_{HTP}/2} \quad (6-27)$$

The HTP 81X thermocouple set was damaged before this testing took place. The HPC side surface thermocouple is not available, so the temperature gradient for the lower HTP must be evaluated between the centerline and the CPV surface.

Conductive heat flux through the rest of the HTP:

$$\dot{Q}''_{8iX} = k_{HTP} \cdot \frac{(TW8i2 - TW8i4)}{Th_{HTP}} \quad (6-28)$$

Where $i = 2$ through 6

As per Assumption □, the heat flux through the HTP is calculated with neglect of the thermal capacitance of the plate. This is justified as acceptable due to the relatively low thermal storage rate of the HTP when compared to the conduction through the plate (as shown in the energy balance).

Average conductive heat flux through the HTP:

$$\dot{Q}''_{HTP} = \sum_{i=1}^6 [Q''_{8iX} \cdot \frac{H_{8iX}}{H_{HTP}}] \quad (6-29)$$

Conductive heat rate through the HTP:

$$\dot{Q}_{HTP} = \dot{Q}''_{HTP} \cdot H_{HTP} \cdot W_{HTP} \quad (6-30)$$

Integral conduction through the HTP:

$$Q_{HTP} = \sum_{i=LB}^{RB} \dot{Q}_{HTP}(i) \cdot dt \quad (6-31)$$

6.3.2.9 Cooling Pool Quantities

Average CPV Temperature:

$$T_{CPV} = \text{extrapolated from } TF903, TF902, TF901 \quad (6-32)$$

As per Assumption □, the temperature along the entire height of the CPV was extrapolated from the three temperatures measured in the upper portion of the pool. A linear relationship was fit to TF901, TF 902, and TF903 at the corresponding elevations El_{901} , El_{902} , and El_{903} using a least-squares method. A second degree polynomial fit was also tried, however this generated non-physical temperature profiles (i.e. getting warmer at the very bottom). Even with added constraints on the polynomial fit, it was decided that a linear fit was a more defensible choice and likely was more physical. The average temperature along the full length of the pool was evaluated by integrating the extrapolated fit. These manipulations were performed with built-in MATLAB functions.

Internal Energy of CPV:

$$E_{CPV} = A_{CPV} \cdot LDP901 \cdot \rho(P_{CPV}, T_{CPV}) \cdot u(P_{CPV}, T_{CPV}) \quad (6-33)$$

6.4 Test Results

The regions of interest for each test are selected to focus analysis on the more steady periods of each test. The transient effects were most significant during the initial moments of the tests as the structures were rapidly heating up. The total duration of the region of interest was kept consistent between the tests and each ends just prior to the termination of steam supply. The left and right bounds for each region are presented in Table 6-7. The ranges of the plots shown in the previous section were modified from the original data set and should not be compared to the bounds list below.

Table 6-7, Left and right bounds of the regions of interest selected for detailed analysis

Test	Left Bound	Right Bound	Duration (s)
Test Set 1			
Test 1.1	3951	7951	4000
Test 1.2	1641	2141	500
Test 1.3	4460	6460	4000
Test 1.4	1595	2095	500
Test 1.5	4918	8918	4000
Test 1.6	1793	2293	500
Test Set 2			
Test 2.1	1523	2523	1000
Test 2.2	3167	4167	1000
Test 2.3	880	1880	1000
Test 2.4	1372	2372	1000
Test 2.5	3842	4842	1000
Test 2.6	1325	2325	1000
Test 2.7	997	1997	1000

Test Results include mass balance, energy balance

6.4.1 Mass Balance

The mass balance consists of comparing the cumulative steam flow into the containment with the instantaneous vapor and liquid mass measured in the HPC. A mass balance evaluation is necessary to validate the mass quantification methods employed in the analysis. To perform the mass balance, the steam mass flow into the HPC must be compared to the calculated mass of condensate and steam in the HPC. While it may be logical to compare the measured steam flow rate from the secondary circuit to the instantaneous rate of change of the vapor and condensate mass in the HPC, a comparison of the integrated flows reduces the 'noise' of those measurements and provides a more meaningful result.

To perform the mass balance, the calculated mass of condensate and vapor in the HPC are added together and compared with the integration of the steam flow across the chosen region of interest. To account for the accumulation of mass prior to the period of interest, the effective change in measured mass is evaluated, as in the following forms:

$$\Delta m_{liq} = m_{liq}(LB:RB) - m_{liq}(LB) \quad (6-34)$$

$$\Delta m_{vap} = m_{vap}(LB:RB) - m_{vap}(LB) \quad (6-35)$$

$$\Delta m_{l+v} = \Delta m_{liq} + \Delta m_{vap} \quad (6-36)$$

$$\Delta m_{stm,in} = m_{stm,in}(LB:RB) - m_{stm,in}(LB) \quad (6-37)$$

Where LB and RB are the left and right bounds of the region of interest. Of course, the bounds must be selected such that the steam flow is directed into the HPC during the entire region of interest.

$$\Delta m_{error} = \Delta m_{l+v} - \Delta m_{stm,in} \quad (6-38)$$

$$\%m_{error} = \frac{\Delta m_{error}}{\Delta m_{stm,in}} \cdot 100 \quad (6-39)$$

A mass error calculation gives insight into the accuracy of the various mass measurement methods and the validity of the associated simplifying assumptions. A positive mass error implies a 'gain' in system mass. That is, more mass is measured in the HTP than is measured entering the HTP from the secondary circuit.

The definition of 'error' should not be equated to traditional instrument or measurement uncertainties. Due to the simplifying assumptions employed in this analysis, the measurement uncertainty associated with the calculated quantities is hard to evaluate meaningfully. Comparing the mass and energy flow calculations provides a more useful evaluation of the accuracy and validity measurements. Admittedly, only limited confidence can be applied to any result as no measurement in the facility is known to be exact.

In lieu of displaying the results for all 13 tests, the mass comparison is presented graphically for Test 1.1, Test 1.6, Test 2.1, and Test 2.7 to represent the limits of the test conditions. Test 1.1 was performed with a low steam flow rate and a near-vacuum initial HPC pressure, while Test 1.6 was performed with a high steam flow rate and atmospheric HPC initial pressure. Test 2.1 was conducted with a near vacuum HPC and achieved a pressure plateau of roughly 5 bar, while Test 2.7 was performed with an atmospheric HPC and reached a pressure plateau of about 16 bar.

In general, the mass balance comparison shows good agreement between the mass measurement methods. It should be noted that the error values presented in Table 6-8 are subject to changing significantly when different bounds are selected for the region of interest. Attention was taken not to manipulate the region of interest to suggest a favorable mass balance.

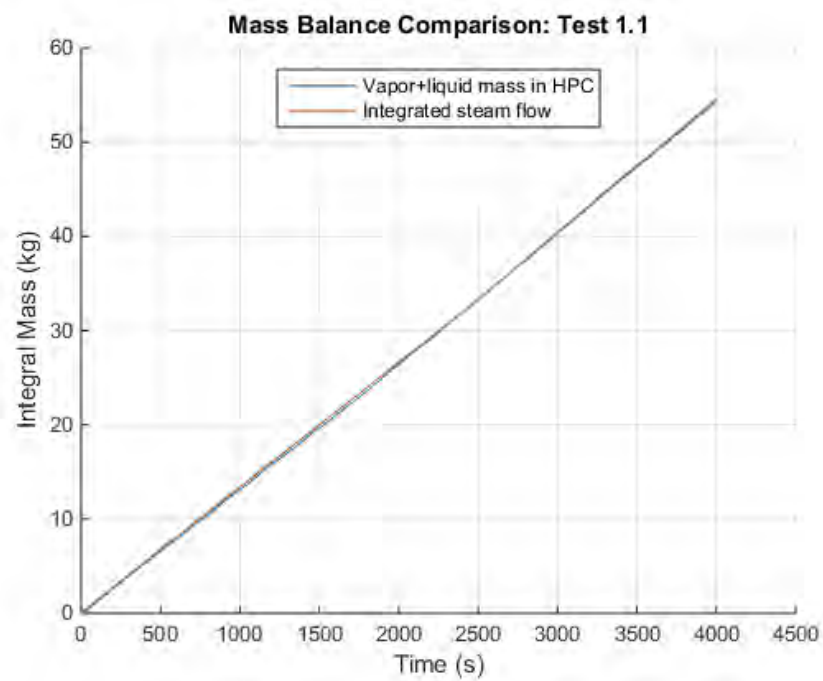


Figure 6-8, HPC mass balance, Test 1.1

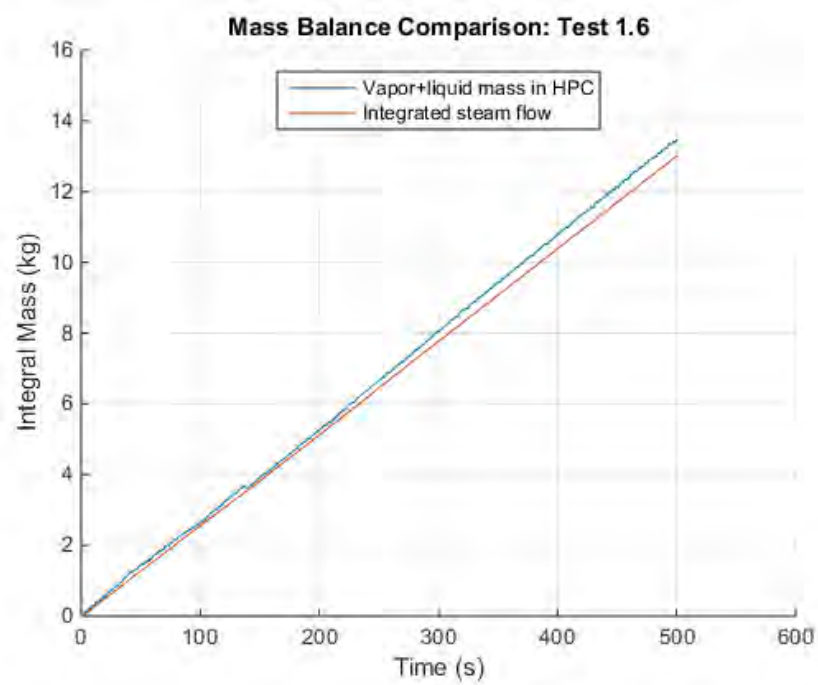


Figure 6-9, HPC mass balance, Test 1.6

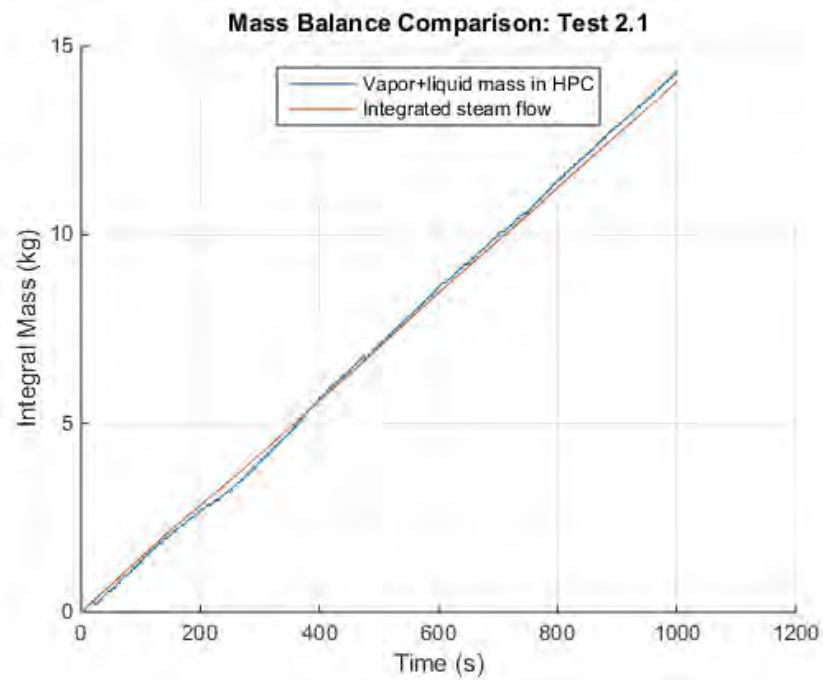


Figure 6-10, HPC mass balance, Test 2.1

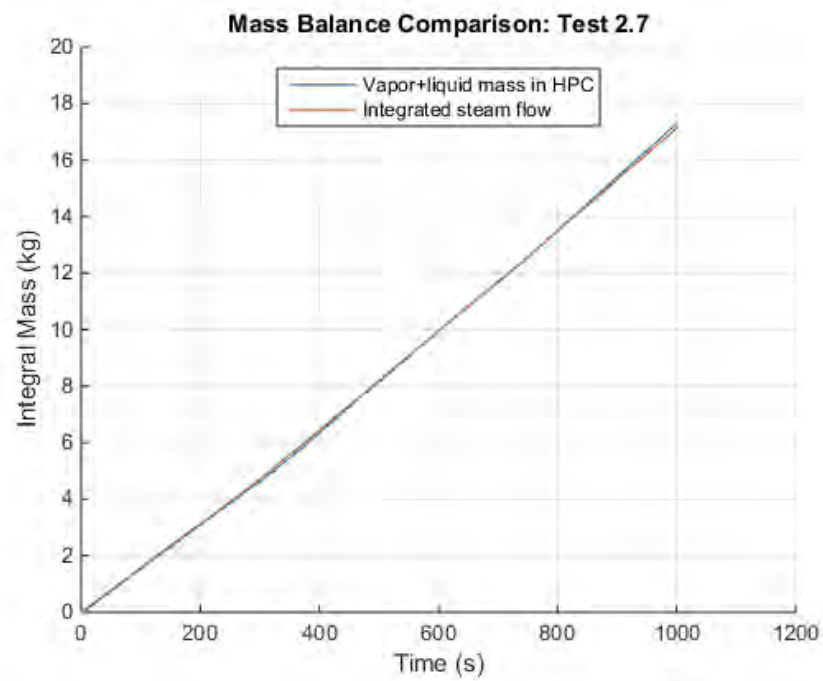


Figure 6-11, HPC mass balance, Test 2.7

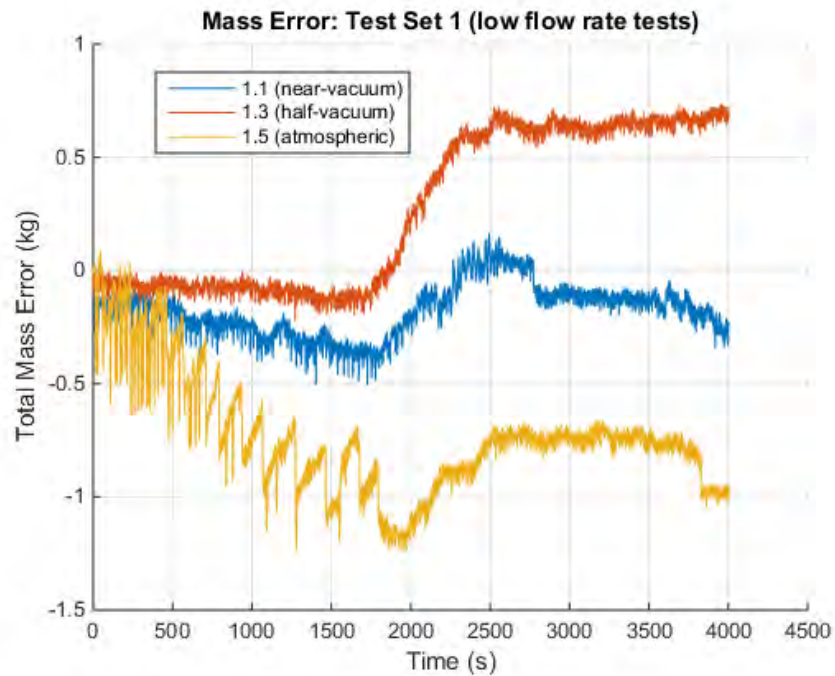


Figure 6-12, Integral mass error for Test Set 1 (low flow rates)

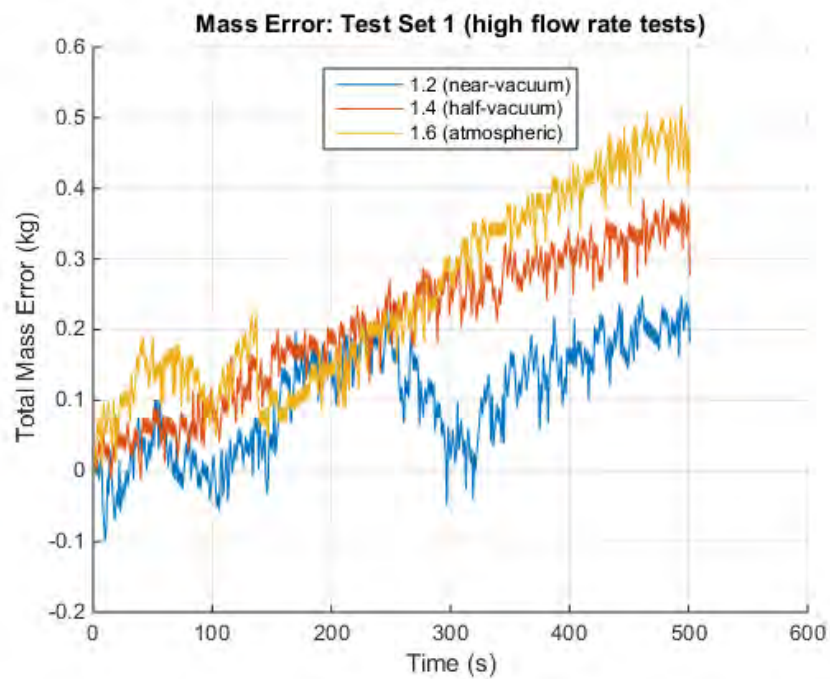


Figure 6-13, Integral mass error for Test Set 1 (high flow rates)

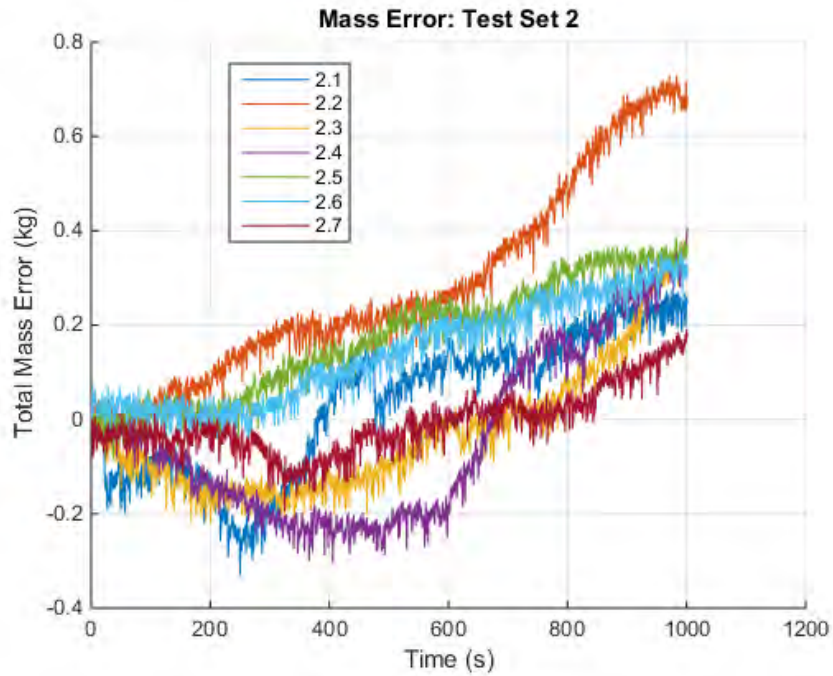


Figure 6-14, Integral mass error for Test Set 2

Table 6-8, Mass error and error percent

Test	Mass Error (kg)	Mass Error Percent
Test Set 1		
Test 1.1	-0.2249	-0.41 %
Test 1.2	0.1817	1.37 %
Test 1.3	0.7228	1.32 %
Test 1.4	0.2762	2.10 %
Test 1.5	-0.9633	-1.82%
Test 1.6	0.4210	3.23 %
Test Set 2		
Test 2.1	0.2476	1.76%
Test 2.2	0.6843	4.26%
Test 2.3	0.3831	2.05%
Test 2.4	0.4077	1.96%
Test 2.5	0.3755	2.99%
Test 2.6	0.3313	2.18%
Test 2.7	0.1731	1.01%

6.4.2 Energy Balance

There are several measured energy flows to consider in these condensation tests. The internal energy of the vapor, condensate, non-condensable gas, HTP, and CPV are compared to the energy carried into the system from the steam supply. Most critically, the HTP conduction calculations are compared to the heat removed from the HPC and the increase in internal energy of the CPV. A representative comparison is detailed for Test 1.1, Test 1.6, Test 2.1, and Test 2.7 while the energy errors are presented for all of the tests.

To account for the entirety of the energy inputs to the various components of the system, the following quantities must be evaluated and compared:

- Enthalpy of steam into the HPC, $H_{stm,in}$
- Enthalpy of phase change, E_{phase}
- Sensible heat removed from vapor, E_{sens}
- Internal energy of vapor, E_{vap}
- Internal energy of condensate, E_{liq}
- Internal energy of non-condensable gas, E_{NCG}
- Internal energy of the cooling pool, E_{CPV}
- Internal energy of the HTP, E_{HTP}
- Integrated conduction through the HTP, Q_{HTP}

As with the mass balance, all of the aforementioned quantities employed in the energy balance are integral quantities. Comparing the integral quantities greatly reduces noise when compared to comparison of instantaneous rates of change. The integral energy flows are compared over a defined region of interest.

$$\Delta H_{stm,in} = H_{stm,in}(LB:RB) - H_{stm,in}(LB) \quad (6-40)$$

$$\Delta E_{phase} = E_{phase}(LB:RB) - E_{phase}(LB) \quad (6-41)$$

$$\Delta E_{sens} = E_{sens}(LB:RB) - E_{sens}(LB) \quad (6-42)$$

$$\Delta E_{vap} = E_{vap}(LB:RB) - E_{vap}(LB) \quad (6-43)$$

$$\Delta E_{liq} = E_{liq}(LB:RB) - E_{liq}(LB) \quad (6-44)$$

$$\Delta E_{NCG} = E_{NCG}(LB:RB) - E_{ncg}(LB) \quad (6-45)$$

$$\Delta E_{CPV} = E_{CPV}(LB:RB) - E_{CPV}(LB) \quad (6-46)$$

$$\Delta E_{HTP} = E_{HTP}(LB:RB) - E_{HTP}(LB) \quad (6-47)$$

$$\Delta Q_{HTP} = Q_{HTP}(LB:RB) - Q_{HTP}(LB) \quad (6-48)$$

For presenting the energy balance, it is beneficial to form meaningful groups from the aforementioned terms.

$$\Delta E_{HPC,stored} = \Delta E_{vap} + \Delta E_{liq} + \Delta E_{NCG} \quad (6-49)$$

Equation 6-47 represents the internal energy of the three HPC components.

$$\Delta E_{HPC,removed} = \Delta E_{phase} + \Delta E_{sens} \quad (6-50)$$

Equation 6-48 represents the heat removed from the HPC components. This includes the heat that was removed from the superheated inlet steam to become the subcooled condensate, as well as the heat removed from the superheated inlet steam to become the saturated vapor.

$$\Delta E_{HPC,total} = \Delta E_{HPC,stored} + \Delta E_{HPC,removed} \quad (6-51)$$

Equation 6-49 represents all of the heat that is stored in or has been removed from the HPC. This should equate to the heat supplied to the HPC.

$$\Delta E_{CPV+HTP} = \Delta E_{CPV} + \Delta E_{HTP} \quad (6-52)$$

Equation 6-50 represents the heat added to the CPV and HTP. This should equate to the heat removed from the HPC.

$$\Delta E_{system,stored} = \Delta E_{HPC,stored} + \Delta E_{CPV+HTP} \quad (6-53)$$

Equation 6-51 represents the heat stored in all of the components of the system. This should equate to the heat supplied to the HPC by the inlet steam.

A relative error can be defined for various parts of the system. The heat removed from the HPC and the sum of the total internal energy in the system are compared to the steam inlet flow enthalpy. The change in internal energy of the cooling pool and the integrated conductive heat flux across the plate are compared to the heat removed from the HPC.

$$\Delta E_{error,HPC} = \Delta E_{HPC,total} - \Delta H_{stm,in} \quad (6-54)$$

$$\%E_{error,HPC} = \frac{\Delta E_{error,HPC}}{\Delta H_{stm,in}} \cdot 100 \quad (6-55)$$

$$\Delta E_{error,CPV} = \Delta E_{CPV+HTP} - \Delta E_{HPC,removed} \quad (6-56)$$

$$\%E_{error,CPV} = \frac{\Delta E_{error,CPV}}{\Delta E_{HPC,removed}} \cdot 100 \quad (6-57)$$

$$\Delta Q_{error,HTP} = \Delta Q_{HTP} - \Delta E_{HPC,removed} \quad (6-58)$$

$$\%Q_{error,HTP} = \frac{\Delta Q_{error,HTP}}{\Delta E_{HPC,removed}} \cdot 100 \quad (6-59)$$

$$\Delta E_{error,system} = \Delta E_{system\ stored} - \Delta H_{stm,in} \quad (6-60)$$

$$\%E_{error,system} = \frac{\Delta E_{error,system}}{\Delta H_{stm,in}} \cdot 100 \quad (6-61)$$

The calculations for the heat removed from the HPC (i.e. latent heat from measured phase change as well as change in sensible heat) relative to the integrated steam inlet flow enthalpy were shown to have approximately the same error as the mass calculations presented above, a logical result as the latent heat is directly proportional to the mass transfer rate. The energy balance shown in Figure 6-15 through Figure 6-18 is a comparison of the change in internal energy of the pool, the HPC heat removed, and the integration of the conductive heat flux through the plate. Of the three energy evaluations, evaluation of the heat removed from the HPC requires the fewest assumptions and is based on the most reliable measurements and as such could be considered a baseline for comparing the other two energy flows.

The energy balance appears to support the assumption employed in calculating the change in internal energy of the CPV. This calculation involved a downward extrapolation of upper CPV temperatures to evaluate an average pool temperature. The error in this measurement was greater over long testing durations. The shape of the axial temperature profiles measured in the upper CPV is observed to change along the duration of the tests, perhaps due to natural circulation timescales. It is accepted that the linear extrapolation for CPV temperatures cannot accurately account for this behavior. This method appears to be more likely to over-predict the change in internal energy when compared to the heat removed from the HPC. While the confidence in the accuracy of the CPV measurement is admittedly low, the tendency to over-predict the internal energy change (when compared to the more reliable heat flow measurement) suggests that most of the heat being removed from the HPC is going into the CPV through the heat transfer plate and the environmental heat losses are small.

Figure 6-22 through Figure 6-24 show that the conductive heat flux measurements for the plate appear to be consistently under predicting the actual heat transfer. This is discussed in detail in Section 6.5, but the primary reason is likely imprecise measurement of HTP surface temperatures with the embedded thermocouples.

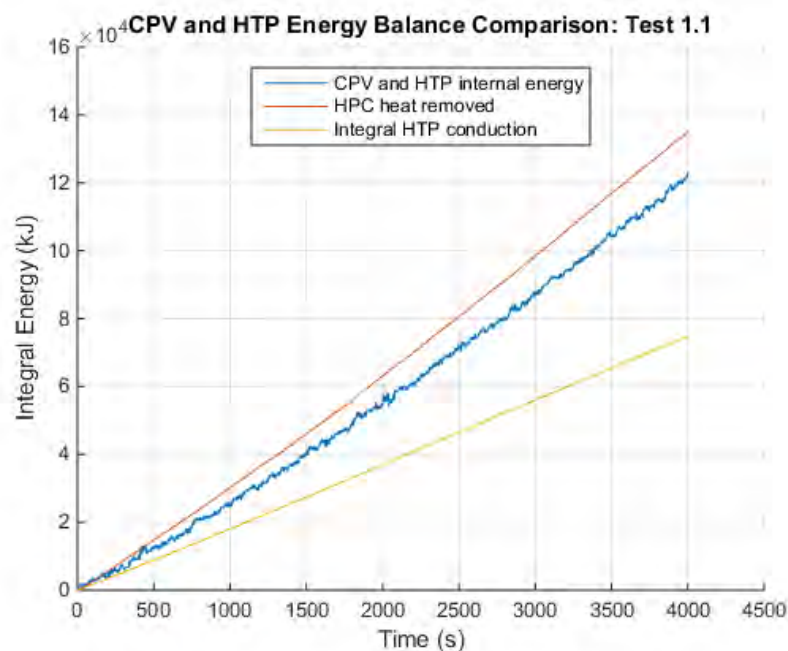


Figure 6-15, Energy balance across HTP, Test 1.1

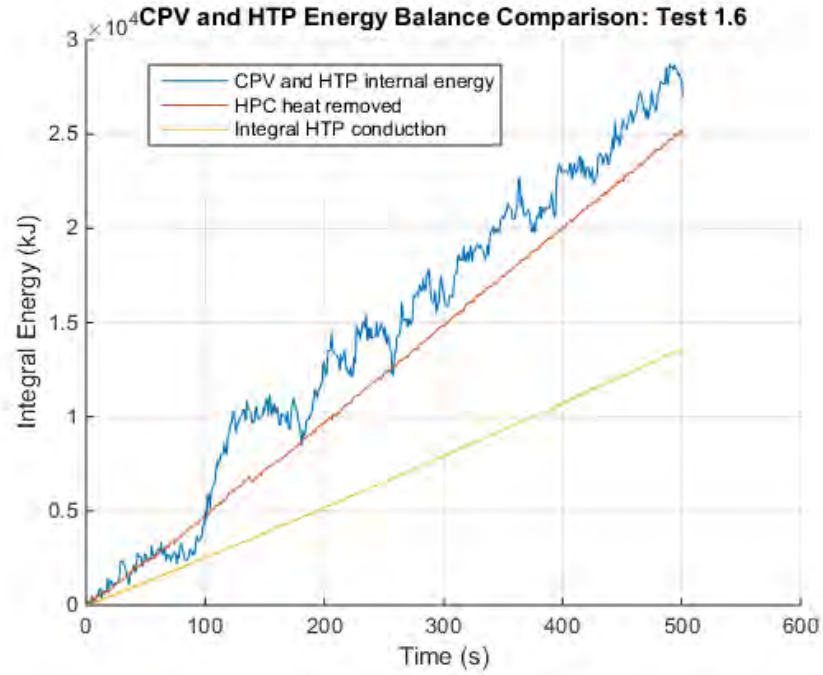


Figure 6-16, Energy balance across HTP, Test 1.6

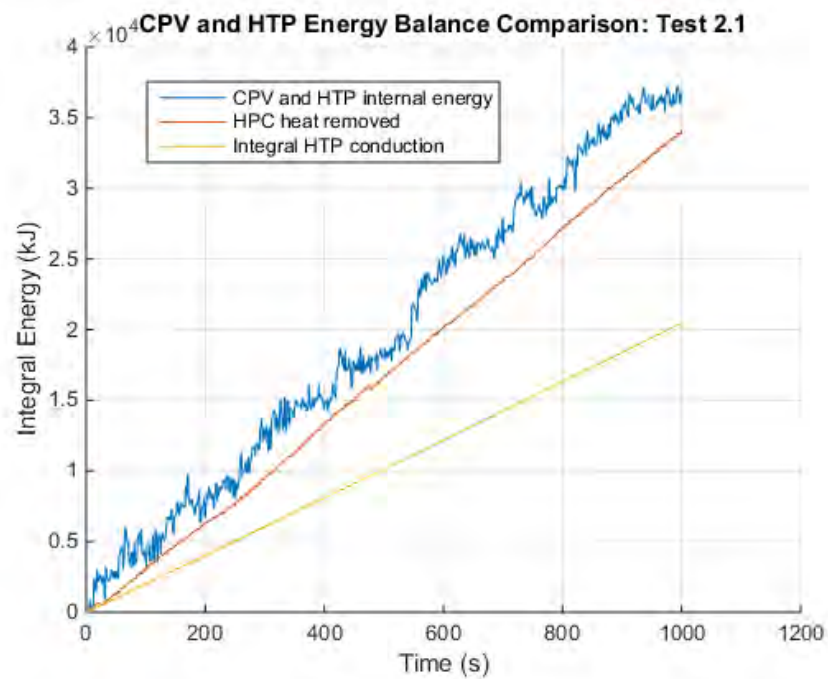


Figure 6-17, Energy balance across HTP, Test 2.1

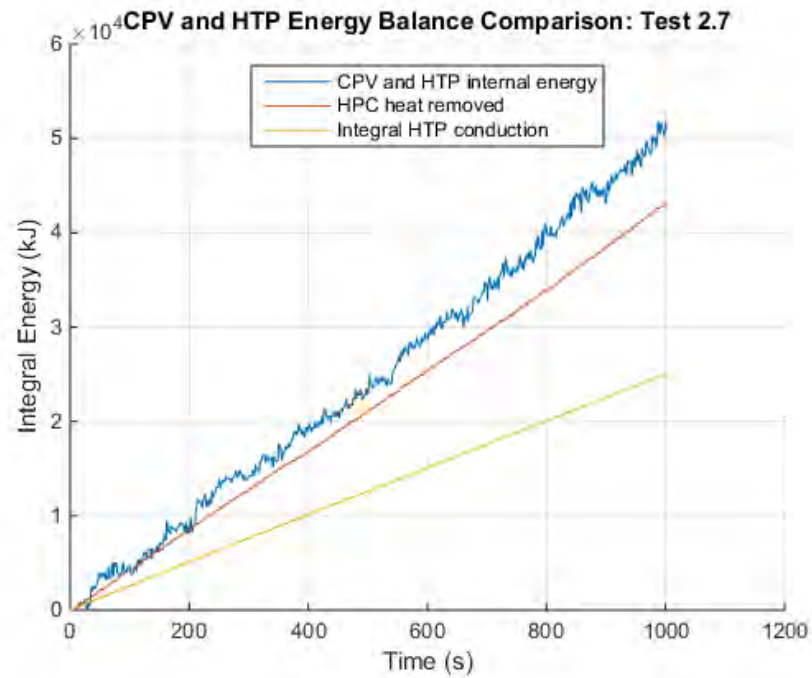


Figure 6-18, Energy balance across HTP, Test 2.7

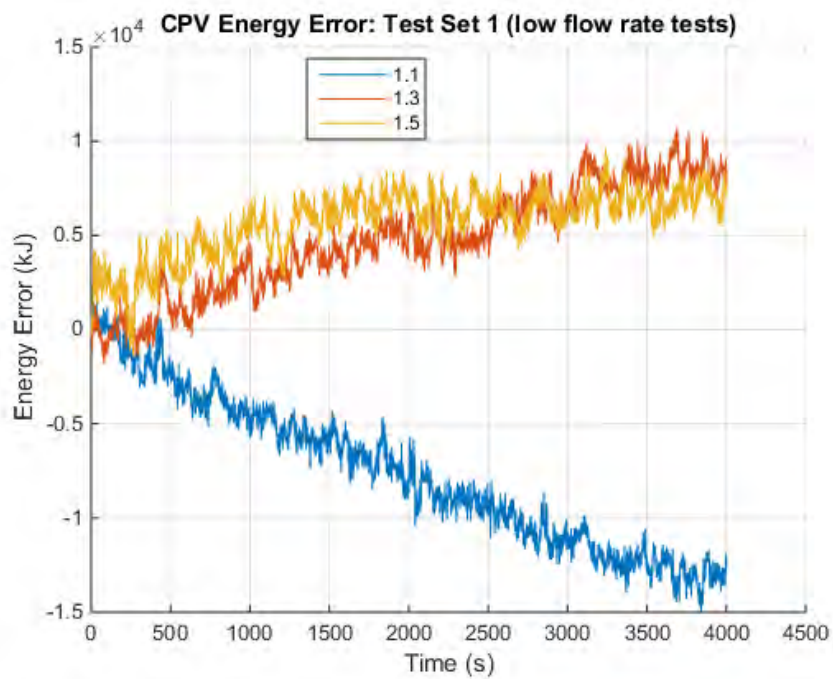


Figure 6-19, Integral CPV energy error for Test Set 1 (low flow rates)

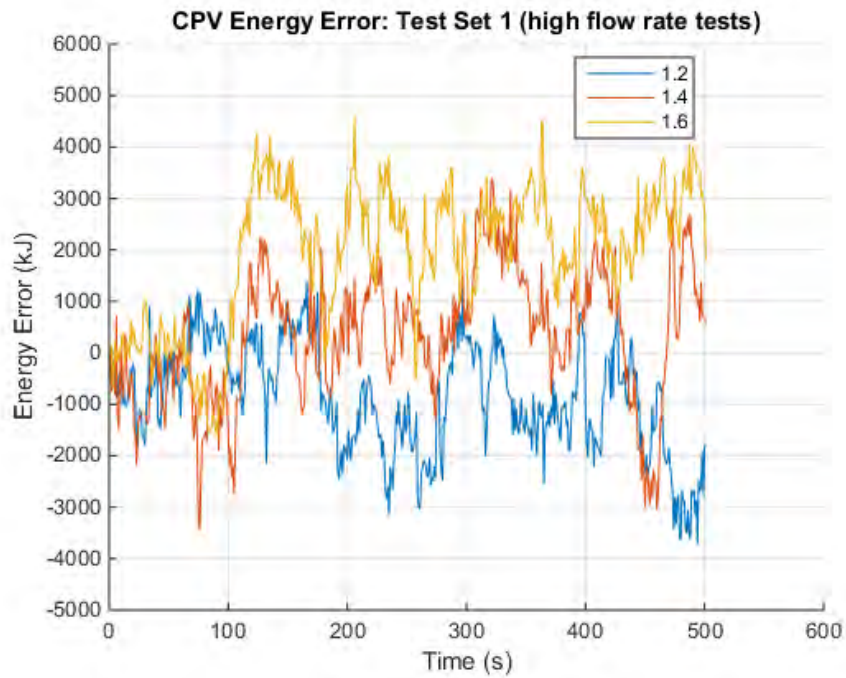


Figure 6-20, Integral CPV energy error for Test Set 1 (high flow rates)

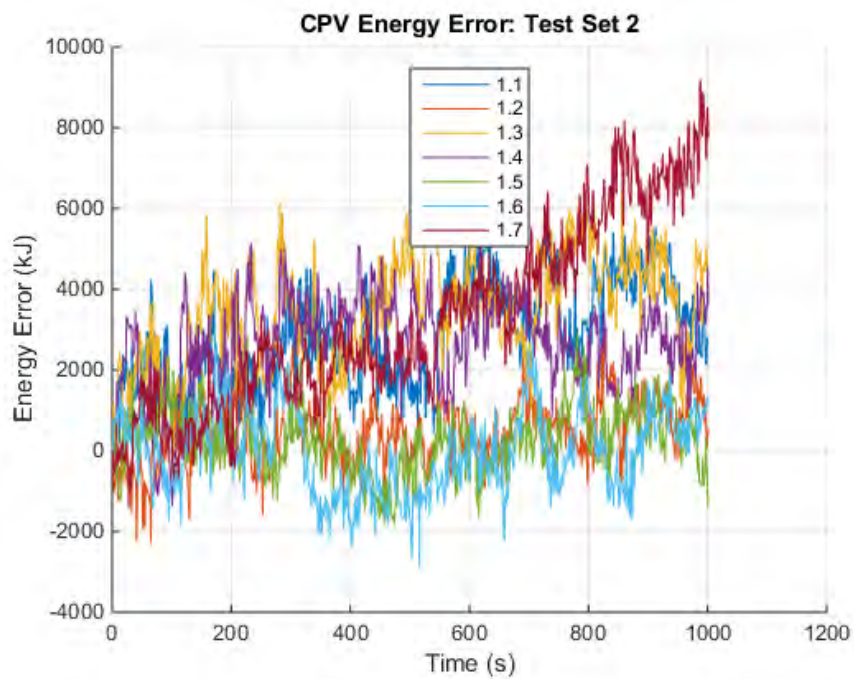


Figure 6-21, Integral CPV energy error for Test Set 2



Figure 6-22, Integral HTP energy error for Test Set 1 (low flow rates)

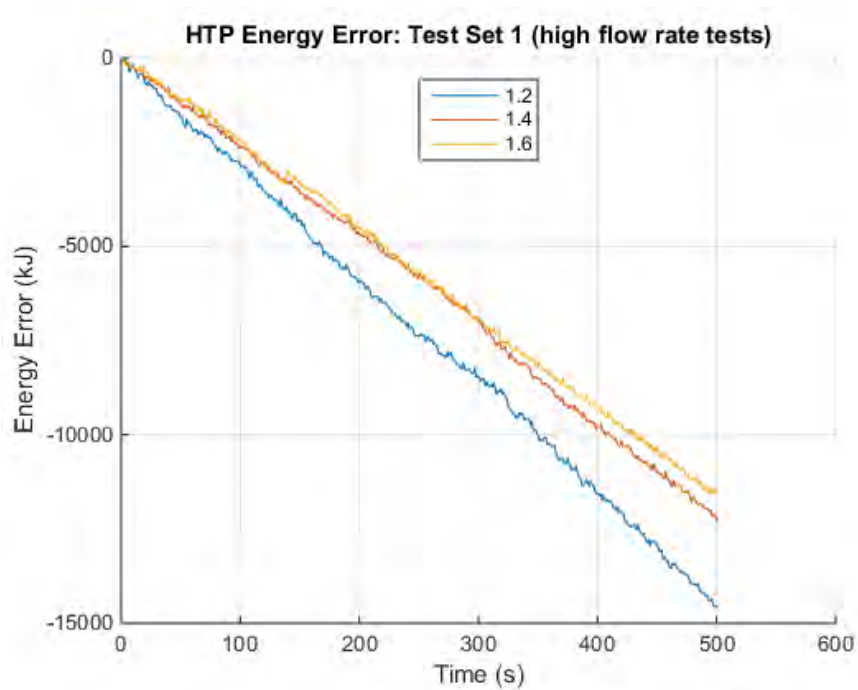


Figure 6-23, Integral HTP energy error for Test Set 1 (high flow rates)

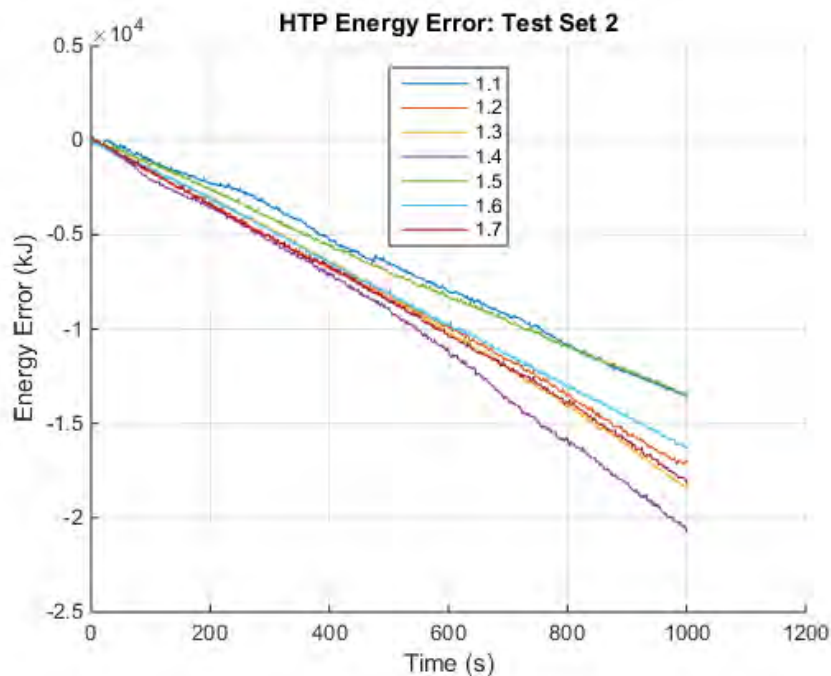


Figure 6-24, Integral HTP energy error for Test Set 2

Table 6-9, Energy errors and percent errors

Test	HPC error (kJ)	HPC error %	CPV error (kJ)	CPV error %	HTP error (kJ)	HTP error %	System error (kJ)	System error %
Set 1								
Test 1.1	-407.6	-0.26	-12332.0	-9.12	-60719.0	-44.9	-12740.0	-8.17
Test 1.2	616.3	1.62	-1808.0	-5.98	-14574.0	-48.2	-708.0	-0.94
Test 1.3	882.3	0.57	7663.0	5.43	-64529.0	-45.7	8545.0	5.49
Test 1.4	916.7	2.43	564.0	2.07	-12205.0	-44.9	1727.0	2.27
Test 1.5	-2213.8	-1.48	6964.0	5.21	-61062.0	-45.7	4750.0	3.17
Test 1.6	1469.8	3.95	1790.0	7.10	-11601.0	-46.0	1813.0	2.44
Set 2								
Test 2.1	231.0	0.56	2623.9	7.70	-13644.0	-40.0	2854.9	6.97
Test 2.2	1608.9	3.46	550.7	1.36	-17125.0	-42.2	2159.6	4.65
Test 2.3	418.2	0.76	4342.5	9.66	-18672.0	-41.5	4760.7	8.85
Test 2.4	481.4	0.81	3579.2	7.16	-20953.0	-41.9	4060.6	6.81
Test 2.5	616.6	1.70	-1423.3	-4.40	-14103.0	-42.6	-806.7	-2.23
Test 2.6	478.0	1.10	1112.3	2.88	-16800.0	-43.5	1590.3	3.64
Test 2.7	224.3	0.46	7723.2	17.85	-18475.0	-42.7	7947.5	16.2

6.4.3 Condensation Rates vs. System Pressure

Although the energy balance showed that the measured conductive heat flux was significantly under predicting actual heat transfer rates (further discussed in Section 6.5), the relative trends observed with those measurements are still relevant. The average heat flux and heat transfer coefficient is shown for each case. The 81X level thermocouple measurements are not included in the averages. Figure 6-25 through Figure 6-28 present the measured condensation heat fluxes and heat transfer coefficients as a function of system pressure. These results are averaged along the length of the plate (the 81X level thermocouples are not included in those averages).

The condensation heat flux as measured with the HTP thermocouples shows a significant increase with pressure. However, this appears to be attributable to the increased temperature gradient as saturation temperature increases. These results suggest heat transfer coefficients do not change significantly with system pressure. This result is consistent throughout the transient and quasi steady tests.

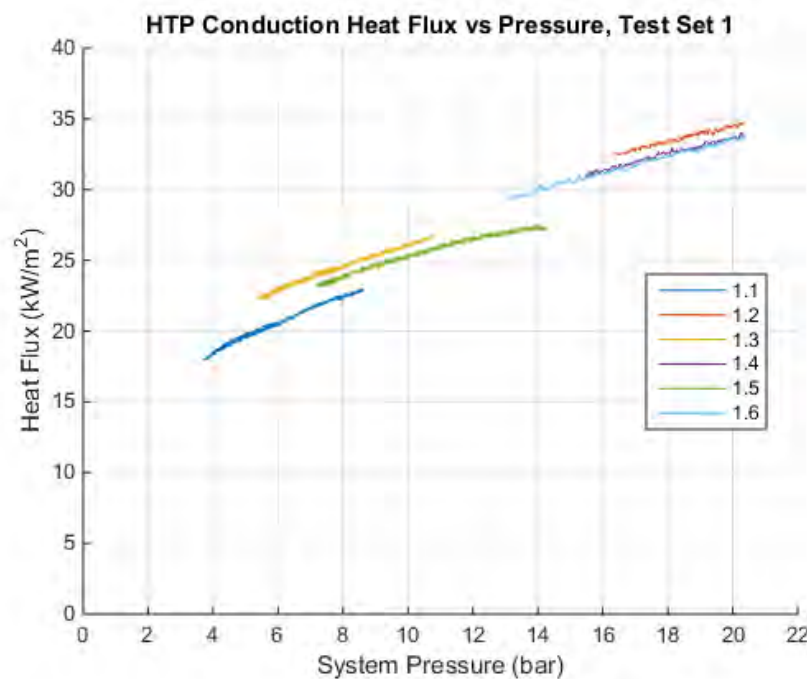


Figure 6-25, Average heat flux from HTP measurements for Test Set 1

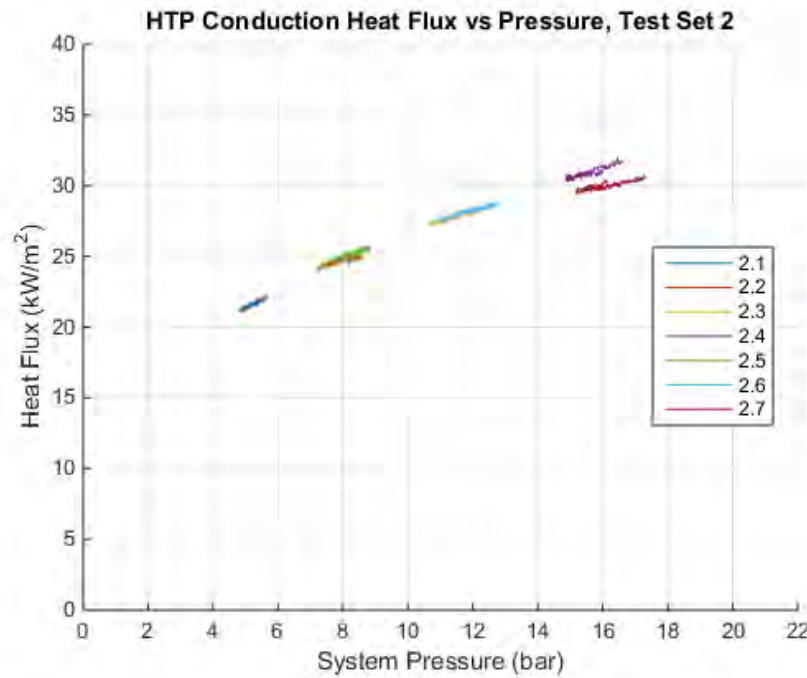


Figure 6-26, Average heat flux from HTP measurements for Test Set 2

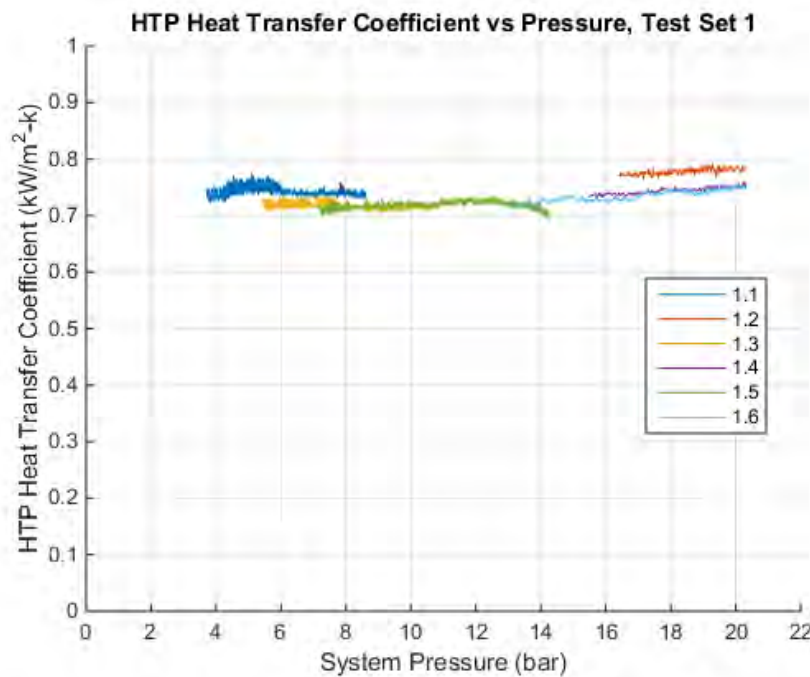


Figure 6-27, Average heat transfer coefficient from HTP measurements for Test Set 1

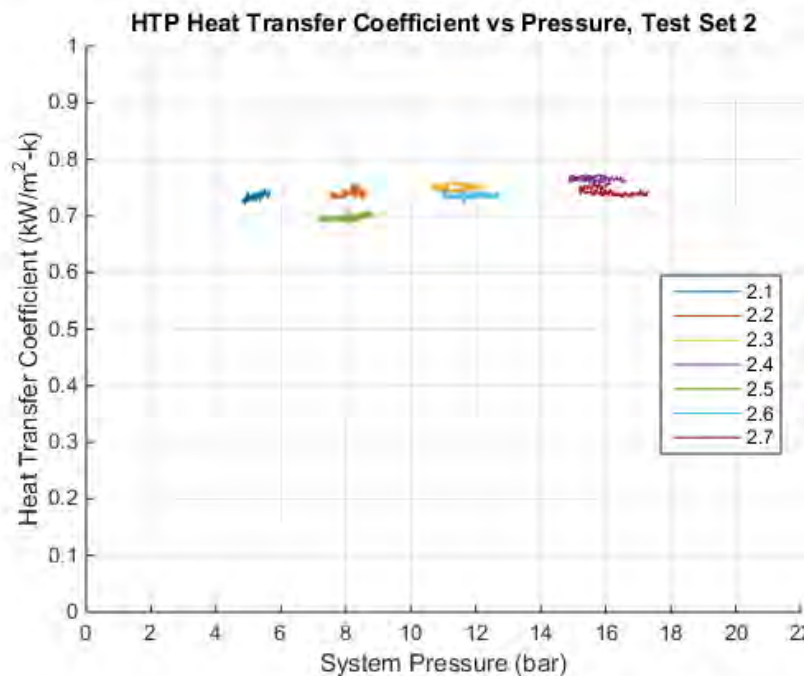


Figure 6-28, Average heat transfer coefficient from HTP measurements for Test Set 2

6.4.4 Condensation Rates vs. Non-condensable Gas Inventory

Figure 6-25 through Figure 6-28 do not show much of a relationship between the initial air inventory and the condensation heat flux measurement. This is because the air seems to settle at the bottom of the containment where the heat fluxes and heat transfer coefficients are not typically evaluated. If the partial set of 81X thermocouples is considered in the analysis, the heat flux reduction at the bottom becomes evident when non-condensables are present. Figure 6-29 shows the heat flux at all 6 thermocouple elevations for Test 2.2 and Test 2.5. These tests maintained the same quasi steady pressure, however the non-condensable inventory is roughly 15 times greater for Test 2.5.

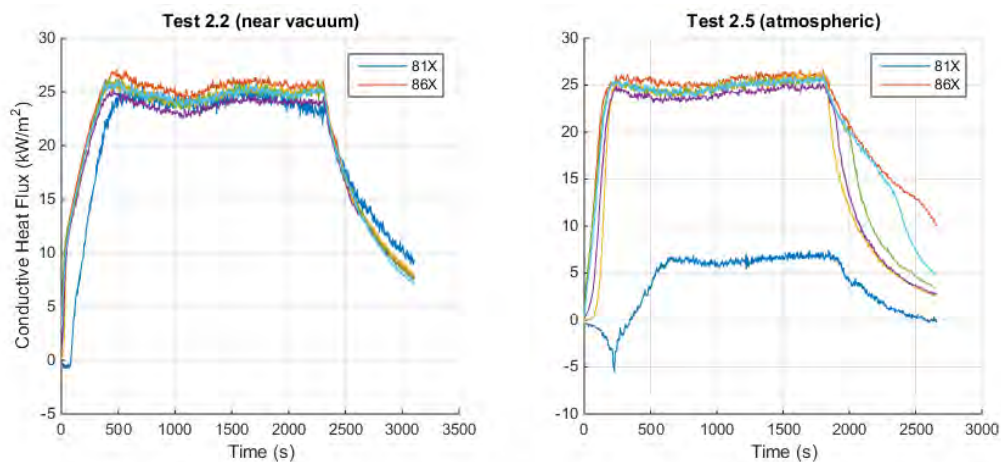


Figure 6-29, Conduction heat flux measured at six axial levels on the HTP

This can also be seen at higher elevations on the HTP when the steam supply is terminated and the remaining steam volume condenses. As the HPC depressurizes, the non-condensable gases expand back up into the containment. A sharp decrease in heat flux climbs the height of the HTP, accompanying the expansion of the gasses.

Figure 6-30 compares this effect for 3 different non-condensable inventories.

Thermocouples on the insulated wall of the HPC (TW892, TW893, TW894) provide a representative measurement of bulk steam temperatures. Regardless of non-condensable inventory, these thermocouples consistently measured temperatures very near saturation for the overall system pressure. This implies the upper region of the containment was relatively free of non-condensable gas as the partial pressure of vapor in the upper regions of the containment was always near the measured system pressure. There are several explanations for this segregation of the species.

- The molecular weight of air at 29g/mol is significantly greater than water at 18g/mol.
- The steam enters near the top of the vessel, hot and superheated.
- The condensation entrains the non-condensable gas towards and down the plate.
- The small diameter of the lower HPC constrains mixing.

The depth of analysis on the influence of non-condensable gases is limited to these observations as there is no reliable method of evaluating local gas concentrations. It is clear that the vapor and gas space may not be considered well mixed, and evidence suggests that the non-condensable concentrations in the upper region of the HPC do not significantly increase when the initial air inventories are greater.

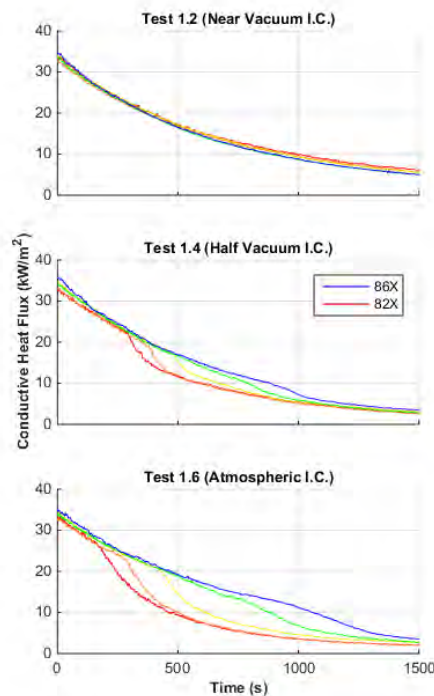


Figure 6-30, Conduction heat flux as measured on the HTP after terminating steam supply

6.5 Error Analysis for Measured Conduction Heat Flux

The measured conduction heat flux appears to under predict the true heat transfer through the plate. As shown in Table 6-9, the conduction heat flux is measured roughly 40% lower than the heat balance suggests. There are several factors that may contribute to this discrepancy:

6.5.1 Edge Effects

Heat transfer through the plate is not 1-D heat conduction as was assumed. Edge effects on the sides of the plate lead to temperature gradient variations along the width of the plate, demonstrated in Figure 6-31. The temperature gradient is lowest where the heat flux is measured (the plate centerline) and greatest on the very edges of the plate.

To investigate this effect, a set of thermocouples were installed to measure the temperature across the edge of the plate and a short distance along the cooling pool and containment vessel wall. These were installed at the elevation of the 83X thermocouples for the second set of tests.

A data point ($t = 2000s$) from the quasi-steady region of Test 2.1 is employed in the following evaluations. The measurements involved are presented in

Table 6-10. The bulk temperature of the pool at this elevation is taken as the elevation weighted average of TF902 and TF903.

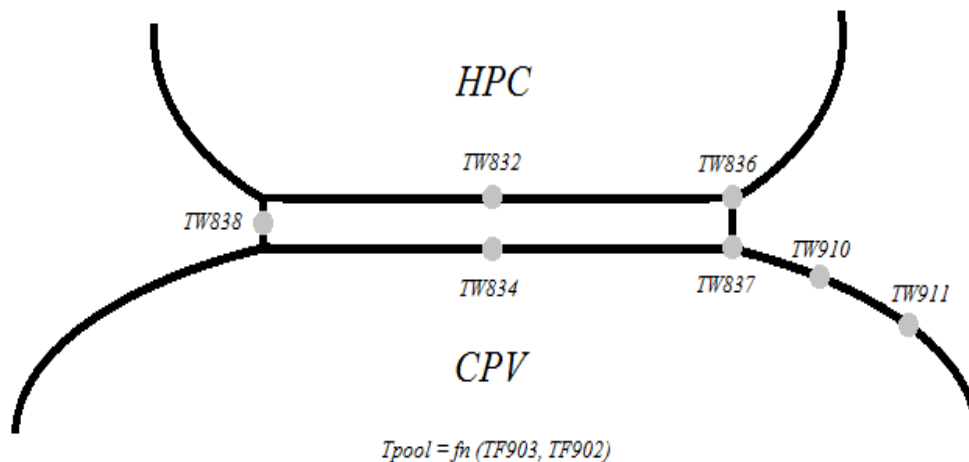


Figure 6-31, Thermocouple placement for investigating edge effect

Table 6-10, Measurements involved in evaluating the edge effect

Parameter	Value
TW832	123.0 °C
TW833	100.3 °C
TW834	73.9 °C
TW836	145.7 °C
TW837	57.8 °C
TW838	110.0 °C
TW910	17.8 °C
TW911	16.8 °C
T _{pool} = (0.9 TF903 + 0.7 TF902) / 1.6	15.9 °C
Heat flux as required from energy balance	35.8 kW/m ²
1-D conduction heat flux measured	21.0 kW/m ²

(A) Interpolation

During the course of the tests, measurement from TW836 and TW837 indicate a much greater temperature gradient at the edge of the plate than at the centerline. The temperature distribution along the width of the plate is known only at the edges and at the centerline; an arbitrary temperature profile may be assigned to estimate the average heat flux across the width of the plate.

Linear temperature profile – This temperature profile is the least credible but should provide an upper bound to the increase in heat transfer from edge effects. The average temperature gradient between the centerline and the edge can provide an average heat flux.

$$\overline{\dot{Q}}''_{83X} = k_{HTP} \cdot \frac{(TW832 - TW834) + (TW836 - TW837)}{2 Th_{HTP}} \quad (6-62)$$

Quadratic temperature profile – This temperature profile is more credible than a linear fit as it implies the rate of change of plate temperature in the lateral direction is continuous and equal to zero at the centerline. This is a second order polynomial fit.

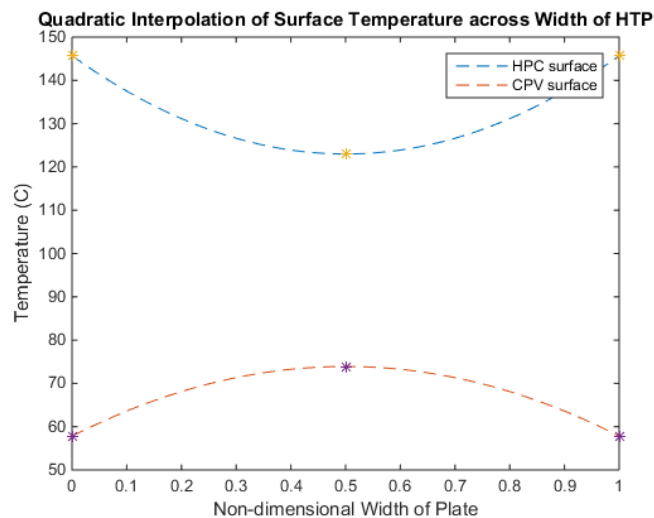


Figure 6-32, Quadratic temperature profile interpolated across width of the heat transfer plate

(B) Fin Effect

Alternatively to estimating the edge effects by interpolating for the surface temperatures across the width of the plate, a fin effect approach is considered. The azimuthal heat flows through the vessel walls in contact with the plate likely account for the majority of the increased heat flux at the edge. This heat flow can be calculated if the vessel walls are considered as fin extensions from the heat transfer plate.

In this case, the length of the fin is assumed to be half of the circumference of the vessel. The vessel wall temperature equal to the bulk pool temperature at the end of the fin and is equal to T_{W837} at the base of the fin. Equation (6-37) can be used to evaluate the heat rate attributable to the fin effect.

$$\dot{Q}_{fin} = \sqrt{hPkA_c}(T_{base} - T_{bulk}) \quad (6-63)$$

Where

h = the natural convection heat transfer coefficient assumed to be $800 \text{ W/m}^2\text{-K}$

P = perimeter of fin taken as height of HTP = 5.64 meters

k = thermal conductivity of SS316 = 16.3 W/m-K

A_c = cross sectional (axial) area of vessel wall in contact with HTP = 0.036 m^2

The result of this calculation is multiplied by a factor of 2 to account for both edges of the plate and then divided by the total plate area to define a contribution to the average heat flux.

(C) Calculated Average Heat Flux for Edge Effect Considerations

Table 6-11, Average heat flux after accounting for the edge effects

Approach Taken	Average Heat Flux
Base Case	21.0 kW/m ²
Linear profile	29.3 kW/m ²
Quadratic profile	26.6 kW/m ²
Fin effect	25.3 kW/m ²
Heat flux as required from energy balance	35.8 kW/m ²

While accounting for the edge effect increases the average heat flux observed, neither method fully satisfies the energy balance. Edge effects may contribute to the overall discrepancy in the energy balance, but they do not explain why the local heat flux and heat transfer coefficients measured at the centerline of the plate are unusually low when compared to existing condensation models. The edge effects act to increase the heat transfer on the edges, not to decrease it at the centerline. For example, if the plate was widened considerably, the influence of the edge effects would decrease and the average temperature gradient across the thickness of the plate would approach the measured centerline temperature gradient.

6.5.2 Spatial Error on Thermocouple Measurements

A source of error contributing to the low measured heat flux at the centerline of the plate may be the spatial error associated with the location of the thermocouple temperature measurements. Slots were drilled in the heat transfer plate for placing the embedded thermocouples. These slots are rectangular with a depth and height of 0.083 inches. It is possible the temperature being measured by the thermocouple is attributable to some location within the slot, as opposed to the surface of the plate.

Table 6-12, Average heat flux accounting for spatial error

Assumed Measurement Location	Average Heat Flux
Base Case (surface)	21.0 kW/m ²
Center of slot	22.2 kW/m ²
Inside of slot	23.6 kW/m ²

6.5.3 Temperature Field Distortion

An additional source of error that may relate to the low measured conduction heat flux is distortion of the temperature field due to the slots, thermal paste, and thermocouples themselves. The magnitude of error or bias that can be associated to distortion of the temperature field is challenging to evaluate with any confidence due to the complexity of the geometry in question (Figure 6-33). In this case, the K type thermocouples and boron nitride thermal paste both have greater thermal conductivities than the SS316 HTP. This could contribute to a reduced heat flux measurement as the thermal resistance across the depth of the plate is reduced by introducing the embedded thermocouples. The degree to which the temperature field is distorted by the presence of the thermocouples is unknown; it is unclear if this effect is sufficient to complete the energy balance.

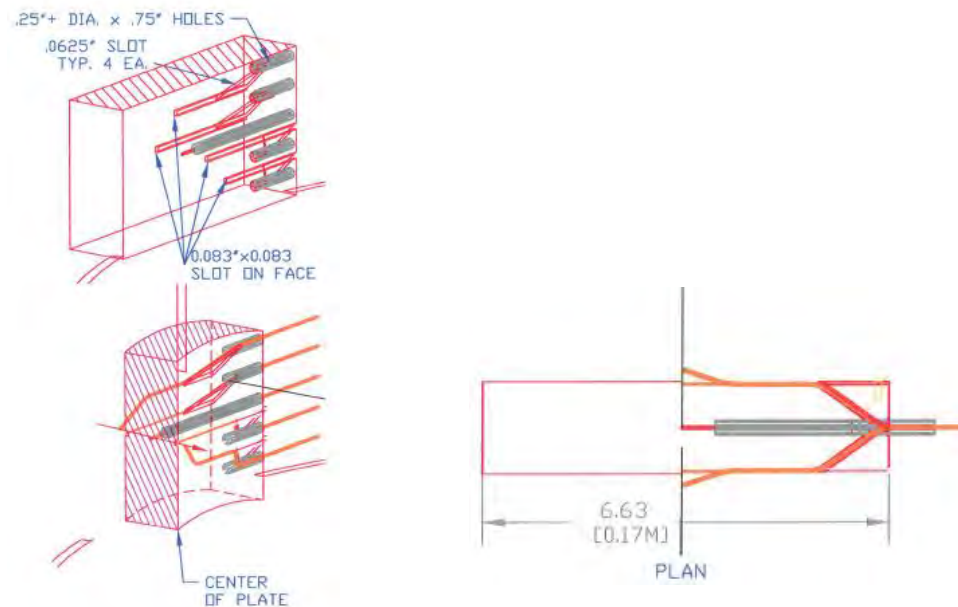


Figure 6-33, Diagram of embedded thermocouple placement

6.5.4 Challenges with Surface Temperature Measurement

Experimentally measuring surface temperatures has always been challenging. The discontinuity between the environmental temperature and the surface temperature offers difficulties not encountered in other types of temperature measurements. Often times, non-contact measurement methods such as the use of infrared sensors are ideal for measuring surface temperatures as these methods do not influence the temperature field. However, in many applications such as this one, embedded thermocouples are the most suitable way to measure surface temperatures and associated heat fluxes.

In an investigation similar to this one, Kim et al. [61] characterized condensation rates with use of embedded thermocouples measuring a temperature gradient across a tube wall. The authors state that this measurement method is often not adopted due to large measurement uncertainties of the inner and outer surface temperatures. The authors report a need to calibrate this method in order to evaluate accurate surface measurements. This was done by applying a known heat flux to the tube and then applying a correction factor on the subsequent test results.

6.6 Correction for HTP Temperatures

Whichever the reason for the low measured heat flux, an alternate method is proposed to evaluate an effective heat flux and heat transfer coefficient. This calculation assumes that there are no environmental heat losses and that all of the heat removal associated with the measured phase change occurs entirely on the unsubmerged surface area of the heat transfer plate.

This allows for the evaluation of an average heat flux and a representative average temperature gradient on the plate. This temperature gradient is placed across the measured plate midline temperatures (TW8i3) to determine effective surface temperatures which can be used to evaluate a heat transfer coefficient.

By substituting in the evaluation for heat flux, the heat transfer coefficient is shown to be calculated as:

$$h_{8iX} = \frac{k_{HTP} \cdot \frac{(TW8i2 - TW8i4)}{Th_{HTP}}}{[T_{sat}(PT801) - TW8i2]} \quad (6-64)$$

It becomes clear that the calculated heat flux is highly sensitive to the HTP thermocouple measurements, particularly the HPC surface temperature, TW8i2. An imprecise or inaccurate HPC side surface temperature measurement will doubly compound the error in measured heat transfer coefficient. The accuracy of the HTP surface temperatures will be made apparent in the energy balance.

An alternate method, while somewhat contrived, may also be used to estimate the heat transfer coefficients. This method involves defining a HTP heat flux from the measured condensate accumulation in the HPC.

The condensate formation measurement is slow to change and does not capture rapidly changing condensation rates. As such, this method is best applied to Test Set 2 where, the condensation rate remains relatively constant through each quasi steady period.

$$E_{latent} = m_{liq} \cdot (h_{sat,v}(PT801) - h_{sat,l}(PT801)) \quad (6-65)$$

$$\Delta \dot{E}_{latent} = \frac{E_{latent}(RB) - E_{latent}(LB)}{RB - LB} \quad (6-66)$$

$$A_{HTP,unsub} = (H_{HTP} - LDP801(LB:RB)) \cdot W_{HTP} \quad (6-67)$$

$$\dot{Q}''_{latent} = \frac{\Delta \dot{E}_{latent}}{\mathbf{mean}[A_{HPT,unsub}]} \quad (6-68)$$

The above equation produces a single value for the average condensation heat flux during the quasi steady region of interest. The effective ΔT required to produce this heat flux across the plate can then be calculated.

$$\Delta T_{effective} = \frac{\dot{Q}''_{latent} \cdot Th_{HTP}}{k_{HTP}} \quad (6-69)$$

The effective ΔT is then centered upon the centerline HTP surface temperature, providing effective surface temperatures.

$$TW8i2_{eff} = TW8i3 + \frac{\Delta T_{effective}}{2} \quad (6-70)$$

The mean pressure across the region of interest is also evaluated to define a saturation temperature and for plotting the results.

$$h_{8ix}^* = \frac{\dot{Q}''_{latent}}{T_{sat}(PT801_{mean}) - TW8i2_{eff}} \quad (6-71)$$

Figure 6-34 shows the corrected heat flux on the plate for each of the tests from the second set. These quasi steady tests were more suitable than the first set of transient tests for the averaging that was required. This alternative method calculates a heat flux which is significantly greater than as calculated from the HTP temperature gradient.

The difference between the non-condensable initial conditions is evident with this method. While the HTP thermocouples don't measure much of a difference in the heat flux on the upper half on the HTP, the condensate level rise reflects the reduced condensation rate on the lower portion.

The HTP thermocouple measurements (Figure 6-27 and Figure 6-28) suggested no influence on the heat transfer coefficient from changes in pressure. Conversely, this alternate method suggests that increased pressure may enhance heat transfer coefficients, though this result carries significant uncertainty.

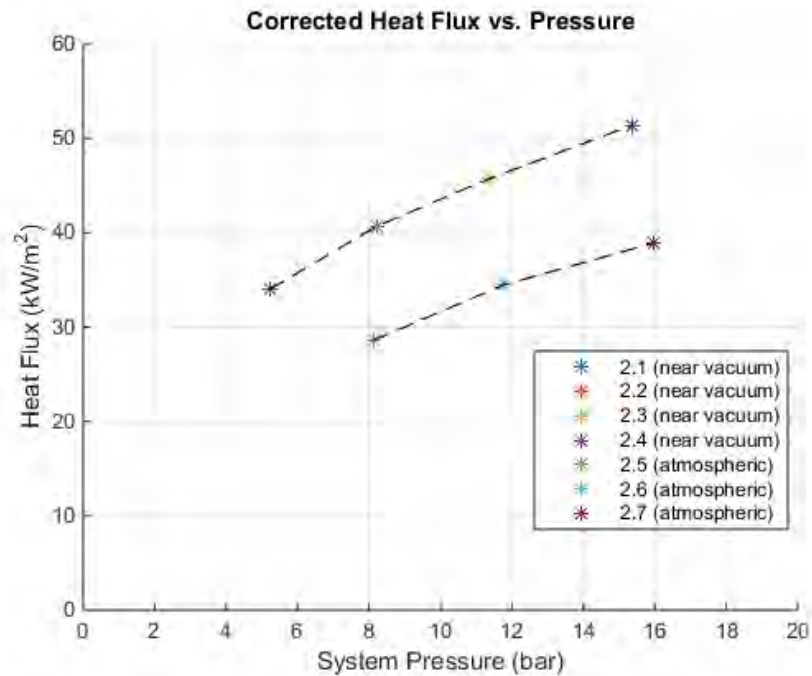


Figure 6-34, Condensation heat flux calculated from alternate method vs. system pressure

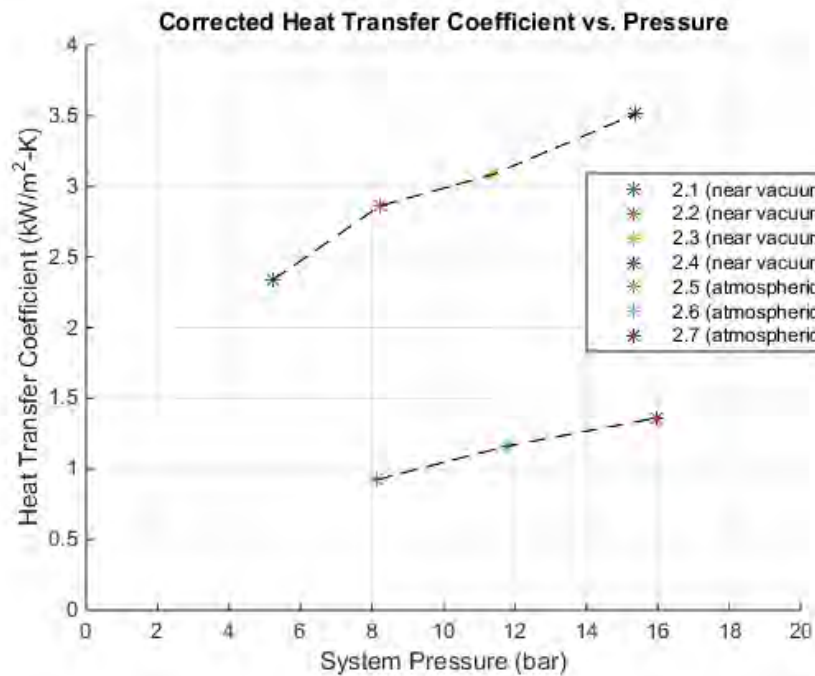


Figure 6-35, Heat transfer coefficients calculated from alternate method vs. system pressure

6.7 Uncertainty Quantification

To clarify displaying the results, the evaluated uncertainty of heat flux and heat transfer coefficient were omitted from the previous figures. Figure 6-36 and Figure 6-37 shows the heat flux, heat transfer coefficient, and associated uncertainties for an individual test. Figure 6-38 and Figure 6-39 shows the uncertainty evaluation of the corrected heat flux and heat transfer coefficients. The correction method for the heat transfer coefficient appears to be quite sensitive to instrument error and that confidence in the validity of the result may be limited. The calculations involved in evaluating uncertainties are described after the plots.

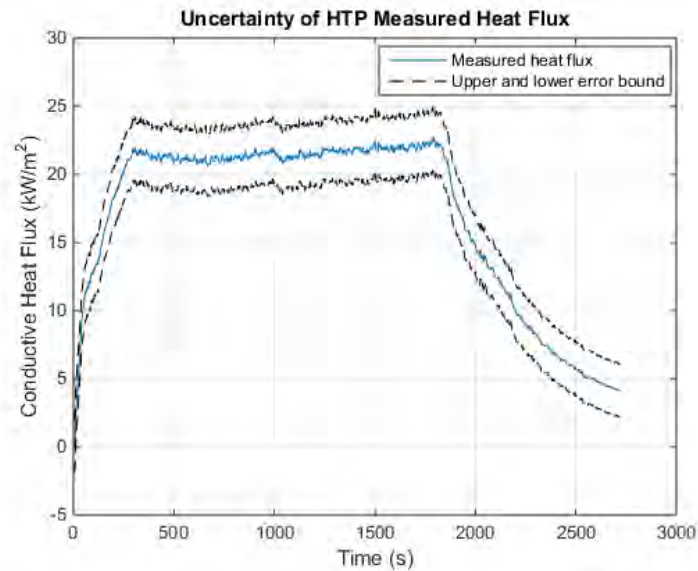


Figure 6-36, Uncertainty of heat flux from HTP measurements (Test 2.1)

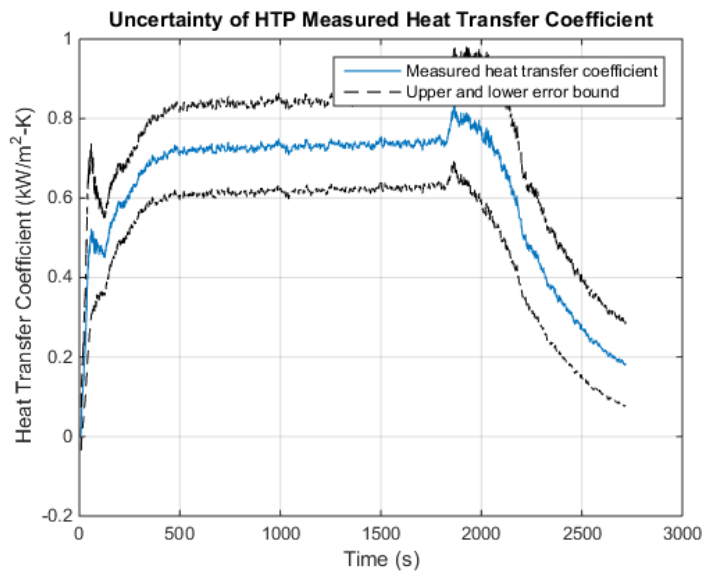


Figure 6-37, Uncertainty of heat transfer coefficient from HTP measured (Test 2.1)

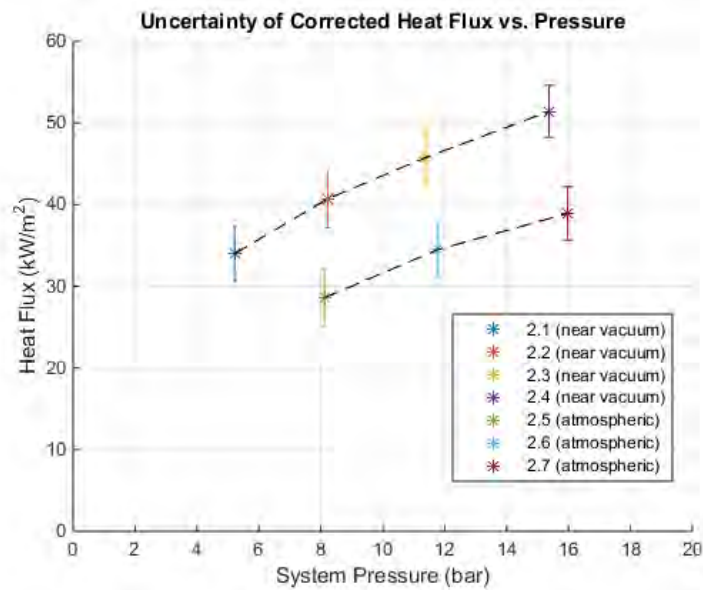


Figure 6-38, Uncertainty of heat flux with corrected surface temperatures

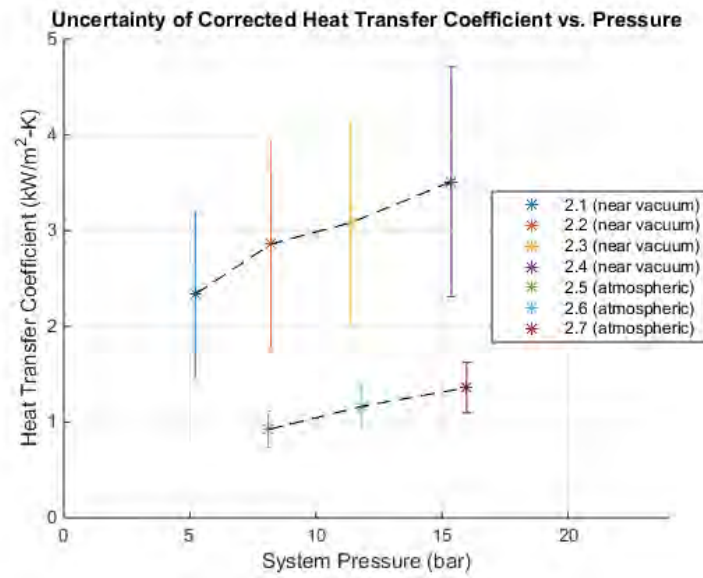


Figure 6-39, Uncertainty of heat transfer coefficient with corrected surface temperatures

The error associated with those evaluations is the combination of various contributing sources of error. The instrument uncertainties necessary for evaluating the heat flux and heat transfer coefficient uncertainties are presented in Table 6-13.

Table 6-13, Relevant Instrument Uncertainties

Measurement Type	Tag Number	Listed Uncertainty
Thermocouples	TW-xxx, TF-xxx, TH-xxx	3.2°C
Pressure Meter	PT-801	1.4 psi
Level Meter	LDP-801	0.772 inches H ₂ O
Plate width (between TCs)	--	0.083 inches

In determining the heat flux using the HTP thermocouple measurements, the contributing sources of error include the thermocouple measurement uncertainty and the spatial uncertainty of the thermocouple measurements. The value used for thermal conductivity is an assumption and does not have a quantified uncertainty associated with it. While the evaluation for heat flux is:

$$\dot{Q}''_{8iX} = k_{HTP} \cdot \frac{(TW8i2 - TW8i4)}{Th_{HTP}} \quad (6-72)$$

The error evaluation for heat flux is:

$$\epsilon_{\dot{Q}''} = \pm \dot{Q}''_{8iX} \cdot \sqrt{\left(\frac{\sqrt{2} \cdot \epsilon_T}{TW8i2 - TW8i4}\right)^2 + \left(\frac{\epsilon_{Th}}{Th_{HTP}}\right)^2} \quad (6-73)$$

Determining the heat transfer coefficient using the HTP measurements also requires evaluating the bulk steam temperature. The bulk steam temperature is assumed to be the saturated temperature at the measured total pressure; there are no quantified uncertainties associated with this assumption.

The evaluation for heat transfer coefficient is:

$$h_{8iX} = \frac{\dot{Q}''_{8iX}}{[T_{sat}(PT801) - TW8i2]} \quad (6-74)$$

The heat flux and associated error were previously evaluated. It is useful to evaluate the error associated with the saturation temperature separately.

$$\epsilon_{T_{sat}} = \pm \frac{T_{sat}(PT801 + |\epsilon_P|) - T_{sat}(PT801 - |\epsilon_P|)}{2} \quad (6-75)$$

The error evaluation for heat transfer coefficient is:

$$\epsilon_h = \pm h_{8iX} \cdot \sqrt{\left(\frac{\epsilon_{\dot{Q}''}}{\dot{Q}''_{8iX}}\right)^2 + \left(\frac{\sqrt{\epsilon_{T_{sat}}^2 + \epsilon_T^2}}{T_{sat}(PT801) - TW8i2}\right)^2} \quad (6-76)$$

Evaluating the error associated with the surface temperature corrections require extensive calculations. The first step is to evaluate the error in the calculated condensate density. The calculated density is a function of temperature and pressure.

$$\rho_{liq} = \rho(PT801, TF804) \quad (6-77)$$

$$\epsilon_{\rho} = \pm \sqrt{\left(\frac{\rho(PT801+|\epsilon_P|, TF804) - \rho(PT801-|\epsilon_P|, TF804)}{2}\right)^2 + \left(\frac{\rho(PT801, TF804+|\epsilon_T|) - \rho(PT801, TF804-|\epsilon_T|)}{2}\right)^2} \quad (6-78)$$

Density and the liquid level measurement are used to calculate instantaneous liquid mass.

$$m_{liq} = \rho_{liq} \cdot LDP801 \cdot A_{HPC} \quad (6-79)$$

$$\epsilon_{mliq} = \pm m_{liq} \cdot \sqrt{\left(\frac{\epsilon_{LDP}}{LDP801}\right)^2 + \left(\frac{\epsilon_{\rho}}{\rho(PT801, TF804)}\right)^2} \quad (6-80)$$

The specific heat of vaporization is based on the saturated pressure.

$$h_{fg} = h_{sat,v}(PT801) - h_{sat,l}(PT801) \quad (6-81)$$

$$\epsilon_{hfg} = \pm \frac{1}{2} \cdot \left[[h_{sat,v}(PT801 + |\epsilon_P|) - h_{sat,l}(PT801 + |\epsilon_P|)] - [h_{sat,v}(PT801 - |\epsilon_P|) - h_{sat,l}(PT801 - |\epsilon_P|)] \right] \quad (6-82)$$

The latent heat released is associated with the instantaneous liquid mass and specific latent heat.

$$E_{latent} = m_{liq} \cdot (h_{sat,v}(PT801) - h_{sat,l}(PT801)) \quad (6-83)$$

$$\epsilon_{latent} = \pm E_{latent} \cdot \sqrt{\left(\frac{\epsilon_{mliq}}{m_{liq}}\right)^2 + \left(\frac{\epsilon_{hfg}}{h_{sat,v}(PT801) - h_{sat,l}(PT801)}\right)^2} \quad (6-84)$$

The rate of change of latent heat is the difference between the initial and final instantaneous latent heat divided by the region of interest (RB-LB).

$$\Delta \dot{E}_{latent} = \frac{E_{latent}(RB) - E_{latent}(LB)}{RB - LB} \quad (6-85)$$

$$\epsilon_{\Delta latent} = \pm \frac{\sqrt{2 \cdot (\epsilon_{latent})^2}}{RB - LB} \quad (6-86)$$

The unsubmerged area of the heat transfer plate is evaluated with the liquid level measurement.

$$A_{HTP, unsub} = (H_{HTP} - LDP801(LB: RB)) \cdot W_{HTP} \quad (6-87)$$

$$\epsilon_{A_{htp}} = \pm \epsilon_{LDP} \cdot W_{HTP} \quad (6-88)$$

The heat flux on the plate is calculated with latent heat rate and available surface area.

$$\dot{Q}''_{latent} = \frac{\Delta \dot{E}_{latent}}{\text{mean}[A_{HTP, unsub}]} \quad (6-89)$$

$$\epsilon_{Q''_{latent}} = \pm \dot{Q}''_{latent} \cdot \sqrt{\left(\frac{\epsilon_{\Delta T_{latent}}}{\Delta \dot{E}_{latent}}\right)^2 + \left(\frac{\epsilon_{A_{HTP}}}{\text{mean}[A_{HTP,unsub}]}\right)^2} \quad (6-90)$$

The effective temperature difference across the plate required to produce that heat flux is evaluated.

$$\Delta T_{effective} = \frac{\dot{Q}''_{latent} \cdot Th_{HTP}}{k_{HTP}} \quad (6-91)$$

$$\epsilon_{\Delta T_{eff}} = \pm \Delta T_{effective} \cdot \left(\frac{\epsilon_{Q''_{latent}}}{\dot{Q}''_{latent}}\right) \quad (6-92)$$

The effective containment side surface temperature is evaluated using the effective temperature difference and the midline HTP temperature (TW8X3).

$$TW8i2_{eff} = TW8i3 + \frac{\Delta T_{effective}}{2} \quad (6-93)$$

$$\epsilon_{TW8i2*} = \pm \sqrt{\epsilon_T^2 + \left(\frac{\epsilon_{\Delta T_{eff}}}{2}\right)^2} \quad (6-94)$$

The effective heat transfer coefficient is evaluated using the effective heat flux and effective surface temperature.

$$h_{8iX}^* = \frac{\dot{Q}''_{latent}}{T_{sat}(PT801_{mean}) - TW8i2_{eff}} \quad (6-95)$$

$$\epsilon_{h*} = \pm h_{8iX}^* \cdot \sqrt{\left(\frac{\epsilon_{Q''_{latent}}}{\dot{Q}''_{latent}}\right)^2 + \left(\frac{\sqrt{\epsilon_{T_{sat}}^2 + \epsilon_{TW8i2*}^2}}{T_{sat}(PT801_{mean}) - TW8i2_{eff}}\right)^2} \quad (6-96)$$

6.8 Test Result Conclusion

A total of 13 condensation tests were conducted with the MASLWR test facility. Two unique testing approaches (transient vs. quasi steady) were employed, providing diversity in the data collected. Steam condensation in the containment was evaluated between pressures of approximately 4 and 21 bar with three different static inventories of non-condensable gas. Condensation and heat transfer rates were evaluated employing several methods, notably from measured temperature gradients in the HTP as well as measured condensate formation rates. A detailed mass and energy accounting was used to assess the various measurement methods and to support simplifying assumptions required for the analysis. Condensation heat fluxes and heat transfer coefficients are calculated and presented as a function of pressure to satisfy the objectives of this investigation.

The heat transfer coefficients calculated using the measured HTP wall temperatures are considerably lower than popular condensation models would predict. The experimentally calculated value of between 700 and 800 W/m²K is just a fraction of the Nusselt prediction, evaluated to be approximately 5000 W/m²-K for the conditions of the test. The correction for surface temperatures proposed in Section 6.6 leads to effective heat transfer coefficients in the range of 3000 W/m²K.

The Uchida and Tagami models are the most widely employed condensation models used in containment analysis. The correlations they developed are attractive in their simplicity, as they relate the heat transfer coefficient to a single parameter, the non-condensable weight fraction. Dehbi expanded upon their work by considering the influence of additional parameters such as pressure and condensing length. According to these experimental models, the air mass fraction required to achieve the same heat transfer coefficients as evaluated with the HTP surface temperatures in the MASLWR facility would have to be roughly 0.3 (Figure 6-40). During the tests, the total air mass fractions were generally much lower than this (between 0.01 and 0.4 at the extremes of testing conditions). The corrected heat transfer coefficients on the order of 3000 W/m²K show considerably better agreement with these correlations. Regardless, application of these models to the MASLWR containment is not appropriate due to the very poor mixing of steam and gas.

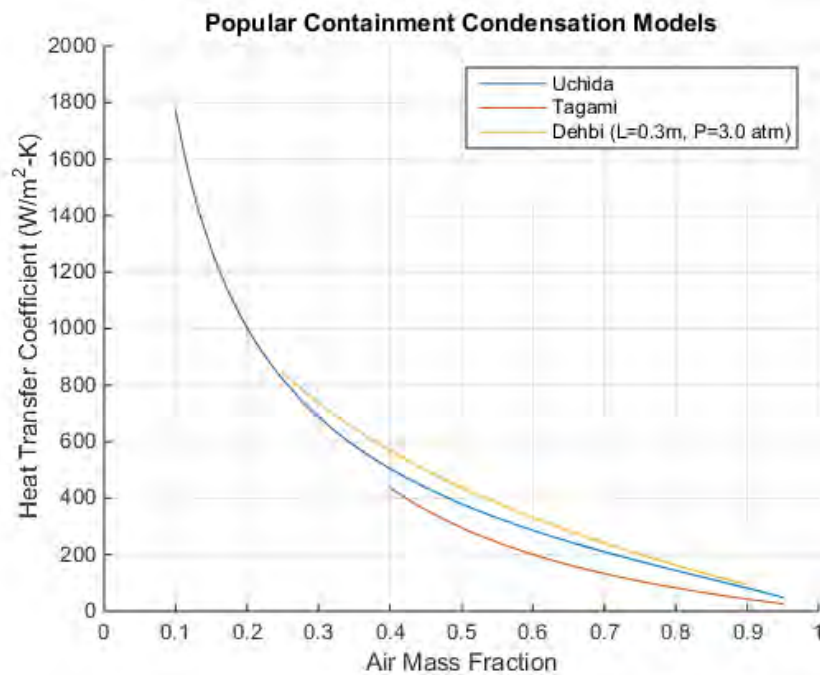


Figure 6-40, Condensation heat transfer coefficient predictions from popular models

A possible explanation for the low measured heat transfer coefficients is a localized concentration of non-condensable gas at the film interface. The theoretical work of Minkowycz and Sparrow concluded that even small concentrations of non-condensable gasses may reduce heat transfer coefficients to within the range observed in these tests. However, if non condensable gases were degrading the heat flux on the plate, one would expect a further reduction in the measured heat flux when the initial air inventory was increased. This was not observed with the tests. The non-condensable gases concentrate at the bottom of the containment while the vapor in the upper containment appears to remain mostly pure.

The energy balance performed with the analysis indicates agreement between the heat removed from the HPC and heat supplied to the CPV and supports the assumption that the large majority of condensation is occurring on the heat transfer plate and not on the insulated surfaces of the HPC. The calculations employed for the change in CPV internal

energy were admittedly somewhat contrived (recall extrapolating temperature measurements) introducing an unknown degree of uncertainty. However, the result of the comparison suggests that environmental heat losses were low and the majority of heat removed from the HPC was conducted through the plate. The energy balance also indicates that the conductive heat transfer measured with the HTP thermocouples was systematically lower than the other two measurements.

An explanation that has been proposed for this inconsistency is that the heat flux across the plate varies significantly along its width and, at the midline, is being measured at the lowest value. The HPC and CPV vessels conduct heat azimuthally and across the edges of the plate where the structures are welded together. The heat flux is hypothesized to be much greater along the edges of the plate and the integration of the heat flux would perhaps match the heat removal calculated from the other methods. Figure 6-41 is a diagram of the scenario described, including representative temperature profiles along both sides of the plate. This concept has been referred to as the fin effect since the HPC and CPV vessels act as extensions of the heat transfer plate.

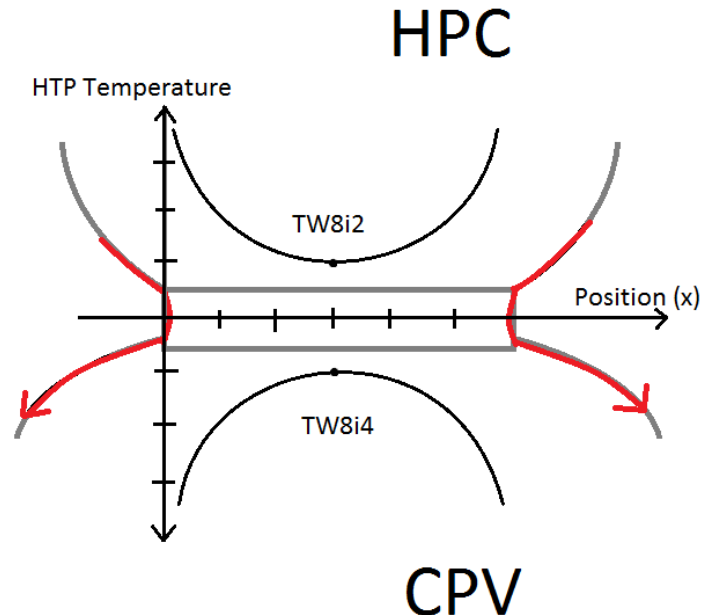


Figure 6-41, Diagram of the theorized fin effect

At a glance, the fin effect theory is attractive for explaining the unusually low heat transfer coefficients measured with the facility. A valid argument is made that heat transfer is not entirely a 1-D conduction problem as per our assumption. While this fin effect likely contributes to the incomplete energy balance, it fails to explain why the local heat transfer coefficients at the midline of the plate are so much lower than expected.

It seems likely that the heat transfer plate thermocouples are not accurately measuring the surface temperature on either side. The thermocouples have been fixed to the plate since the construction of the facility and cannot be individually removed and calibrated. It could be that distortion of the thermal field from the measurement device and difficulties in accurately measuring interface temperatures lead to this discrepancy. As was reported

by Kim et al.[1][61], the best solution may be to calibrate the system by applying a known heat flux.

The objectives of this investigation included determining whether there was a pressure effect on condensation heat transfer rates. The results of the work remains somewhat indecisive on this matter. The heat transfer coefficient, as measured with the HTP thermocouples, suggest that there is no pressure effect on heat transfer rates. Many of the prior works relating to pure vapors support this conclusion, including implications of the Nusselt theory. However, most investigation into the pressure effect in the presence of non-condensable gases conclude that heat transfer coefficients are substantially improved with increasing pressure. This suggests that increased pressure may be reducing the heat transfer resistances involved with diffusion across the steam-vapor boundary layer (which doesn't exist with pure vapors). Conversely to the HTP measurements, the alternate method for calculating heat transfer coefficients employed in the investigation seemed to indicate a pressure dependence however the uncertainties invoked with this method appear to be significant.

The MASLWR facility that provided the opportunity for this investigation has been largely dismantled. Use of the renovated facility which includes a brand new HPC and CPV will likely not be offered for academic investigations as it embodies highly proprietary technology that will play a critical role in certification of the NuScale Power Module™ design.

To continue with the experimental investigation, the dismantling of the facility presents an intriguing opportunity. While this would require substantial funding, the old HPC and CPV, currently in storage, could be refurbished into a sort of separate effects facility. The proposed work would involve replacing the CPV with a thin rectangular flow channel along the heat transfer plate. Cooling on the pool side of the plate could be performed with a single phase flow, allowing for a very accurate average heat flux evaluation. Additionally, a pressurized vessel may be connected to the drain at the bottom of the containment. This would allow condensate to continuously drain into the storage tank during testing and may help flush out any non-condensable gas. The steam would continue to be supplied by the secondary system of the (now renovated) MASWLR facility. This separate effects facility would be capable of achieving steady state conditions and could address many of the limitations encountered with this investigation.

7 MODELING OF THE TESTS USING MELCOR

The numerical modeling of the tests was carried out at the University of Wisconsin, Madison, using a containment analysis code, MELCOR, a fully integrated, engineering level computer code that models the progression of severe accidents in light-water reactor nuclear power plants. It is being developed at Sandia National Laboratories for the U.S. Nuclear Regulatory Commission (US NRC) as a second-generation plant risk assessment tool and the successor to the Source Term Code package.

The MELCOR consists of a main executive driver and a number of different packages. Each package deals with specific physical phenomenon or section of a plant. Those packages together model the major systems of a reactor plant and their coupled interactions. Three packages in particular are used to model the experiments at OSU: control volume hydraulics (CVH), flow path (FL) and heat structure (HS). Other important packages not used for this specific case include, but are not limited to, cavity, core, and decay heat.

The CVH and the FL packages together are responsible for modeling the thermal-hydraulic behavior of fluids. The CVH package defines the thermal-hydraulic control volumes. Each control volume is specified with its content (type(s) of fluid), thermodynamic state (equilibrium/non-equilibrium), temperature and pressure. If only gas/liquid is present, saturation condition needs to be specified as well (superheated/subcooled or saturated). If both liquid and gas phases are present, the user must input the pool surface (atmosphere/pool boundary). This package does not differentiate different geometries and each control volume is only defined with tabular altitude-dependent volume (volume vs. altitude table; VAT). Each control volume can be stratified in two layers: atmosphere and pool. Atmosphere and pool do not necessarily indicate gas and liquid as liquid can be present in atmosphere as fog and gas in pool as bubble.

A control volume can either be active or time-independent. In default, a control volume is active. Active control volume indicates that the contents of the control volume is thermodynamically active. In other words, in an active control volume, states are advanced with time by integrating the conservation equations. Time-independent control volume, on the other hand, has fixed content, that is, the content of the time-independent control volume does not change over time regardless of the flow from or to. In most cases, control volumes are active. However, to represent ambient volumes or specific sources, time-independent control volumes can be used.

The FL package defines flow paths which connect the control volumes defined previously by the CVH package. Each flow path connects two control volumes and is specified with 'from' and 'to' junctions. 'from' junction is the middle altitude where the flow path is attached with the upstream control volume and 'to' with the downstream control volume. This package assumes circular cross-sectional area with the user-inputted hydraulic diameter, flow area, and flow length. A one-dimensional momentum equation governs the mass transport in the flow path. Unlike a typical computational fluid dynamics code, MELCOR allows more than two flow paths to be attached to one control volume. The direct heat transfer from/to a flow path to another flow path or a specific control volume is prohibited.

The HS package defines solid structures. Each structure can have different materials with different properties. The HS package calculates one-dimensional heat conduction within such heat structures and energy transfer across their boundary surfaces. The thickness

and the materials constructing each heat structure are defined by multiple nodes as shown by Figure 7-1.

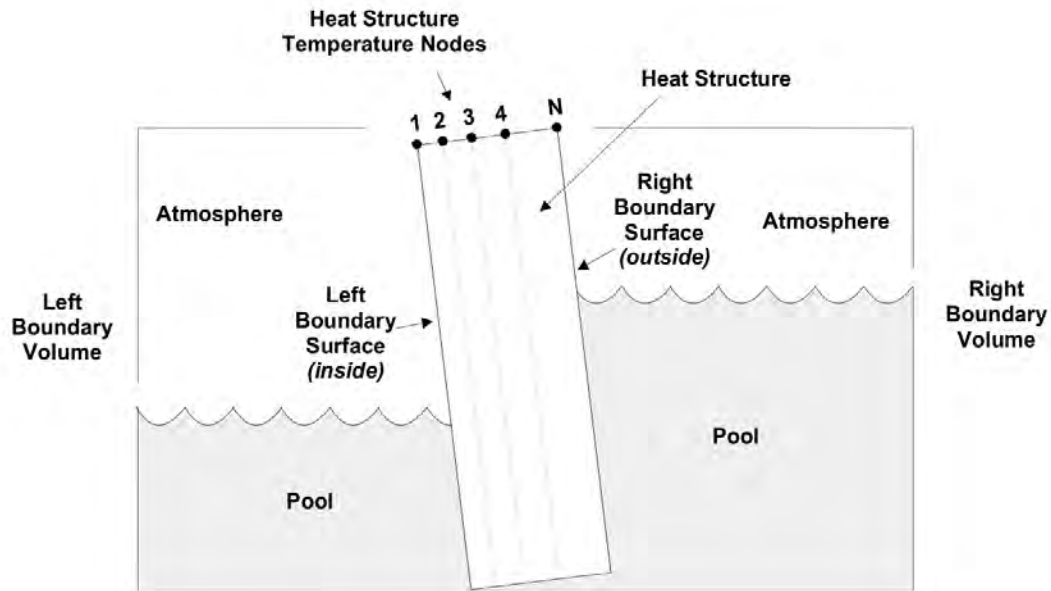


Figure 7-1 Heat Structure in a Control Volume

The initial temperature at each node must be supplied as well as the material between two adjacent nodes. Boundary conditions must also be specified at the first and last nodes (left and right ends for rectangular geometry or inside and outside surfaces for cylindrical and spherical geometry). The MELCOR offers a number of different boundary condition options which include, but are not limited to, symmetry (adiabatic), constant or time-dependent heat flux, and convective boundary (requires an adjacent control volume). The direct heat transfer from a heat structure to another is prohibited.

7.1 Simplifications/Assumptions

Due to limitations posed by MELCOR and for simplicity of modeling, following simplifications or assumptions are made to model the experiments.

(1) Adiabatic Vessel Shells

The insulated surfaces of the HPC and the CPV are assumed to be adiabatic. In other words, the Thermo-12 hydrous calcium silicate insulation layer was ignored, and instead, the outer shell surfaces are given an adiabatic boundary condition. HPC tank mass, however, is still accounted for as it acts as a significant heat sink in the early stage of the experiment.

In similar manner, the electrical heating of the HPC outer shell is also ignored. Because the electrical heating is to ensure that there is no heat transfer from the HPC to its surroundings, specifying adiabatic boundary condition is sufficient to eliminate such heat transfer.

(2) Constant Steam Source

The detailed mechanisms in the RPV are removed from the MELCOR model. Instead, the properties of the superheated steam produced in the RPV are taken as a time-independent source which continuously enters the HPC. In theory, the produced steam should have constant thermodynamic properties as the output of the electrical heater in the steam generator is constant. However, the experimental data indicate that there exists small variance in temperature and pressure as well as the flowrate of the produced steam. Nevertheless, the steam properties are assumed to be constant throughout each test for MELCOR simulation.

(3) Simplified Initial Conditions

Numbers of thermocouples in the HPC and CPV report different initial temperatures at different locations in the same tank. However, local temperatures of the air in the HPC deviate very little from the measured ambient temperature and those of the water in the CPV generally vary very little from one another. Therefore, the initial air temperature in the HPC is assumed to be the same as ambient temperature and the initial water temperature in the CPV as the average of each different local temperature.

(4) Ignoring Cooling Pool Vessel Tank Mass

Unlike the vessel material of the HPC which was included in the MELCOR model, the vessel material of the CPV was ignored. The temperature of water in the CPV does not change significantly during the experiment as the water volume in the CPV is significantly larger than the volume of the HPC.

(5) Non-condensable Gas Composition

The air which initially fills the HPC acts as non-condensable gas during the condensation process. The composition of air is assumed to have the following composition: 80% N₂ and 20% O₂.

7.2 Model Constituents

(1) Reactor Pressure Vessel

As mentioned in the previous section, the detailed mechanisms which take place in the RPV are ignored. The generated steam is assumed to have constant temperature, pressure and flowrate. A time-independent control volume, the content of which is only the superheated steam with fixed temperature and pressure, is defined, with a flow path that connects the steam control volume to the control volume that represents the specific inlet location at the HPC. The flow path connecting the steam source and the HPC has the characteristics (hydraulic diameter, altitude, length, etc.) of the ADS vent line discussed above.

(2) High Pressure Containment

The inside volume of the HPC is represented with numbers of control volumes. Because one control volume acts as a cell inside which the thermodynamic properties are averaged by state (liquid/gas), finer control volumes generally produces better results. However, having a myriad of fine control volumes lead to increased computational cost. In this case, the containment volume is represented with 23 by 2 control volumes; two columns of

horizontally divided control volumes to allow natural circulation. Both vertical and horizontal flow across the control volumes are allowed.

The vessel surrounding the inside volume is represented with numbers of heat structures (defined by the HS package). Cylindrical geometry heat structures are modelled to completely surround the control volumes representing the HPC volume excluding the region connected to the heat transfer plate.

(3) Cooling Pool Vessel

The inside volume of the CPV is also subdivided with control volumes in a manner similar to above (two columns of horizontally divided control volumes to allow natural circulation). The volume is represented with 32 by 2 control volumes. As mentioned in previous section, the vessel surrounding the CPV volume is not included in the model.

(4) Heat Transfer Plate

The heat transfer plate which connects the HPC and the CPV are divided horizontally in the same way as the HPC and CPV volumes are divided horizontally. In other words, a specific control volume in the HPC, that in the CPV and the section of heat transfer plate all have the same height. Detailed description is included in the next section.

7.3 Nodalization

As noted in the previous section, the inside volumes in the HPC and the CPV are represented by numbers of smaller control volumes. Also, the horizontal slices for the HPC, the CPV and the heat transfer plate are done so that at each axial location, the volume representing the HPC and the CPV and the section of heat transfer plate all have the same height.

The geometry of the HPC is used as the reference geometry. As mentioned earlier, the HPC can be divided into three different sections; LCS, ECS and UCS. Each section was sliced nine times so that, in each section, there are ten rows of control volumes. However, the ECS section was sliced only once so that there are two rows of control volumes. Each control volume, therefore, has height equivalent to one tenth of the total section height (half in case of the ECS volumes) and base area equivalent to half of the section base area.

The shape of the ECS section is modified. Originally, the section is a cone-like shape with diameter linearly increasing with elevation. This cone-like shape is replaced with two by two stacks of control volumes with the bottom two having the base area equivalent to that at the lowest elevation and the top two at the highest elevation. Conceptually, the eccentric cone shape is replaced with a stack of two thin cylinders with different diameters. Flow areas between the top and bottom volumes are equivalent to the cross-sectional area at the matching elevation.

The CPV extends further to the top and the bottom of the HPC. The section of the CPV where it is connected to the HPC is divided in the same manner as the HPC is divided. The sections that extends to the top and the bottom of the HPC are divided into three and two rows of control volumes, respectively. Two additional rows of control volumes are added to the very top of the CPV to account for the open top.

Complete nodalization of the system is illustrated in Figure 7-2. Table 7-1 summarizes how the system is nodalized.

Table 7-1 Nodalization detail

Section	Numbers of rows		Height (cm)
	HPC	CPV	
BOT	-	2	32.385
LCS	10	10	38.70
ECS	2	2	25.40
UCS	10	10	12.10
UCS TOP	1	1	16.50
TOP	-	3	32.31

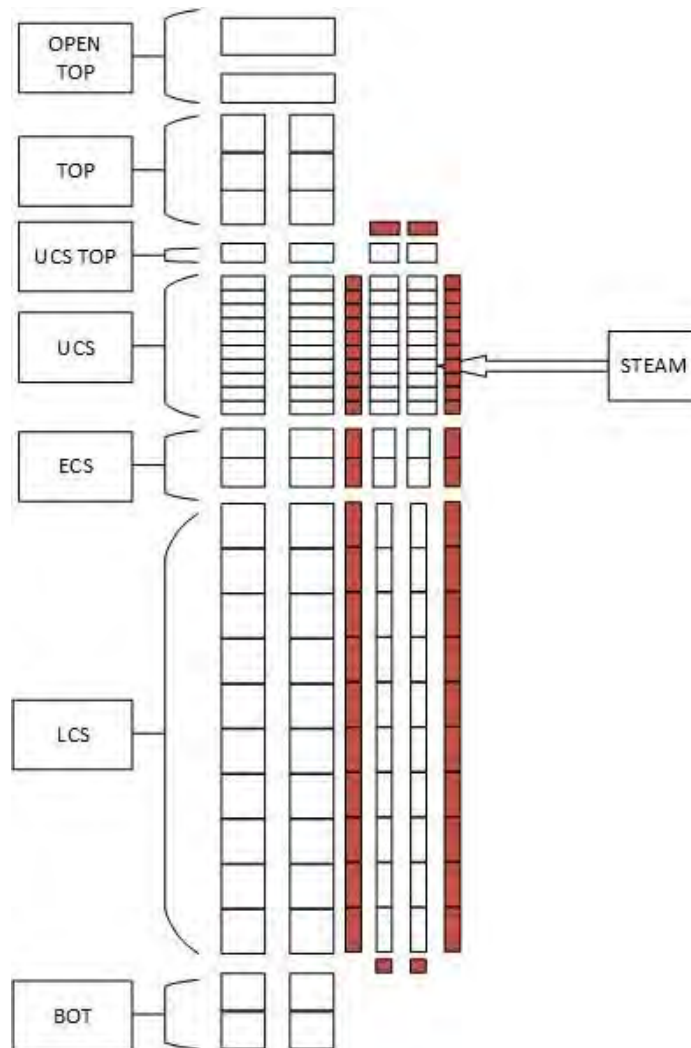


Figure 7-2 Nodalization of the Containment and Cooling system

BOT and TOP represent sections of the CPV that extend to the bottom and top from the end of the HPC because the CPV is taller than the HPC. UCS TOP section is included to account for the height of the hemispherical top in the HPC.

7.4 Initial Conditions

Table 7-2 summarizes the initial conditions used for simulation of the complete set of experiments. The initial conditions are based on aforementioned simplifications and assumptions. Additionally, the inlet steam flowrates were appropriately adjusted in order for simulation containment pressure to match experimental pressure data for the quasi-steady test phase. For simplicity of modeling, the flowrates before and after the sudden drop are assumed to be constant for CCT's.

Table 7-2 Initial conditions for simulation

Test	HPC Pressure (Pa)	HPC Temp. (K)	CPV Temp. (K)	Ambient Temp. (K)	Steam Flow Rate (kg/s)		Steam Pressure (Pa)
Near Vacuum	6.845 E+03	329.85	301.73	295.19	0.0112		2.0684 E+06
	6.844 E+03	321.13	292.32	291.97	0.0235		
Half Vacuum	5.020 E+04	346.73	290.11	292.69	0.0125		
	4.936 E+04	338.40	287.50	292.52	0.0233		
Near Atmospheric	1.281 E+05	359.17	296.92	294.63	0.0124		
	1.298 E+05	355.17	290.11	292.30	0.0223		
Near Vacuum	7.809 E+03	288.82	289.94	296.45	0.0365	0.0119	5.1711 E+05
	1.850 E+04	289.32	287.17	297.17	0.0346	0.0130	1.0342 E+06
	7.578 E+03	288.71	290.27	296.06	0.0364	0.0163	1.7237 E+06
	7.567 E+03	288.26	289.28	296.11	0.0369	0.0182	2.0684 E+06
Near Atmospheric	1.014 E+05	287.21	286.51	296.22	0.0348	0.0102	1.0342 E+06
	1.009 E+05	287.88	287.34	295.22	0.0357	0.0126	1.3790 E+06
	1.029 E+05	298.15	301.51	296.34	0.0357	0.0145	2.648 E+06

7.5 MELCORE Model Results

This report focuses on the analysis of the CCT's. As mentioned previously, the SET's provide transient behaviors whereas the CCT's include steady state behaviors of the containment where the containment pressure stays relatively constant.

Assuming the initial conditions stay relatively unchanged for each test (excluding the initial containment pressure), three parameters were varied during the CCT experiments: initial containment pressure, inlet steam flowrate, and steam feed pressure. The initial containment pressure signifies the amount of non-condensable gases later during the steady state because only pure steam flows during the experiment. Steam flowrate determines how fast the containment pressure builds up and steam feed pressure affects the steady state pressure.

Following figures represent simulation results for one of the near vacuum CCT's, Test 2.4.

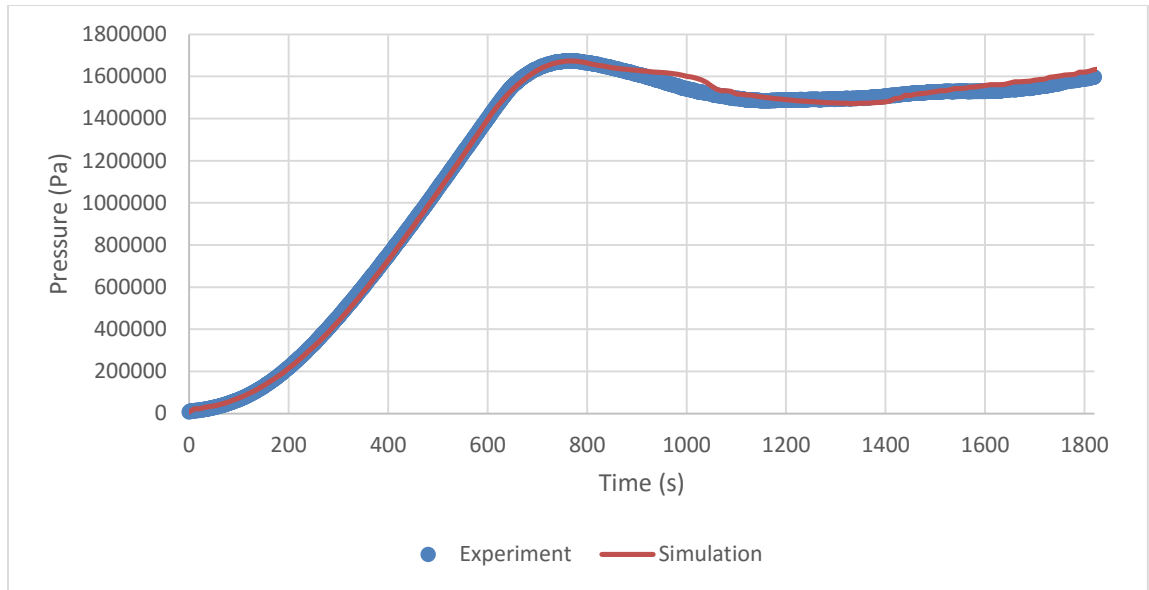


Figure 7-3 Containment Pressure for Test 2.4

As mentioned before, the inlet steam flowrate is purposely adjusted in an effort to match simulation pressure development to the experimental data.

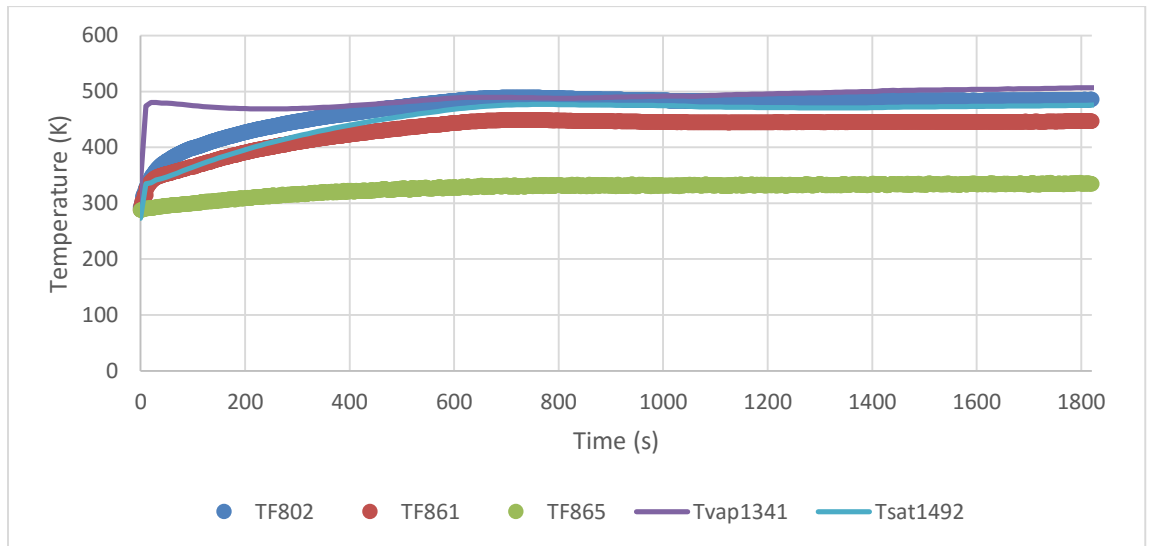


Figure 7-4 Containment Temperature for Test 2.4

Different temperature measurements (TF000) refer to temperature measured by thermocouples in different locations. Tvp1341 and Tsat1492 refer to simulation vapor temperature and simulation saturated temperature at similar locations. Four digit numbers after Tvp or Tsat refer to the specific control volume identifier. The numbers can be found in the full MELCOR user inputs included in the appendix.

The experimental data do not directly supply heat flux data. Therefore, the heat flux through the heat transfer plate for the experiment is calculated using the Fourier's law of thermal conduction:

$$q'' = k \frac{\Delta T}{\Delta x} \quad (7-1)$$

where k , ΔT and Δx refer to the thermal conductivity of the plate (SS304), temperature gradient across the plate and the thickness of the plate. MELCOR uses tabular data for temperature dependent thermal conductivity as shown in Table 7-3. In an attempt to use thermal conductivity for experimental heat flux calculation as close as what MELCOR actually uses for the simulation, the thermal conductivity values for the middle plate temperature averaged throughout the steady state period are obtained via linear interpolation.

Table 7-3 Thermal Conductivity of SS304

Temperature (K)	Thermal Conductivity (W/m k)
300.00	13.00
400.00	14.60
500.00	16.20

It should be noted that, as shown in Figure 4-5, the thermocouples measuring wall or fluid temperature are located at six different axial positions in the HPC. And in a given axial position, five thermocouples are present; the outer two are located very close to the wall in the CPV (left end) and the HPC (right end) while the three in the middle are inside the heat transfer plate. Of the three inside the heat transfer plate, the outer two are located very near the wall and supposed to measure temperature very close to the wall temperature. However, they are not exactly on the wall and so the measured temperatures do not exactly correspond to the real wall temperatures. Likewise, the two thermocouples measuring fluid temperature in the CPV and the HPC side are located very near the wall but not exactly on the wall. Therefore, the temperature gradient across the wall measured using the thermocouples inside the plate would be an underestimate while that using those in the HPC and CPV sides would be an overestimate. As will be shown shortly, the experimental heat flux values are represented as high and low, each referring to the overestimation and the underestimation.

Also, the instrumental uncertainty for the thermocouples is ± 1.1 K. Therefore, the instrumental uncertainty for heat flux measurements are calculated as follows:

$$\sigma_q = k \frac{2\sigma_T}{\Delta x} \approx 14.6 \frac{2.2}{0.0381} \approx 843 \text{ W/m}^2 \quad (7-2)$$

Above sample calculation assumes 400 K for heat transfer plate temperature in the centerline.

Among total of six axial locations, heat flux values at upper five locations are compared. Heat flux at the uppermost axial location is shown in the figure below as an example (location 6; lower locations are marked as location 5 through 2 with location 2 being the lowest). The general behavior of heat flux progression stays relatively unchanged for all other locations and tests. Full sets of plots for all other locations and tests are included in Appendix A.

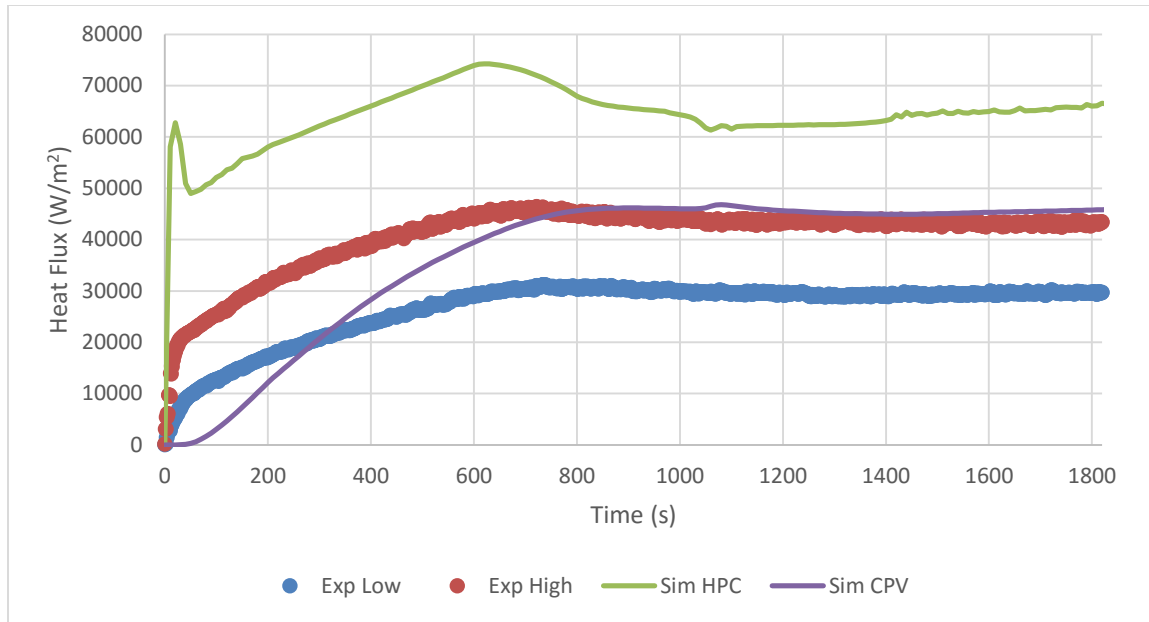


Figure 7-5 Heat flux at location 6 for Test 2.4

As mentioned earlier, underestimation and overestimation for experimental heat flux are represented as Exp Low and Exp High, respectively, in the figure above.

For the simulation heat flux, Sim HPC represents heat flux on the right side of the wall (HPC side) and Sim CPV (CPV side) represents the left side of the wall. In other words, Sim HPC represents the heat flux due to condensation and convection on the HPC side, and simulation pool represents the heat removed via pool convection on CPV side. In theory, those two should equal one another because what goes in must come out. This difference is believed to be due to the way MELCOR represents energy flux (energy released or absorbed) due to phase change. For convective heat flux, MELCOR directly reports the convective heat flux corresponding to a surface of interest. This is made possible because MELCOR requires the user to specify boundary volume (as well as its geometry) in case where convective heat transfer is present. However, the energy released from the process of condensation is not directional nor has specific surface where the heat flux is applied. MELCOR only reports total energy change per time (or energy flux; change in energy per unit time per unit area). Therefore, the energy flux that MELCOR reports on the HPC side includes the heat flux going through the heat transfer plate to CPV side (to the left in this case), as well as other forms of energy flowing to any other directions. In this case, the condensate flowing downward corresponds to this other form of energy included in the energy flux term. Because the water condensate carries energy and is flowing downward on the wall, the energy carried by the condensate film is not transferred to the wall but simply flows downward and accumulates in the HPC. This also explains why Sim HPC is always higher than Sim CPV, as shown in Figure 7-4 and figures included in Appendix A.

It is apparent that for all of the results, the heat flux is overestimated by MELCOR. It was previously mentioned that the temperature gradient across the wall can be estimated in two ways: underestimation and overestimation. It is only logical that the real heat flux should lie somewhere between the two. However, the simulation results show that the heat flux is never significantly below the overestimated value, except for a few local

perturbations. This is thought to be partly due to the liquid film models that MELCOR uses to model the heat transfer resistance. The effects of condensate film waviness is not considered with a simple film model.

Also, it was previously noted that MELCOR only allows one-dimensional heat conduction. Although the edges of the heat transfer plate are well insulated, one dimensional heat flow is not always guaranteed due to the test geometry. Figure 7-6 represents a top view of horizontally sliced test section. During the experiment, direct heat flow from the HPC to CPV (indicated as red straight arrow) as well as transverse heat flow through the plate edges (indicated as blue curved arrow) are both present. Near the centerline, the divergent heat flow is at a minimum due to well-defined rectangular geometry. However, the divergent heat flow can become significant relative to the direct one dimensional heat flow near the edges. Because the thermocouples measuring temperature gradient are located in the middle of the plate (indicated as black x mark), the measured temperature gradient does not capture the fin effect near the edges and likely reduces the measured temperature gradient. In other words, due to the complexity of test geometry and the way thermocouples are located, the thermocouples in the heat transfer plate are underestimating the total heat flow and the temperature gradient across the plate.

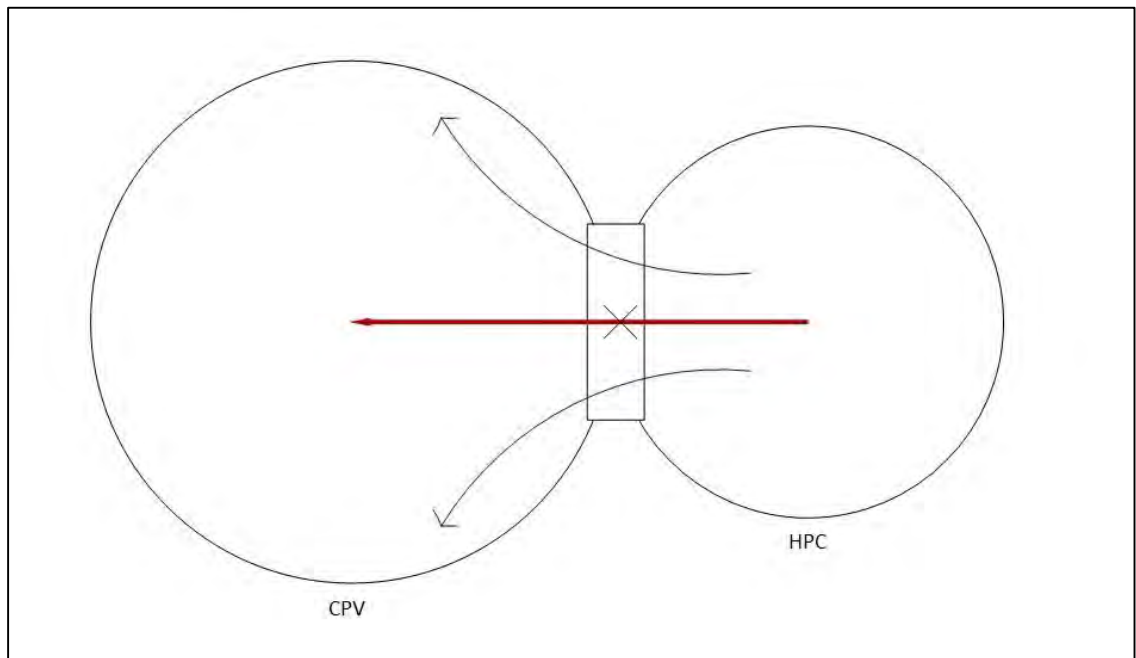


Figure 7-6 Direct and digressing heat flow

Following figures represent simulation results for Test 2.7 (near atmospheric CCT with the same steam feed pressure as Test 2.4).

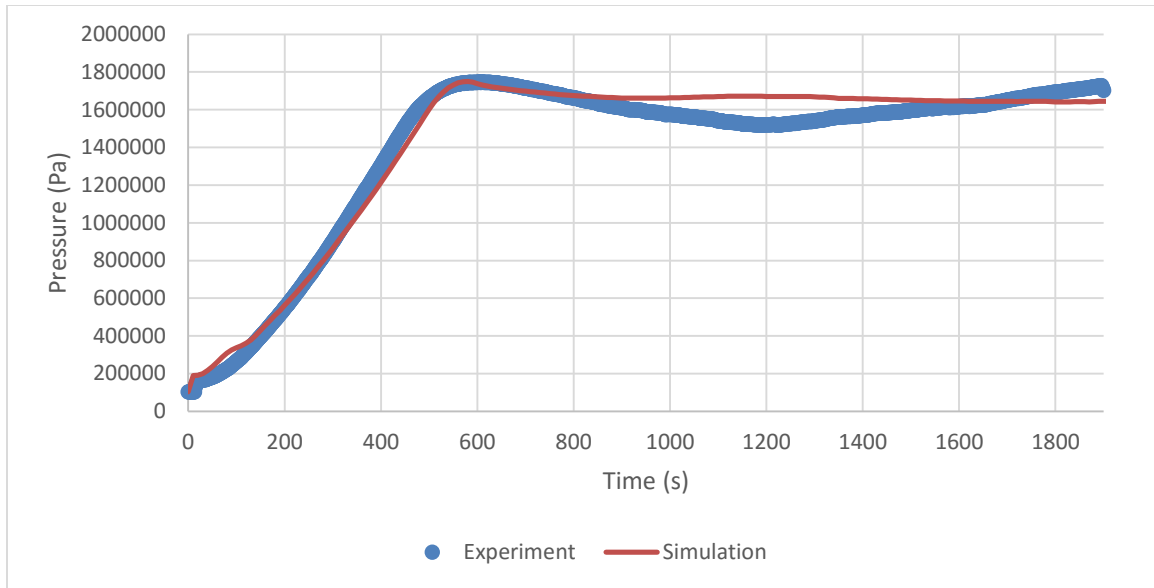


Figure 7-7 Containment Pressure for Test 2.7

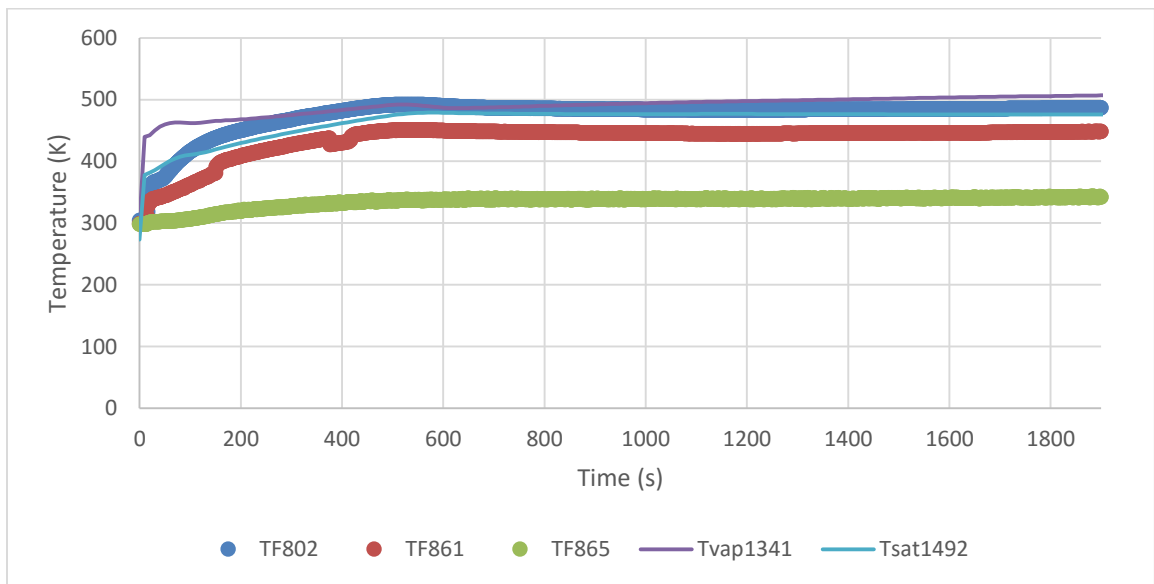


Figure 7-8 Containment Temperature for Test 2.7

Compared to Test 2.4, Test 2.7 has significantly higher initial containment pressure (near atmospheric whereas Test 2.4 begins with near vacuum HPC). Because there is no non-condensable gas input during the experiment, initial amount of air determines the amount of non-condensable gas during the steady state. And since the presence of non-condensable gas impedes the process of condensation, it is expected that steady state heat flux for Test 2.7 to be lower than that for Test 2.4.

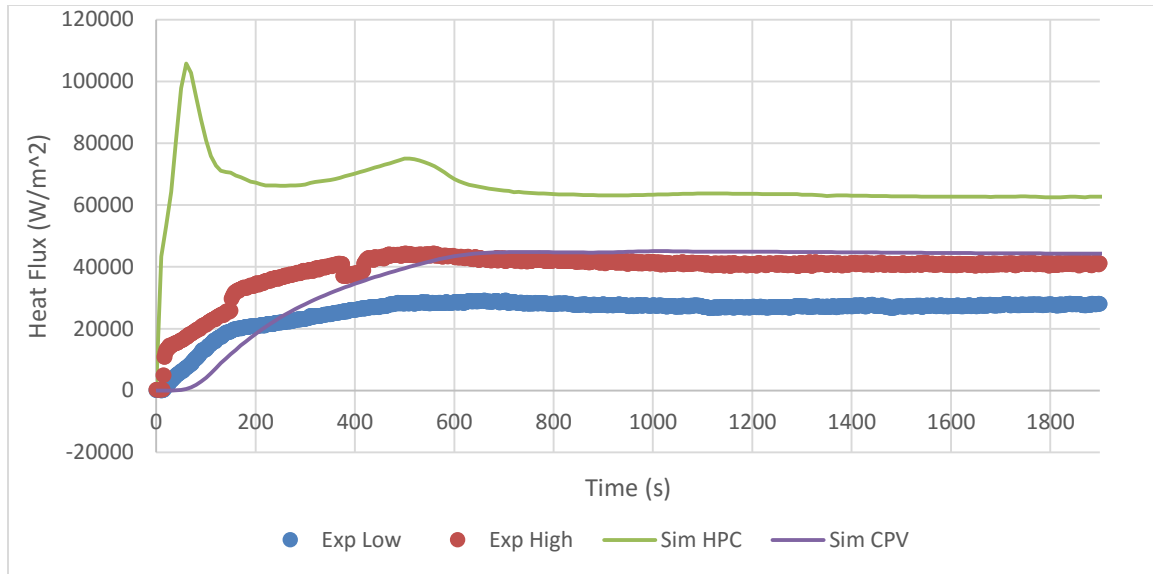


Figure 7-9 Heat Flux at location 6 for Test 2.7

As shown in Figure 7-5 and Figure 7-9, the steady state heat flux (simulation) for Test 2.4 generally lies somewhere between 40 and 50 kW/m² while that for Test 2.7 generally lies on 40 kW/m². Experimental data also agree with that the heat flux with greater air (non-condensable gas) content is generally lower than that with less air content. This trend is shown in the following figure.

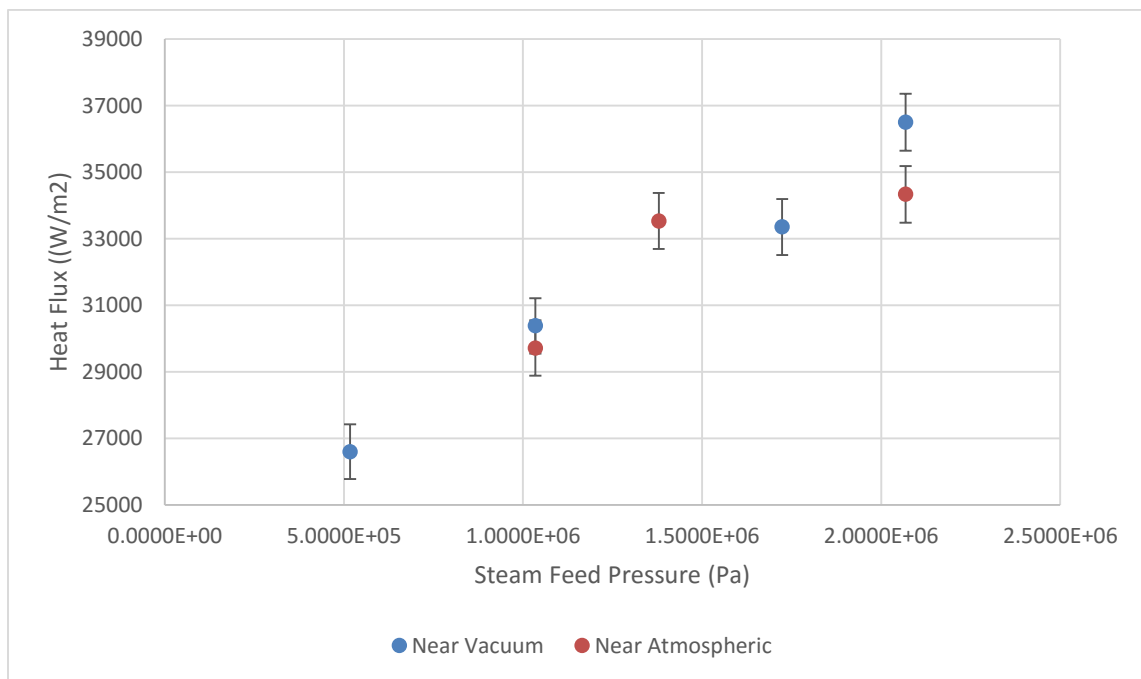


Figure 7-10 Experimental Steady State Heat Flux of all CCT's at Location 6

Figure 10 compares the averaged heat flux for each CCT during the steady state period at the uppermost axial location. The average of overestimation (Exp High) and underestimation (Exp Low) is used to show the general trend. Among near vacuum tests (indicated as blue in above plot), lowest feed pressure to highest feed pressure points correspond to Test 2.1 to Test 2.4. Likewise, among near atmospheric tests (indicated as red), lowest to highest feed pressure correspond to Test 2.5 to Test 2.7. As shown in above plot, the negative effect of the non-condensable gas seems to increase as the steam feed pressure increases.

In most cases, the liquid film (condensate film flowing downward) thickness lies around the order of 100 microns. Following figure illustrates the film thickness profile along the axial length of the HPC during the steady state period of Test 2.4 and 2.7.

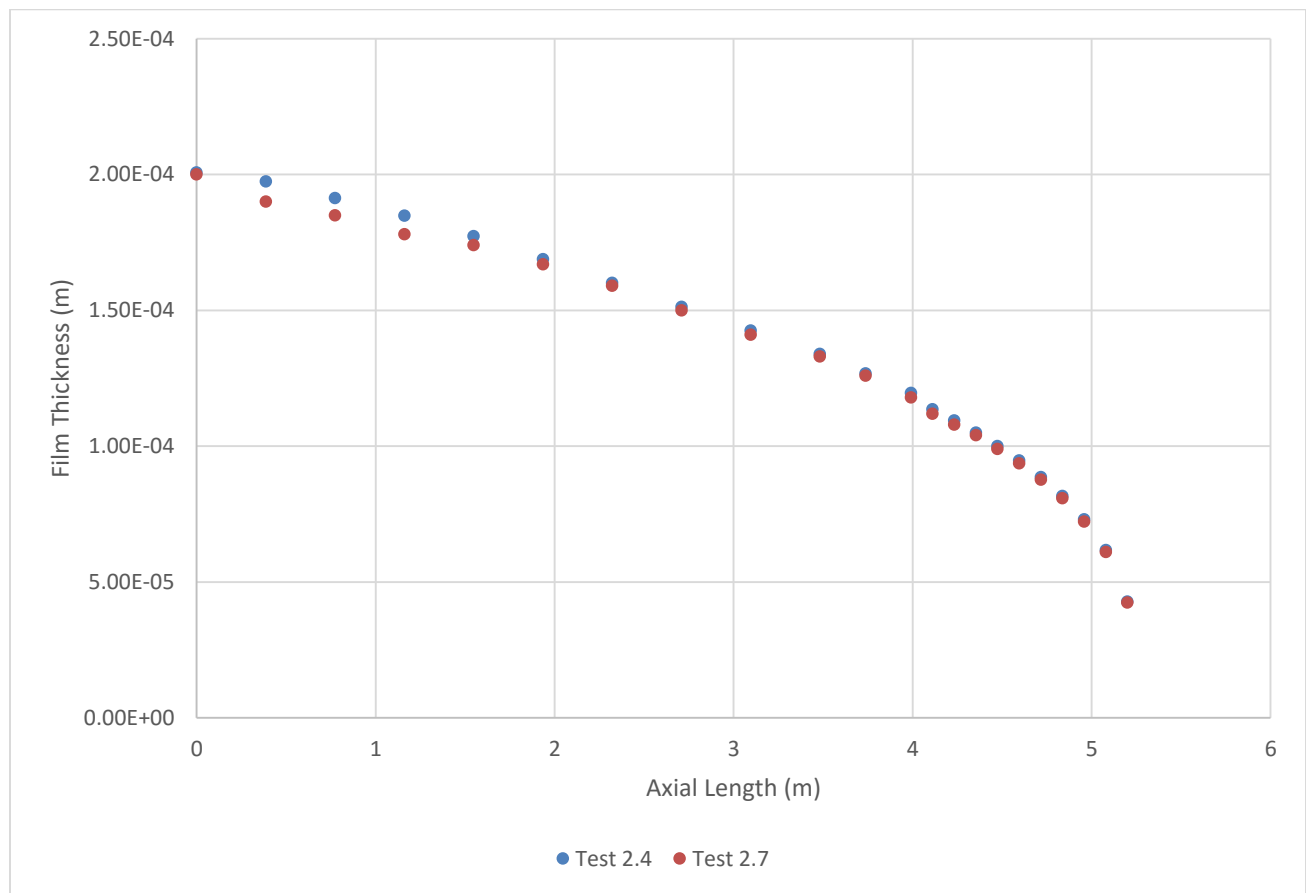


Figure 7-11 Simulation Film Thickness during Steady State for Test 2.4 and 2.7

The steady state film thickness profile shown above compares the thickness for Test 2.4 and 2.7. Axial length of 0 m corresponds to the bottom of the HPC and 5 m corresponds to the top. As mentioned earlier, Test 2.4 represents an experiment with lower non-condensable content (~1 psia), whereas Test 2.7 contains more non-condensable gas (14.7 psia). It appears that the effect of such is not significant on the film thickness. Higher non-condensable gas content would lead to more resistance to the condensation and consequently thinner liquid film. The film thickness for Test 2.7 is visibly less than that for Test 2.4 at lower axial locations, but the different is a second order effect.

The general shape of film thickness profile agrees with Nusselt's analysis on condensation without the presence of non-condensable gas such that the thickness varies with the length to the 1/4 power.

7.6 MELCOR Model Conclusion

Condensation experiments of steam in the presence of non-condensable gas in the containment of MASLWR test facility at Oregon State University are simulated using the MELCOR code developed by Sandia National Laboratories. The inlet steam flowrate for each test is purposely adjusted so that the containment pressure for simulation generally matches with experimental data.

In general, simulation results agree with the experimental data. However, it is observed that the MELCOR overpredicts the heat flux for all analyzed tests. The MELCOR predicts that the heat fluxes for CCT's approximately range from 30 to 45 kW/m² whereas the experimental data (averaged) ranges from about 25 to 40 kW/m². This may be due to the limited availability of liquid film models included in MELCOR. Also, it is believed that due to complex test geometry, measured temperature gradients across the heat transfer plate may have been underestimated and thus the heat flux had been underestimated.

The predicted film thickness is on the order of 100 microns. The general shape of the film thickness development along the axial length is reasonable. However, the expected differences in film thicknesses for near vacuum and near atmospheric test conditions are not significant.

Further study on the behavior of condensate film is expected to refine the simulation results. Possible refinements include but are not limited to, the followings: CFD simulation focusing on the liquid film behavior and benchmarking with experimental analyses for simpler geometries.

8 SUMMARY AND CONCLUSIONS

The experimental, numerical and analytical studies on high-pressure steam condensation phenomena in a steel containment vessel connected to a water cooling tank were carried out at Oregon State University (OrSU) and the University of Wisconsin at Madison (UW-Madison). In the three years of investigation duration, following the original proposal, the planned tasks have been completed:

- (1) Performed a scaling study for the full pressure test facility applicable to the reference design for the condensation heat transfer process during design basis accidents (DBAs), modified the existing test facility to route the steady-state secondary steam flow into the high pressure containment for controllable condensation tests, and extended the operations at negative gage pressure conditions (OrSU).
- (2) Conducted a series of DBA and quasi-steady experiments using the full pressure test facility to provide a reliable high pressure condensation database (OrSU).
- (3) Analyzed experimental data and evaluated condensation model for the experimental conditions, and predicted the prototypic containment performance under accidental conditions (UW-Madison).

A film flow model was developed for the scaling analysis, and the results suggest that the 1/3 scaled test facility covers large portion of laminar film flow, leading to a lower average heat transfer coefficient comparing to the prototypic value. Although it is conservative in reactor safety analysis, the significant reduction of heat transfer coefficient (50%) could under estimate the prototypic condensation heat transfer rate, resulting in inaccurate prediction of the decay heat removal capability. Further investigation is thus needed to quantify the scaling distortion for safety analysis code validation.

Experimental investigations were performed in the existing MASLWR test facility at OrST with minor modifications. A total of 13 containment condensation tests were conducted for pressure ranging from 4 to 21 bar with three different static inventories of non-condensable gas. Condensation and heat transfer rates were evaluated employing several methods, notably from measured temperature gradients in the HTP as well as measured condensate formation rates. A detailed mass and energy accounting was used to assess the various measurement methods and to support simplifying assumptions required for the analysis. Condensation heat fluxes and heat transfer coefficients are calculated and presented as a function of pressure to satisfy the objectives of this investigation. The major conclusions for those tests are summarized below:

- (1) In the steam blow-down tests, the initial condensation heat transfer process involves the heating-up of the containment heat transfer plate. An inverse heat conduction model was developed to capture the rapid transient transfer characteristics, and the analysis method is applicable to SMR safety analysis.
- (2) The average condensation heat transfer coefficients for different pressure conditions and non-condensable gas mass fractions were obtained from the integral test facility, through the measurements of the heat conduction rate across the containment heat transfer plate, and from the water condensation rates measurement based on the total energy balance equation.

- (3) The test results using the measured HTP wall temperatures are considerably lower than popular condensation models would predict mainly due to the side wall conduction effects in the existing MASLWR integral test facility. The data revealed the detailed heat transfer characteristics of the model containment, important to the SMR safety analysis and the validation of associated evaluation model. However this approach, unlike separate effect tests, cannot isolate the condensation heat transfer coefficient over the containment wall, and therefore is not suitable for the assessment of the condensation heat transfer coefficient against system pressure and non-condensable gas mass fraction.
- (4) The average condensation heat transfer coefficients measured from the water condensation rates through energy balance analysis are appropriate, however, with considerable uncertainties due to the heat loss and temperature distribution on the containment wall. With the consideration of the side wall conduction effects, the results indicate that the measured heat transfer coefficients in the tests is about 20% lower than the prediction of Dehbi's correlation, mainly due to the side wall conduction effects. The investigation also indicates an increase in the condensation heat transfer coefficient at high containment pressure conditions, but the uncertainties invoked with this method appear to be substantial.
- (5) Non-condensable gas in the tests has little effects on the condensation heat transfer at high elevation measurement ports. It does affect the bottom measurements near the water level position. The results suggest that the heavier non-condensable gas is accumulated in the lower portion of the containment due to stratification in the narrow containment space. The overall effects of the non-condensable gas on the heat transfer process should thus be negligible for tall containments of narrow condensation spaces in most SMR designs. Therefore, the previous correlations with non-condensable gas effects are not appropriate to those small SMR containments due to the very poor mixing of steam and non-condensable gas.

The MELCOR simulation results agree with the experimental data reasonably well. However, it is observed that the MELCOR overpredicts the heat flux for all analyzed tests. The MELCOR predicts that the heat fluxes for CCT's approximately range from 30 to 45 kW/m² whereas the experimental data (averaged) ranges from about 25 to 40 kW/m². This may be due to the limited availability of liquid film models included in MELCOR. Also, it is believed that due to complex test geometry, measured temperature gradients across the heat transfer plate may have been underestimated and thus the heat flux had been underestimated.

The MELCOR model predicts a film thickness on the order of 100 microns, which agrees very well with film flow model developed in this study for scaling analysis. However, the expected differences in film thicknesses for near vacuum and near atmospheric test conditions are not significant. Further study on the behavior of condensate film is expected to refine the simulation results. Possible refinements include but are not limited to, the followings: CFD simulation focusing on the liquid film behavior and benchmarking with experimental analyses for simpler geometries.

REFERENCES

- [1] Uchida, H., Oyama, A., Togo, Y., 1965. Evaluation of post-incident cooling systems of light-water power reactors. Proc. Int. Conf. on Peaceful Uses of Atomic Energy, Geneva, Switzerland, vol. 13, pp. 93–102.
- [2] Herr, J.F., Kadambi, J.R., 1993. Effect of non-condensable gases on condensation heat transfer. Proc. Fluid Eng. Conf., pp. 77–86.
- [3] Collier, J.G., Thome, J.R., 1994. Convective Boiling and Condensation, Ch. 10, 3rd ed. Oxford University Press, Oxford.
- [4] Kim, M.H., Corradini, M.L., 1990. Modeling of condensation heat transfer in a reactor containment. Nucl. Eng. Des. 118, 193–212.
- [5] Peterson, P.F., Shrock, V.E., Kageyama, T., 1993. Diffusion layer theory for turbulent vapor condensation with non-condensable gases. J. Heat Transf. 115, 998–1003.
- [6] Herranz, L.E., Anderson, M.H., Corradini, M.L., 1998. The effect of light gases in non-condensable mixtures on condensation heat transfer. Int. Heat Transf. Conf., Korea.
- [7] Anderson, M.H., Herranz, L.E., Corradini, M.L., 1998. Experimental analysis of heat transfer within the AP600 containment under postulated accident conditions. Nucl. Eng. Des. 185, 153-172.
- [8] Herranz, L.E., Anderson, M.H. Michael L. Corradini, M.L., 1998. A diffusion layer model for steam condensation within the AP600 containment. Nucl. Eng. Des. 183, 133–150.
- [9] Dehbi, A.A., Golay, M.W., Kazimi, M.S., 1991. Condensation experiments in steam–air and steam–air–helium mixtures under turbulent natural convection, National Conference of Heat Transfer (1991). AIChE Symp. Ser. 19–28.
- [10] IAEA, Advances in Small Modular Reactor Technology Development - A Supplement to IAEA Advanced Reactors Information System (ARIS). Vienna, Austria: IAEA, September 2014.
- [11] ANS, "Special Section: Advanced Reactors," in Nuclear News vol. 57, ed: American Nuclear Society, Dec 2014, pp. 43-87.
- [12] J. Vujic, R. M. Bergmann, R. Skoda, and M. Miletic, "Small modular reactors: Simpler, safer, cheaper?," Energy, vol. 45, pp. 288-295, Sep 2012.
- [13] T. L. Bergman and F. P. Incropera, Fundamentals of heat and mass transfer, 7th ed. Hoboken, NJ: Wiley, 2011.
- [14] A. Faghri, Y. Zhang, and J. Howell, "Condensation and Evaporation," in Advanced Heat and Mass Transfer, ed: Global Digital Press, 2010.
- [15] D. C. Slaughterbeck, "Review of Heat Transfer Coefficients for Condensing Steam in a Containment Building Following a LOCA," Idaho Nuclear Corp. 1970.
- [16] W. A. Miller, Keyhani, M, "The Effect of Roll Waves on the Hydrodynamics of Falling Films Observed in Vertical Column Absorbers," presented at the ASME Heat Pump Technical Session, New York City, 2001.
- [17] W. Nusselt, "De oberflächenkondensation des wasserdampfes," Z Vereines Deutch. Ing., vol. 60, pp. 541-546, 569-575, 1916.
- [18] W. J. Minkowycz and E. M. Sparrow, "Condensation Heat Transfer in Presence of Non-condensables Interfacial Resistance Superheating Variable Properties and Diffusion," International Journal of Heat and Mass Transfer, vol. 9, pp. 1125-1144, 1966.
- [19] J. A. Fillo, "Condensation Wall Heat Transfer in Presence of Non-condensable Gas," presented at the American Society of Mechanical Engineers winter annual meeting, Miami, FL, USA, 1985.
- [20] S. Oh and S. T. Revankar, "Boundary Layer Analysis for Steam Condensation in a Vertical Tube with Non-condensable Gases," Int. J. Heat Exchanger, vol. 6, pp. 93-124, 2005.
- [21] J. F. Herr and J. R. Kadambi, "Effect of non-condensable gases on condensation heat transfer," in Fluid Eng. Conf., 1993, pp. 77-86.

- [22] A. P. Colburn and O. A. Hougen, "Design of Cooler Condensers for Mixtures of Vapors with Noncondensing Gases," *Ind. Eng. Chem.*, vol. 26, pp. 1178-1182, 1934.
- [23] M. H. Kim and M. L. Corradini, "Modeling of Condensation Heat-Transfer in a Reactor Containment," *Nuclear Engineering and Design*, vol. 118, pp. 193-212, Mar 1990.
- [24] P. F. Peterson, V. E. Schrock, and T. Kageyama, "Diffusion Layer Theory for Turbulent Vapor Condensation with Non-condensable Gases," *Journal of Heat Transfer-Transactions of the Asme*, vol. 115, pp. 998-1003, Nov 1993.
- [25] L. E. Herranz, M. H. Anderson, and M. L. Corradini, "A Diffusion Layer Model for Steam Condensation within the AP600 Containment," *Nuclear Engineering and Design*, vol. 183, pp. 133-150, Jul 1998.
- [26] W. Rohsenow, "Heat Transfer and Temperature Distribution in Laminar Film Condensation," *Trans. ASME*, vol. 78, pp. 1645-1648, 1956.
- [27] S. S. Kutateladze, "Semi-Empirical Theory of Film Condensation of Pure Vapors," *International Journal of Heat and Mass Transfer*, vol. 25, pp. 653-660, 1982.
- [28] D. A. Labuntsov, "Heat Transfer in Film Condensation of Steam on a Vertical Surface and Horizontal Tubes," *Teploenergetika*, vol. 4, pp. 72-80, 1957.
- [29] K. R. Chun and R. A. Seban, "Heat Transfer to Evaporating Liquid Films," *Journal of Heat Transfer*, vol. 93, pp. 391-8, 1971.
- [30] D. Butterworth, "Film Condensation of Pure Vapor," in *Heat Exchanger Design Handbook*, Washington, DC.: Hemisphere, 1983.
- [31] H. Uchida, A. Oyama, and Y. Togo, "Evaluation of post-incident cooling systems of light-water power reactors," in *Proceedings of the Third International Conference on the Peaceful Uses of Atomic Energy*, United Nations, New York, 1964, pp. 93-102.
- [32] T. Tagami, "Interim Report on Safety Assessments and Facilities," Japanese Atomic Energy Research Agency, unpublished work 1965.
- [33] Y. Kataoka, T. Fukui, S. Hatamiya, T. Nakao, M. Naitoh, and I. Sumida, "Experiments on Convection Heat-Transfer Along a Vertical Flat-Plate between Pools with Different Temperatures," *Nuclear Technology*, vol. 99, pp. 386-396, Sep 1992.
- [34] J. A. Green, "The impact of bulk atmospheric motion upon condensation heat transfer in the presence of non-condensable gases," 1994.
- [35] H. Liu, N. E. Todreas, and M. J. Driscoll, "An experimental investigation of a passive cooling unit for nuclear plant containment," *Nuclear Engineering and Design*, vol. 199, pp. 243-255, Jul 2000.
- [36] J. Green and K. Almenas, "An Overview of the Primary Parameters and Methods for Determining Condensation Heat Transfer to Containment Structures," *Nuclear Safety*, vol. 37, pp. 26-48, 1996.
- [37] P. F. Peterson, "Theoretical Basis for the Uchida Correlation for Condensation in Reactor Containments," *Nuclear Engineering and Design*, vol. 162, pp. 301-306, 1996.
- [38] J.-D. Li, "CFD simulation of water vapour condensation in the presence of non-condensable gas in vertical cylindrical condensers," *International Journal of Heat and Mass Transfer*, vol. 57, pp. 708-721, 2013.
- [39] P. K. Sharma, B. Gera, R. K. Singh, and K. K. Vaze, "Computational Fluid Dynamics Modeling of Steam Condensation on Nuclear Containment Wall Surfaces Based on Semiempirical Generalized Correlations," *Science and Technology of Nuclear Installations*, 2012.
- [40] J. C. de la Rosa, A. Escriva, L. E. Herranz, T. Cicero, and J. L. Munoz-Cobo, "Review on Condensation on the Containment Structures," *Progress in Nuclear Energy*, vol. 51, pp. 32-66, Jan 2009.
- [41] Y. Q. Yu, S. J. Wei, Y. H. Yang, and X. Cheng, "Experimental study of water film falling and spreading on a large vertical plate," *Progress in Nuclear Energy*, vol. 54, pp. 22-28, Jan 2012.

- [42] S. Kalliadasis, C. Ruyer-Quil, B. Scheid, and M. G. Velarde, *Falling liquid films*. London ; New York: Springer, 2012.
- [43] I. Zadrazil, O. K. Matar, and C. N. Markides, "An experimental characterization of downwards gas-liquid annular flow by laser-induced fluorescence: Flow regimes and film statistics," *International Journal of Multiphase Flow*, vol. 60, pp. 87-102, Apr 2014.
- [44] H. C. Chang, "Wave Evolution on a Falling Film," *Annual Review of Fluid Mechanics*, vol. 26, pp. 103-136, 1994.
- [45] I. Morioka, M. Kiyota, and R. Nakao, "Absorption of Water-Vapor into a Film of Aqueous-Solution of Libr Falling Along a Vertical Pipe," *Jsmc International Journal Series B-Fluids and Thermal Engineering*, vol. 36, pp. 351-356, May 1993.
- [46] P. L. S. P. K. Kapitza, "Wave Flow of Thin Layers of a Viscous Fluid: III. Experimental Study of Undulatory Flow Conditions," *Zhurnal Eksperimental'noi i Teoreticheskoi Fiziki* (in Russian), vol. 19, pp. 105–120, 1949.
- [47] G. D. Fulford, "The Flow of Liquids in Thin Films," in *Advances in Chemical Engineering*. vol. 5, T. B. Drew, J. W. Hopes, and J. V. Vermeulen, Eds., ed, 1964, pp. 115-237.
- [48] N. Brauner, "Roll Wave Celerity and Average Film Thickness in Turbulent Wavy Film Flow," *Chemical Engineering Science*, vol. 42, pp. 265-273, 1987.
- [49] P. L. Kapitza and S. P. Kapitza, "Wave Flow of Thin Layers of a Viscous Liquid," *Zh. Eksp. Teor. Fiz*, vol. 18, pp. 3-28, 1948.
- [50] H. Brauer, "VDI-Forschungsheft 457," *Forschung auf dem Gebiete des Ingenieurwesens*, vol. 22, 1956.
- [51] H. Takahama and S. Kato, "Longitudinal Flow Characteristics of Vertically Falling Liquid-Films without Concurrent Gas-Flow," *International Journal of Multiphase Flow*, vol. 6, pp. 203-215, 1980.
- [52] T. D. Karapantsios, S. V. Paras, and A. J. Karabelas, "Statistical Characteristics of Free Falling Films at High Reynolds-Numbers," *International Journal of Multiphase Flow*, vol. 15, pp. 1-21, Jan-Feb 1989.
- [53] Kataoka, Y., FuLui, T., Hatamiya, S., Nakao, T., Naitoh, M., Sumida, I., 1992. Experiments on convection heat transfer along a vertical flat between pools with different temperatures. *Nucl. Technol.* 99, 386–396.
- [54] Tagami, T., 1965. Interim report on Safety Assessments and Facilities Establishment Project for June 1965, No. 1. Japanese Atomic Energy Research Agency, unpublished.
- [55] Modro, S.M., Fisher, J.E., Weaver, K. D., Reyes, J. N., Jr., Groome, J. T., Babka, P. and Carlson, T. M., "Multi-Application Small Light Water Reactor Final Report", INEEL/EXT-04-01626, 2003.
- [56] Reyes, J.N., Jr., MASLWR Scaling Analysis, DOE NEER Program Progress Report, 2002.
- [57] Zuber, N., "A Hierarchical, Two-Tiered Scaling Analysis", NUREG-CR 5809, Appendix D, 1991.
- [58] Dongyoung Lee, *Flow Dynamics and Condensation of Film Flows in Small Modular Reactors*, Ph.D. Thesis, Oregon State University, 2015.
- [59] Labuntso.Da and S. I. Smirnov, "Heat Transfer in Condensation of Liquid Metal Vapors," *Chemical Engineering Progress*, vol. 62, pp. 86-&, 1966.
- [60] B. C. Yen, "Open channel flow resistance," *Journal of Hydraulic Engineering-Asce*, vol. 128, pp. 20-39, Jan 2002.
- [61] J. S. Kim and H. C. No, "Turbulent film condensation of high pressure steam in a vertical tube," *Int. J. Heat Mass Transfer*, vol. 43, pp. 4031-4042, 2000.
- [62] "MELCOR Computer Code Manuals". Sandia National Laboratories, 2008.

APPENDIX A – COMPLETE SIMULATION RESULTS

SET (1st set of tests)

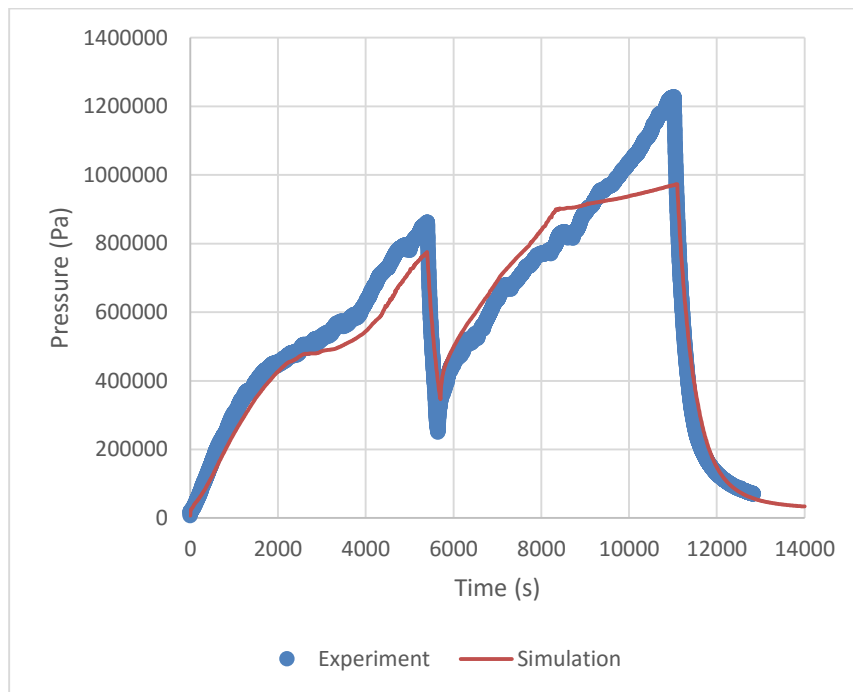


Figure A-1 Containment Pressure for Test 1.1

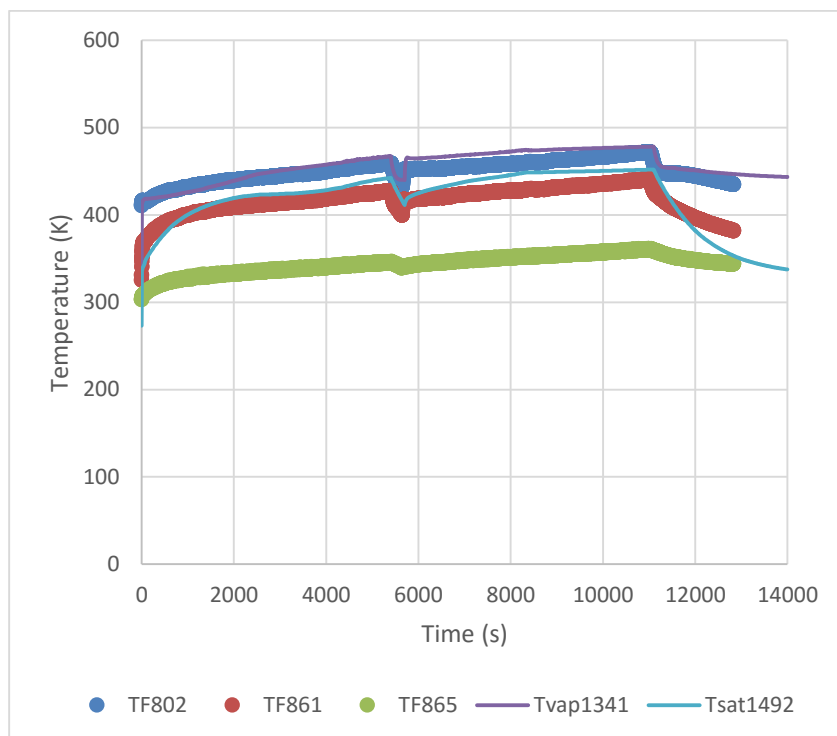


Figure A-2 Containment Temperature for Test 1.1

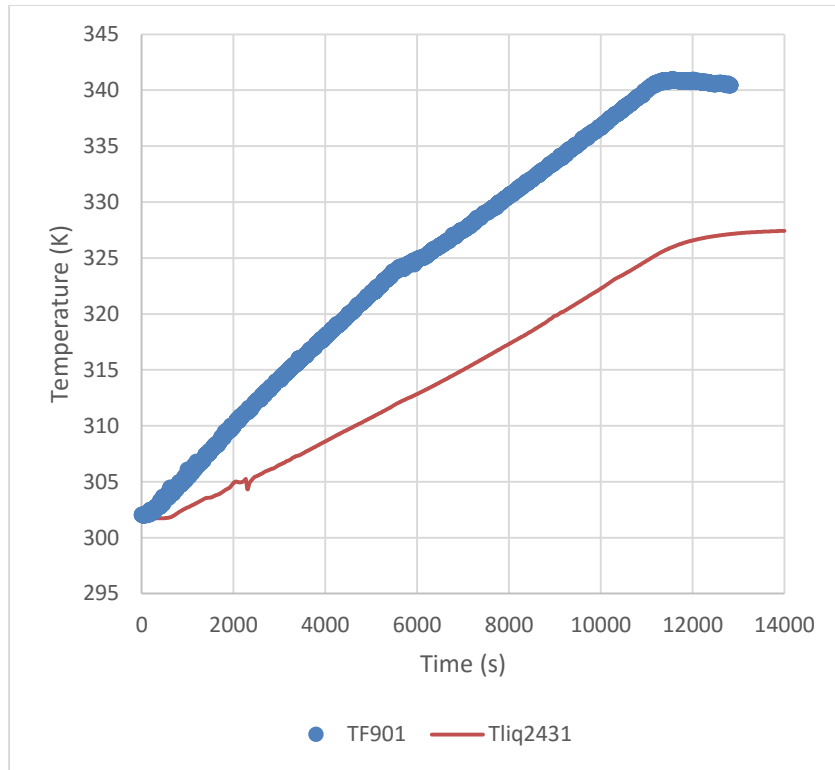


Figure A-3 CPV Temperature for Test 1.1

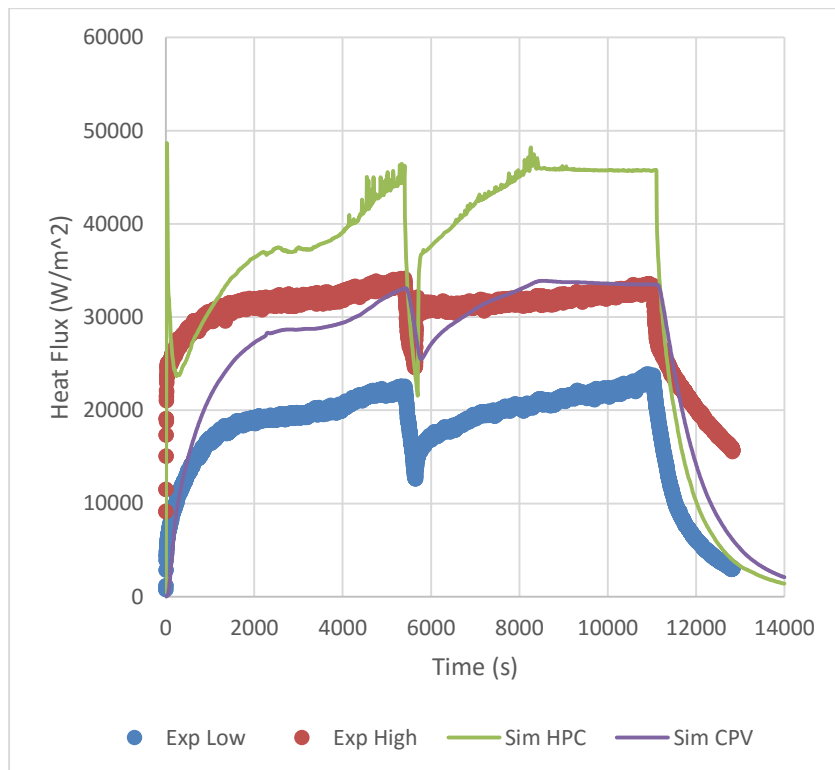


Figure A-4 Heat Flux at Location 6 for Test 1.1

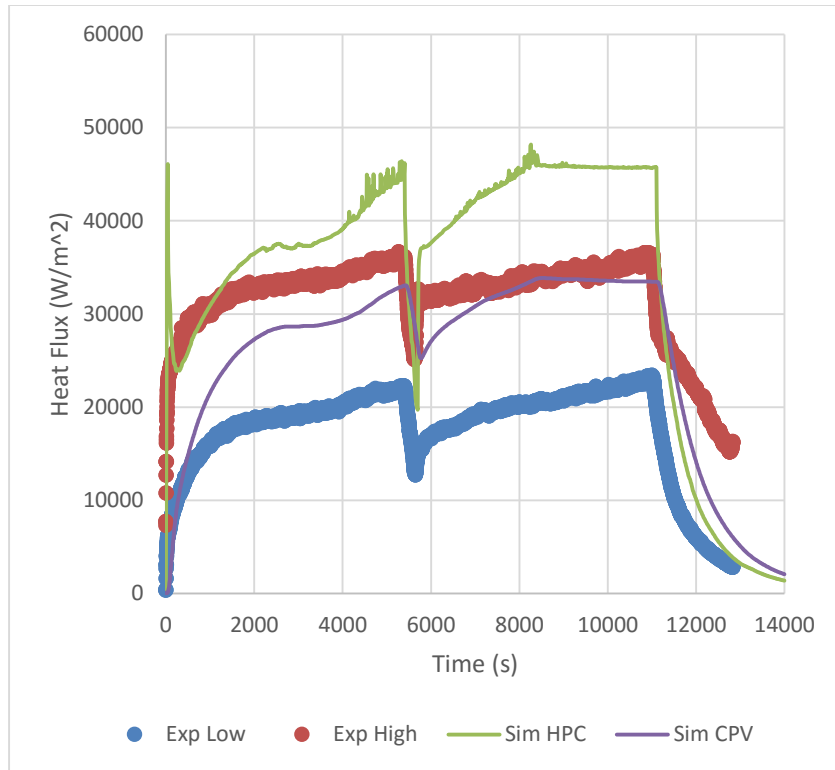


Figure A-5 Heat Flux at Location 5 for Test 1.1

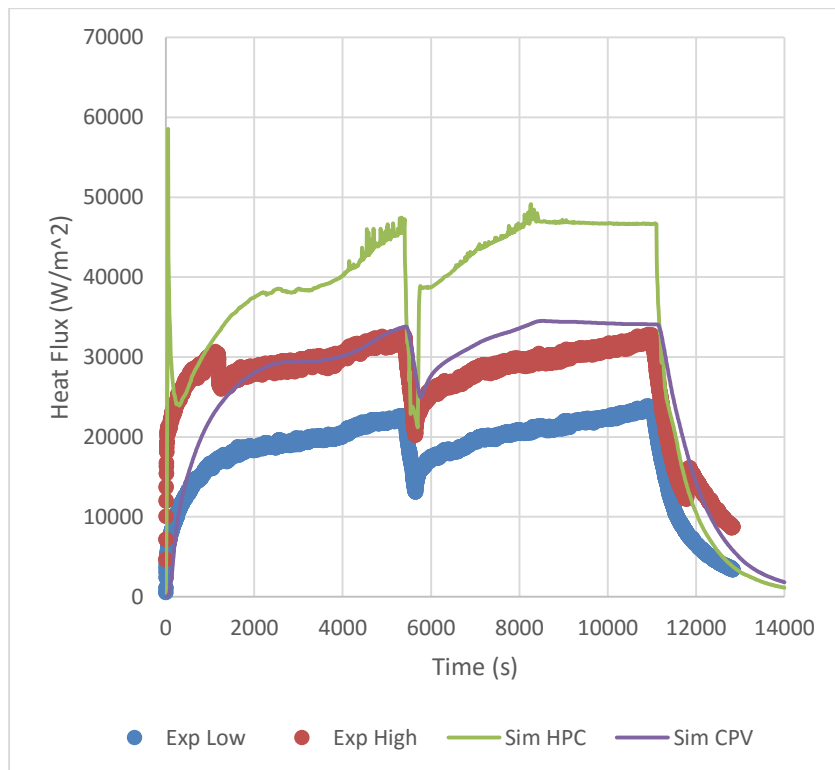


Figure A-6 Heat Flux at Location 4 for Test 1.1

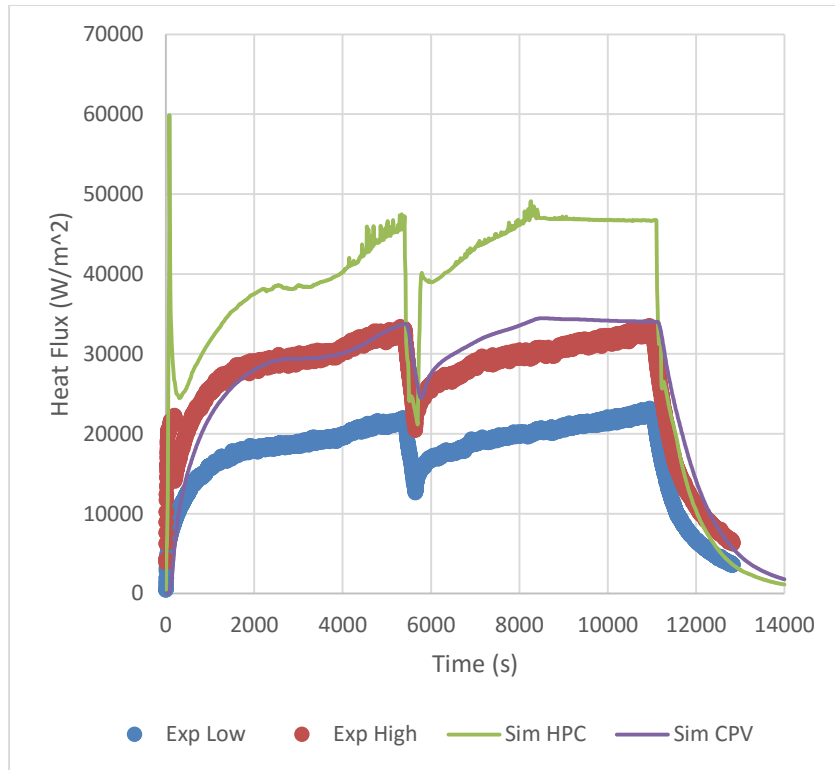


Figure A-7 Heat Flux at Location 3 for Test 1.1

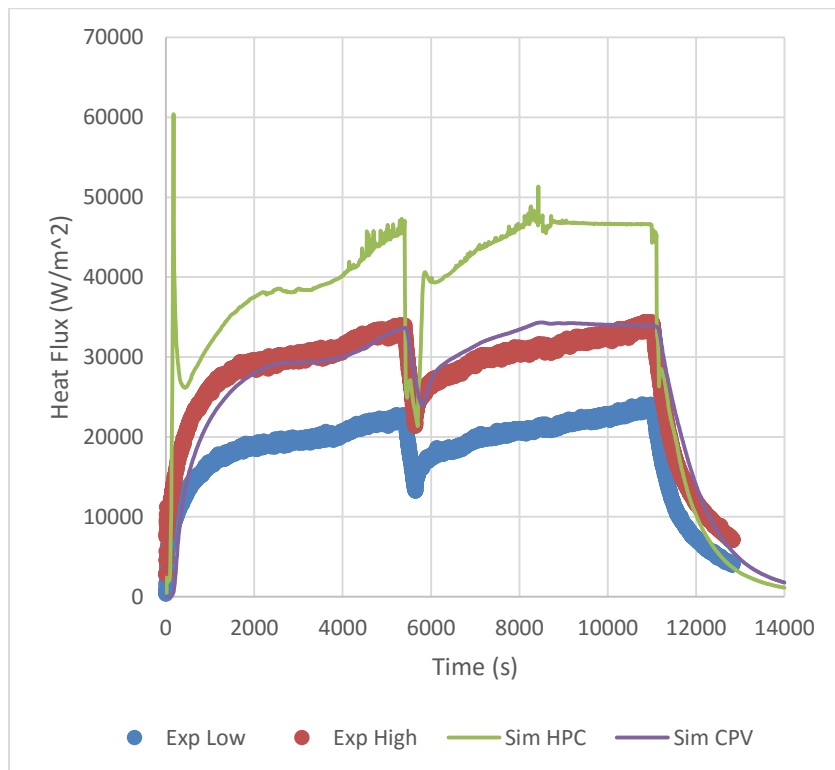


Figure A-8 Heat Flux at Location 2 for Test 1.1

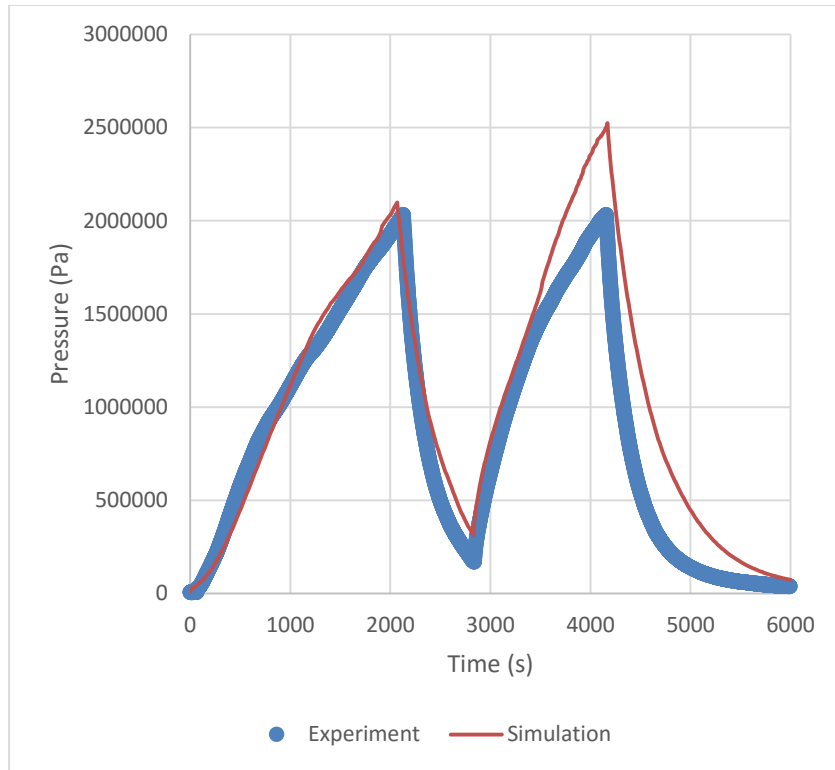


Figure A-9 Containment Pressure for Test 1.2

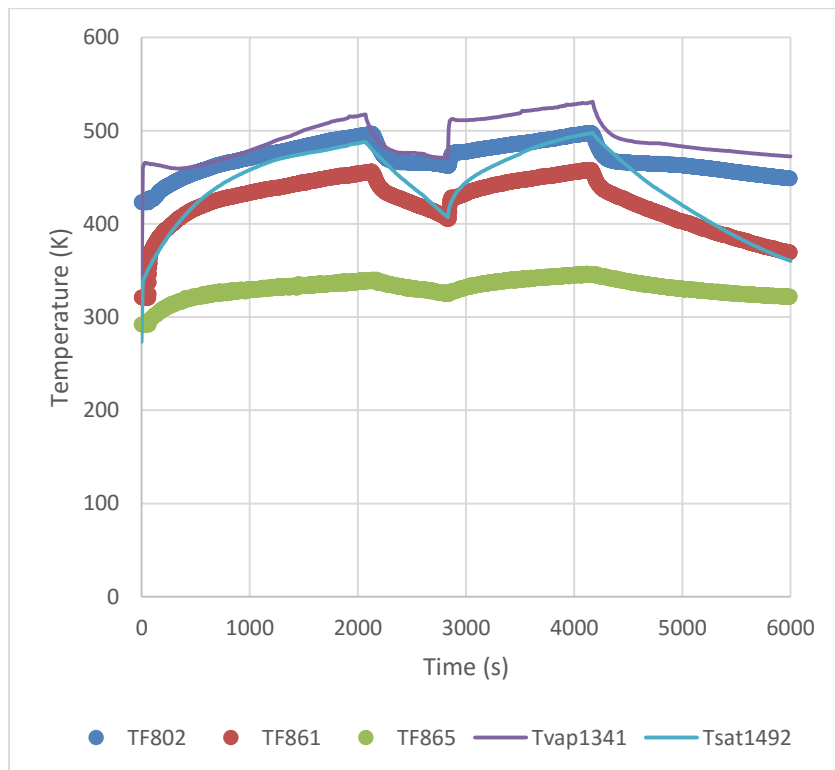


Figure A-10 Containment Temperature for Test 1.2

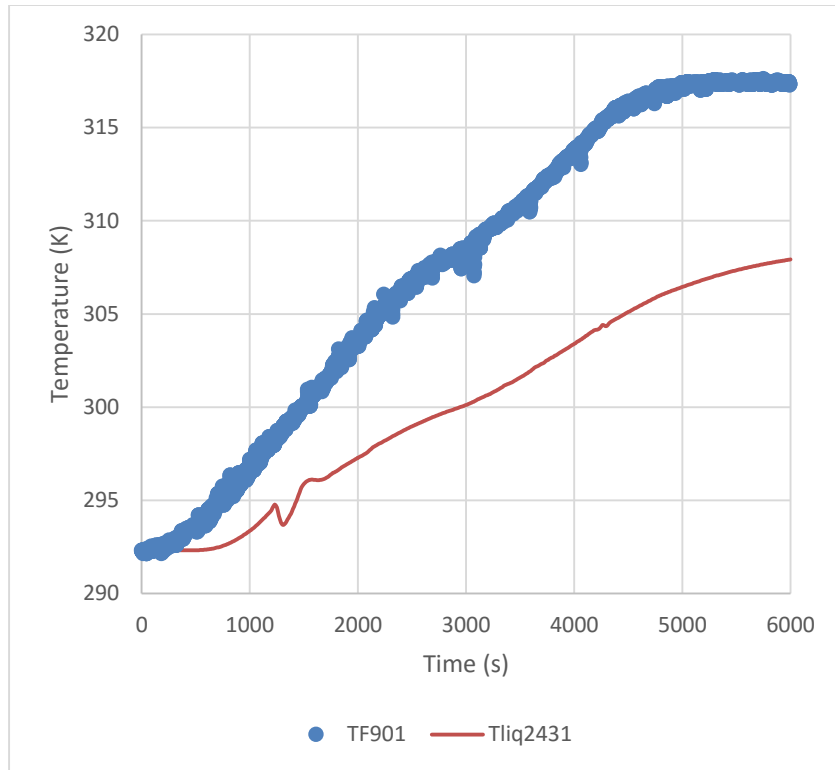


Figure A-11 CPV Temperature for Test 1.2

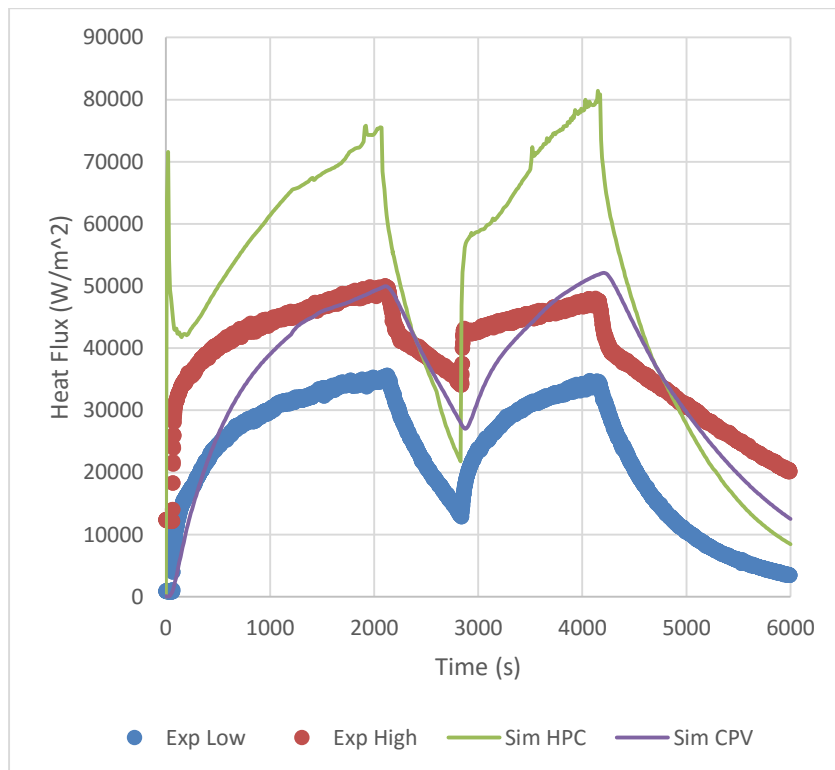


Figure A-12 Heat Flux at Location 6 for Test 1.2

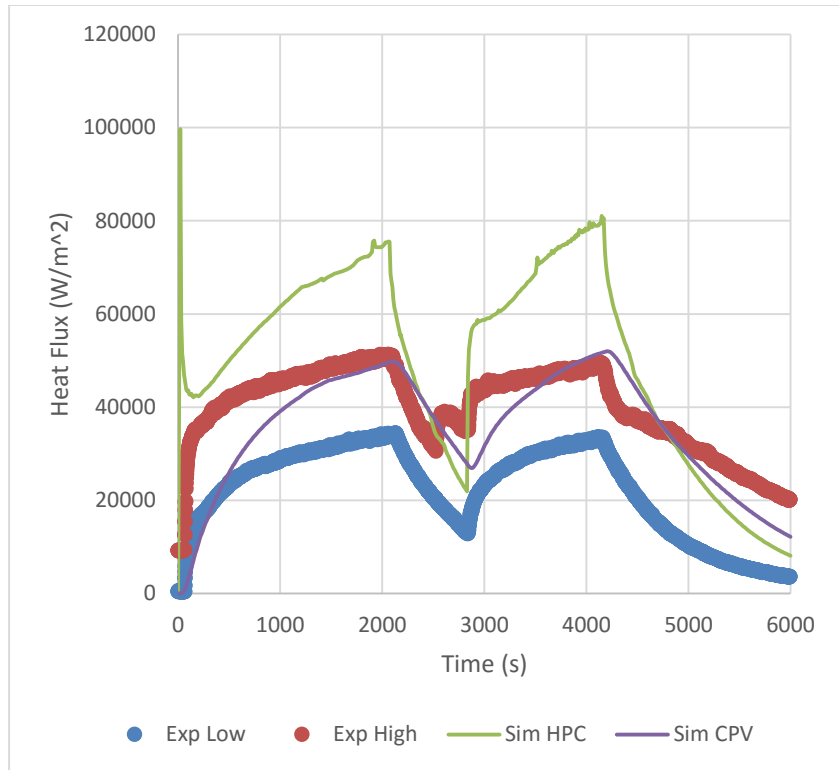


Figure A-13 Heat Flux at Location 5 for Test 1.2

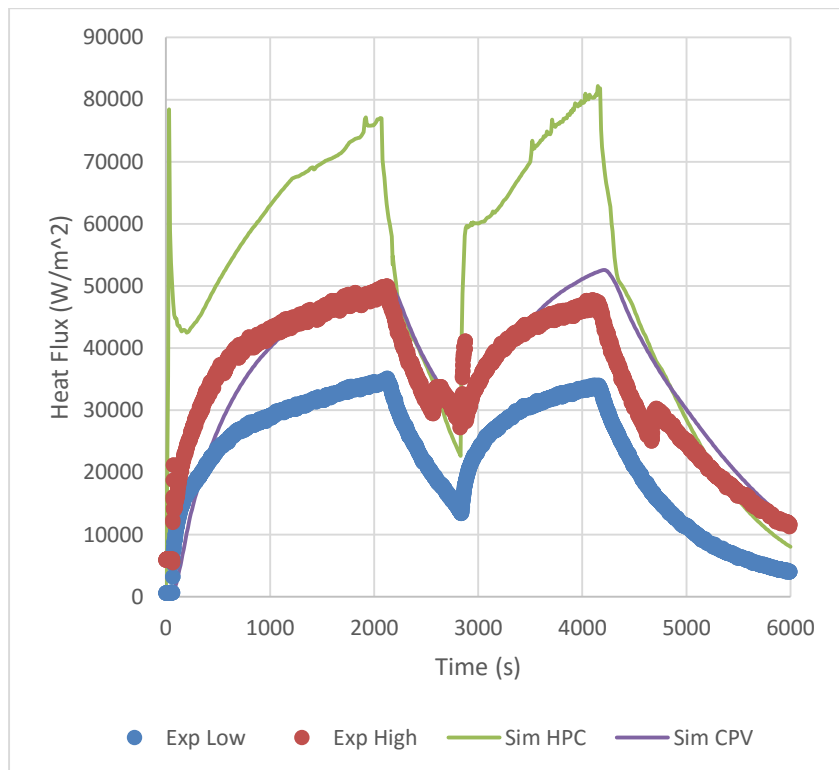


Figure A-14 Heat Flux at Location 4 for Test 1.2

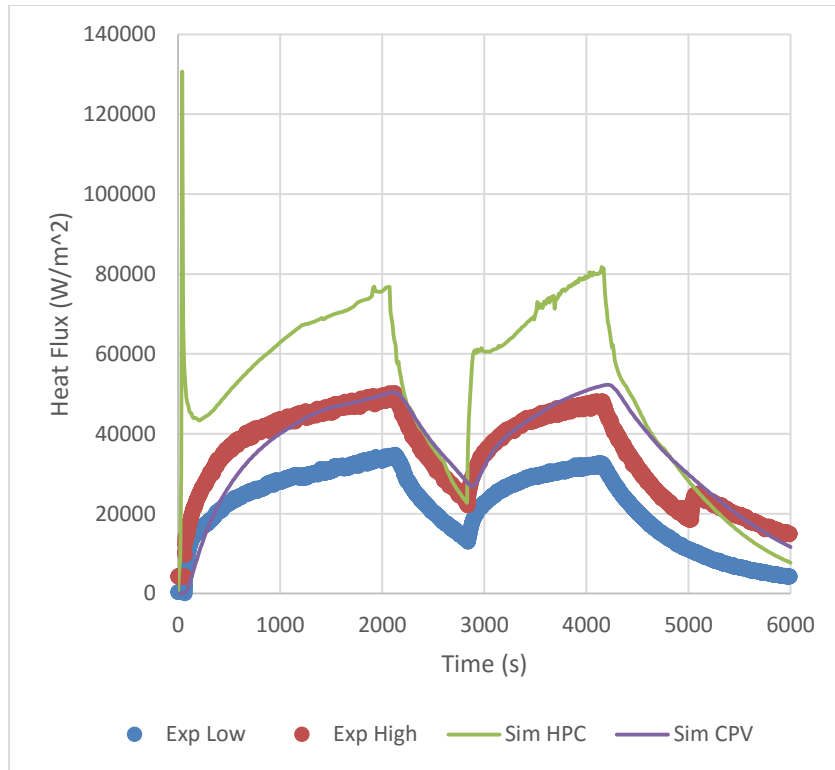


Figure A-15 Heat Flux at Location 3 for Test 1.2

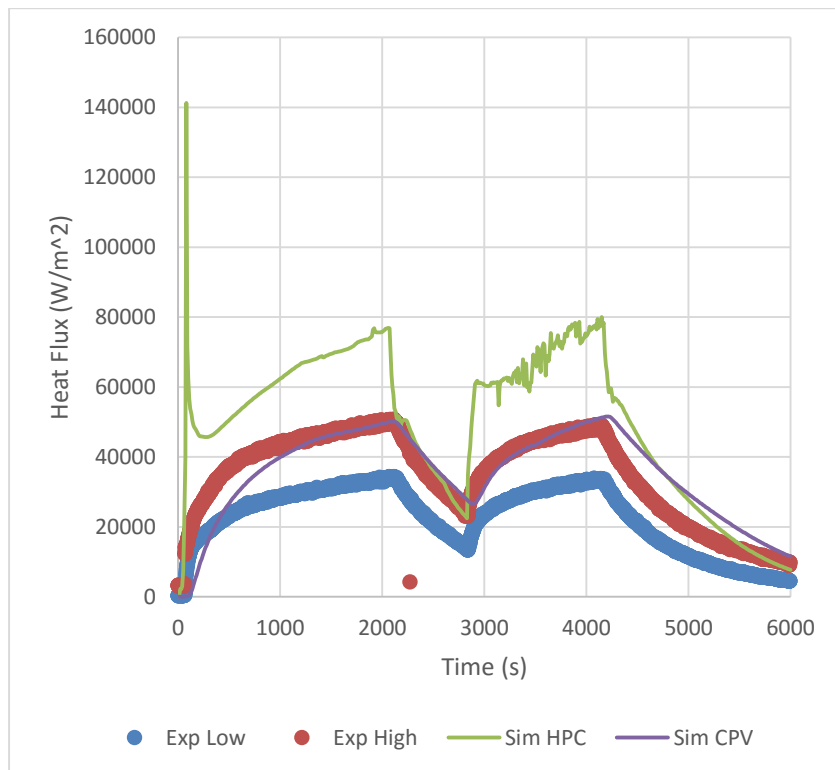


Figure A-16 Heat Flux at Location 2 for Test 1.2

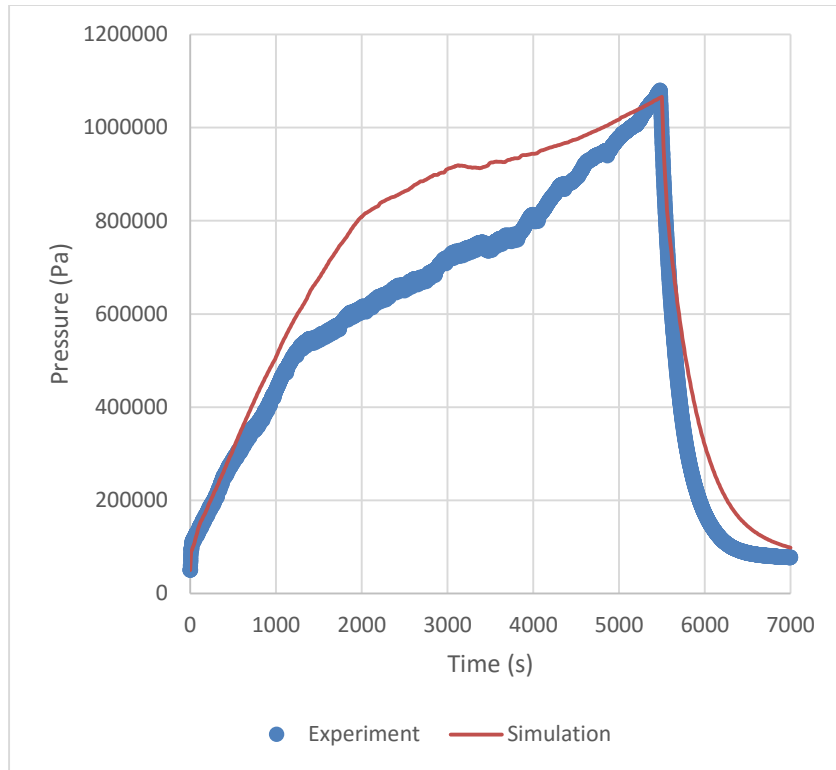


Figure A-17 Containment Pressure for Test 1.3

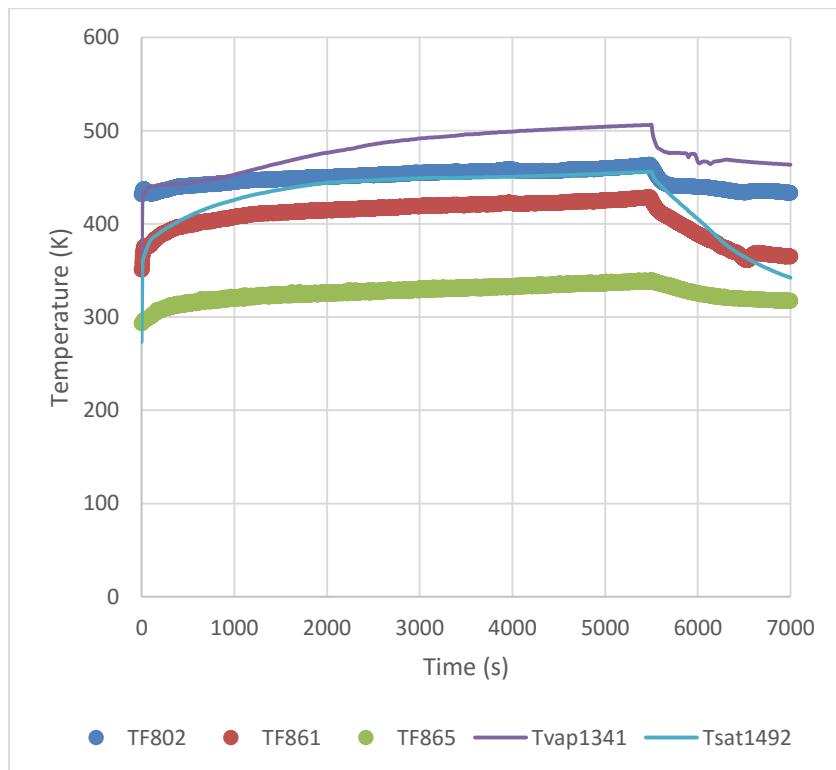


Figure A-18 Containment Temperature for Test 1.3

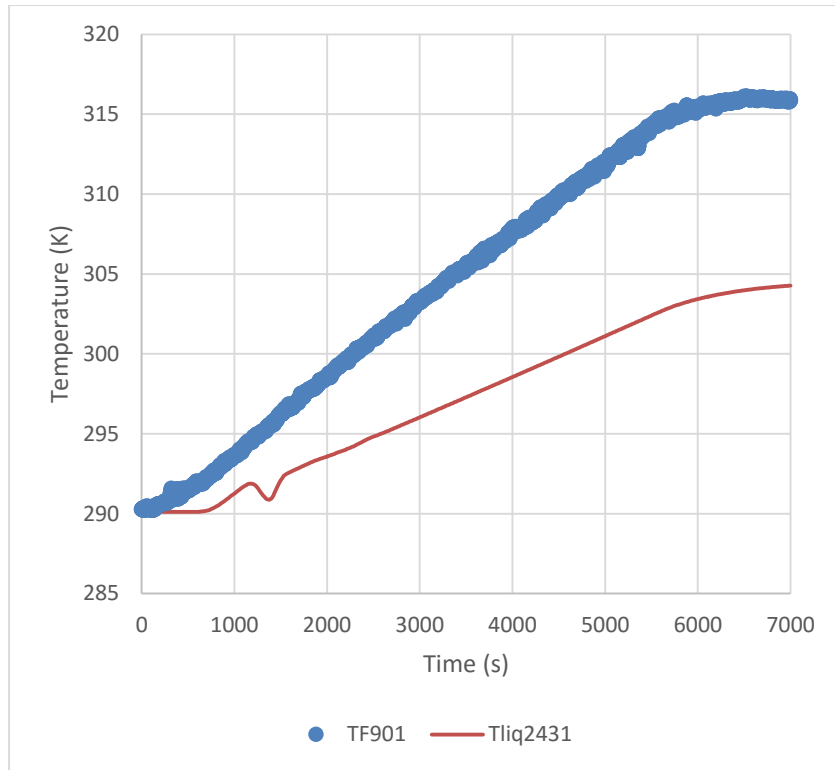


Figure A-19 CPV Temperature for Test 1.3

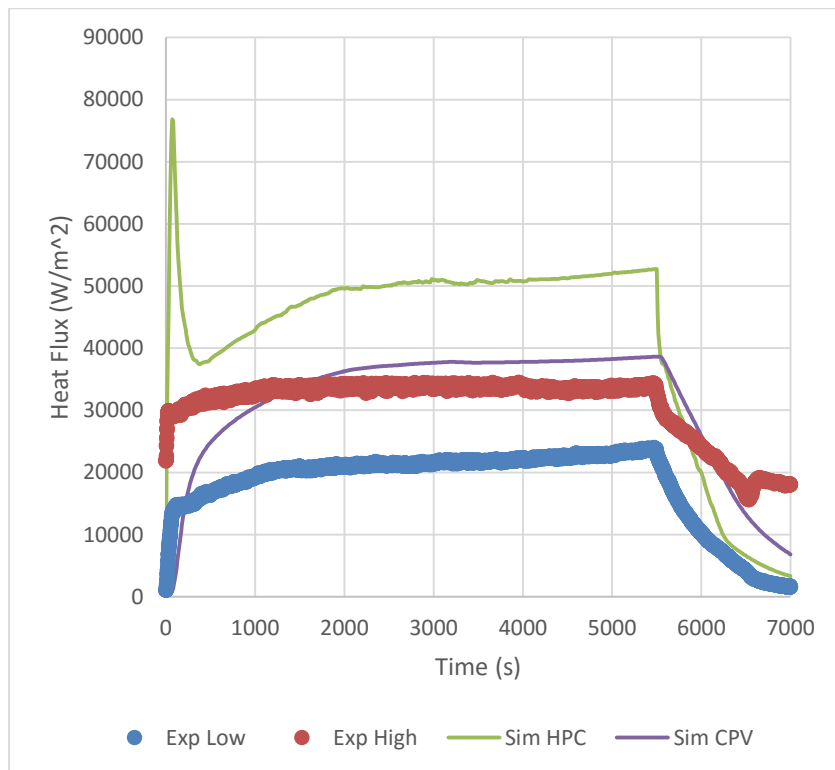


Figure A-20 Heat Flux at Location 6 for Test 1.3

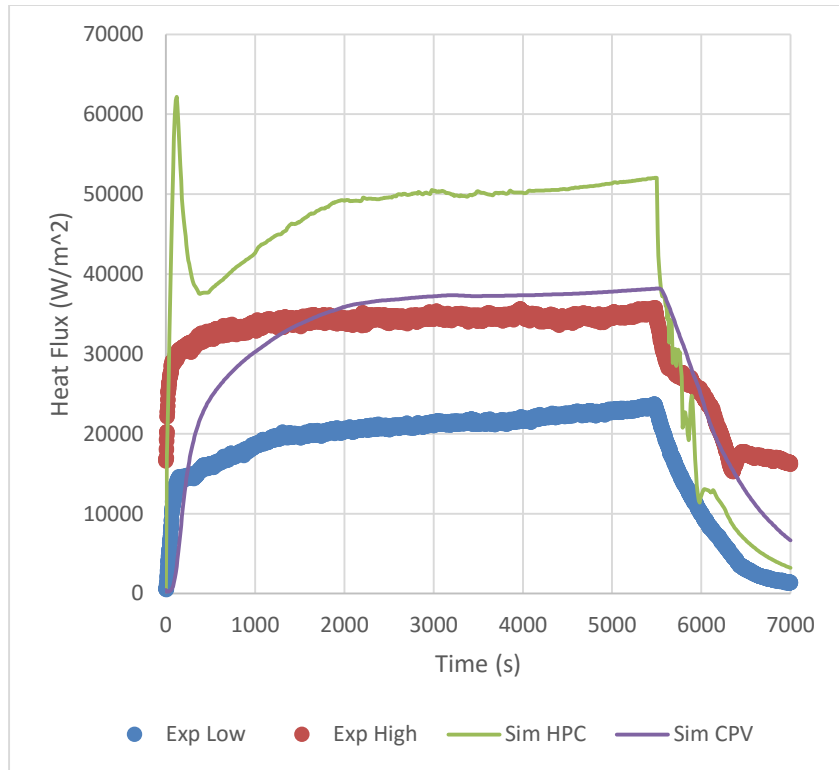


Figure A-21 Heat Flux at Location 5 for Test 1.3

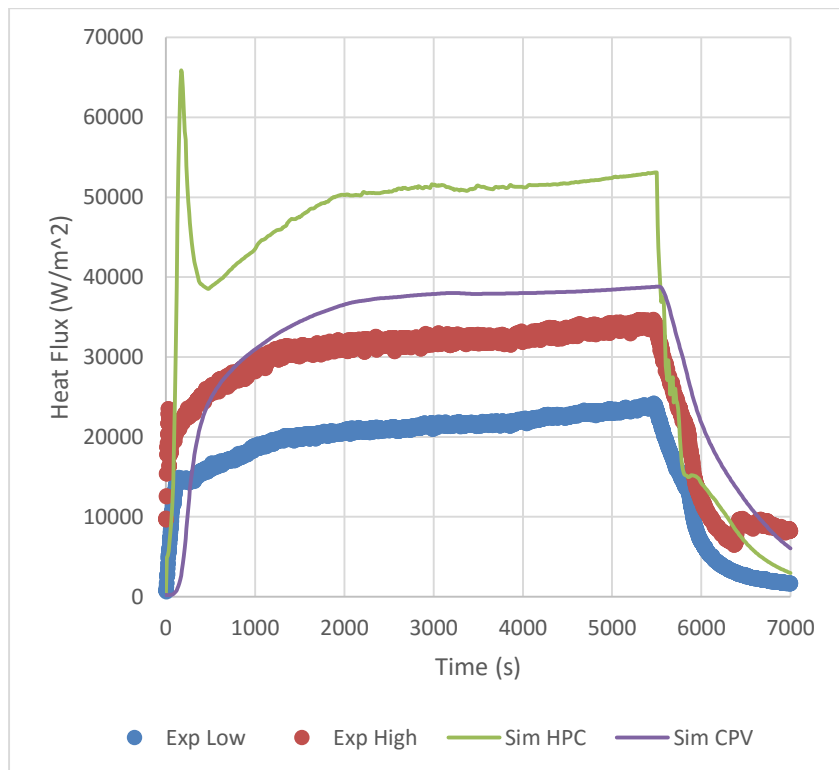


Figure A-22 Heat Flux at Location 4 for Test 1.3

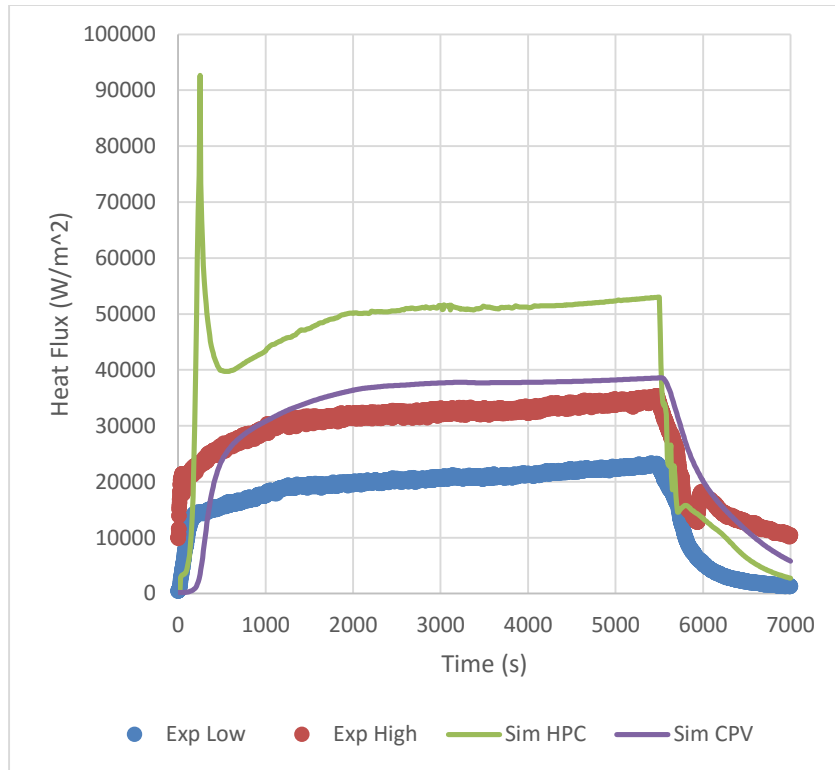


Figure A-23 Heat Flux at Location 3 for Test 1.3

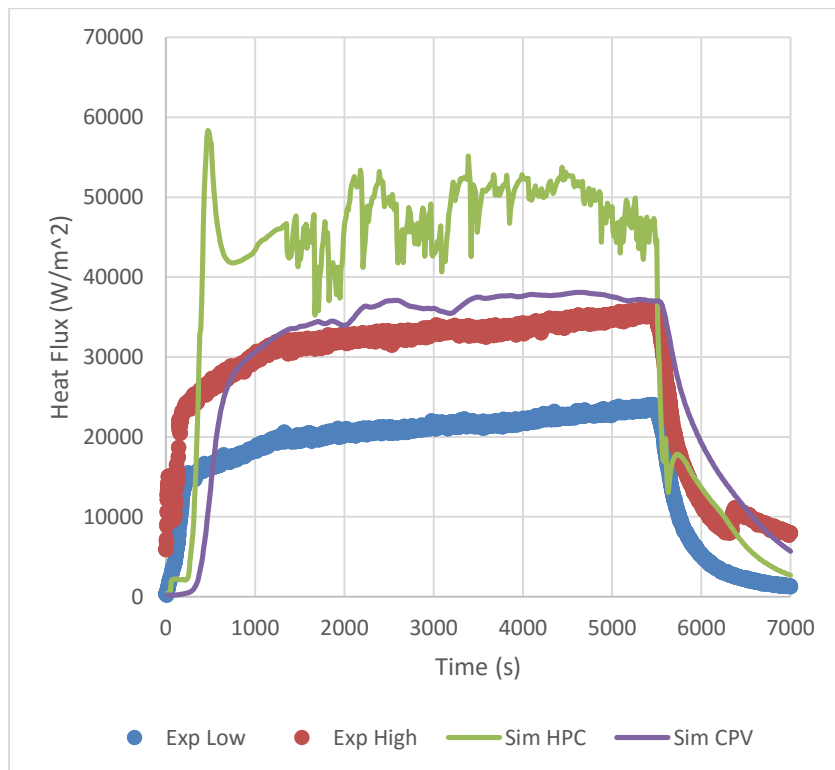


Figure A-24 Heat Flux at Location 2 for Test 1.3

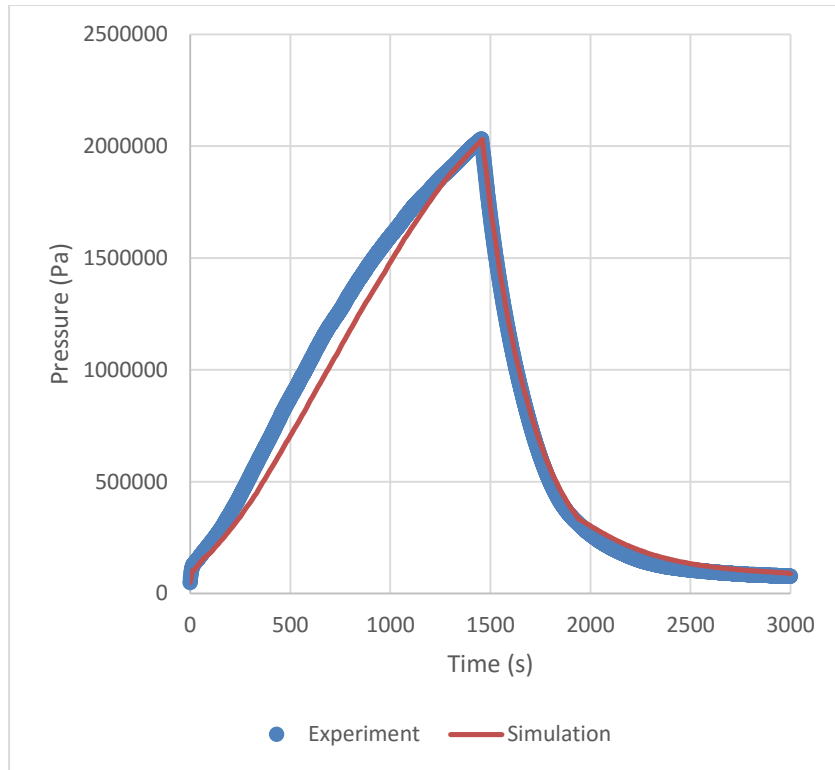


Figure A-25 Containment Pressure for Test 1.4

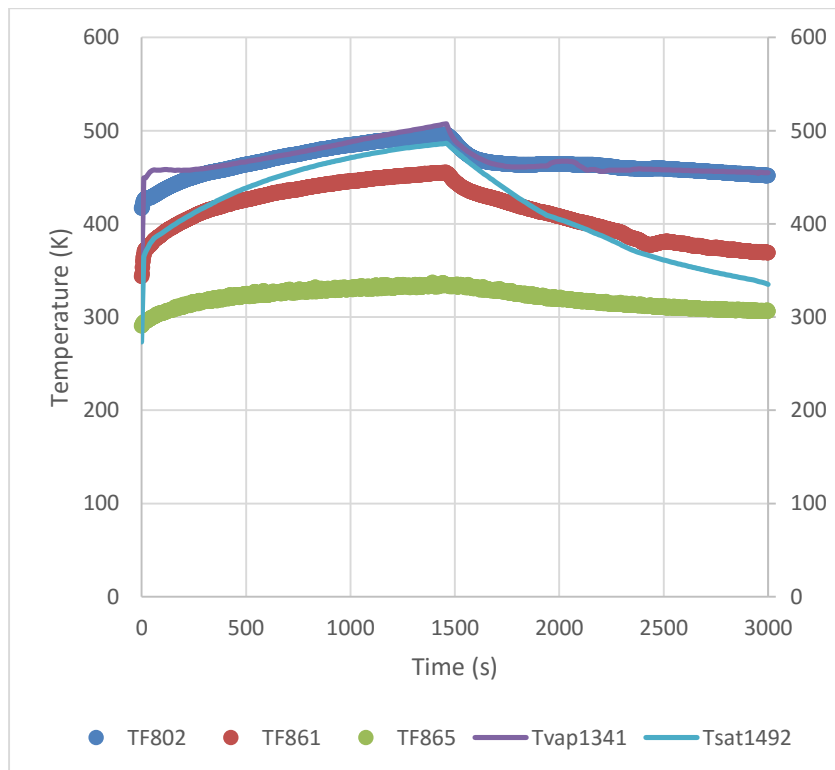


Figure A-26 Containment Temperature for Test 1.4

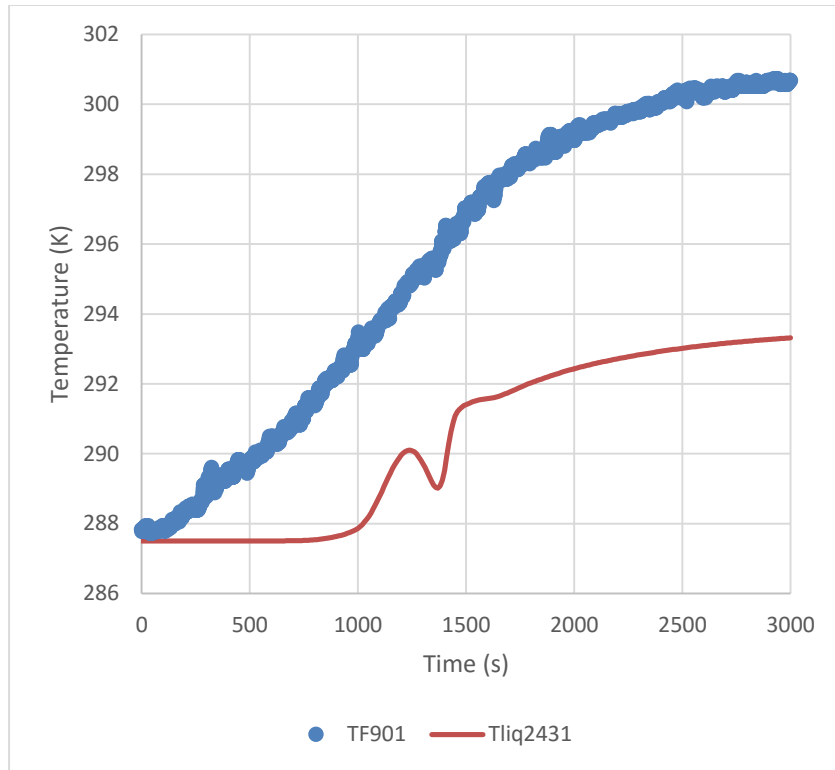


Figure A-27 CPV Temperature for Test 1.4

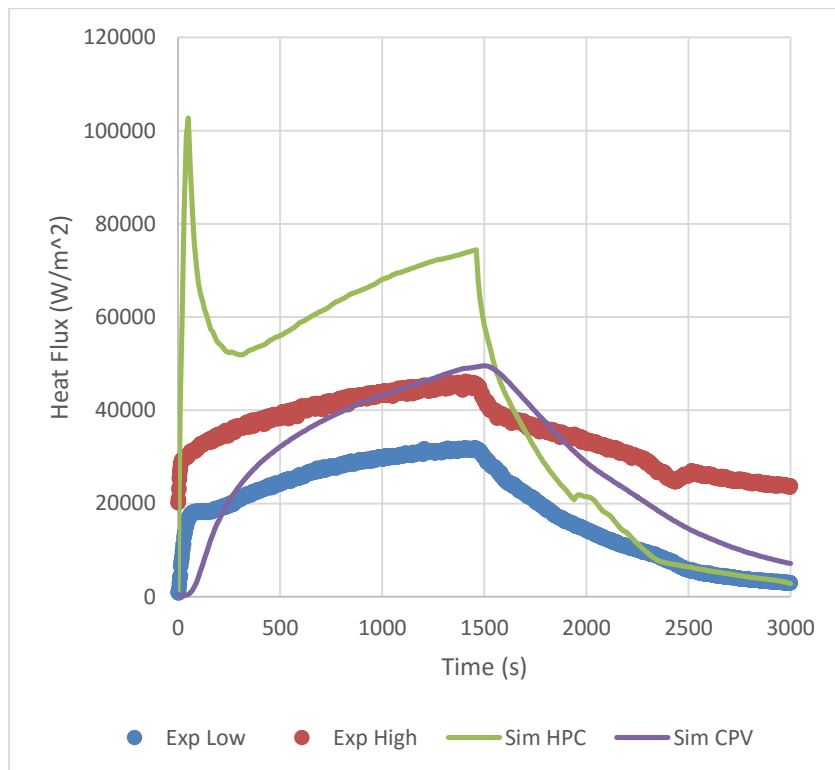


Figure A-28 Heat Flux at Location 6 for Test 1.4

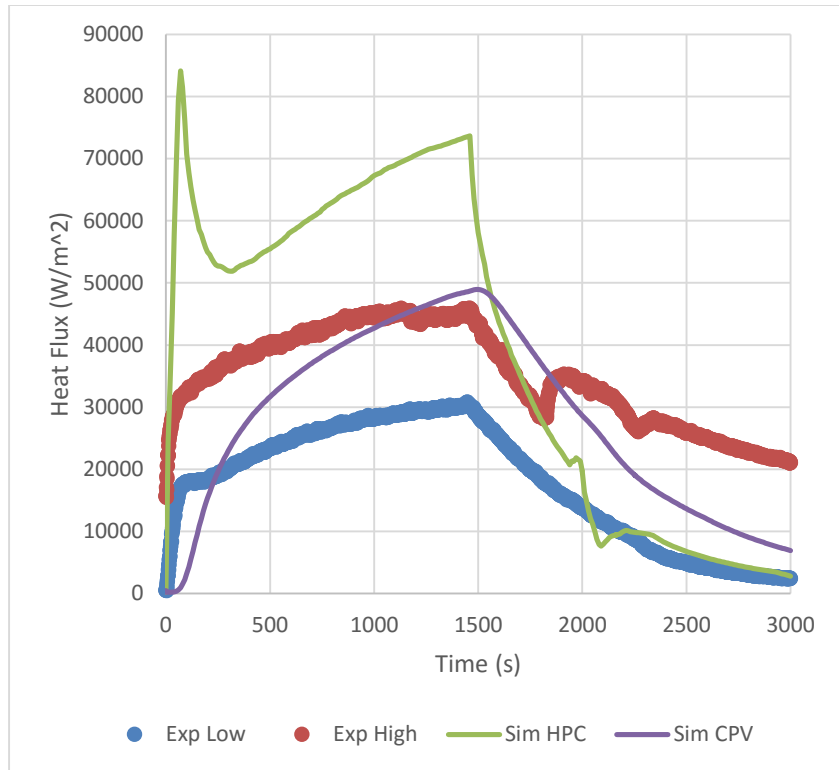


Figure A-29 Heat Flux at Location 5 for Test 1.4

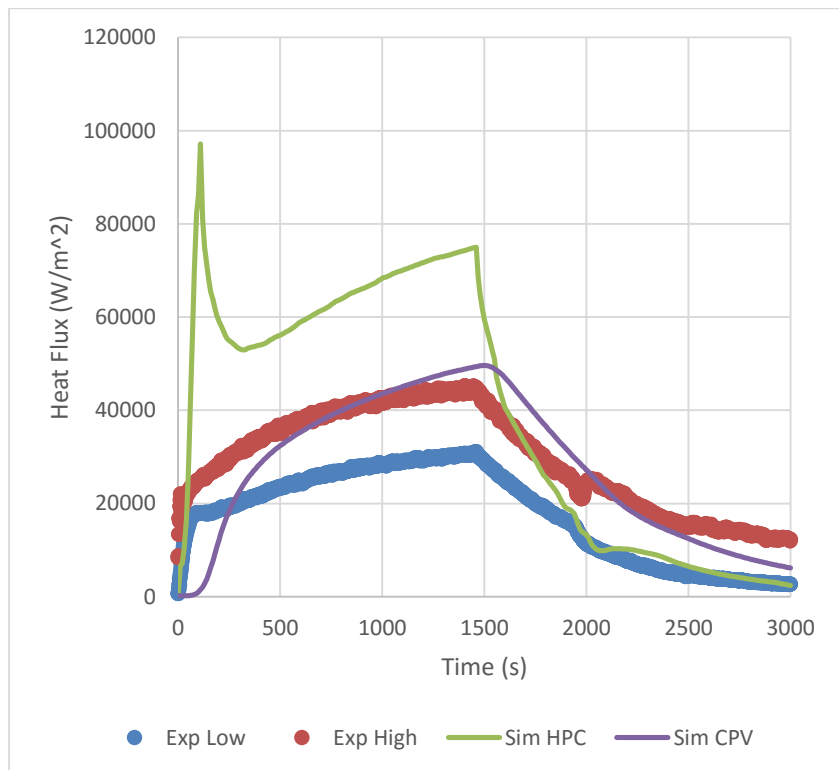


Figure A-30 Heat Flux at Location 4 for Test 1.4

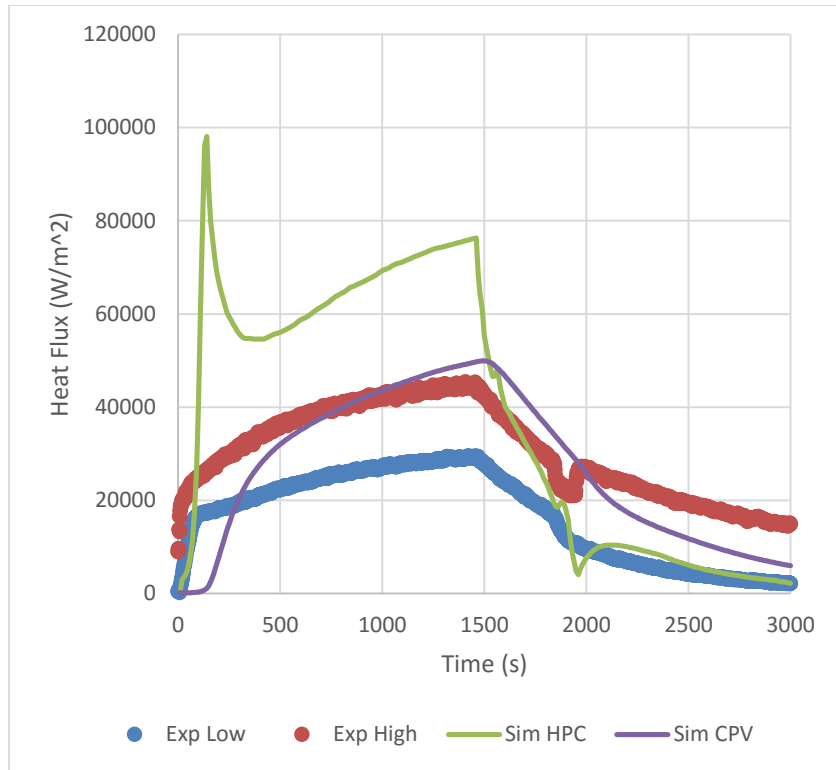


Figure A-31 Heat Flux at Location 3 for Test 1.4

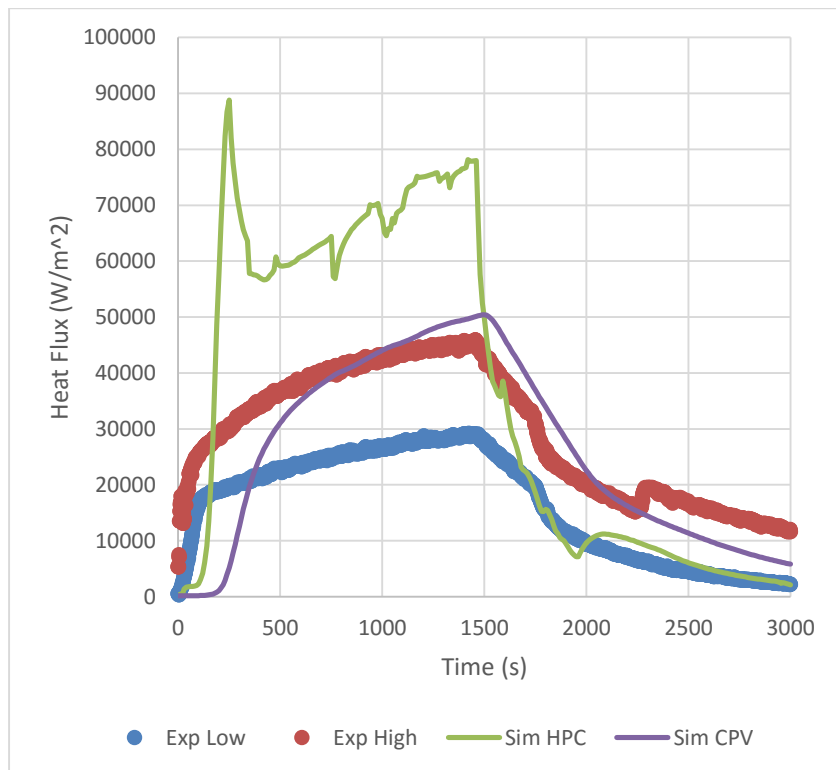


Figure A-32 Heat Flux at Location 2 for Test 1.4

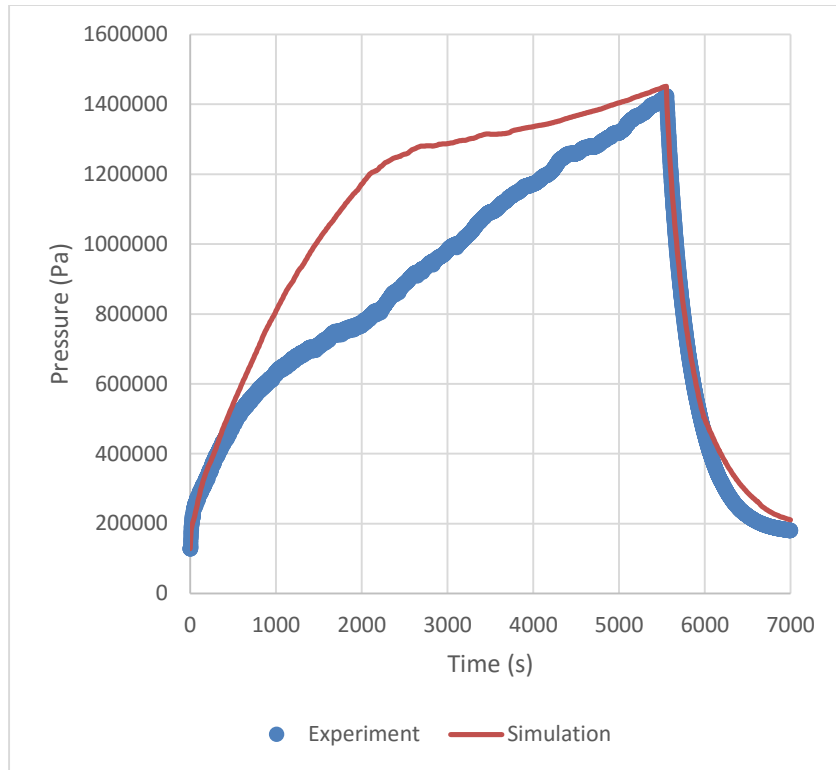


Figure A-33 Containment Pressure for Test 1.5

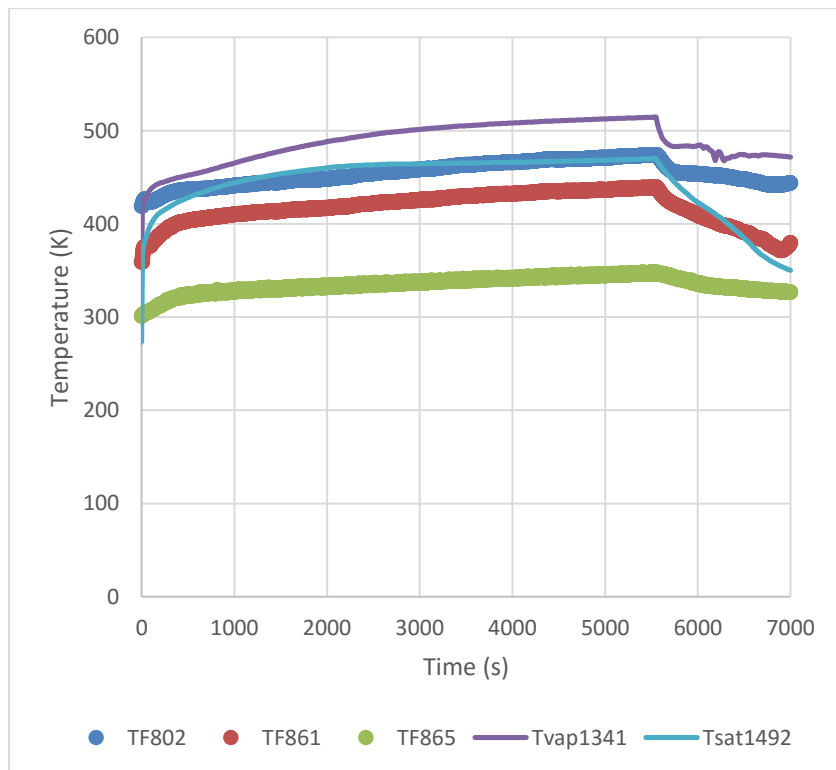


Figure A-34 Containment Temperature for Test 1.5

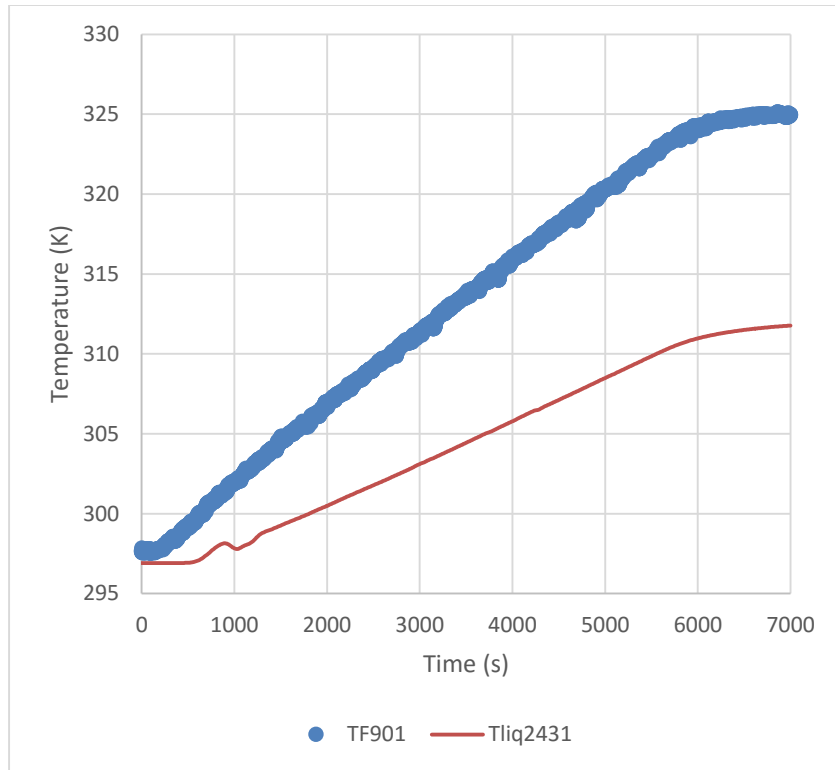


Figure A-35 CPV Temperature for Test 1.5

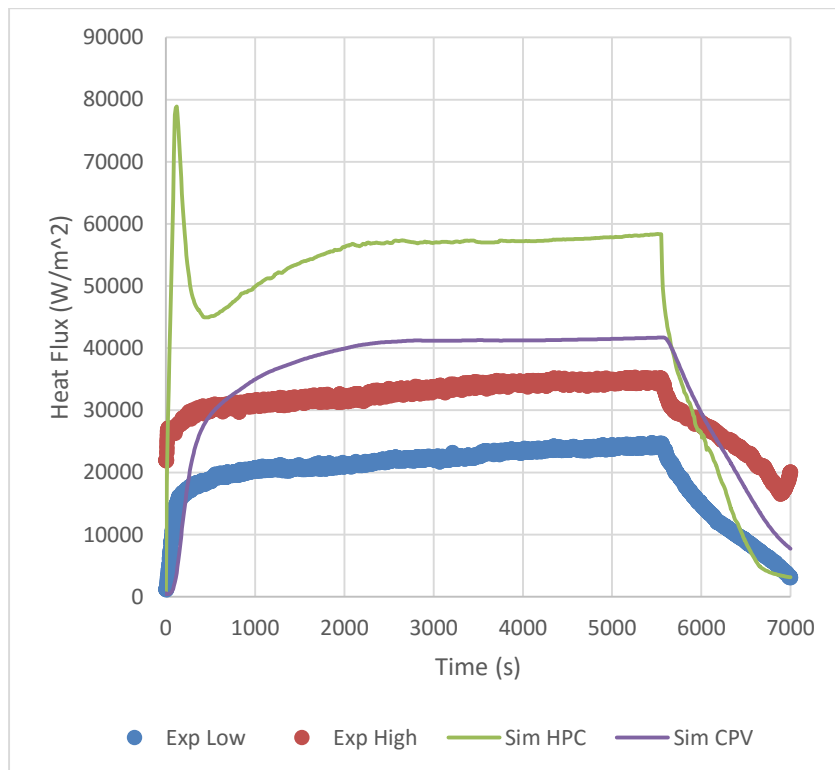


Figure A-36 Heat Flux at Location 6 for Test 1.5

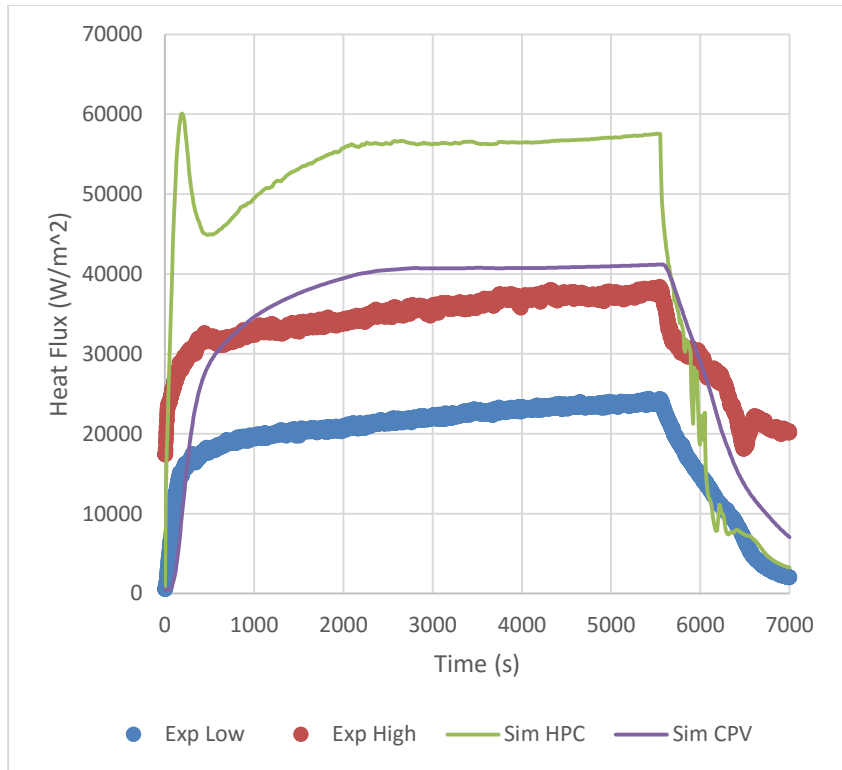


Figure A-37 Heat Flux at Location 5 for Test 1.5

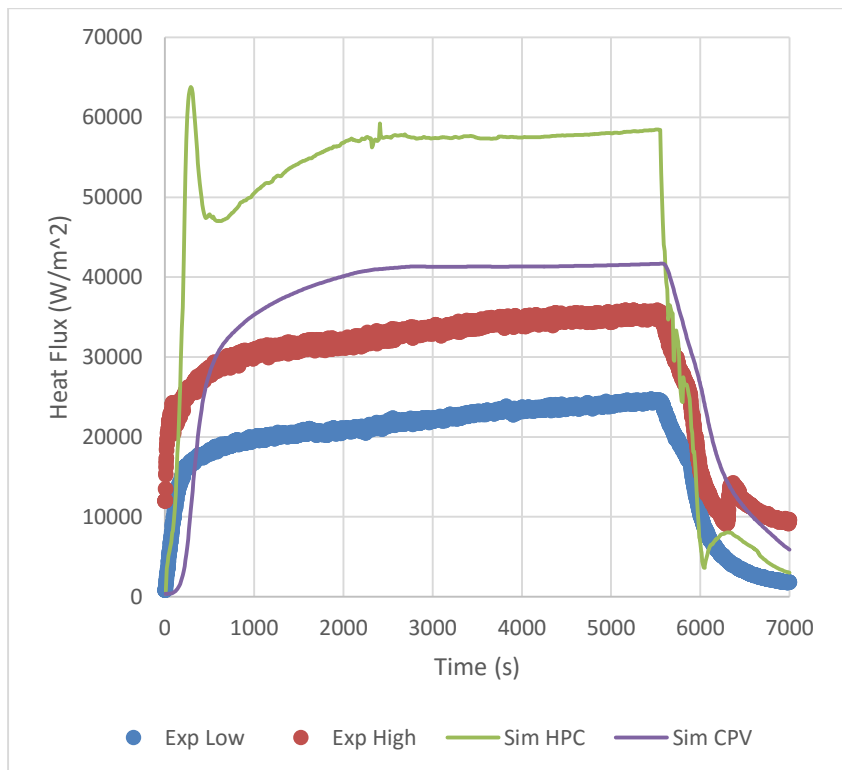


Figure A-38 Heat Flux at Location 4 for Test 1.5

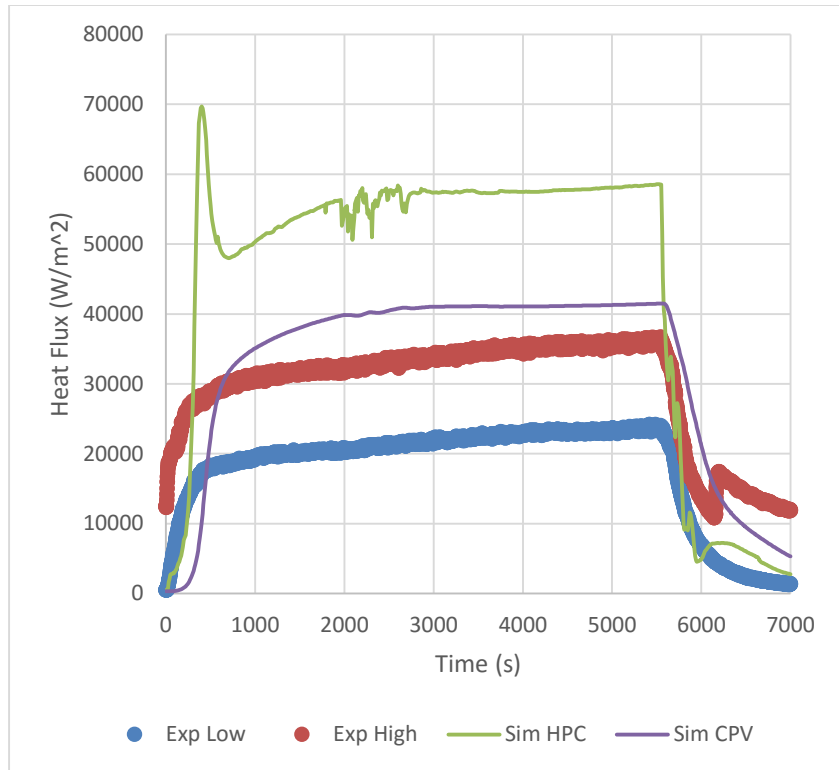


Figure A-39 Heat Flux at Location 3 for Test 1.5

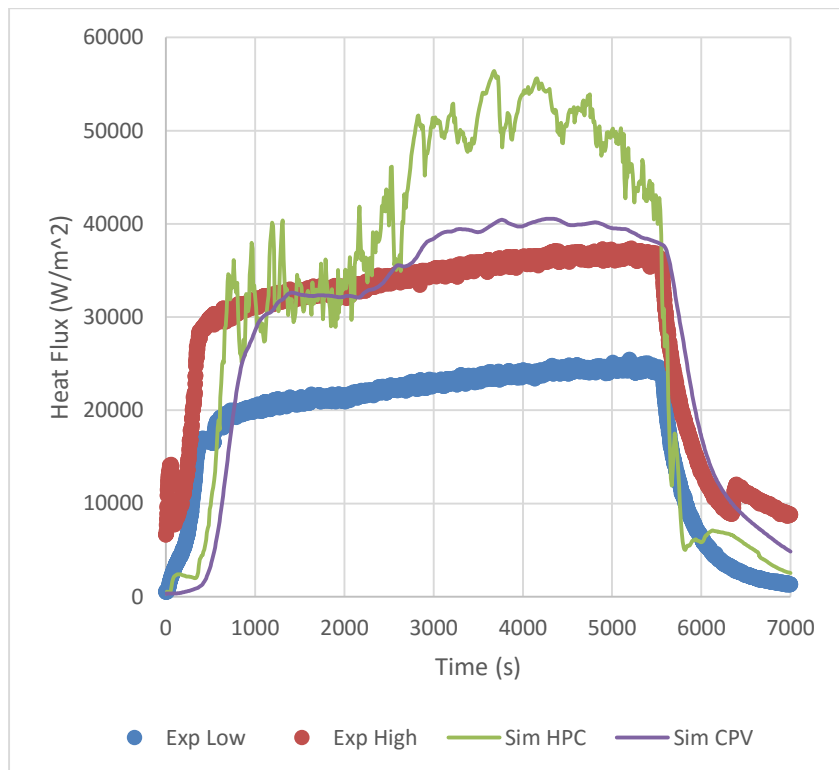


Figure A-40 Heat Flux at Location 2 for Test 1.5

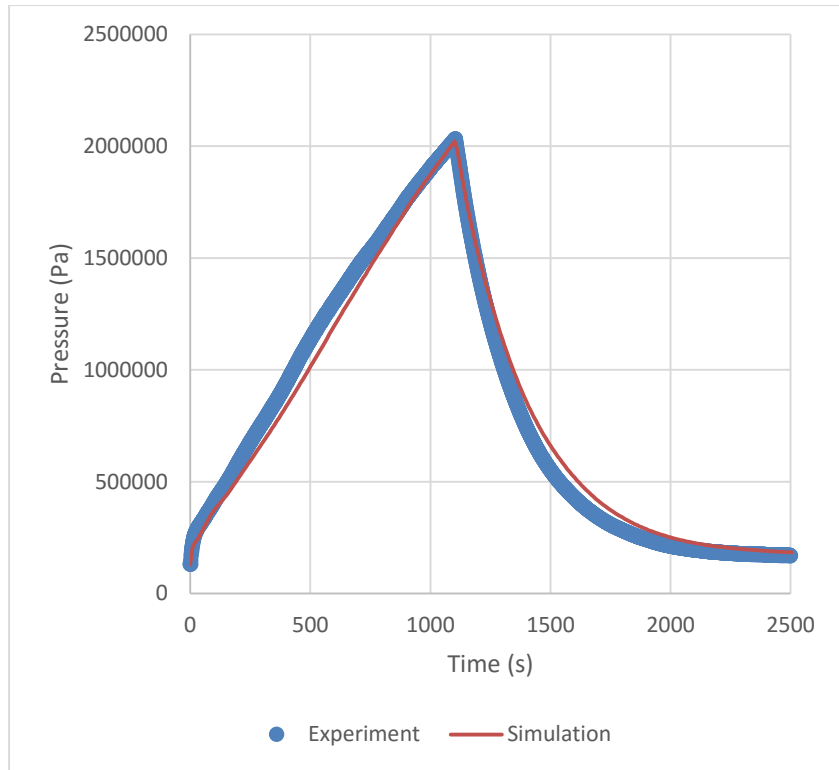


Figure A-41 Containment Pressure for Test 1.6

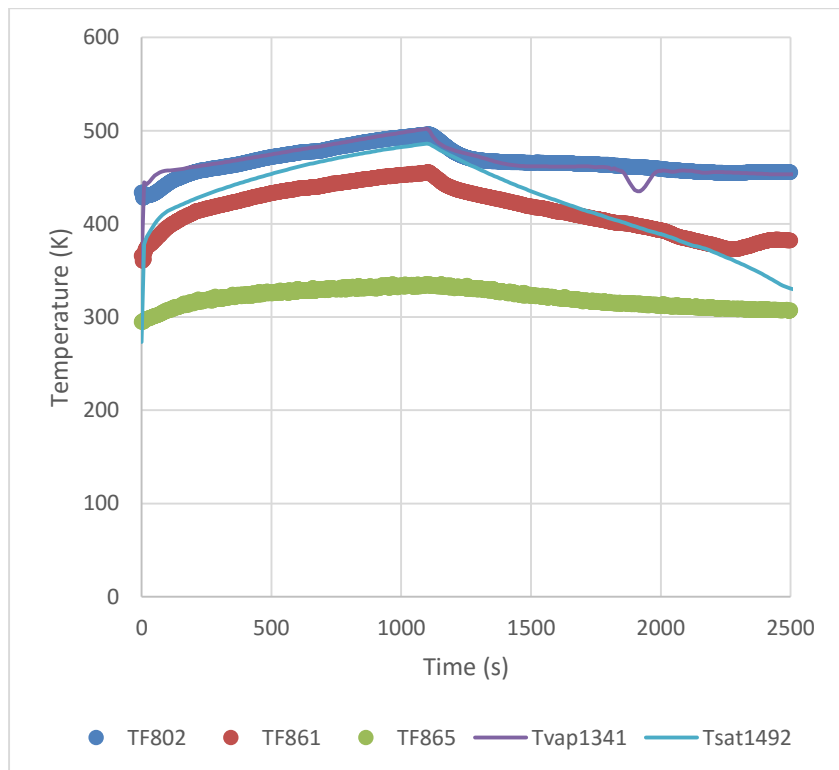


Figure A-42 Containment Temperature for Test 1.6

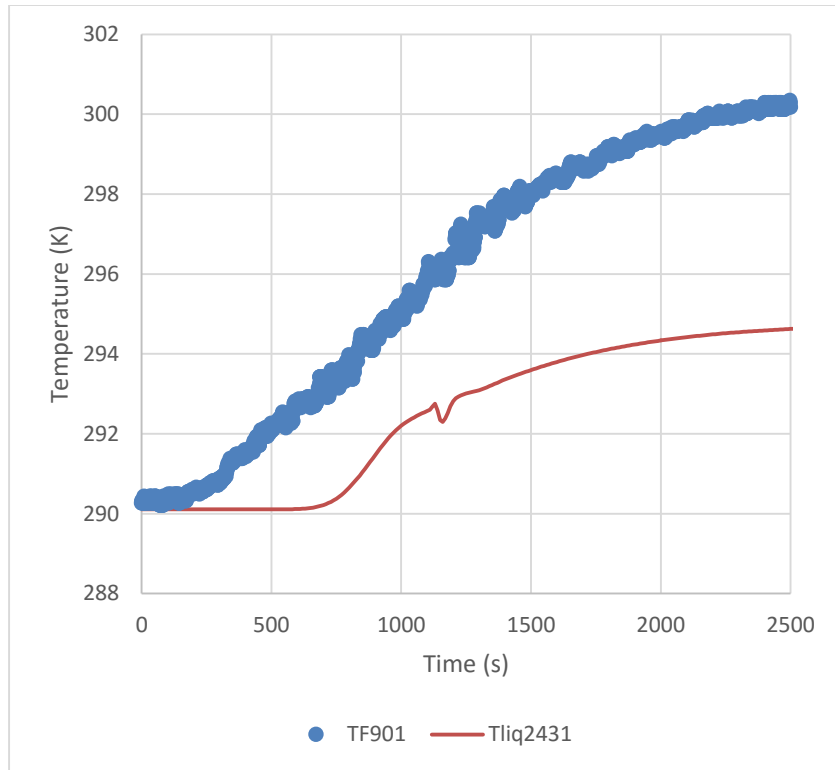


Figure A-43 CPV Temperature for Test 1.6

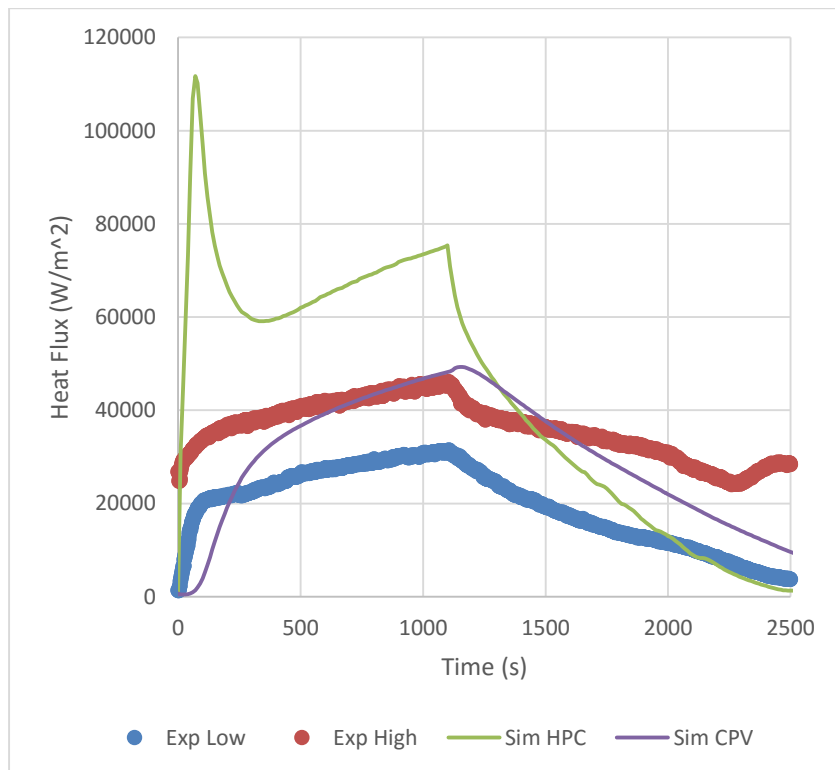


Figure A-44 Heat Flux at Location 6 for Test 1.6

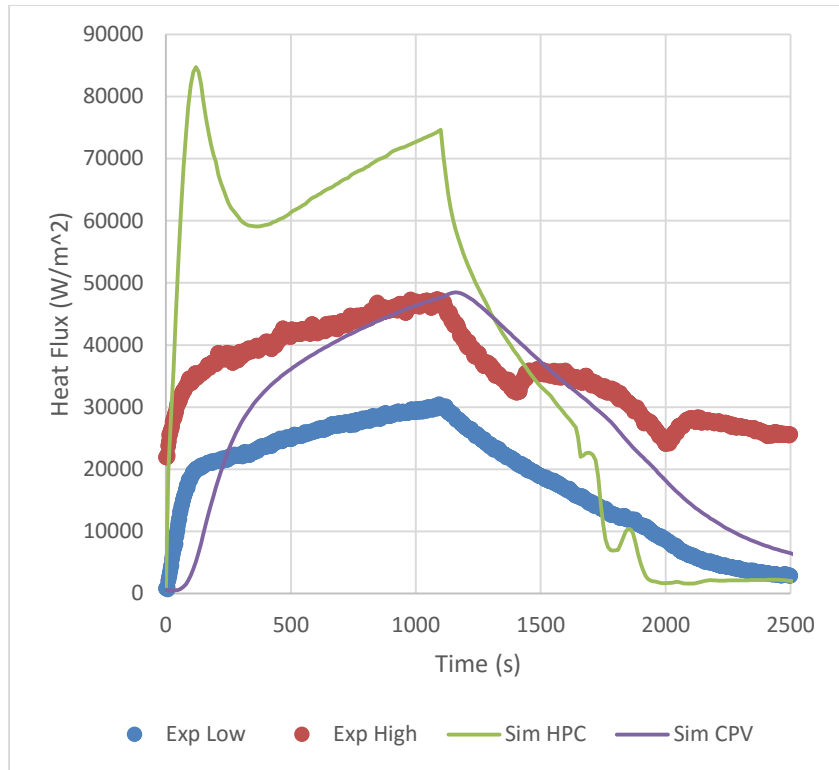


Figure A-45 Heat Flux at Location 5 for Test 1.6

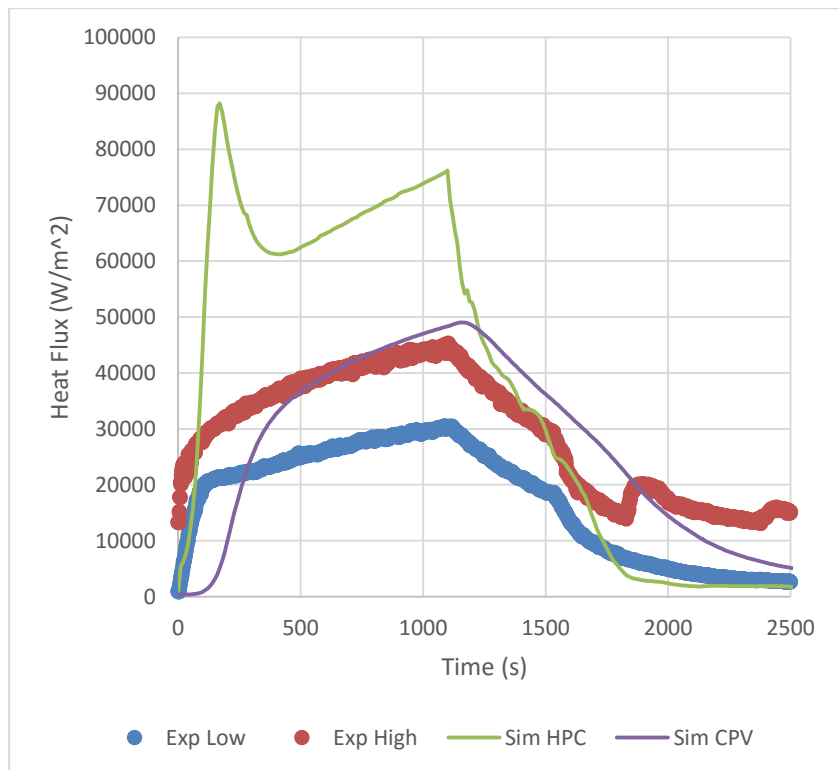


Figure A-46 Heat Flux at Location 4 for Test 1.6

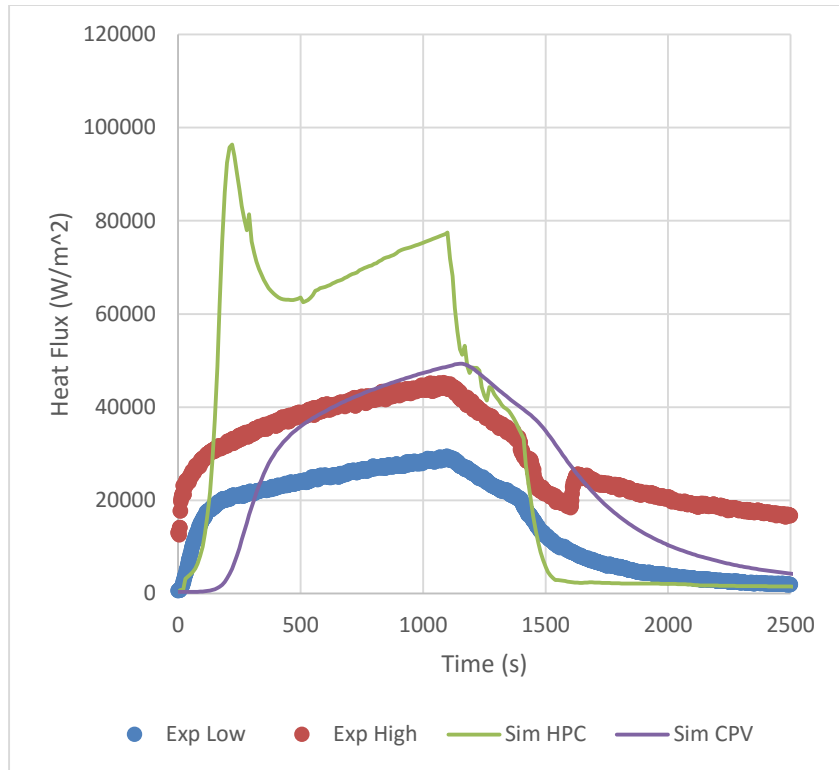


Figure A-47 Heat Flux at Location 3 for Test 1.6

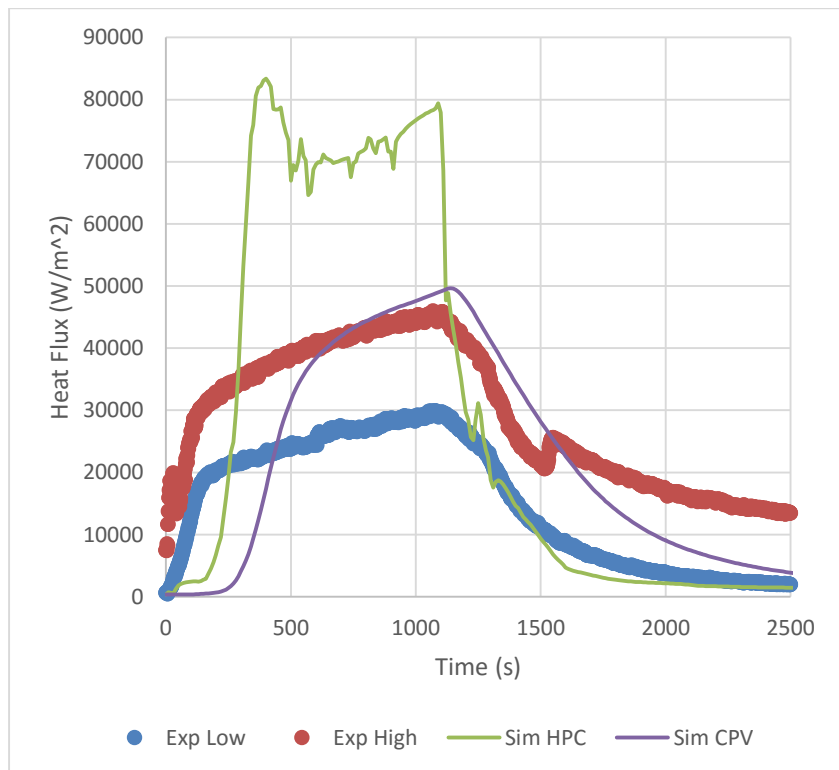


Figure A-48 Heat Flux at Location 2 for Test 1.6

CCT (2nd set of tests)

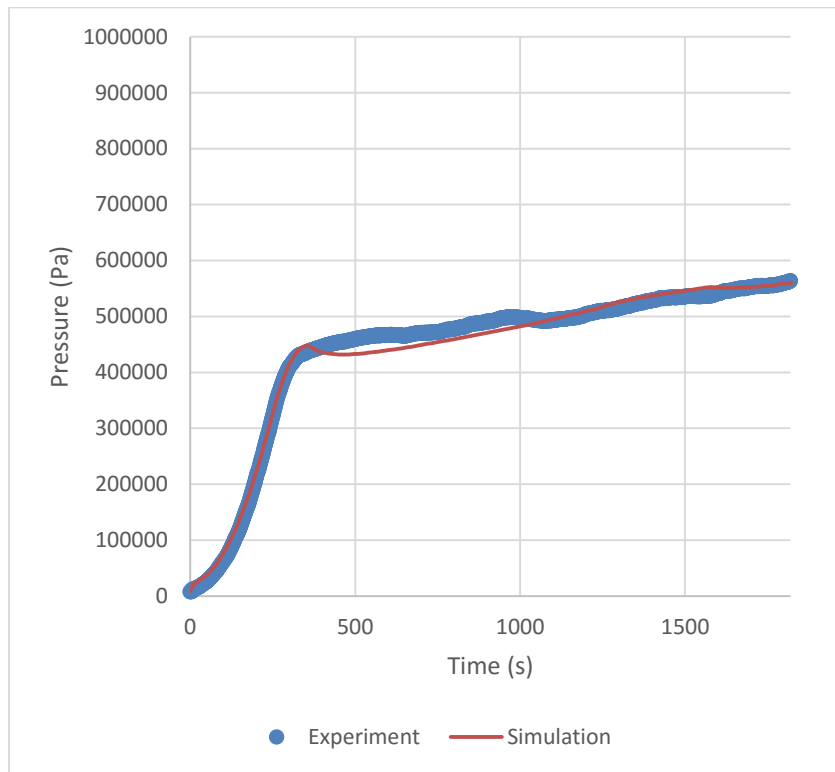


Figure A-49 Containment Pressure for Test 2.1

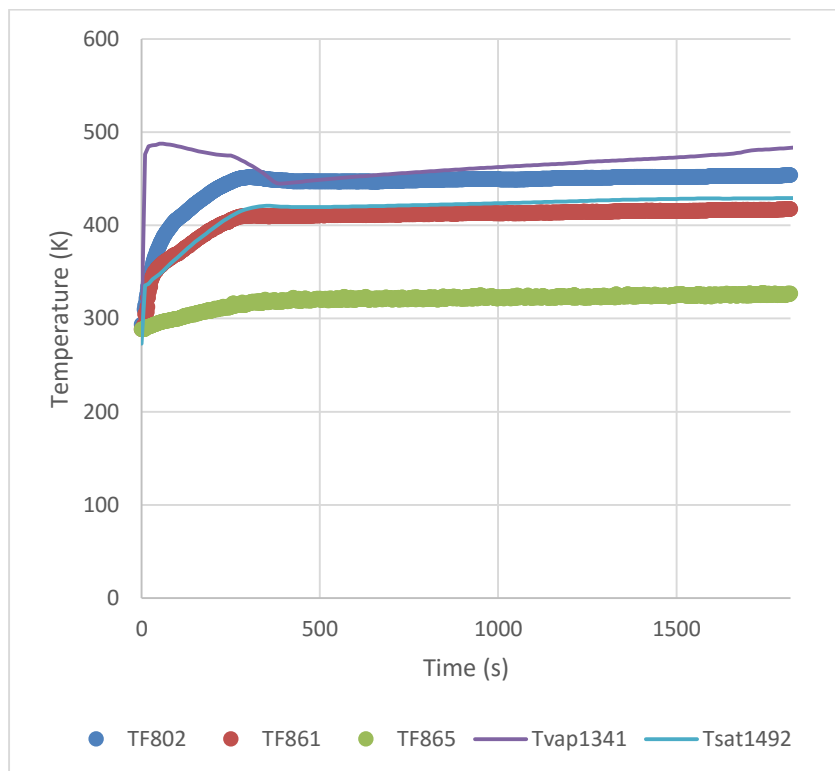


Figure A-50 Containment Temperature for Test 2.1

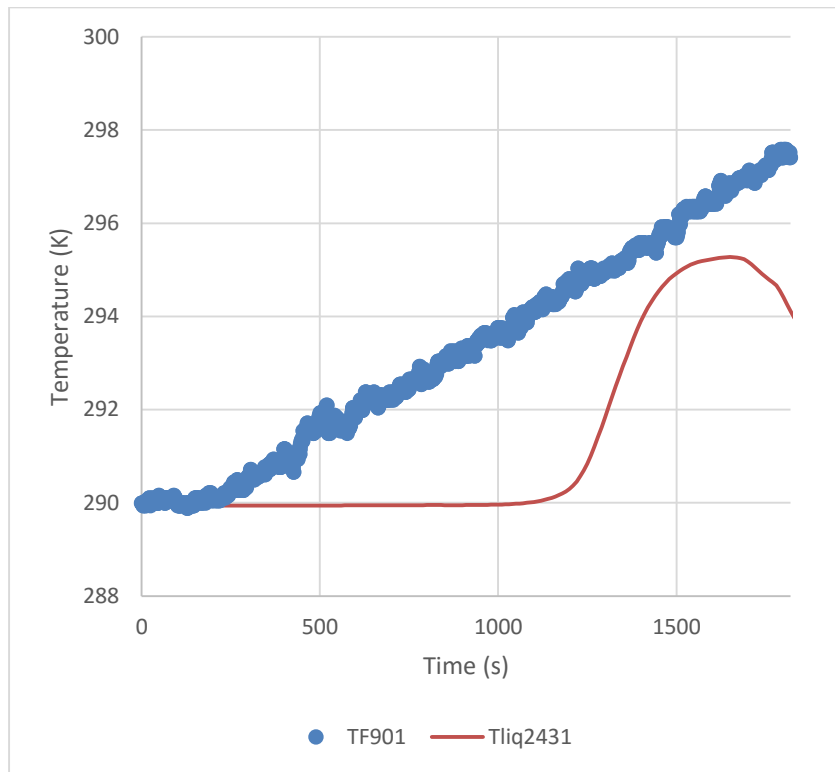


Figure A-51 CPV Temperature for Test 2.1

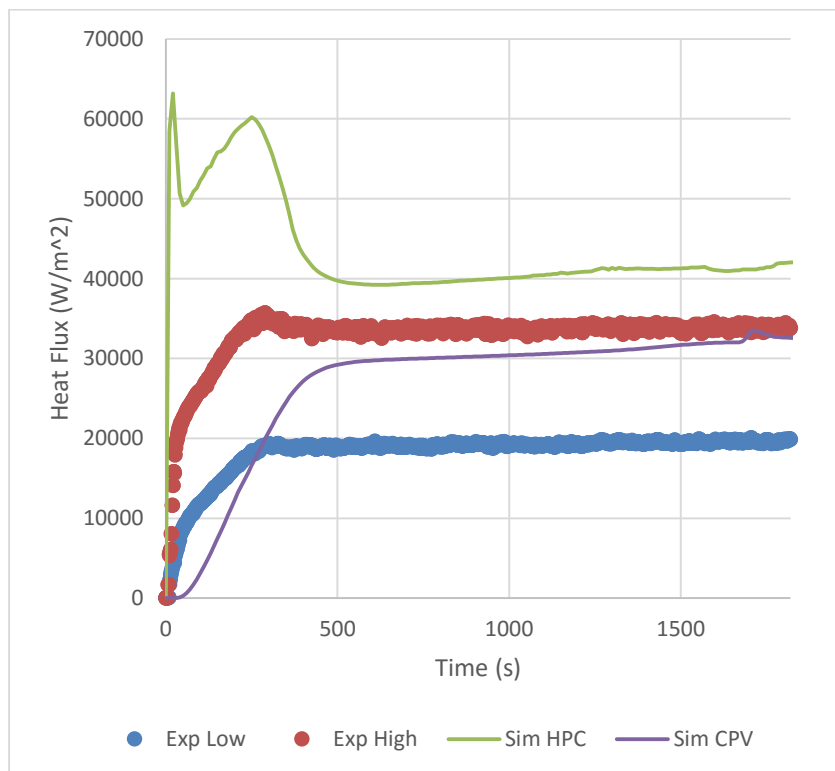


Figure A-52 Heat Flux at Location 6 for Test 2.1

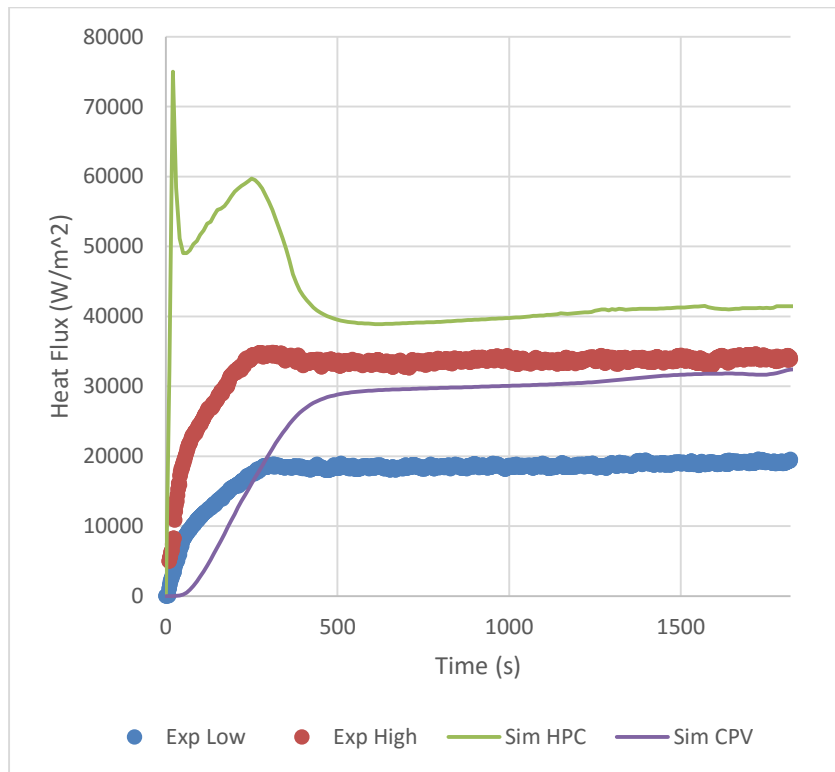


Figure A-53 Heat Flux at Location 5 for Test 2.1

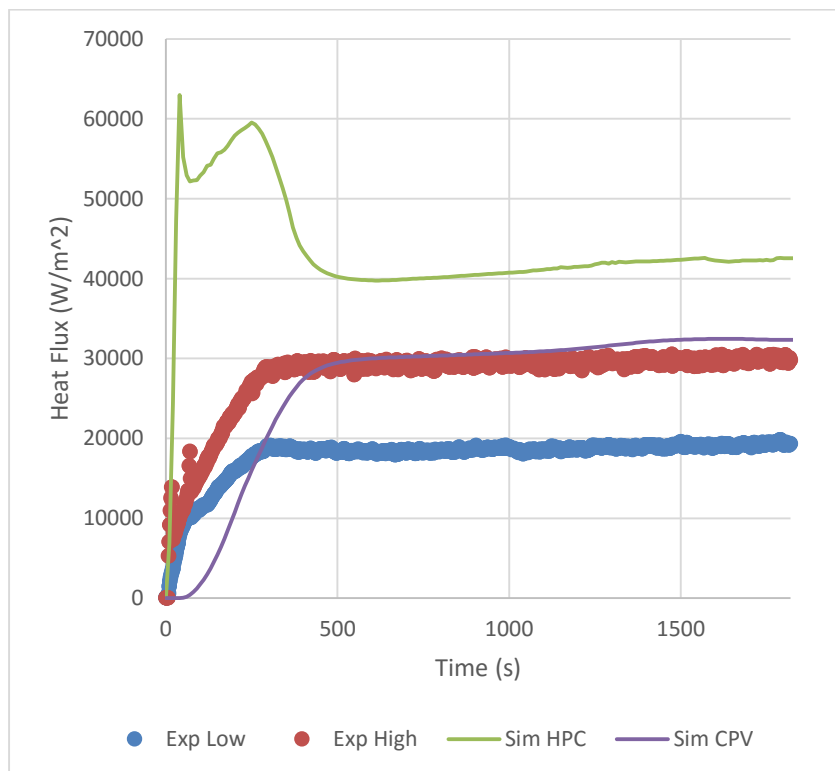


Figure A-54 Heat Flux at Location 4 for Test 2.1

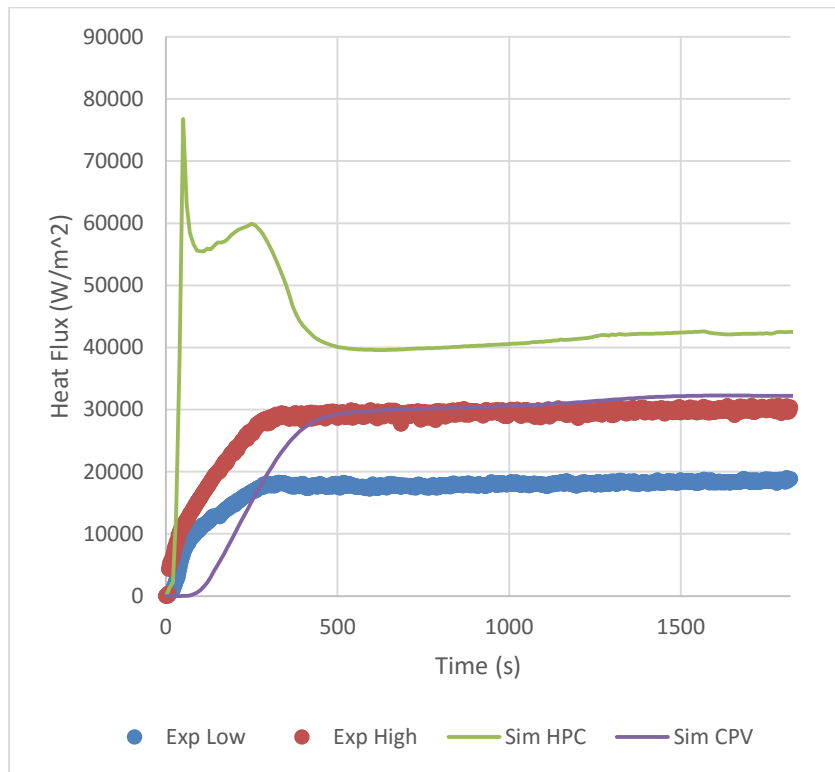


Figure A-55 Heat Flux at Location 3 for Test 2.1

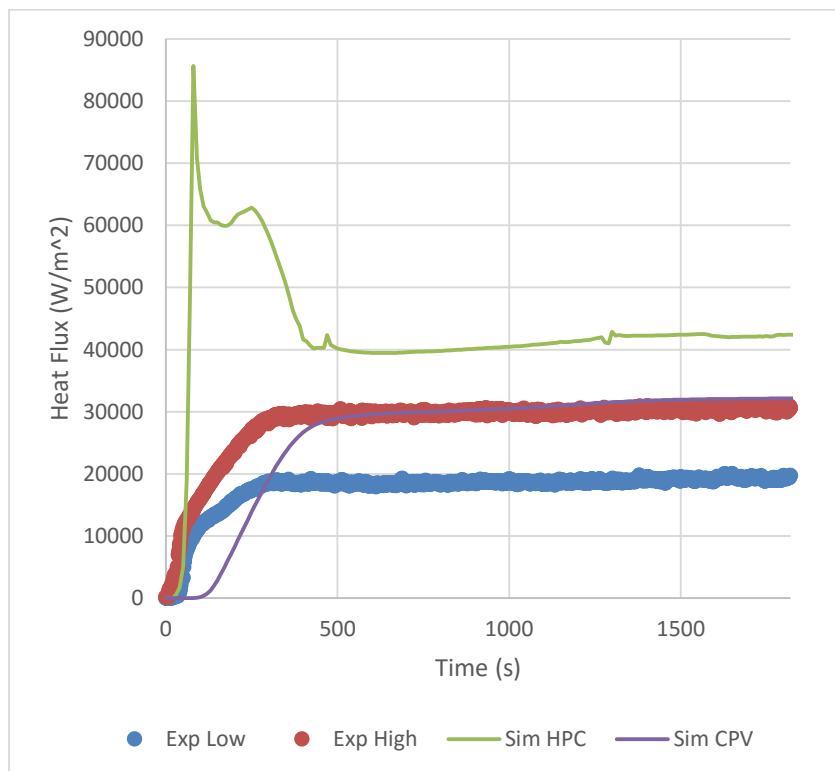


Figure A-56 Heat Flux at Location 2 for Test 2.1

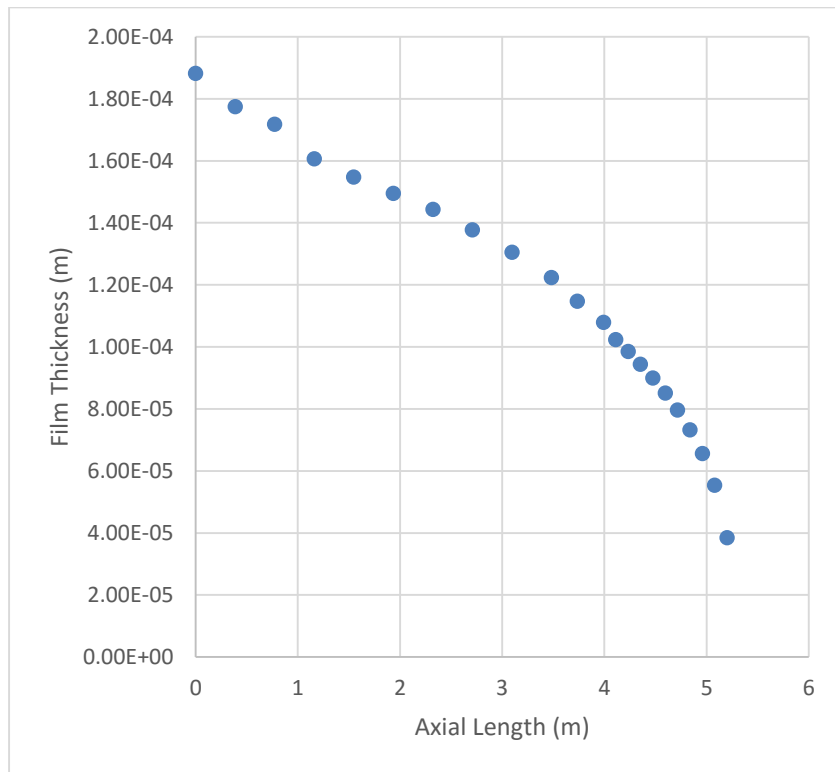


Figure A-57 Steady State Film Thickness for Test 2.1

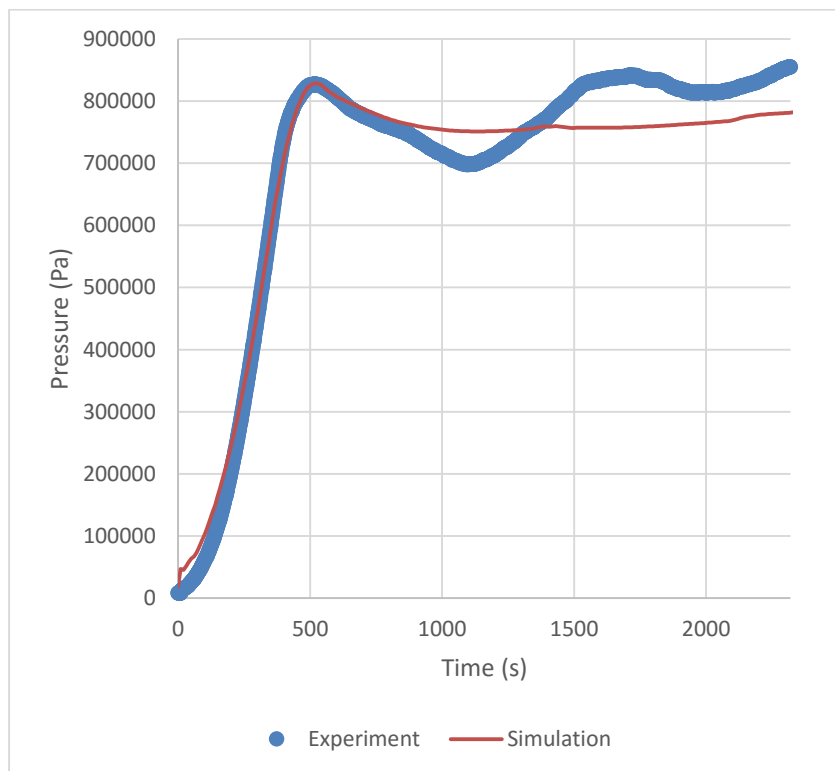


Figure A-58 Containment Pressure for Test 2.2

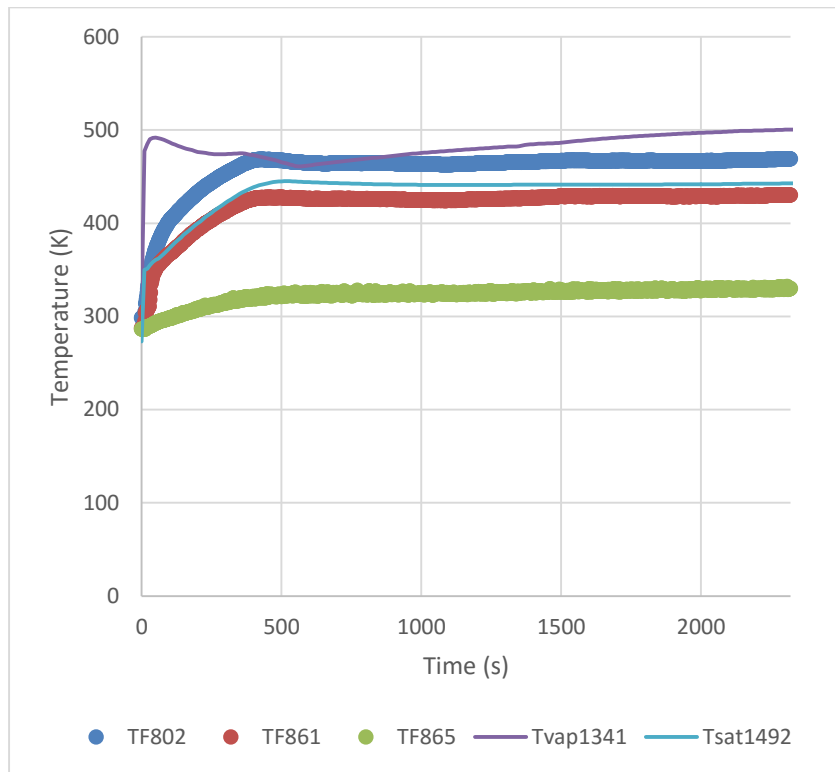


Figure A-59 Containment Temperature for Test 2.2

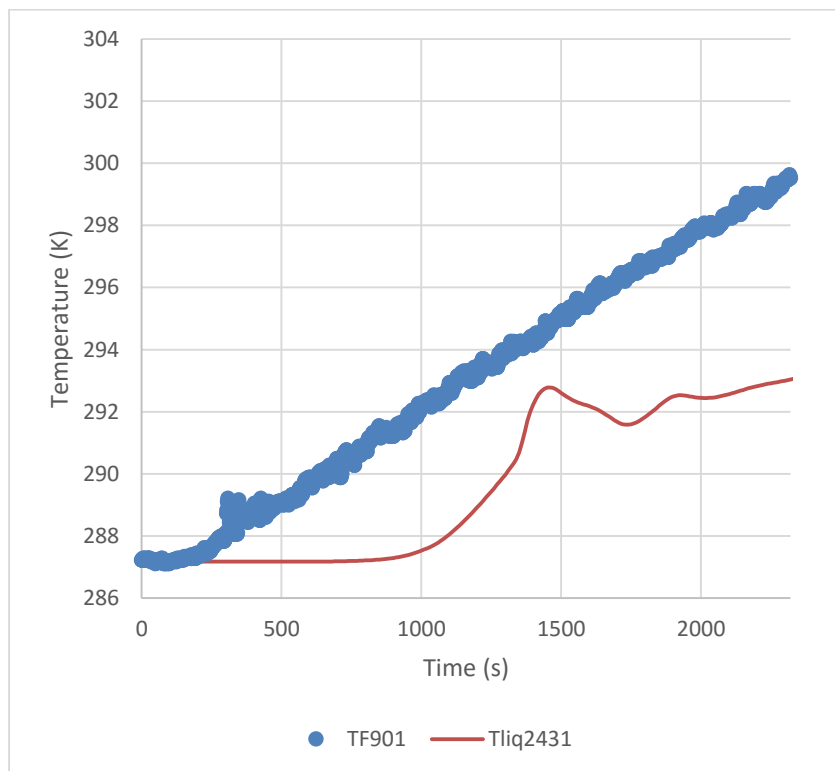


Figure A-60 CPV Temperature for Test 2.2

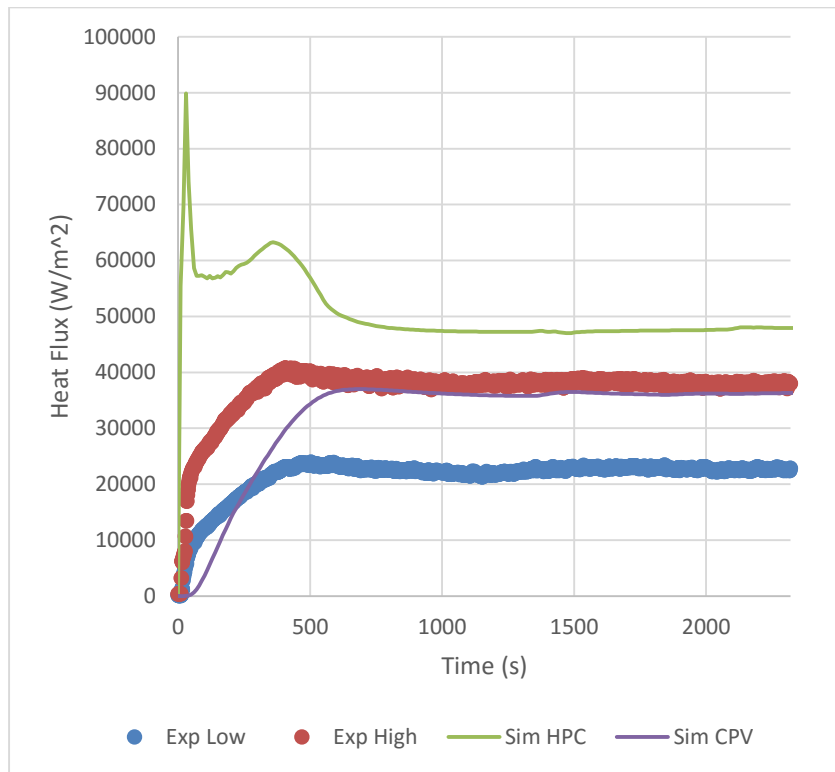


Figure A-61 Heat Flux at Location 6 for Test 2.2

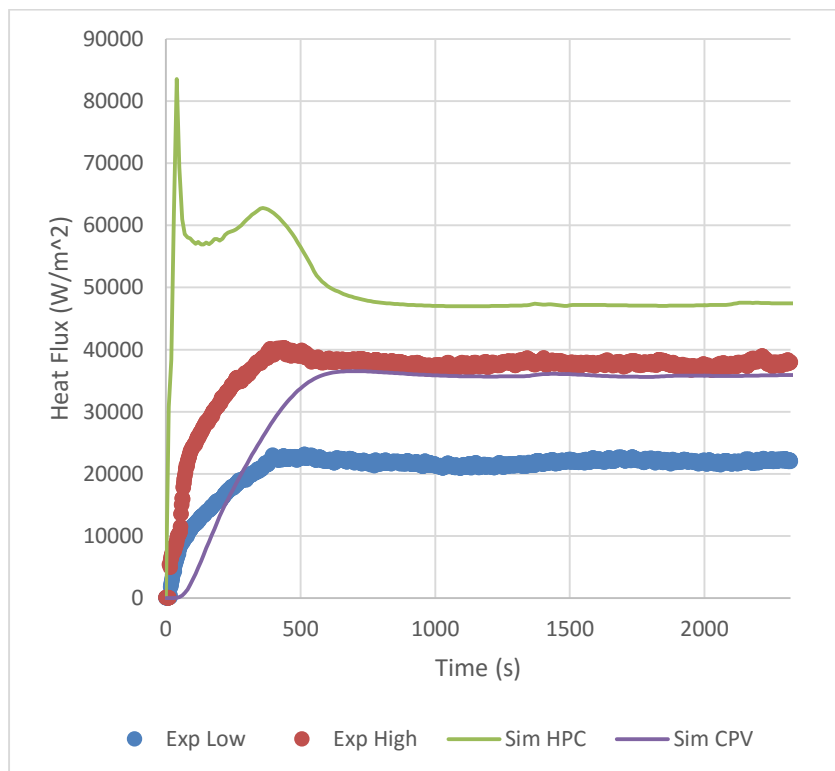


Figure A-62 Heat Flux at Location 5 for Test 2.2

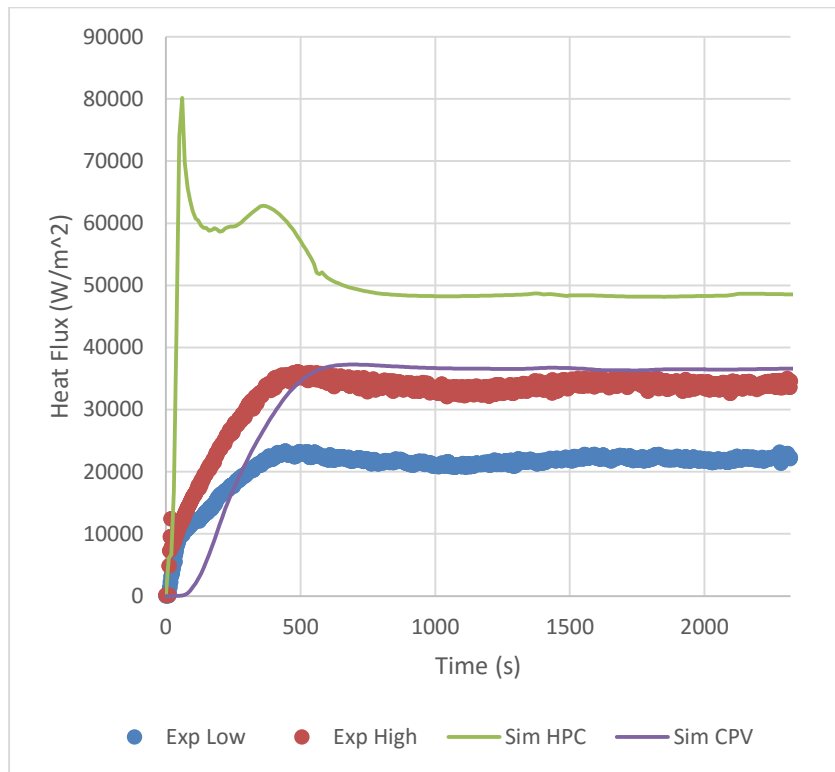


Figure A-63 Heat Flux at Location 4 for Test 2.2

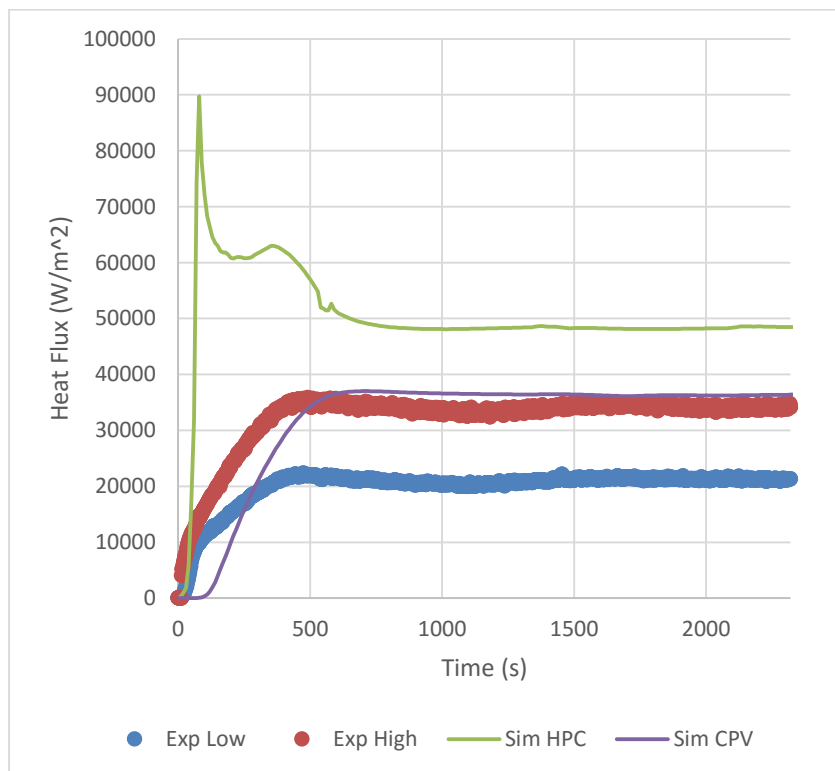


Figure A-64 Heat Flux at Location 3 for Test 2.2

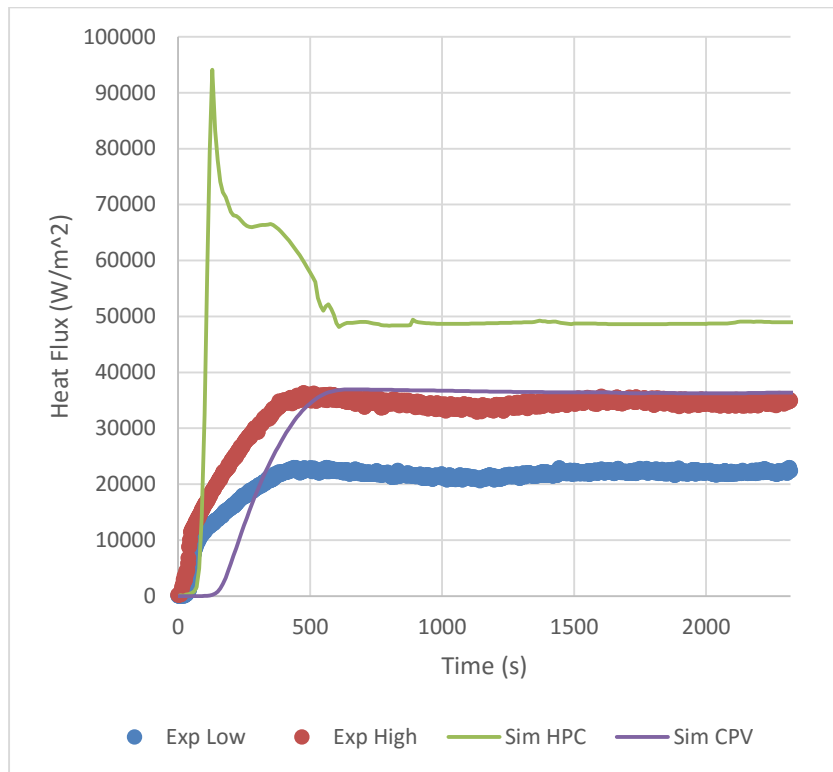


Figure A-65 Heat Flux at Location 2 for Test 2.2

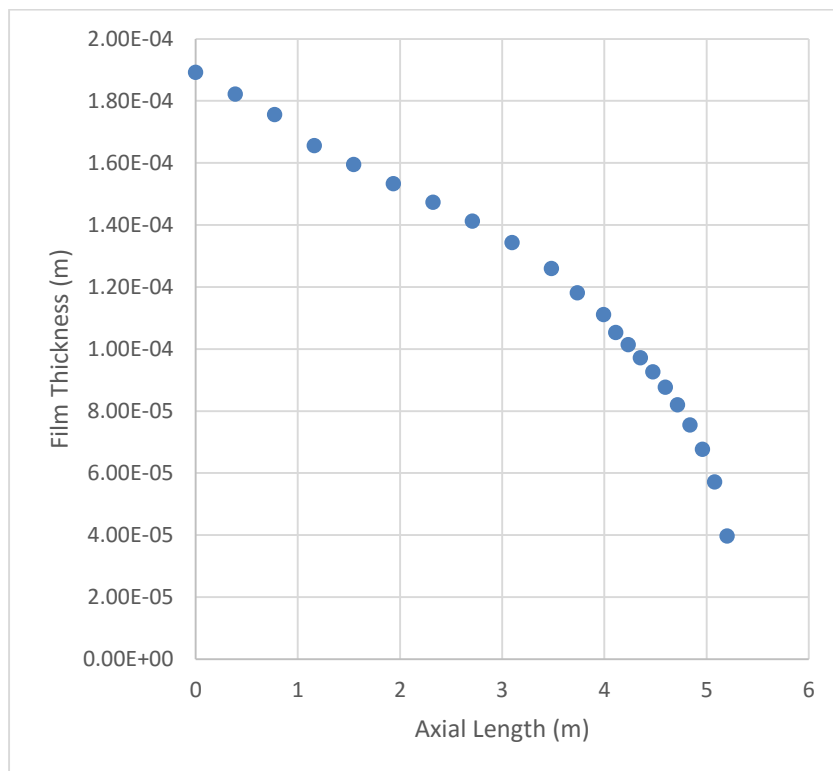


Figure A-66 Steady State Film Thickness for Test 2.2

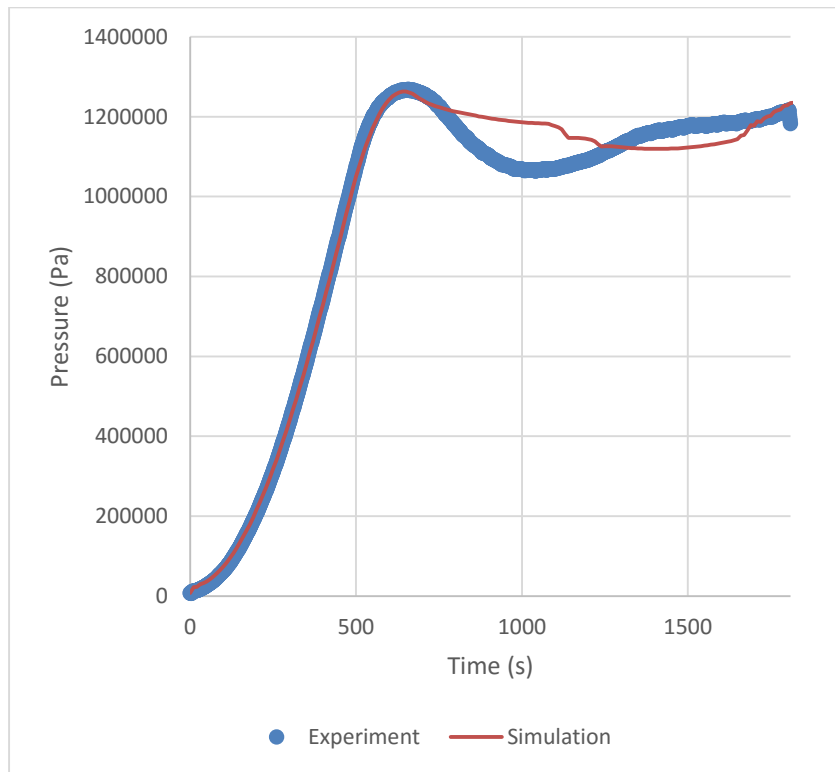


Figure A-67 Containment Pressure for Test 2.3

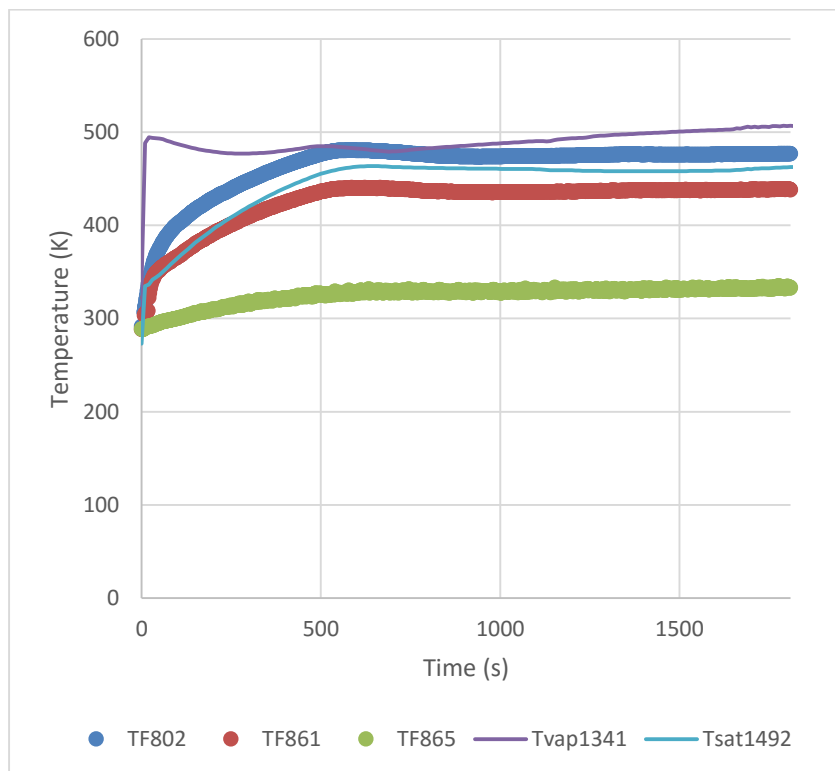


Figure A-68 Containment Temperature for Test 2.3

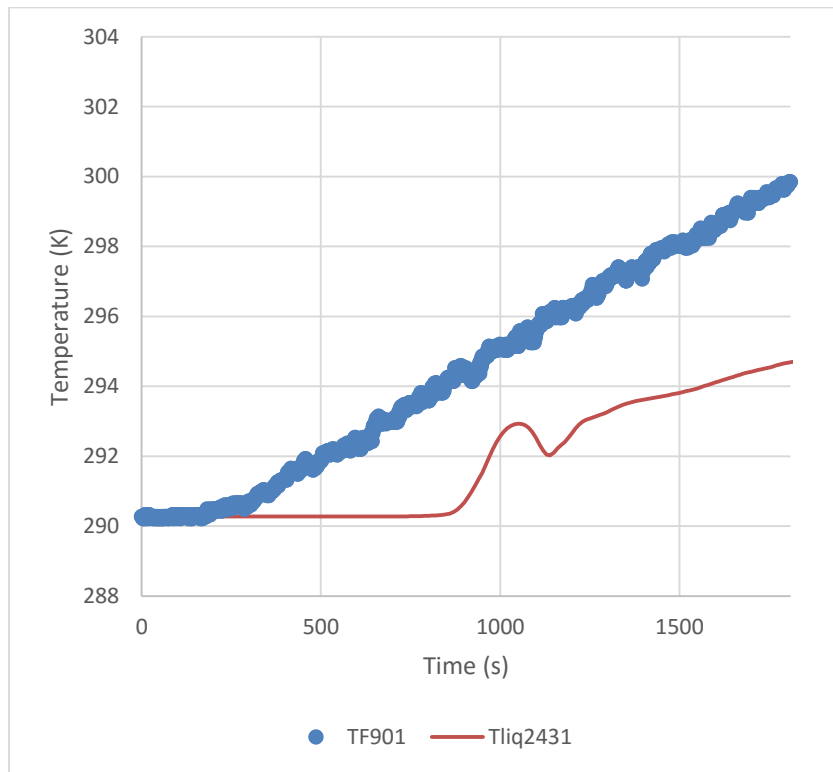


Figure A-69 CPV Temperature for Test 2.3

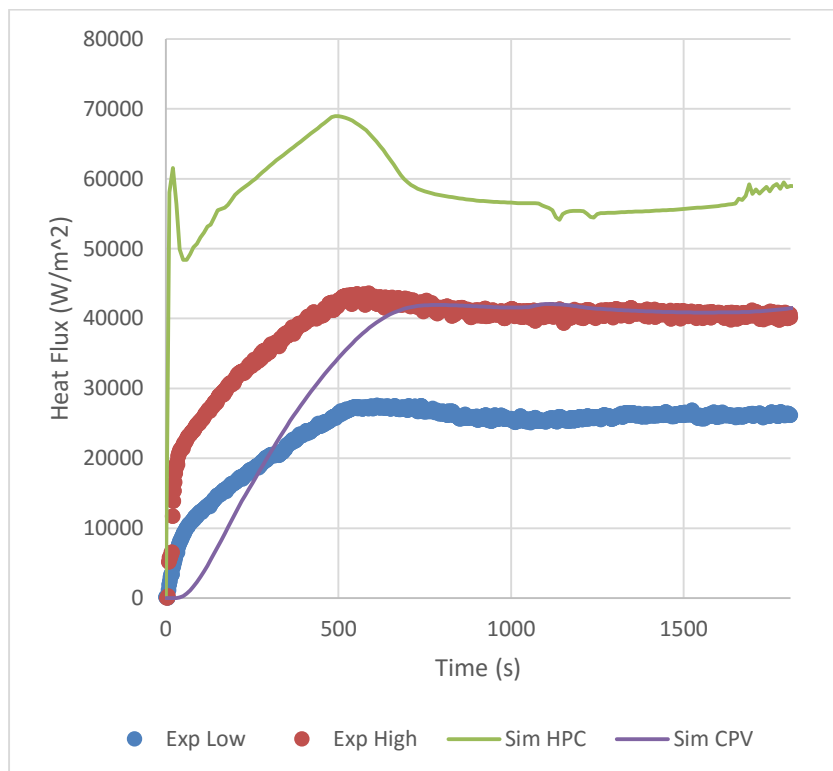


Figure A-70 Heat Flux at Location 6 for Test 2.3

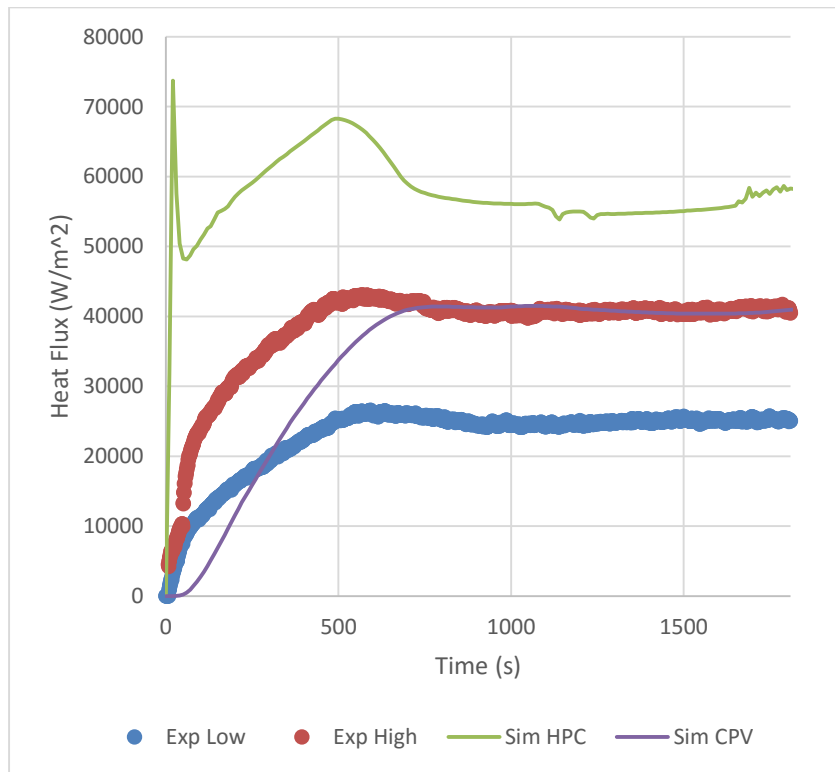


Figure A-71 Heat Flux at Location 5 for Test 2.3

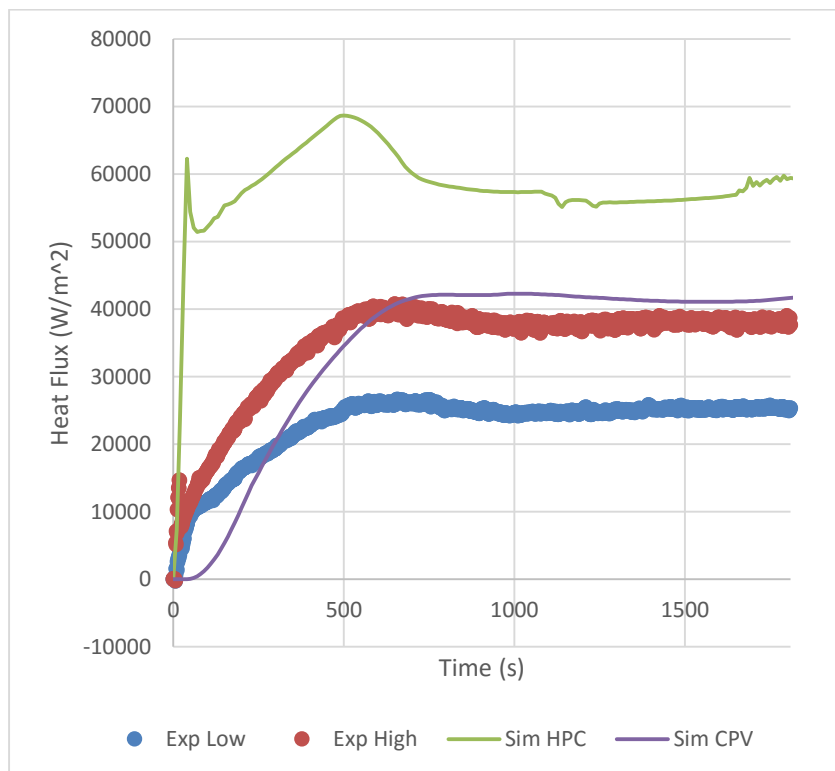


Figure A-72 Heat Flux at Location 4 for Test 2.3

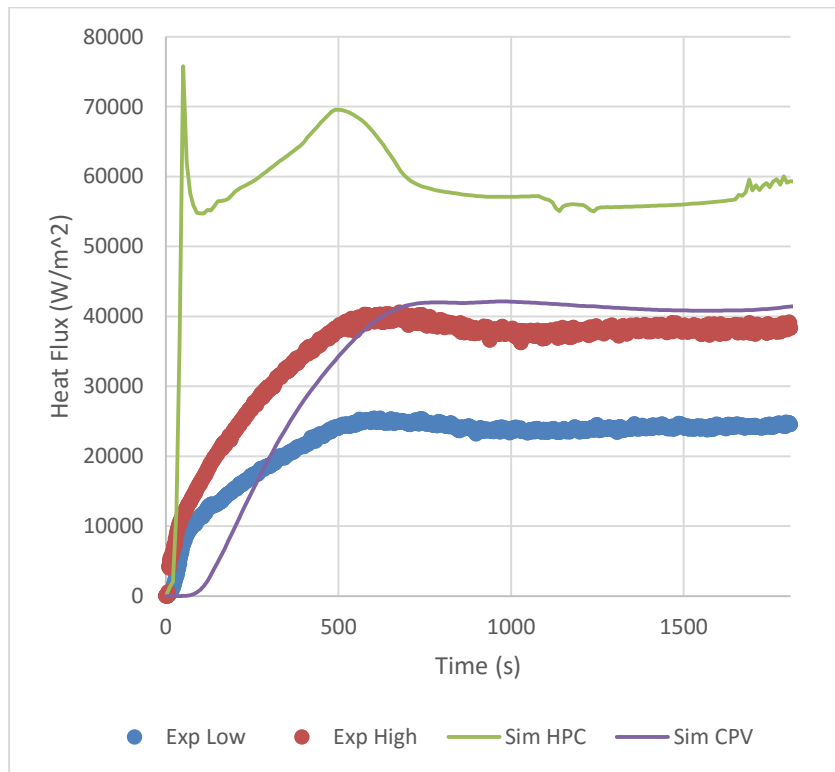


Figure A-73 Heat Flux at Location 3 for Test 2.3

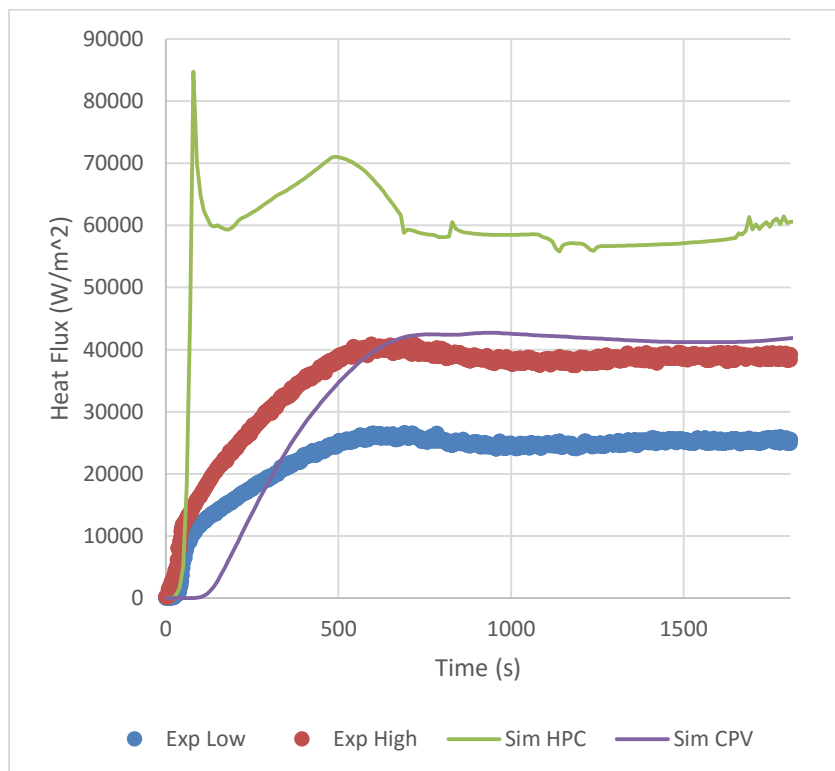


Figure A-74 Heat Flux at Location 2 for Test 2.3

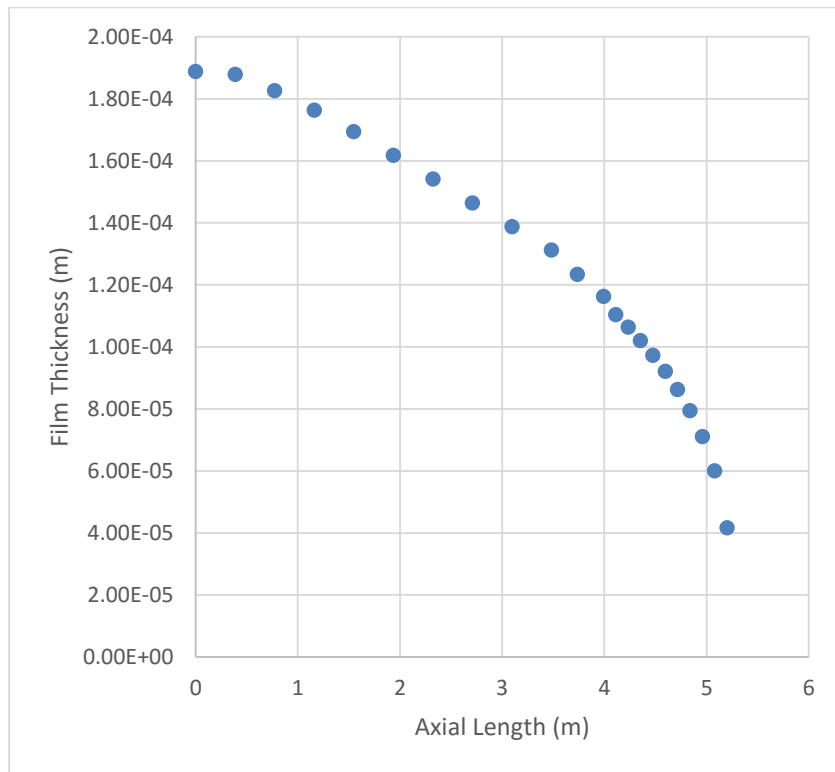


Figure A-75 Steady State Film Thickness for Test 2.3

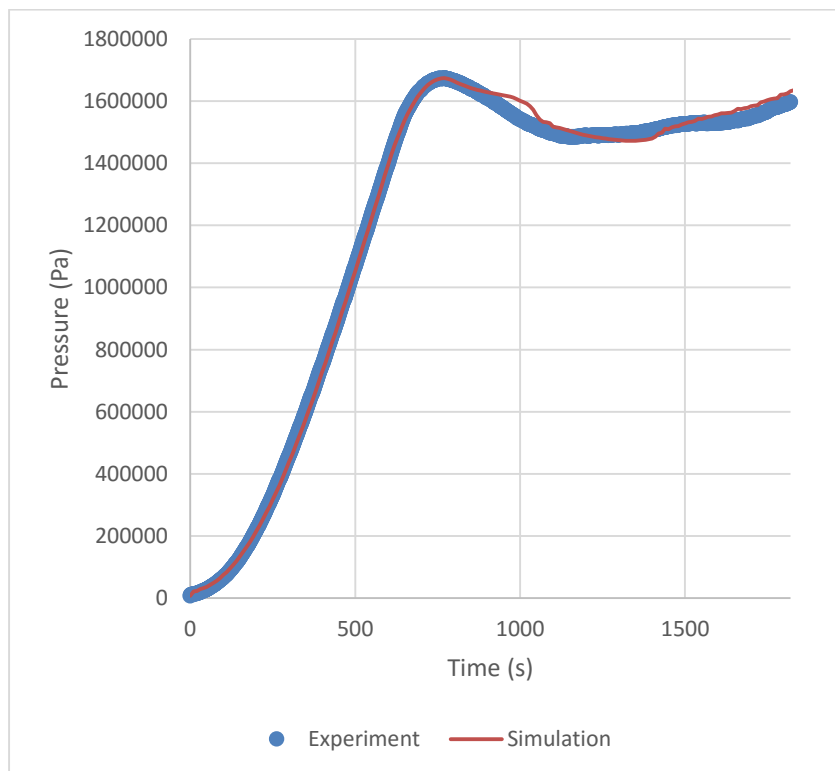


Figure A-76 Containment Pressure for Test 2.4

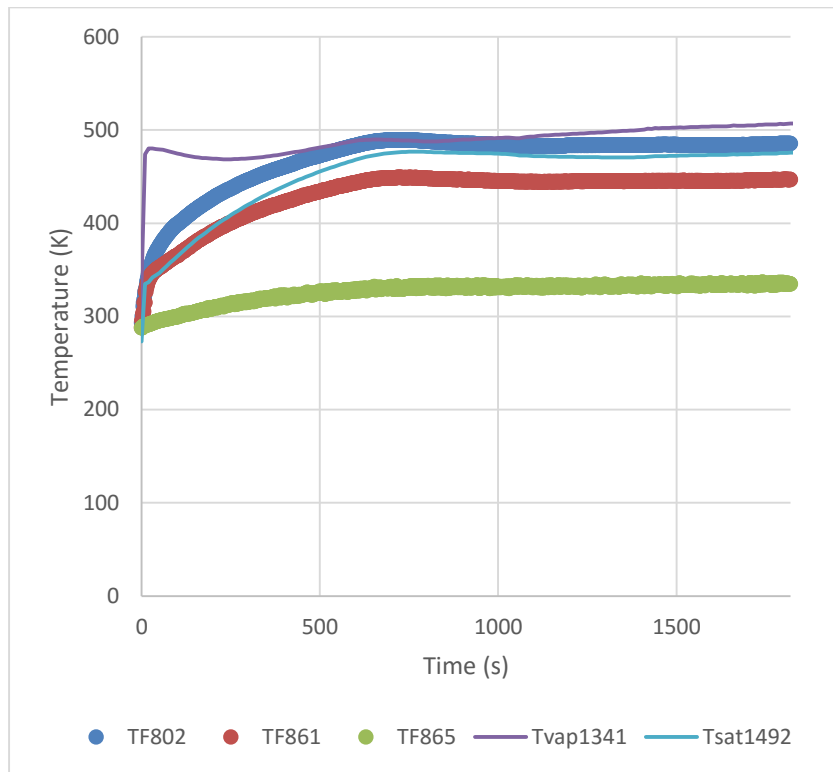


Figure A-77 Containment Temperature for Test 2.4

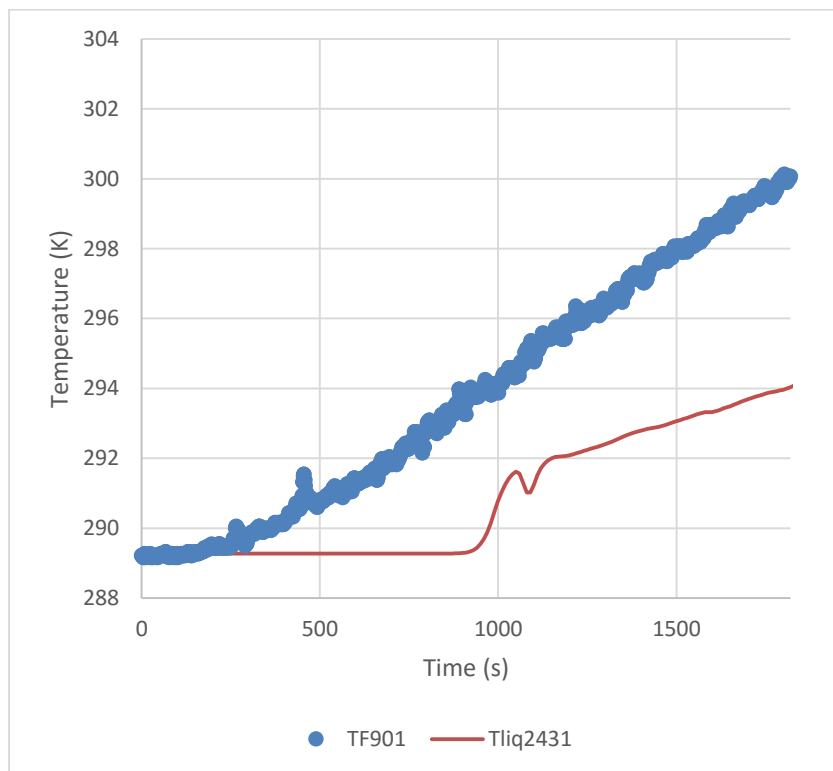


Figure A-78 CPV Temperature for Test 2.4

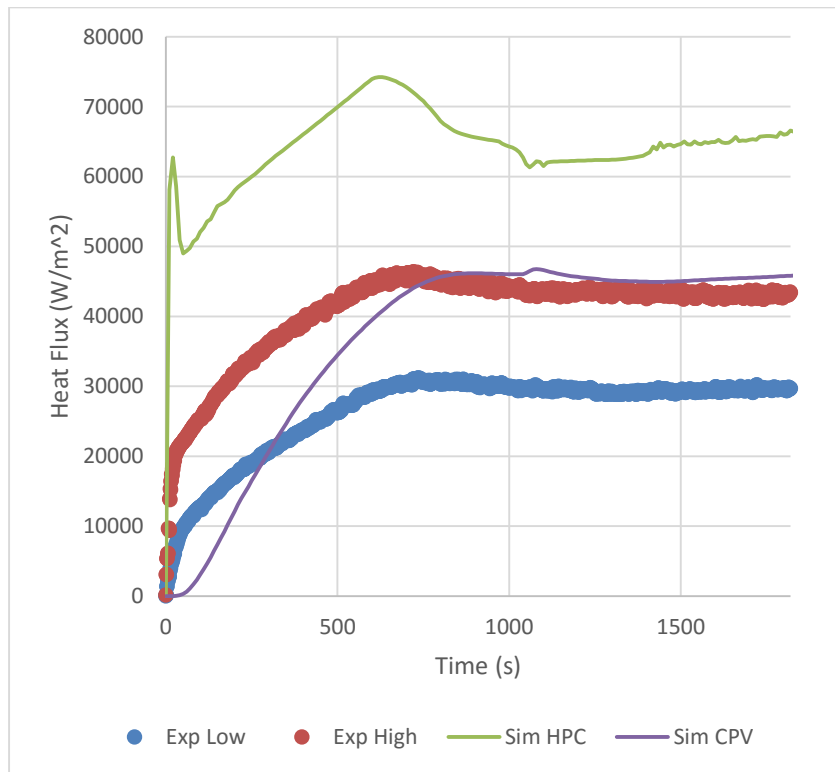


Figure A-79 Heat Flux at Location 6 for Test 2.4

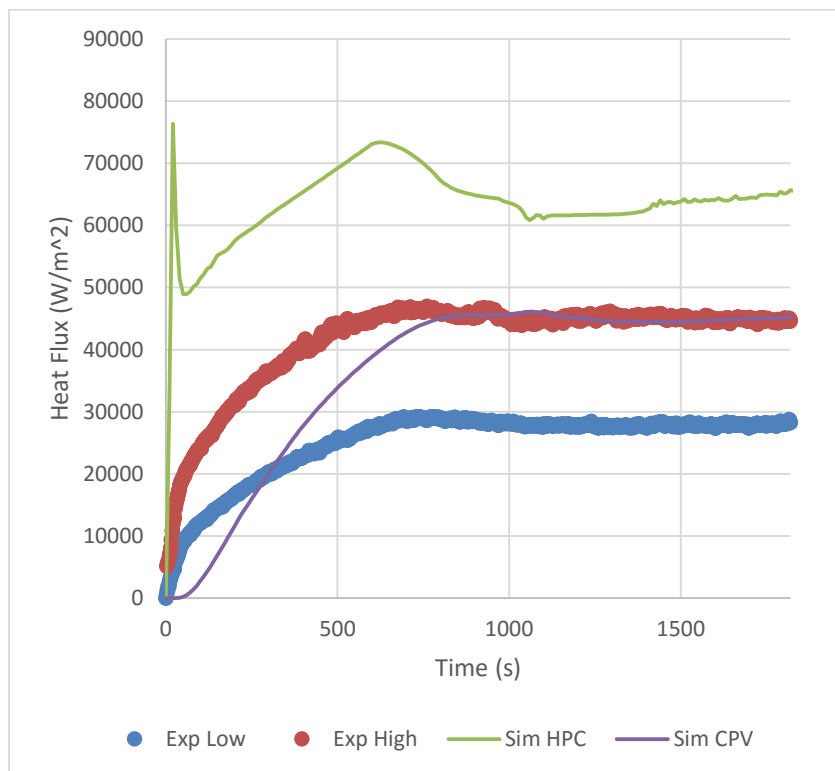


Figure A-80 Heat Flux at Location 5 for Test 2.4

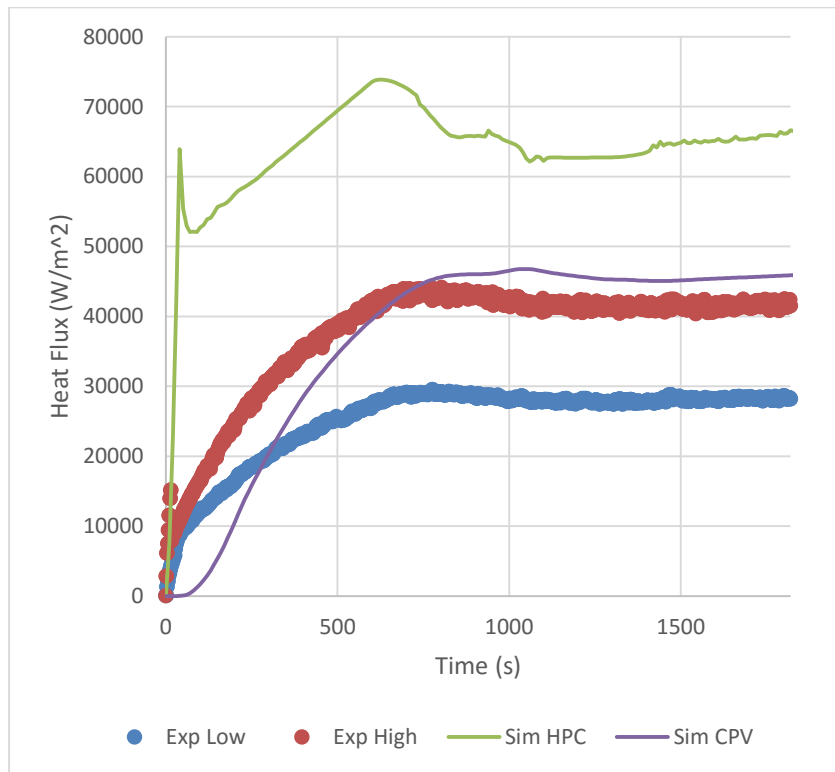


Figure A-81 Heat Flux at Location 4 for Test 2.4

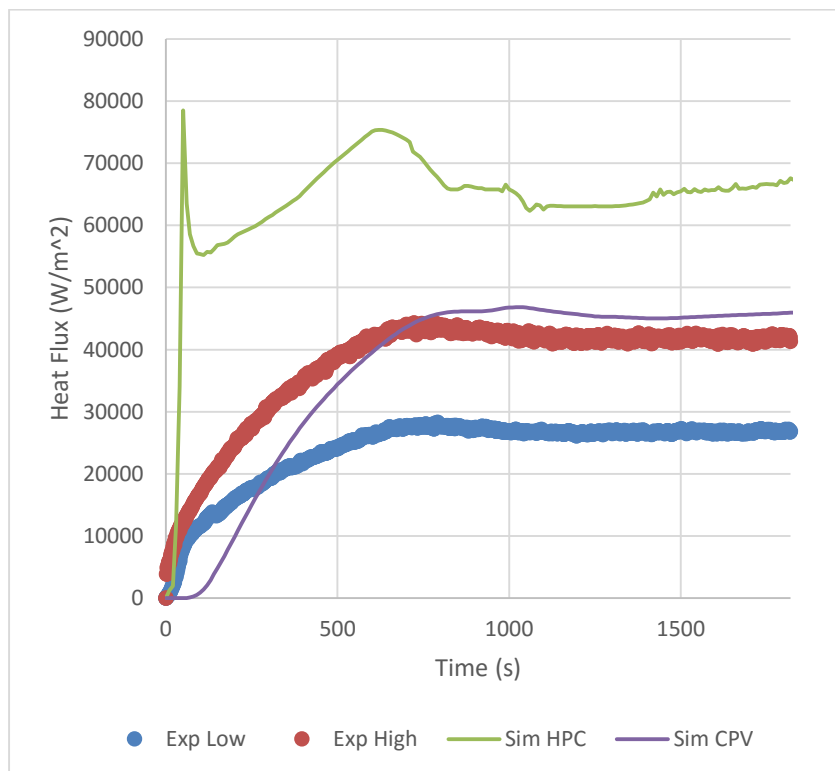


Figure A-82 Heat Flux at Location 3 for Test 2.4

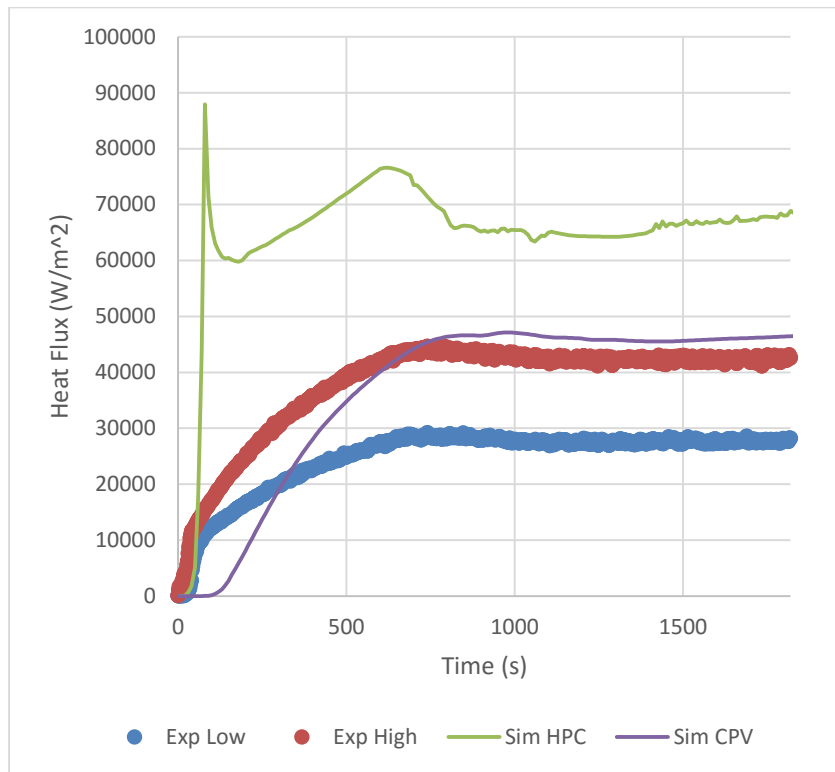


Figure A-83 Heat Flux at Location 2 for Test 2.4

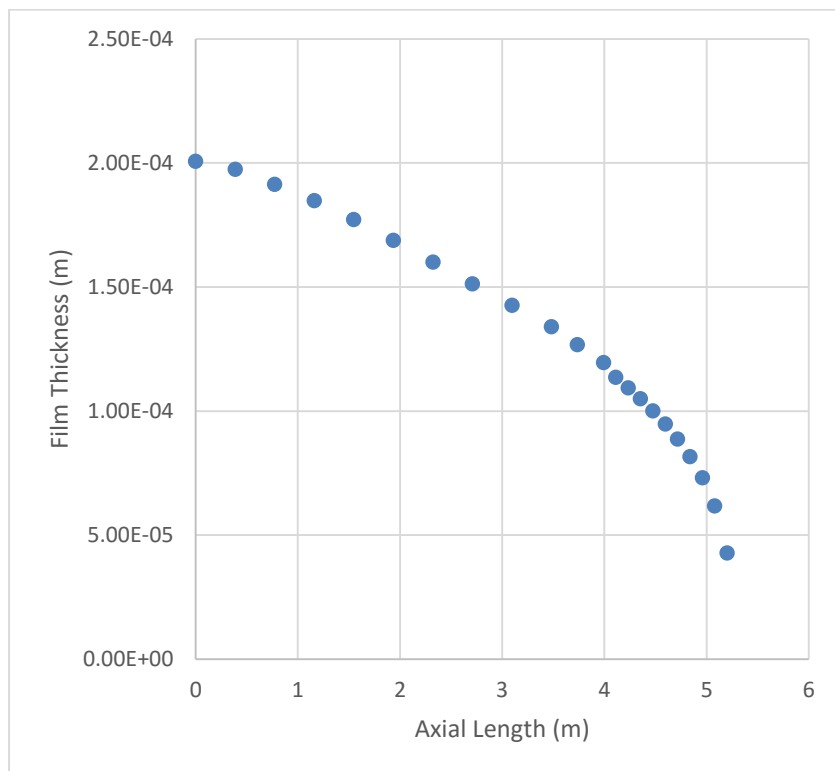


Figure A-84 Steady State Film Thickness for Test 2.4

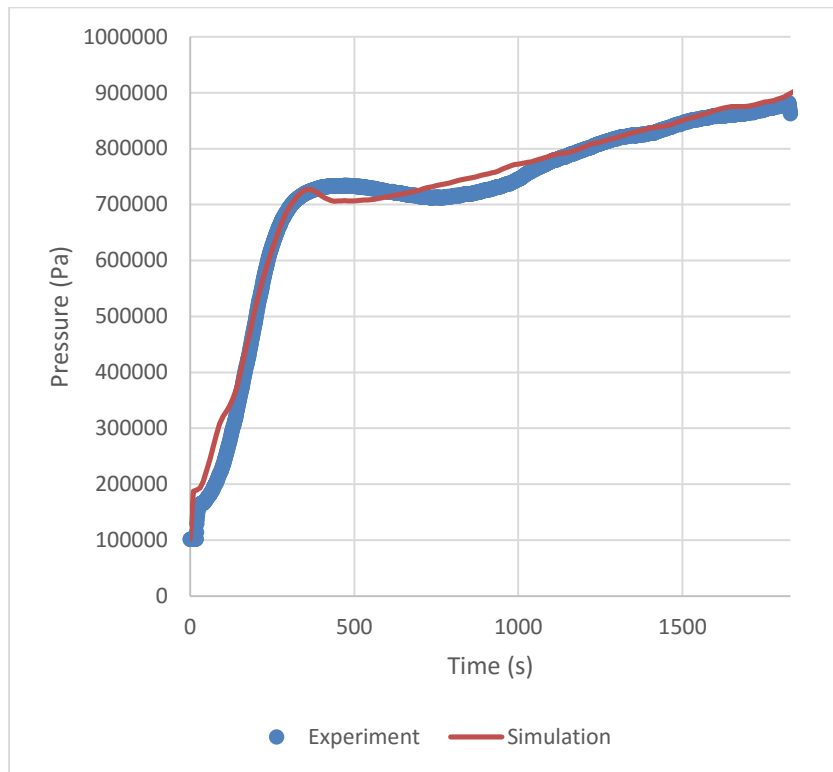


Figure A-85 Containment Pressure for Test 2.5

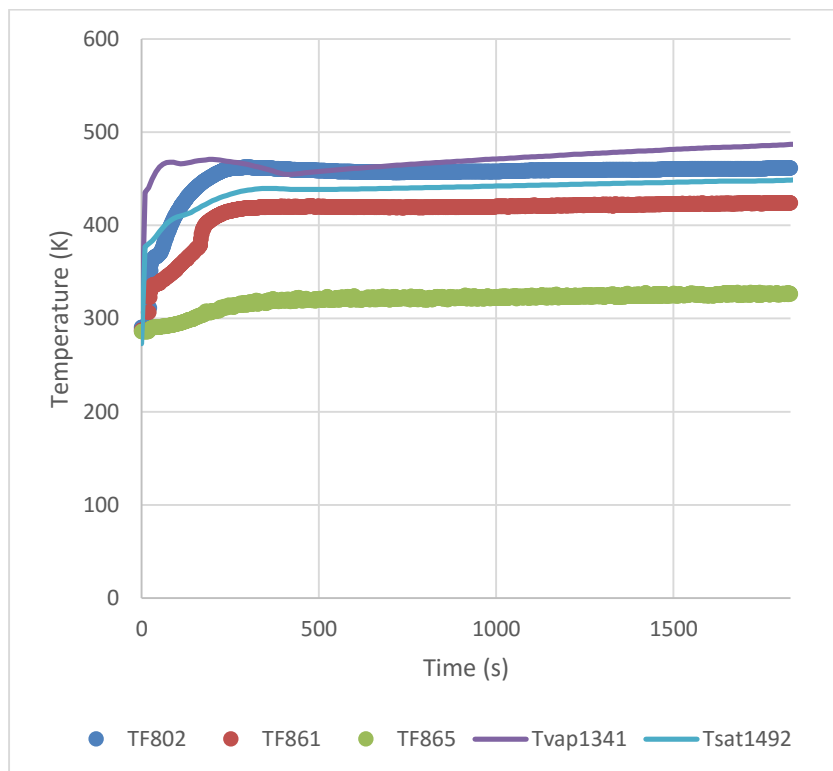


Figure A-86 Containment Temperature for Test 2.5

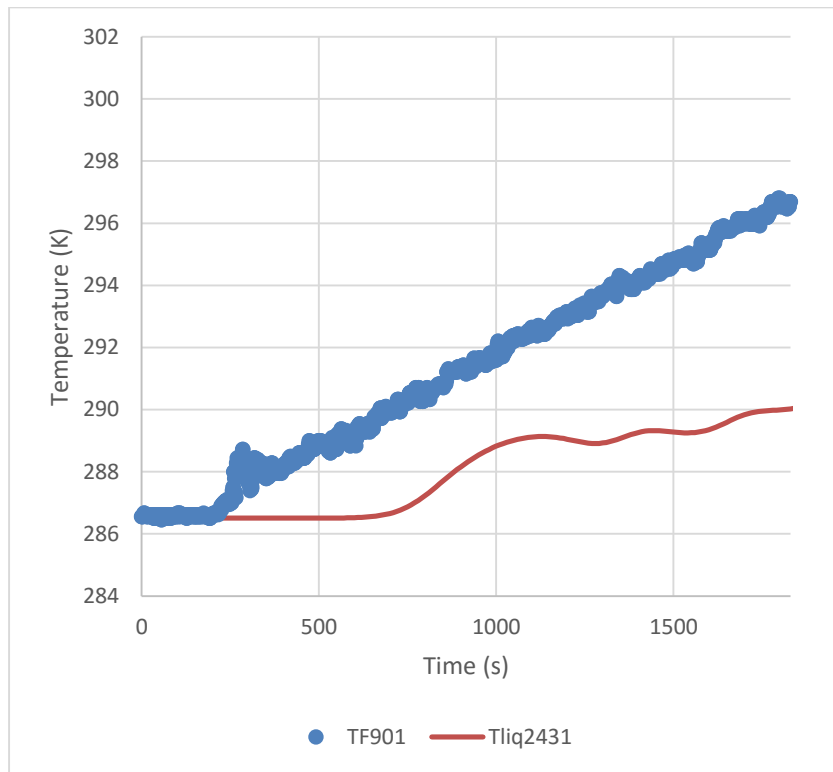


Figure A-87 CPV Temperature for Test 2.5

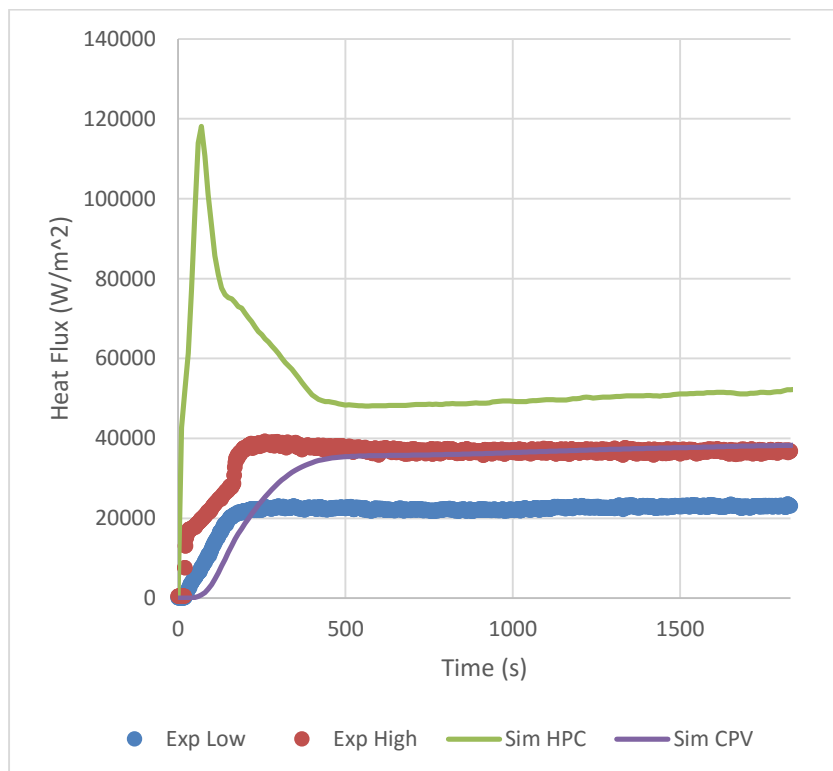


Figure A-88 Heat Flux at Location 6 for Test 2.5

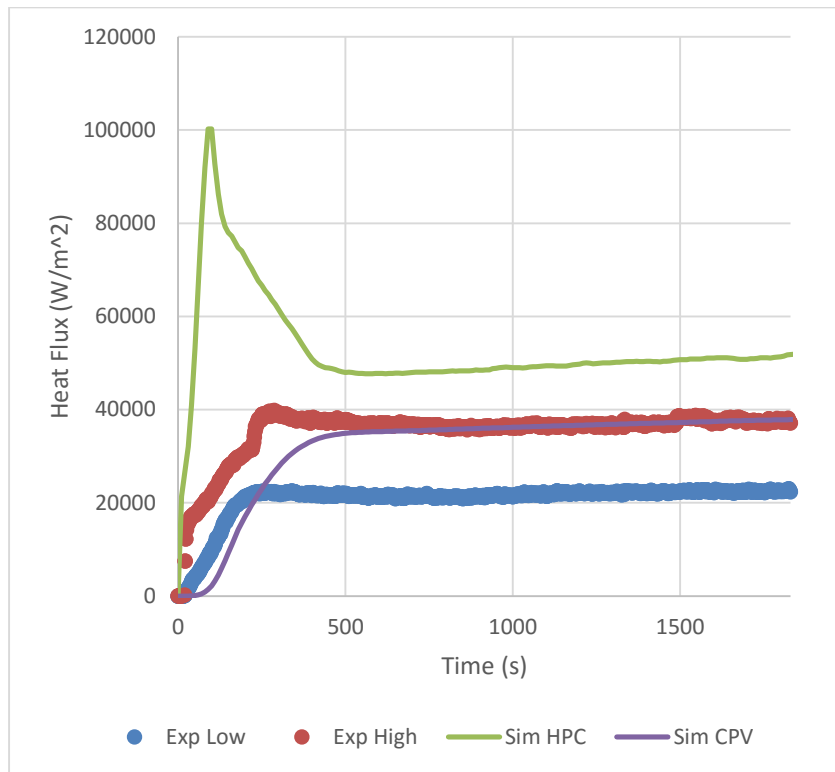


Figure A-89 Heat Flux at Location 5 for Test 2.5

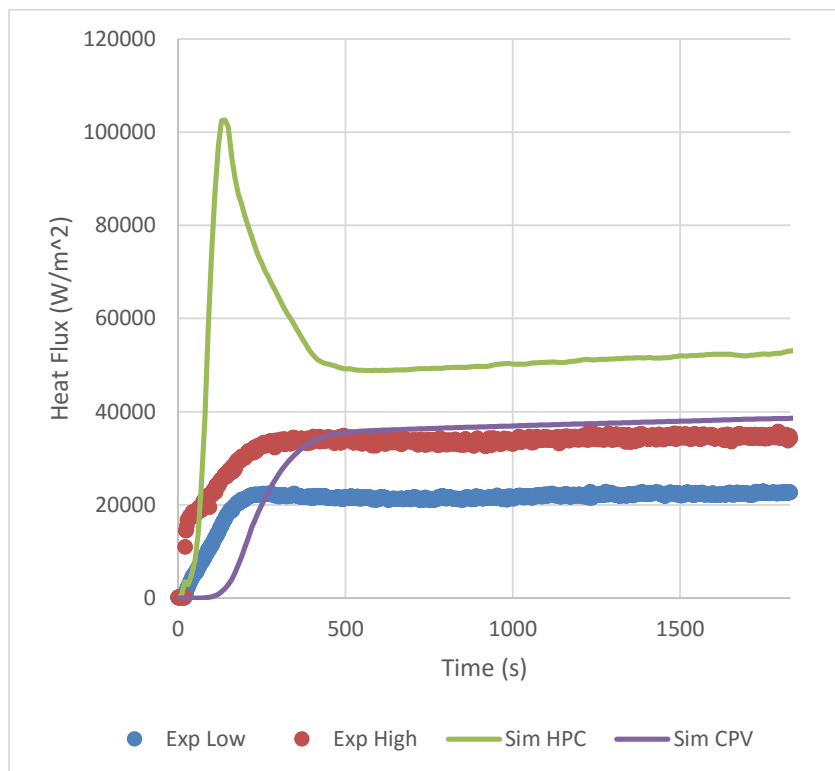


Figure A-90 Heat Flux at Location 4 for Test 2.5

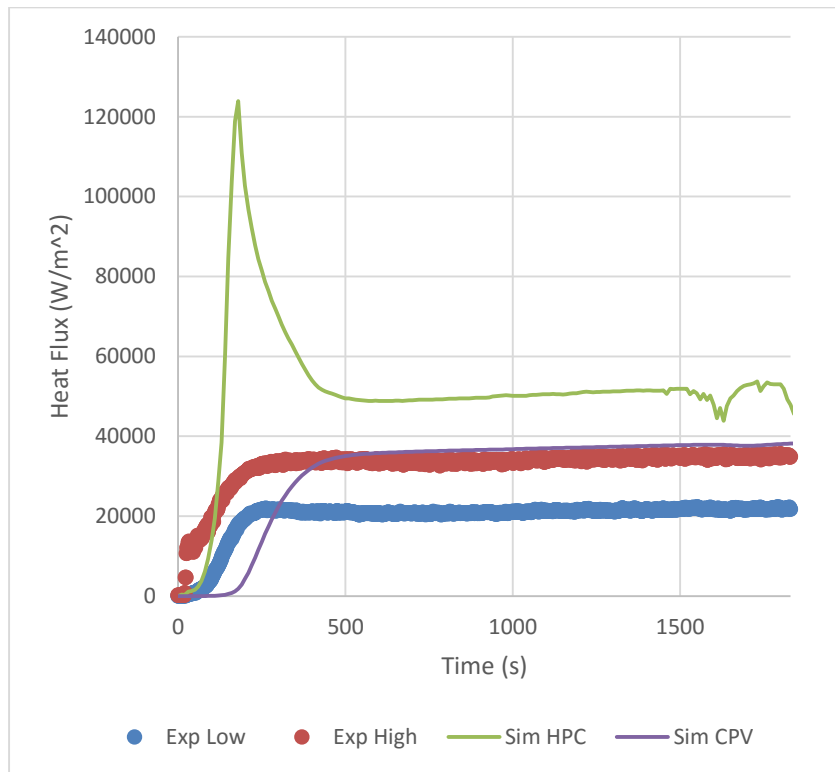


Figure A-91 Heat Flux at Location 3 for Test 2.5

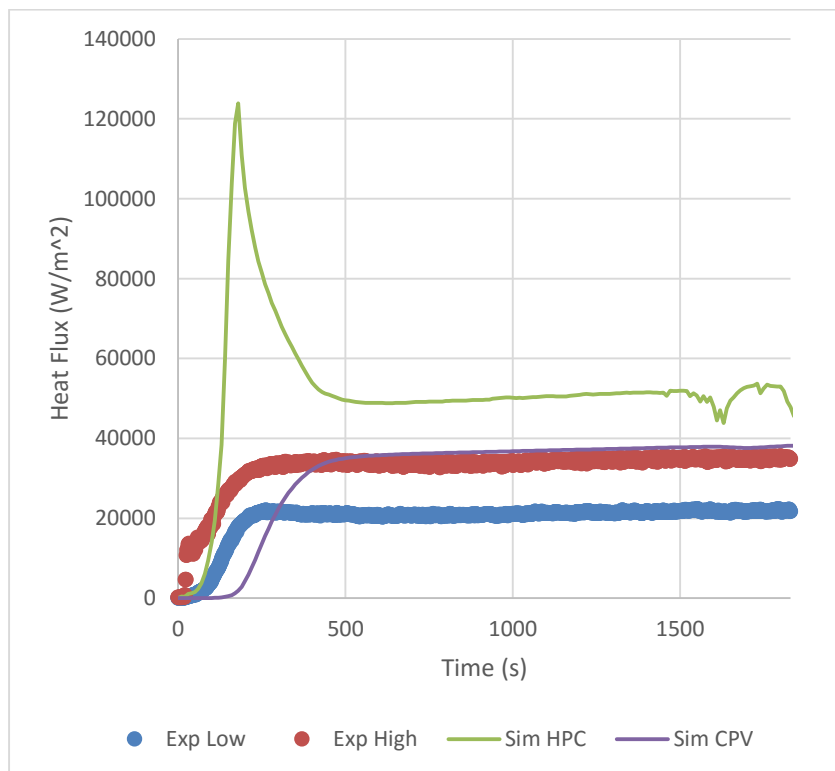


Figure A-92 Heat Flux at Location 2 for Test 2.5

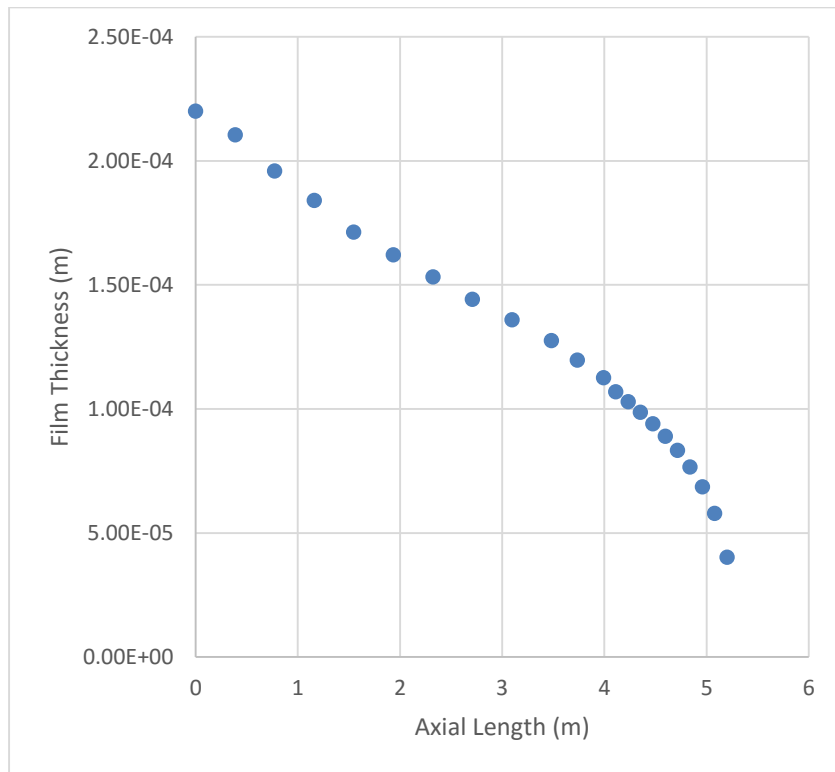


Figure A-93 Steady State Film Thickness for Test 2.5

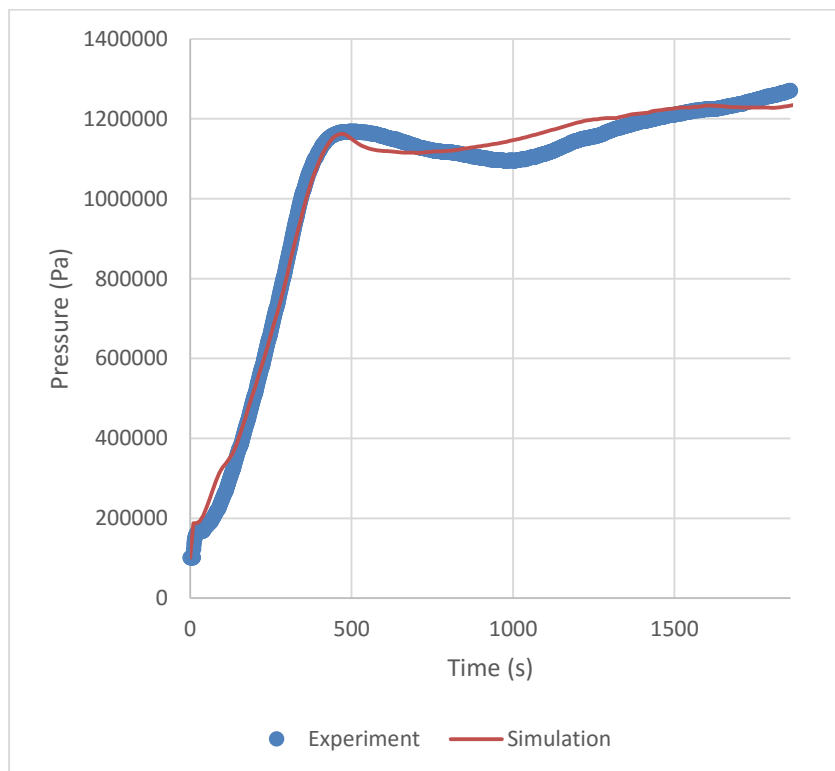


Figure A-94 Containment Pressure for Test 2.6

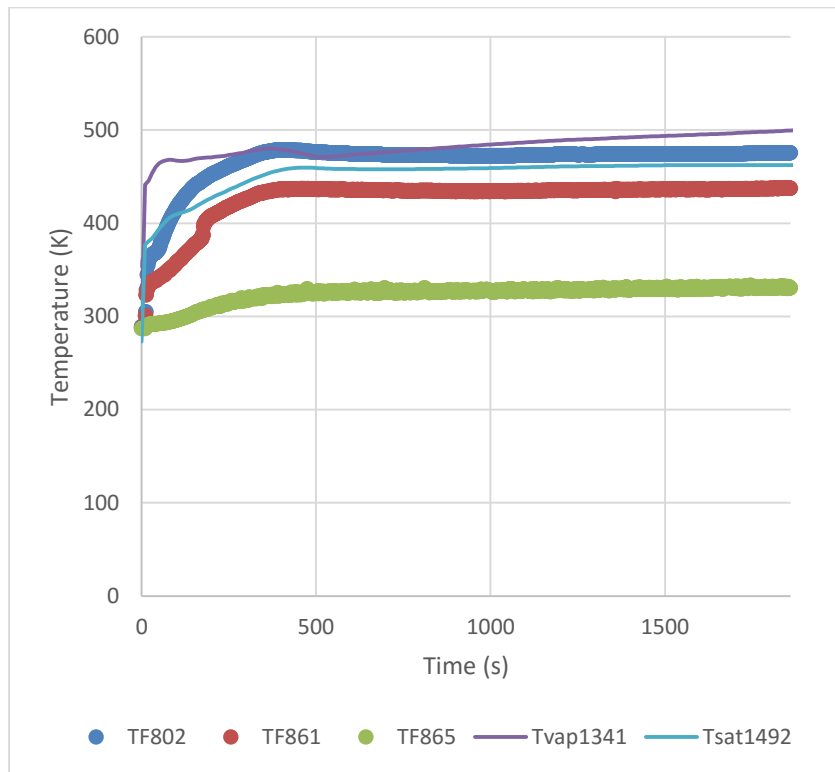


Figure A-95 Containment Temperature for Test 2.6

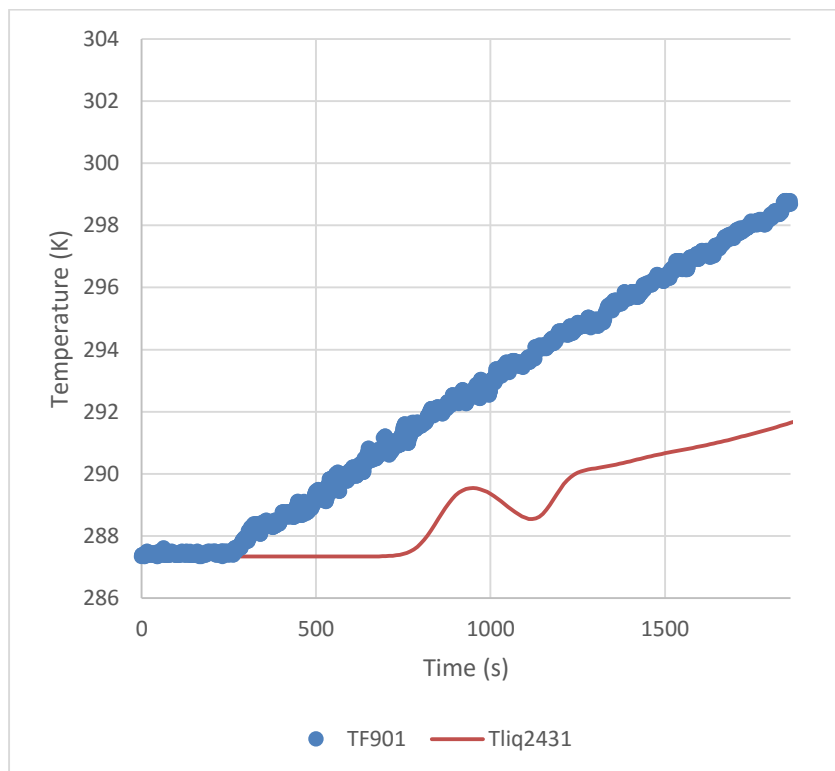


Figure A-96 CPV Temperature for Test 2.6

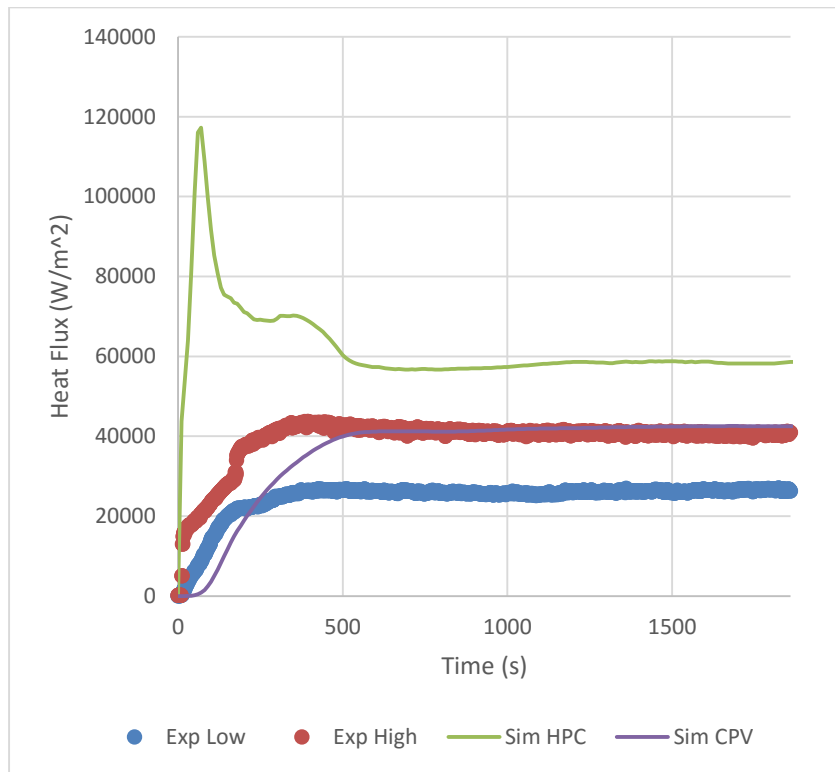


Figure A-97 Heat Flux at Location 6 for Test 2.6

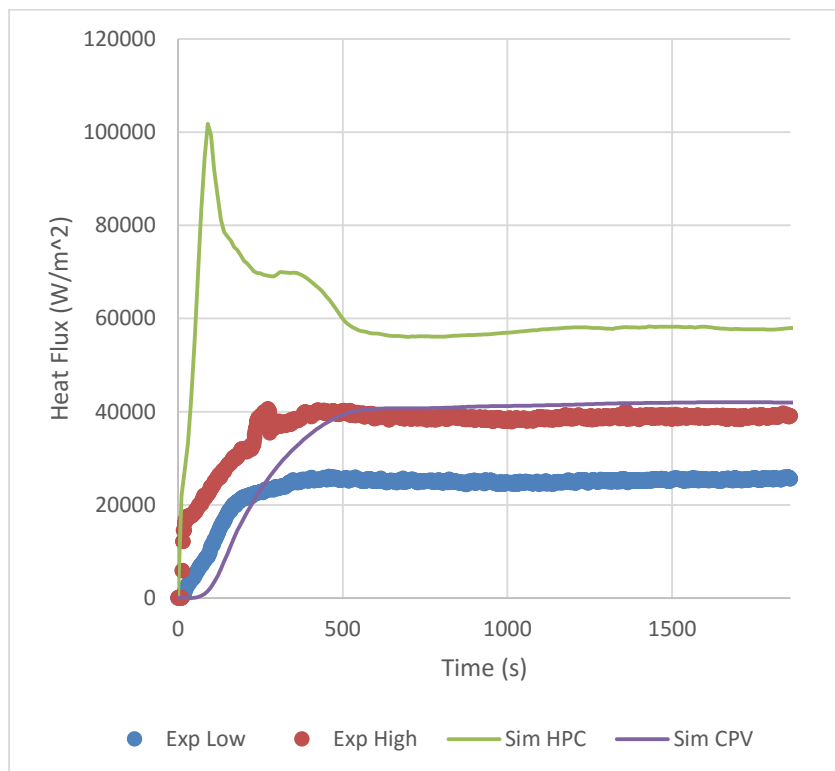


Figure A-98 Heat Flux at Location 5 for Test 2.6

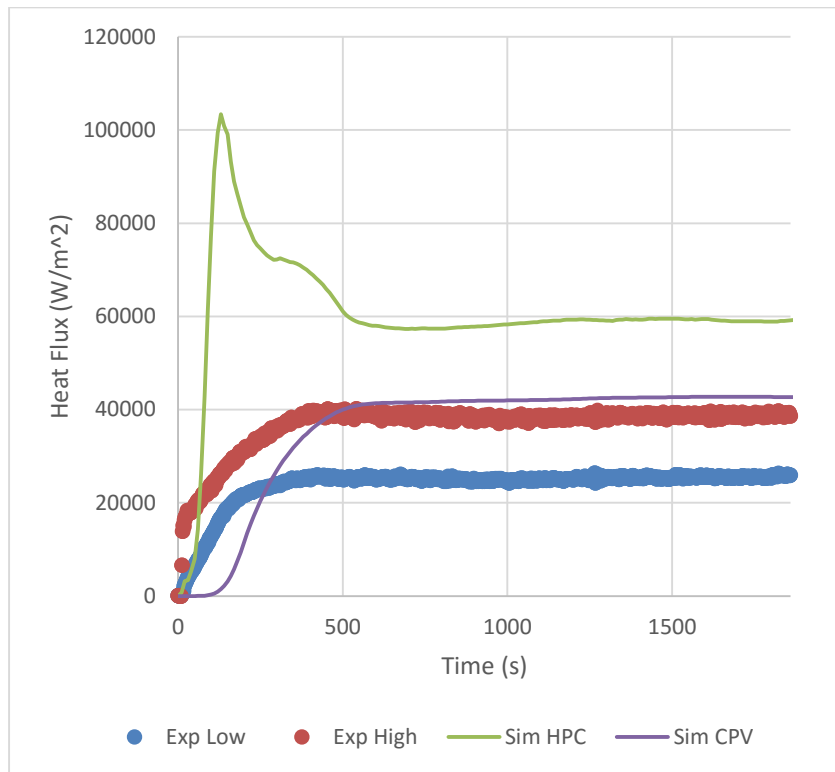


Figure A-99 Heat Flux at Location 4 for Test 2.6

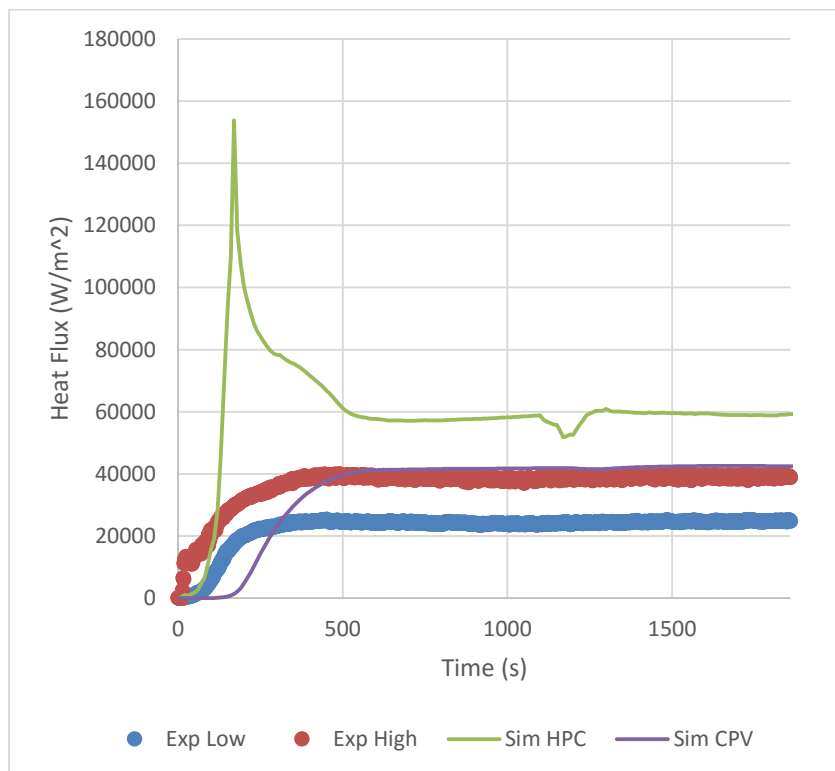


Figure A-100 Heat Flux at Location 3 for Test 2.6

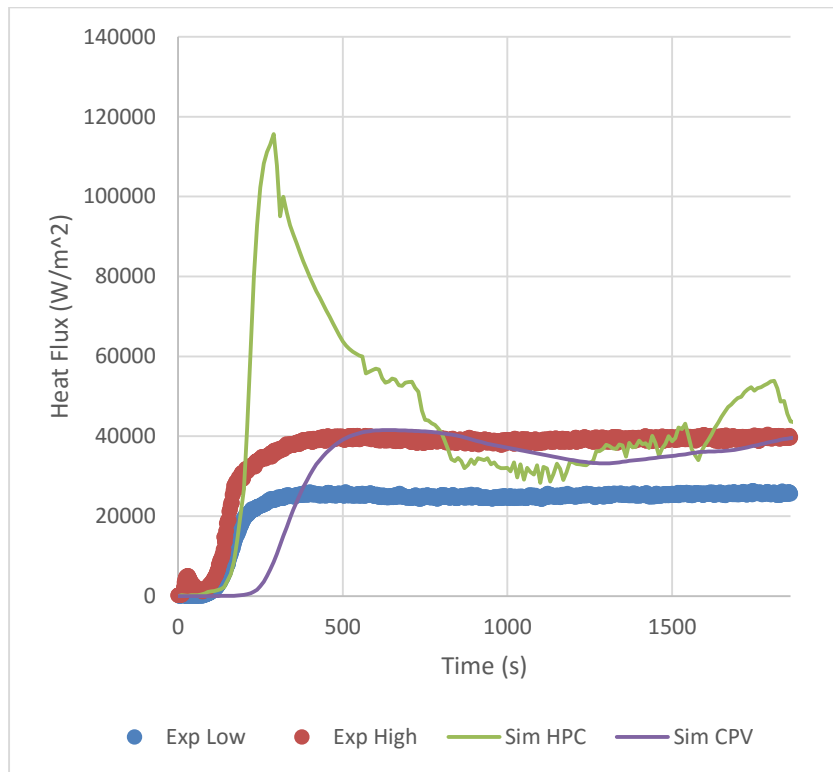


Figure A-101 Heat Flux at Location 2 for Test 2.6

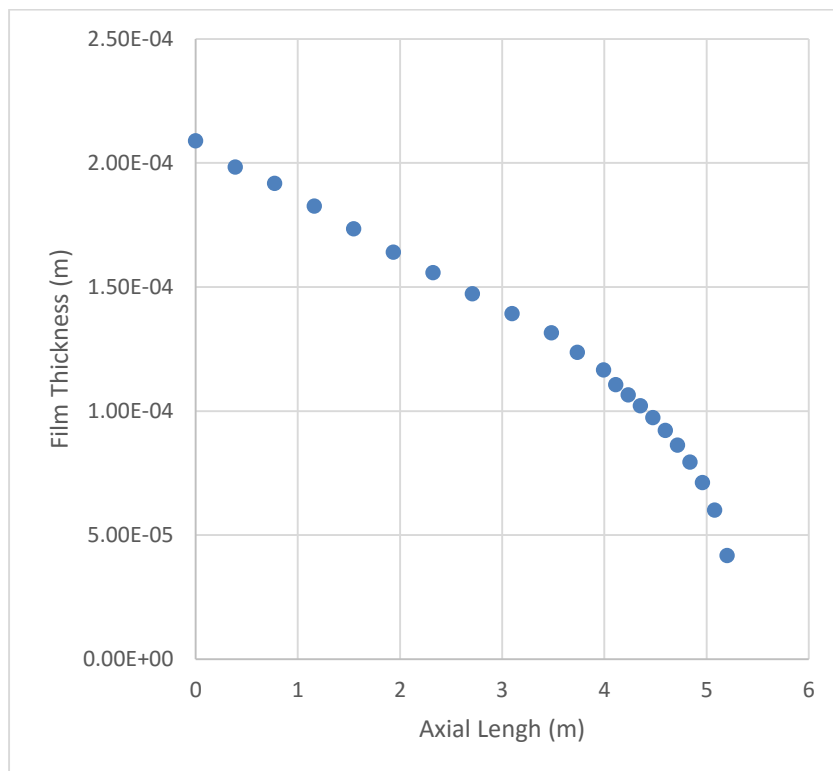


Figure A-102 Steady State Film Thickness for Test 2.6

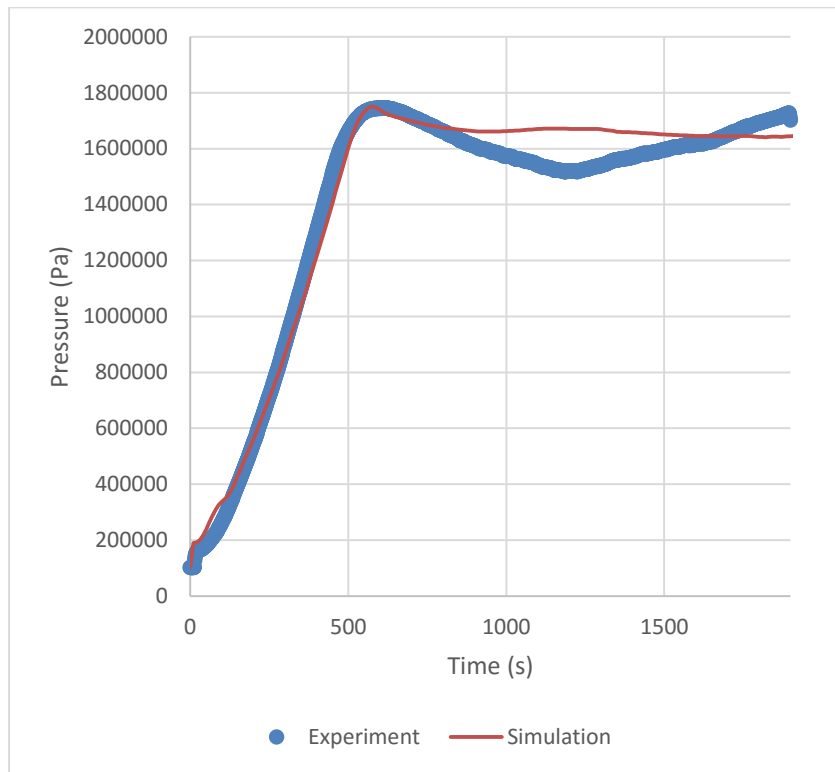


Figure A-103 Containment Pressure for Test 2.7

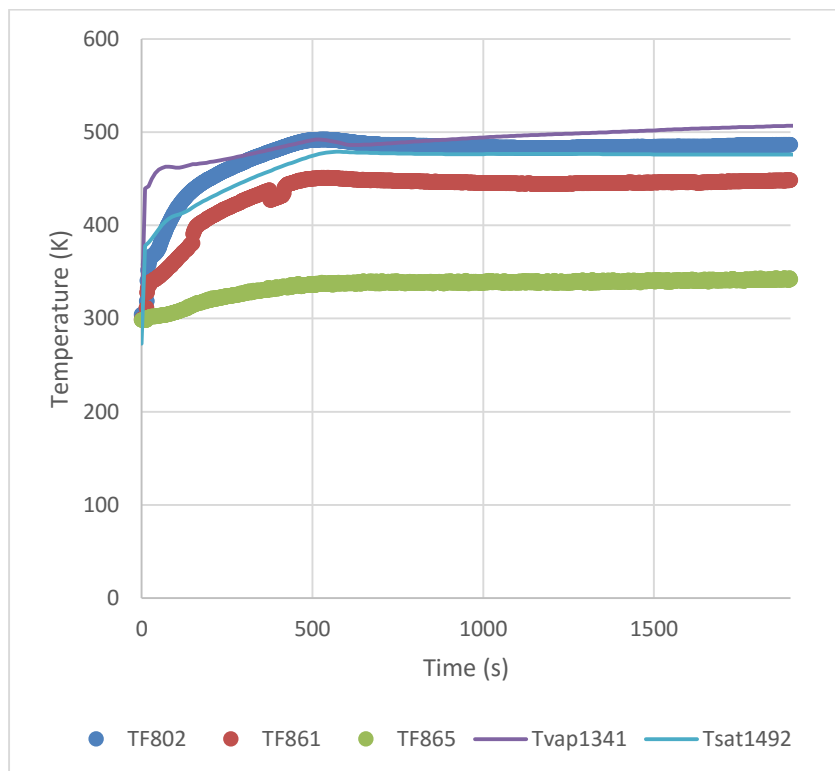


Figure A-104 Containment Temperature for Test 2.7

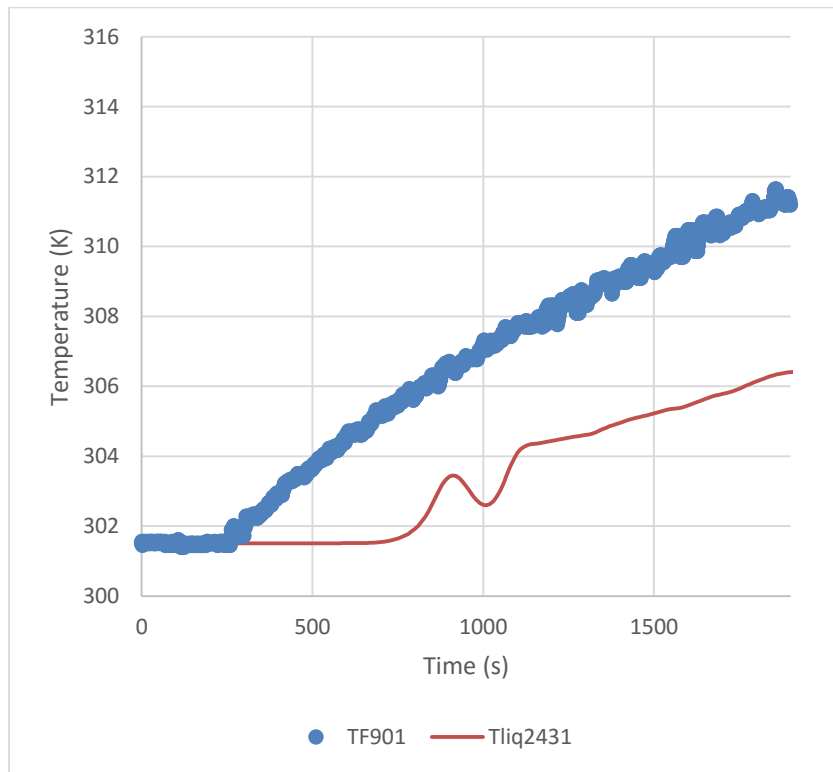


Figure A-105 CPV Temperature for Test 2.7

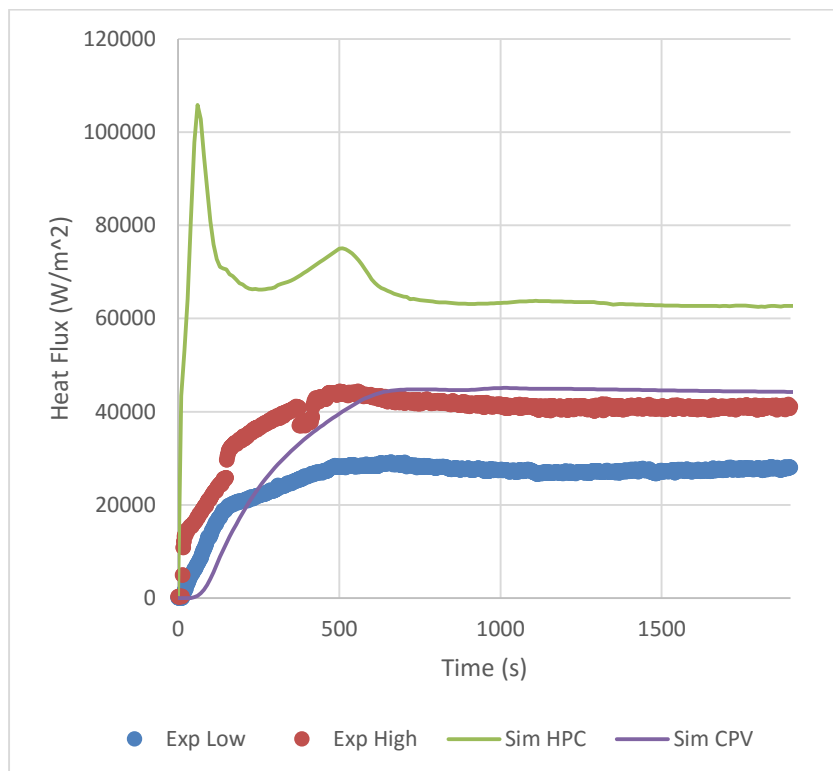


Figure A-106 Heat Flux at Location 6 for Test 2.7

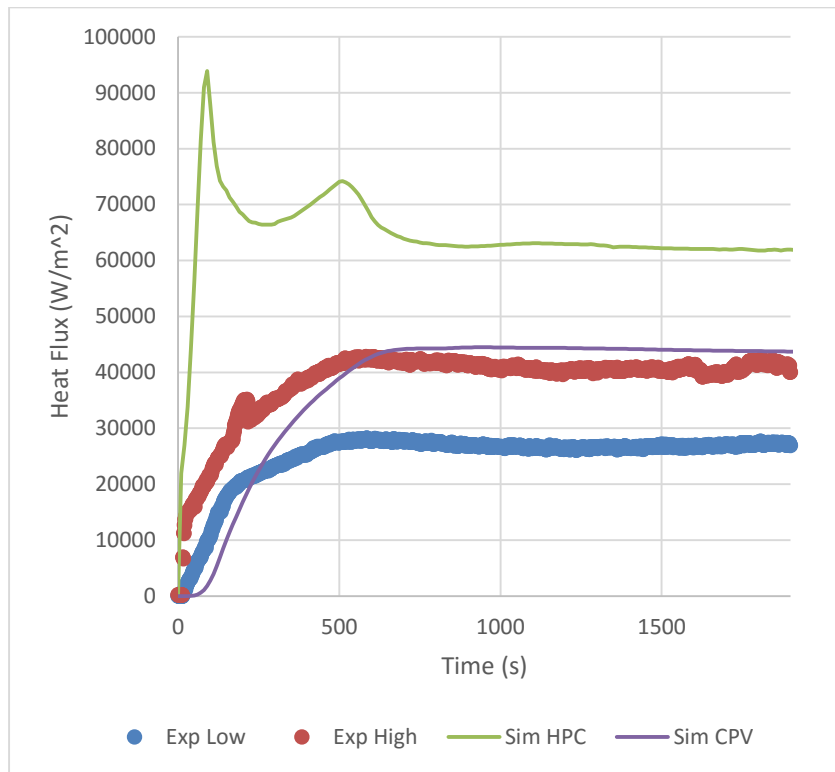


Figure A-107 Heat Flux at Location 5 for Test 2.7

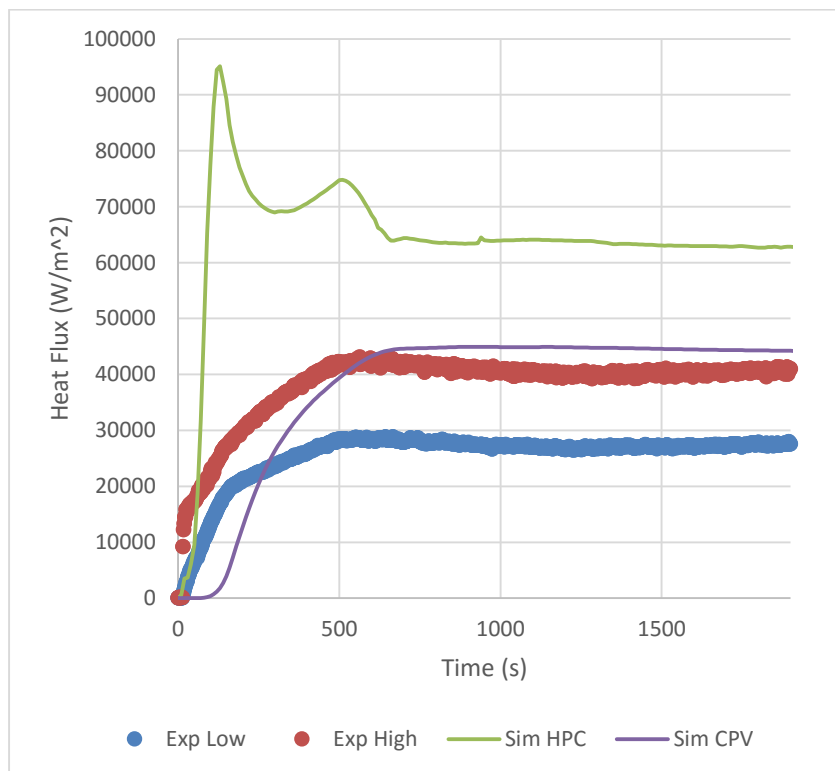


Figure A-108 Heat Flux at Location 4 for Test 2.7

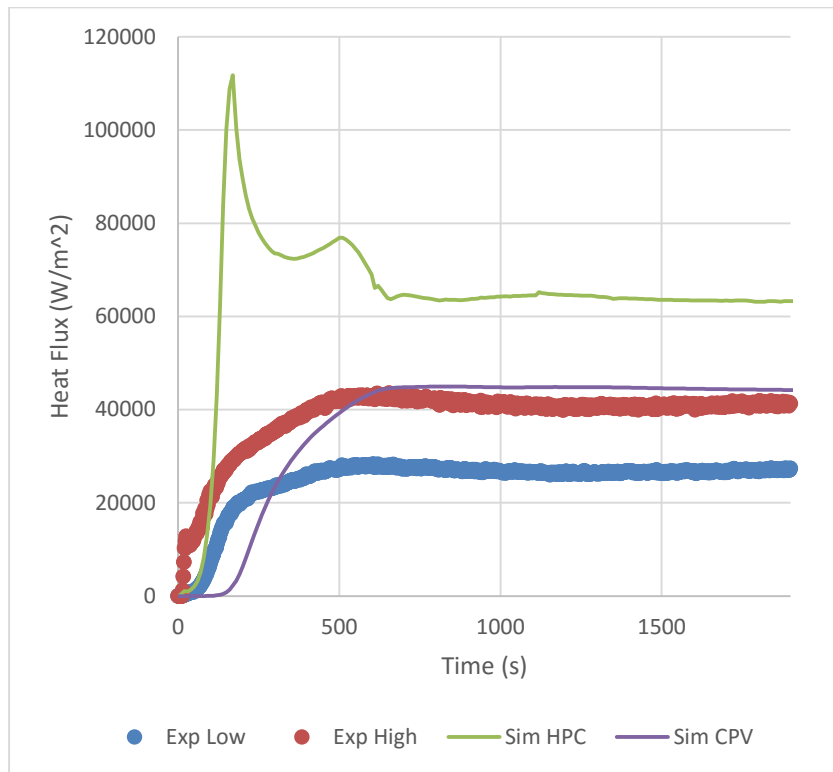


Figure A-109 Heat Flux at Location 3 for Test 2.7

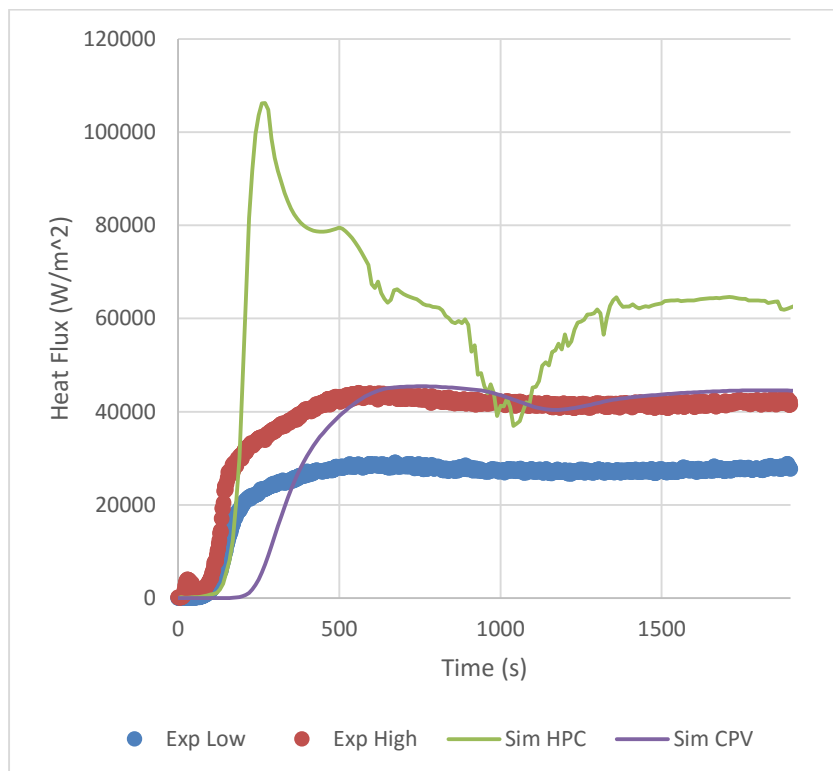


Figure A-110 Heat Flux at Location 2 for Test 2.7

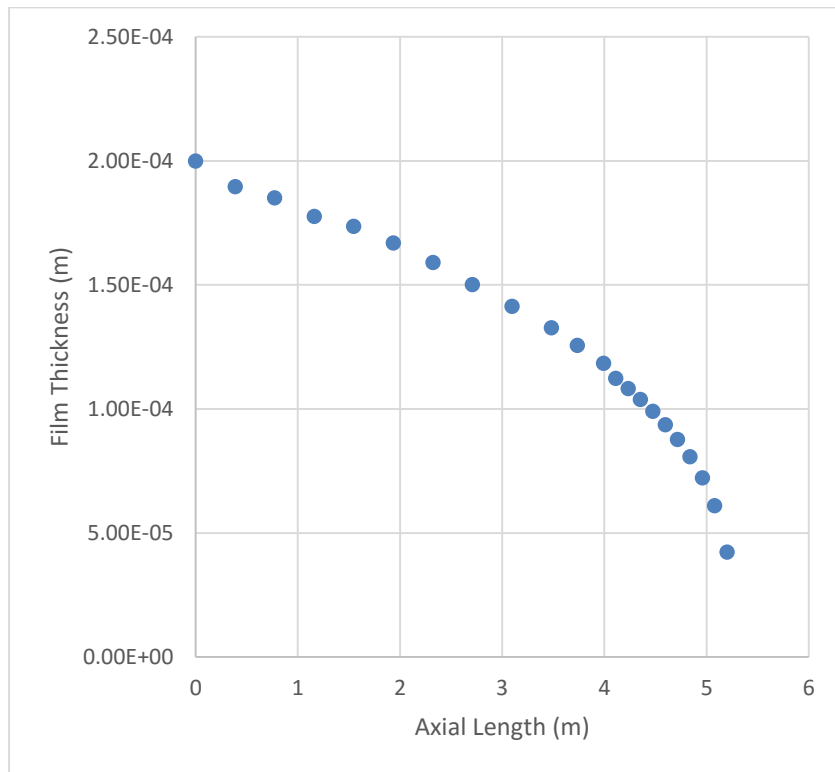


Figure A-111 Steady State Film Thickness for Test 2.7

APPENDIX B – FULL INPUT FOR MELCOR

MELCOR allows user to have multiple files for one trial. Following full input files are for Test 2.1. Total 11 files are included. Differences between different trials are listed in Table B-2.

Table B-1 MELCOR files and descriptions

	File name	Description
1	main.inp	main setup and simulation detail
2	cvh-steaminj.inp	steam source and steam injection
3	cvh-hpc.inp	control volumes for the HPC
4	cvh-cpv.inp	control volumes for the CPV
5	fl-hpc-h.inp	horizontal flow paths for the HPC
6	fl-hpc-v.inp	vertical flow paths for the HPC
7	fl-cpv-h.inp	horizontal flow paths for the CPV
8	fl-cpv-v.inp	vertical flow paths for the CPV
9	hs-hsfon.inp	heat structures for heat transfer plate
10	hs-tankfon.inp	heat structures for the HPC tank mass
11	mp.inp	material properties

Table B-2 Necessary changes in input between different tests

	Associated file name	Modification Target	Description
1	main.inp	EXEC_TEND	Total test length
2	cvh-steaminj.inp	TF_TAB	Steam flowrate and disturbances in flowrate
3	cvh-hpc.inp	CV_PTD	Initial tank pressure
4		CV_NCG	
5		CV_AAD	Initial tank temperature
5	cvh-cpv.inp	CV_AAD	Initial water temperature

```
main.inp
!NuScale Condensation Containment Simulation
!Initiated on 04/21/2015
!Test 2.1
!=====
=====
MEG_DiagFile      'MELGEN.diag'
MEL_DiagFile      'Dumps\MELCOR.diag'
MEG_OutputFile    'Dumps\MELGEN-output.dump'
MEL_OutputFile    'Dumps\MELCOR-output.dump'
MEG_RestartFile   'Dumps\MELGEN.rst'
MEL_RestartFile   'Dumps\MELCORControls.rst'  NCYCLE -1
MessageFile       'Dumps\Messages.dump'
StatusFile        'Dumps\MELCOR-status.dump'
StopFile          'Dumps\MELCOR-stop.dump'
WriteNewInp       'Dumps\NewInpInput.can'
ExtDiagFile       'Dumps\MELCOR.diag.xtnd'
PlotFile          'PTFs\output.ptf'
!=====
=====
! MELGEN INPUT
```

```
Program MELGEN
=====
=====
EXEC_INPUT                                EXEC_TITLE                                'NS'
=====
=====
NCG_INPUT                                !air
      NCG_ID                             N2
      NCG_ID                             O2
      NCG_ID                             He

! file inclusions here
! <<<<<<<<<<>>>>>>>>
include    'cvh-stminj.inp'
include    'cvh-hpc.inp'
include    'cvh-cpv.inp'
include    'fl-hpc-h.inp'
include    'fl-hpc-v.inp'
include    'fl-cpv-h.inp'
include    'fl-cpv-v.inp'
include    'hs-hsfon.inp'
```



```

include 'hs-tankfon.inp'
include 'tfs.inp'
include 'calc.inp'
include 'mp.inp'
!include 'edf.inp'
! <<<<<<<<>>>>>>>>>>>>
!=====
=====
End Program MELGEN Data
!=====
=====
! MELCOR INPUT
Program MELCOR
!=====
=====
EXEC_INPUT
EXEC_CPULEFT      50.
EXEC_CPULIM              1.0E+10
EXEC_TEND              2.E+3
EXEC_TIME              1
1.E-6      1.      10.      10.      1.E+9
EXEC_TITLE              'NS'
CVH_INPUT
CVH_TRACE 100
!=====
=====
End Program MELCOR Data

cvh-steam.inj.inp
AllowReplace
!=====STEAM
SUPPLY=====
CVH_INPUT
CV_ID      VSTM      9999      lsteam dummy volume
CV_THR      EQUIL      NOFOG      TIME-INDEP
CV_PAS      SEPARATE      ONLYATM      SUPERHEATED
CV_PTD      PVOL      5.1711E+5
CV_AAD      TATM      523.71
!=====
=====
CV_VAT      2
1      5.3887      0.
2      5.5097      1.0

!=====
=====
FL_INPUT
FL_ID      FLSTM
FL_FT      VSTM      UCS04B      5.445      5.445
FL_GEO      2.7907E-4      2.02      1.
FL_JSW      3      NOBUBBLERISE      NOBUBBLERISE
FL_USL      1.      0.      0.      0.
FL_SEG      3
1      4.04496E-5      .08
.00636
2      1.936E-4      1.72      1.57E-2
3      2.7907E-4      .22      1.885E-2
FL_VTM      1
1      FLSTM      TF      STMSRC
!=====
=====
TF_INPUT
TF_ID STMSRC      1676.2204
TF_TAB      4
1      0.      0.0358
2      250.      0.0358
3      370.      0.0117
4      3000.      0.0117

cvh-hpc.inp

```

```

AllowReplace
CVH_INPUT
!=====LOWER
CYLINDRICAL
SECTION=====
CV_ID      LCS01A      1201
CV_THR      NONEQUILNOFOG      ACTIVE
CV_PAS      SEPARATE      ONLYATM      SUPERHEATED
CV_PTD      PVOL      7809.064
CV_AAD      TATM      288.819
CV_NCG      2      PNCG      7809.064
1      N2      .8
2      O2      .2
CV_VAT      2
1      .6477      0.
2      1.0347      1.04E-2
!=====
=====
CV_ID      LCS02A      1211
CV_THR      NONEQUILNOFOG      ACTIVE
CV_PAS      SEPARATE      ONLYATM      SUPERHEATED
CV_PTD      PVOL      7809.064
CV_AAD      TATM      288.819
CV_NCG      2      PNCG      7809.064
1      N2      .8
2      O2      .2
CV_VAT      2
1      1.0347      0.
2      1.4217      1.04E-2
!=====
=====
CV_ID      LCS3A      1221
CV_THR      NONEQUILNOFOG      ACTIVE
CV_PAS      SEPARATE      ONLYATM      SUPERHEATED
CV_PTD      PVOL      7809.064
CV_AAD      TATM      288.819
CV_NCG      2      PNCG      7809.064
1      N2      .8
2      O2      .2
CV_VAT      2
1      1.4217      0.
2      1.8087      1.04E-2
!=====
=====
CV_ID      LCS04A      1231
CV_THR      NONEQUILNOFOG      ACTIVE
CV_PAS      SEPARATE      ONLYATM      SUPERHEATED
CV_PTD      PVOL      7809.064
CV_AAD      TATM      288.819
CV_NCG      2      PNCG      7809.064
1      N2      .8
2      O2      .2
CV_VAT      2
1      1.8087      0.
2      2.1957      1.04E-2
!=====
=====
CV_ID      LCS05A      1241
CV_THR      NONEQUILNOFOG      ACTIVE
CV_PAS      SEPARATE      ONLYATM      SUPERHEATED
CV_PTD      PVOL      7809.064
CV_AAD      TATM      288.819
CV_NCG      2      PNCG      7809.064
1      N2      .8
2      O2      .2
CV_VAT      2
1      2.1957      0.
2      2.5827      1.04E-2
!=====
=====
CV_ID      LCS06A      1251
CV_THR      NONEQUILNOFOG      ACTIVE

```

```

CV_PAS SEPARATE ONLYATM SUPERHEATED
CV_PTD PVOL 7809.064
CV_AAD TATM 288.819
CV_NCG 2 PNCG 7809.064
      1 N2 .8
      2 O2 .2

CV_VAT 2
      1 2.5827 0.
      2 2.9697 1.04E-2

=====
=====
CV_ID LCS07A 1261
CV_THR NONEQUILNOFOG ACTIVE
CV_PAS SEPARATE ONLYATM SUPERHEATED
CV_PTD PVOL 7809.064
CV_AAD TATM 288.819
CV_NCG 2 PNCG 7809.064
      1 N2 .8
      2 O2 .2

CV_VAT 2
      1 2.9697 0.
      2 3.3567 1.04E-2

=====
=====
CV_ID LCS08A 1271
CV_THR NONEQUILNOFOG ACTIVE
CV_PAS SEPARATE ONLYATM SUPERHEATED
CV_PTD PVOL 7809.064
CV_AAD TATM 288.819
CV_NCG 2 PNCG 7809.064
      1 N2 .8
      2 O2 .2

CV_VAT 2
      1 3.3567 0.
      2 3.7437 1.04E-2

=====
=====
CV_ID LCS09A 1281
CV_THR NONEQUILNOFOG ACTIVE
CV_PAS SEPARATE ONLYATM SUPERHEATED
CV_PTD PVOL 7809.064
CV_AAD TATM 288.819
CV_NCG 2 PNCG 7809.064
      1 N2 .8
      2 O2 .2

CV_VAT 2
      1 3.7437 0.
      2 4.1307 1.04E-2

=====
=====
CV_ID LCS10A 1291
CV_THR NONEQUILNOFOG ACTIVE
CV_PAS SEPARATE ONLYATM SUPERHEATED
CV_PTD PVOL 7809.064
CV_AAD TATM 288.819
CV_NCG 2 PNCG 7809.064
      1 N2 .8
      2 O2 .2

CV_VAT 2
      1 4.1307 0.
      2 4.5177 1.04E-2

=====
=====
CV_ID LCS01B 1202
CV_THR NONEQUILNOFOG ACTIVE
CV_PAS SEPARATE ONLYATM SUPERHEATED
CV_PTD PVOL 7809.064
CV_AAD TATM 288.819
CV_NCG 2 PNCG 7809.064
      1 N2 .8
      2 O2 .2

```

```

CV_VAT 2
      1 .6477 0.
      2 1.0347 1.04E-2

=====
=====
CV_ID LCS02B 1212
CV_THR NONEQUILNOFOG ACTIVE
CV_PAS SEPARATE ONLYATM SUPERHEATED
CV_PTD PVOL 7809.064
CV_AAD TATM 288.819
CV_NCG 2 PNCG 7809.064
      1 N2 .8
      2 O2 .2

CV_VAT 2
      1 1.0347 0.
      2 1.4217 1.04E-2

=====
=====
CV_ID LCS3B 1222
CV_THR NONEQUILNOFOG ACTIVE
CV_PAS SEPARATE ONLYATM SUPERHEATED
CV_PTD PVOL 7809.064
CV_AAD TATM 288.819
CV_NCG 2 PNCG 7809.064
      1 N2 .8
      2 O2 .2

CV_VAT 2
      1 1.4217 0.
      2 1.8087 1.04E-2

=====
=====
CV_ID LCS04B 1232
CV_THR NONEQUILNOFOG ACTIVE
CV_PAS SEPARATE ONLYATM SUPERHEATED
CV_PTD PVOL 7809.064
CV_AAD TATM 288.819
CV_NCG 2 PNCG 7809.064
      1 N2 .8
      2 O2 .2

CV_VAT 2
      1 1.8087 0.
      2 2.1957 1.04E-2

=====
=====
CV_ID LCS05B 1242
CV_THR NONEQUILNOFOG ACTIVE
CV_PAS SEPARATE ONLYATM SUPERHEATED
CV_PTD PVOL 7809.064
CV_AAD TATM 288.819
CV_NCG 2 PNCG 7809.064
      1 N2 .8
      2 O2 .2

CV_VAT 2
      1 2.1957 0.
      2 2.5827 1.04E-2

=====
=====
CV_ID LCS06B 1252
CV_THR NONEQUILNOFOG ACTIVE
CV_PAS SEPARATE ONLYATM SUPERHEATED
CV_PTD PVOL 7809.064
CV_AAD TATM 288.819
CV_NCG 2 PNCG 7809.064
      1 N2 .8
      2 O2 .2

CV_VAT 2
      1 2.5827 0.
      2 2.9697 1.04E-2

=====
=====
CV_ID LCS07B 1262

```

```

CV_THR  NONEQUILNOFOG  ACTIVE
CV_PAS  SEPARATE ONLYATM SUPERHEATED
CV_PTD  PVOL      7809.064
CV_AAD  TATM      288.819
CV_NCG  2         PNCG      7809.064
              1         N2         .8
              2         O2         .2

CV_VAT  2
              1         2.9697  0.
              2         3.3567  1.04E-2

=====
=====
CV_ID    LCS08B  1272
CV_THR  NONEQUILNOFOG  ACTIVE
CV_PAS  SEPARATE ONLYATM SUPERHEATED
CV_PTD  PVOL      7809.064
CV_AAD  TATM      288.819
CV_NCG  2         PNCG      7809.064
              1         N2         .8
              2         O2         .2

CV_VAT  2
              1         3.3567  0.
              2         3.7437  1.04E-2

=====
=====
CV_ID    LCS09B  1282
CV_THR  NONEQUILNOFOG  ACTIVE
CV_PAS  SEPARATE ONLYATM SUPERHEATED
CV_PTD  PVOL      7809.064
CV_AAD  TATM      288.819
CV_NCG  2         PNCG      7809.064
              1         N2         .8
              2         O2         .2

CV_VAT  2
              1         3.7437  0.
              2         4.1307  1.04E-2

=====
=====
CV_ID    LCS10B  1292
CV_THR  NONEQUILNOFOG  ACTIVE
CV_PAS  SEPARATE ONLYATM SUPERHEATED
CV_PTD  PVOL      7809.064
CV_AAD  TATM      288.819
CV_NCG  2         PNCG      7809.064
              1         N2         .8
              2         O2         .2

CV_VAT  2
              1         4.1307  0.
              2         4.5177  1.04E-2

=====
=====
=====ECCENTRIC                                CONE
SECTION=====
CV_ID    ECS01A  1301
CV_THR  NONEQUILNOFOG  ACTIVE
CV_PAS  SEPARATE ONLYATM SUPERHEATED
CV_PTD  PVOL      7809.064
CV_AAD  TATM      288.819
CV_NCG  2         PNCG      7809.064
              1         N2         .8
              2         O2         .2

CV_VAT  2
              1         4.5177  0.
              2         4.7717  1.487E-2

=====
=====
CV_ID    ECS02A  1311
CV_THR  NONEQUILNOFOG  ACTIVE
CV_PAS  SEPARATE ONLYATM SUPERHEATED
CV_PTD  PVOL      7809.064
CV_AAD  TATM      288.819

```

```

CV_NCG  2         PNCG      7809.064
              1         N2         .8
              2         O2         .2

CV_VAT  2
              1         4.7717  0.
              2         5.0257  1.487E-2

=====
=====
CV_ID    ECS01B  1302
CV_THR  NONEQUILNOFOG  ACTIVE
CV_PAS  SEPARATE ONLYATM SUPERHEATED
CV_PTD  PVOL      7809.064
CV_AAD  TATM      288.819
CV_NCG  2         PNCG      7809.064
              1         N2         .8
              2         O2         .2

CV_VAT  2
              1         4.5177  0.
              2         4.7717  1.487E-2

=====
=====
CV_ID    ECS02B  1312
CV_THR  NONEQUILNOFOG  ACTIVE
CV_PAS  SEPARATE ONLYATM SUPERHEATED
CV_PTD  PVOL      7809.064
CV_AAD  TATM      288.819
CV_NCG  2         PNCG      7809.064
              1         N2         .8
              2         O2         .2

CV_VAT  2
              1         4.7717  0.
              2         5.0257  1.487E-2

=====
=====
=====UPPER                                CYLINDRICAL
SECTION=====
CV_ID    UCS01A  1401
CV_THR  NONEQUILNOFOG  ACTIVE
CV_PAS  SEPARATE ONLYATM SUPERHEATED
CV_PTD  PVOL      7809.064
CV_AAD  TATM      288.819
CV_NCG  2         PNCG      7809.064
              1         N2         .8
              2         O2         .2

CV_VAT  2
              1         5.0257  0.
              2         5.1467  1.18E-2

=====
=====
CV_ID    UCS02A  1411
CV_THR  NONEQUILNOFOG  ACTIVE
CV_PAS  SEPARATE ONLYATM SUPERHEATED
CV_PTD  PVOL      7809.064
CV_AAD  TATM      288.819
CV_NCG  2         PNCG      7809.064
              1         N2         .8
              2         O2         .2

CV_VAT  2
              1         5.1467  0.
              2         5.2677  1.18E-2

=====
=====
CV_ID    UCS3A   1421
CV_THR  NONEQUILNOFOG  ACTIVE
CV_PAS  SEPARATE ONLYATM SUPERHEATED
CV_PTD  PVOL      7809.064
CV_AAD  TATM      288.819
CV_NCG  2         PNCG      7809.064
              1         N2         .8
              2         O2         .2

CV_VAT  2

```

```

1      5.2677  0.
2      5.3887  1.18E-2
=====
=====
CV_ID   UCS04A  1431
CV_THR  NONEQUILNOFOG  ACTIVE
CV_PAS  SEPARATE ONLYATM SUPERHEATED
CV_PTD  PVOL     7809.064
CV_AAD  TATM     288.819
CV_NCG  2        PNCG     7809.064
1        N2        .8
2        O2        .2
CV_VAT  2
1        5.3887  0.
2        5.5097  1.18E-2
=====
=====
CV_ID   UCS05A  1441
CV_THR  NONEQUILNOFOG  ACTIVE
CV_PAS  SEPARATE ONLYATM SUPERHEATED
CV_PTD  PVOL     7809.064
CV_AAD  TATM     288.819
CV_NCG  2        PNCG     7809.064
1        N2        .8
2        O2        .2
CV_VAT  2
1        5.5097  0.
2        5.6307  1.18E-2
=====
=====
CV_ID   UCS06A  1451
CV_THR  NONEQUILNOFOG  ACTIVE
CV_PAS  SEPARATE ONLYATM SUPERHEATED
CV_PTD  PVOL     7809.064
CV_AAD  TATM     288.819
CV_NCG  2        PNCG     7809.064
1        N2        .8
2        O2        .2
CV_VAT  2
1        5.6307  0.
2        5.7517  1.18E-2
=====
=====
CV_ID   UCS07A  1461
CV_THR  NONEQUILNOFOG  ACTIVE
CV_PAS  SEPARATE ONLYATM SUPERHEATED
CV_PTD  PVOL     7809.064
CV_AAD  TATM     288.819
CV_NCG  2        PNCG     7809.064
1        N2        .8
2        O2        .2
CV_VAT  2
1        5.7517  0.
2        5.8727  1.18E-2
=====
=====
CV_ID   UCS08A  1471
CV_THR  NONEQUILNOFOG  ACTIVE
CV_PAS  SEPARATE ONLYATM SUPERHEATED
CV_PTD  PVOL     7809.064
CV_AAD  TATM     288.819
CV_NCG  2        PNCG     7809.064
1        N2        .8
2        O2        .2
CV_VAT  2
1        5.8727  0.
2        5.9937  1.18E-2
=====
=====
CV_ID   UCS09A  1481
CV_THR  NONEQUILNOFOG  ACTIVE

```

```

CV_PAS  SEPARATE ONLYATM SUPERHEATED
CV_PTD  PVOL     7809.064
CV_AAD  TATM     288.819
CV_NCG  2        PNCG     7809.064
1        N2        .8
2        O2        .2
CV_VAT  2
1        5.9937  0.
2        6.1147  1.18E-2
=====
=====
CV_ID   UCS10A  1491
CV_THR  NONEQUILNOFOG  ACTIVE
CV_PAS  SEPARATE ONLYATM SUPERHEATED
CV_PTD  PVOL     7809.064
CV_AAD  TATM     288.819
CV_NCG  2        PNCG     7809.064
1        N2        .8
2        O2        .2
CV_VAT  2
1        6.1147  0.
2        6.2357  1.18E-2
=====
=====
CV_ID   UCS01B  1402
CV_THR  NONEQUILNOFOG  ACTIVE
CV_PAS  SEPARATE ONLYATM SUPERHEATED
CV_PTD  PVOL     7809.064
CV_AAD  TATM     288.819
CV_NCG  2        PNCG     7809.064
1        N2        .8
2        O2        .2
CV_VAT  2
1        5.0257  0.
2        5.1467  1.18E-2
=====
=====
CV_ID   UCS02B  1412
CV_THR  NONEQUILNOFOG  ACTIVE
CV_PAS  SEPARATE ONLYATM SUPERHEATED
CV_PTD  PVOL     7809.064
CV_AAD  TATM     288.819
CV_NCG  2        PNCG     7809.064
1        N2        .8
2        O2        .2
CV_VAT  2
1        5.1467  0.
2        5.2677  1.18E-2
=====
=====
CV_ID   UCS3B   1422
CV_THR  NONEQUILNOFOG  ACTIVE
CV_PAS  SEPARATE ONLYATM SUPERHEATED
CV_PTD  PVOL     7809.064
CV_AAD  TATM     288.819
CV_NCG  2        PNCG     7809.064
1        N2        .8
2        O2        .2
CV_VAT  2
1        5.2677  0.
2        5.3887  1.18E-2
=====
=====
CV_ID   UCS04B  1432
CV_THR  NONEQUILNOFOG  ACTIVE
CV_PAS  SEPARATE ONLYATM SUPERHEATED
CV_PTD  PVOL     7809.064
CV_AAD  TATM     288.819
CV_NCG  2        PNCG     7809.064
1        N2        .8
2        O2        .2

```

```

CV_VAT  2
          1      5.3887  0.
          2      5.5097  1.18E-2
=====
=====
CV_ID    UCS05B  1442
CV_THR   NONEQUILNOFOG  ACTIVE
CV_PAS   SEPARATE ONLYATM SUPERHEATED
CV_PTD   PVOL     7809.064
CV_AAD   TATM     288.819
CV_NCG   2        PNCG   7809.064
          1        N2     .8
          2        O2     .2
CV_VAT  2
          1      5.5097  0.
          2      5.6307  1.18E-2
=====
=====
CV_ID    UCS06B  1452
CV_THR   NONEQUILNOFOG  ACTIVE
CV_PAS   SEPARATE ONLYATM SUPERHEATED
CV_PTD   PVOL     7809.064
CV_AAD   TATM     288.819
CV_NCG   2        PNCG   7809.064
          1        N2     .8
          2        O2     .2
CV_VAT  2
          1      5.6307  0.
          2      5.7517  1.18E-2
=====
=====
CV_ID    UCS07B  1462
CV_THR   NONEQUILNOFOG  ACTIVE
CV_PAS   SEPARATE ONLYATM SUPERHEATED
CV_PTD   PVOL     7809.064
CV_AAD   TATM     288.819
CV_NCG   2        PNCG   7809.064
          1        N2     .8
          2        O2     .2
CV_VAT  2
          1      5.7517  0.
          2      5.8727  1.18E-2
=====
=====
CV_ID    UCS08B  1472
CV_THR   NONEQUILNOFOG  ACTIVE
CV_PAS   SEPARATE ONLYATM SUPERHEATED
CV_PTD   PVOL     7809.064
CV_AAD   TATM     288.819
CV_NCG   2        PNCG   7809.064
          1        N2     .8
          2        O2     .2
CV_VAT  2
          1      5.8727  0.
          2      5.9937  1.18E-2
=====
=====
CV_ID    UCS09B  1482
CV_THR   NONEQUILNOFOG  ACTIVE
CV_PAS   SEPARATE ONLYATM SUPERHEATED
CV_PTD   PVOL     7809.064
CV_AAD   TATM     288.819
CV_NCG   2        PNCG   7809.064
          1        N2     .8
          2        O2     .2
CV_VAT  2
          1      5.9937  0.
          2      6.1147  1.18E-2
=====
=====
CV_ID    UCS10B  1492

```

```

CV_THR   NONEQUILNOFOG  ACTIVE
CV_PAS   SEPARATE ONLYATM SUPERHEATED
CV_PTD   PVOL     7809.064
CV_AAD   TATM     288.819
CV_NCG   2        PNCG   7809.064
          1        N2     .8
          2        O2     .2
CV_VAT  2
          1      6.1147  0.
          2      6.2357  1.18E-2
=====
=====
!=====HEMISPHERE
SECTION=====
CV_ID    HEMA     1501
CV_THR   NONEQUILNOFOG  ACTIVE
CV_PAS   SEPARATE ONLYATM SUPERHEATED
CV_PTD   PVOL     7809.064
CV_AAD   TATM     288.819
CV_NCG   2        PNCG   7809.064
          1        N2     .8
          2        O2     .2
CV_VAT  2
          1      6.2357  0.
          2      6.4007  2.937E-3
=====
=====
CV_ID    HEMB     1502
CV_THR   NONEQUILNOFOG  ACTIVE
CV_PAS   SEPARATE ONLYATM SUPERHEATED
CV_PTD   PVOL     7809.064
CV_AAD   TATM     288.819
CV_NCG   2        PNCG   7809.064
          1        N2     .8
          2        O2     .2
CV_VAT  2
          1      6.2357  0.
          2      6.4007  2.937E-2
=====
=====
cvh-cpv.inp
AllowReplace
CVH_INPUT
!=====BOT=====
=====
CV_ID    CPVBOT01A      2101
CV_THR   NONEQUILNOFOG  ACTIVE
CV_PAS   SEPARATE ONLYPOOLSUBCOOLED
CV_PTD   PVOL     101325.
CV_PAD   289.9405
CV_VAT  2
          1      0.
          2      .32385  7.14E-2
=====
=====
CV_ID    CPVBOT02A      2111
CV_THR   NONEQUILNOFOG  ACTIVE
CV_PAS   SEPARATE ONLYPOOLSUBCOOLED
CV_PTD   PVOL     101325.
CV_PAD   289.9405
CV_VAT  2
          1      .32385  0.
          2      .6477   7.14E-2
=====
=====
CV_ID    CPVBOT01B      2102
CV_THR   NONEQUILNOFOG  ACTIVE
CV_PAS   SEPARATE ONLYPOOLSUBCOOLED
CV_PTD   PVOL     101325.
CV_PAD   289.9405

```

```

CV_VAT 2
          1      0.      0.
          2      .32385  7.14E-2
=====
=====
CV_ID    CPVBOT02B      2112
CV_THR   NONEQUILNOFOG  ACTIVE
CV_PAS   SEPARATE ONLYPOOLSUBCOOLED
CV_PTD   PVOL    101325.
CV_PAD   289.9405
CV_VAT   2
          1      .32385  0.
          2      .6477   7.14E-2
=====
=====
=====LCS=====
=====
CV_ID    CPVLC01A      2201
CV_THR   NONEQUILNOFOG  ACTIVE
CV_PAS   SEPARATE ONLYPOOLSUBCOOLED
CV_PTD   PVOL    101325.
CV_PAD   289.9405
CV_VAT   2
          1      .6477   0.
          2      1.0347  8.5326E-2
=====
=====
CV_ID    CPVLC02A      2211
CV_THR   NONEQUILNOFOG  ACTIVE
CV_PAS   SEPARATE ONLYPOOLSUBCOOLED
CV_PTD   PVOL    101325.
CV_PAD   289.9405
CV_VAT   2
          1      1.0347  0.
          2      1.4217  8.5326E-2
=====
=====
CV_ID    CPVLC03A 2221
CV_THR   NONEQUILNOFOG  ACTIVE
CV_PAS   SEPARATE ONLYPOOLSUBCOOLED
CV_PTD   PVOL    101325.
CV_PAD   289.9405
CV_VAT   2
          1      1.4217  0.
          2      1.8087  8.5326E-2
=====
=====
CV_ID    CPVLC04A      2231
CV_THR   NONEQUILNOFOG  ACTIVE
CV_PAS   SEPARATE ONLYPOOLSUBCOOLED
CV_PTD   PVOL    101325.
CV_PAD   289.9405
CV_VAT   2
          1      1.8087  0.
          2      2.1957  8.5326E-2
=====
=====
CV_ID    CPVLC05A      2241
CV_THR   NONEQUILNOFOG  ACTIVE
CV_PAS   SEPARATE ONLYPOOLSUBCOOLED
CV_PTD   PVOL    101325.
CV_PAD   289.9405
CV_VAT   2
          1      2.1957  0.
          2      2.5827  8.5326E-2
=====
=====
CV_ID    CPVLC06A      2251
CV_THR   NONEQUILNOFOG  ACTIVE
CV_PAS   SEPARATE ONLYPOOLSUBCOOLED
CV_PTD   PVOL    101325.

```

```

CV_PAD 289.9405
CV_VAT 2
          1      2.5827  0.
          2      2.9697  8.5326E-2
=====
=====
CV_ID    CPVLC07A      2261
CV_THR   NONEQUILNOFOG  ACTIVE
CV_PAS   SEPARATE ONLYPOOLSUBCOOLED
CV_PTD   PVOL    101325.
CV_PAD   289.9405
CV_VAT   2
          1      2.9697  0.
          2      3.3567  8.5326E-2
=====
=====
CV_ID    CPVLC08A      2271
CV_THR   NONEQUILNOFOG  ACTIVE
CV_PAS   SEPARATE ONLYPOOLSUBCOOLED
CV_PTD   PVOL    101325.
CV_PAD   289.9405
CV_VAT   2
          1      3.3567  0.
          2      3.7437  8.5326E-2
=====
=====
CV_ID    CPVLC09A      2281
CV_THR   NONEQUILNOFOG  ACTIVE
CV_PAS   SEPARATE ONLYPOOLSUBCOOLED
CV_PTD   PVOL    101325.
CV_PAD   289.9405
CV_VAT   2
          1      3.7437  0.
          2      4.1307  8.5326E-2
=====
=====
CV_ID    CPVLC10A      2291
CV_THR   NONEQUILNOFOG  ACTIVE
CV_PAS   SEPARATE ONLYPOOLSUBCOOLED
CV_PTD   PVOL    101325.
CV_PAD   289.9405
CV_VAT   2
          1      4.1307  0.
          2      4.5177  8.5326E-2
=====
=====
CV_ID    CPVLC01B      2202
CV_THR   NONEQUILNOFOG  ACTIVE
CV_PAS   SEPARATE ONLYPOOLSUBCOOLED
CV_PTD   PVOL    101325.
CV_PAD   289.9405
CV_VAT   2
          1      .6477   0.
          2      1.0347  8.5326E-2
=====
=====
CV_ID    CPVLC02B      2212
CV_THR   NONEQUILNOFOG  ACTIVE
CV_PAS   SEPARATE ONLYPOOLSUBCOOLED
CV_PTD   PVOL    101325.
CV_PAD   289.9405
CV_VAT   2
          1      1.0347  0.
          2      1.4217  8.5326E-2
=====
=====
CV_ID    CPVLC03B 2222
CV_THR   NONEQUILNOFOG  ACTIVE
CV_PAS   SEPARATE ONLYPOOLSUBCOOLED
CV_PTD   PVOL    101325.
CV_PAD   289.9405

```

CV_VAT	2			
	1	1.4217	0.	
	2	1.8087	8.5326E-2	

=====

=====
CV_ID CPVLC04B 2232
CV_THR NONEQUILNOFOG ACTIVE
CV_PAS SEPARATE ONLYPOOLSUBCOOLED
CV_PTD PVOL 101325.
CV_PAD 289.9405
CV_VAT 2

	1	1.8087	0.	
	2	2.1957	8.5326E-2	

=====

=====
CV_ID CPVLC05B 2242
CV_THR NONEQUILNOFOG ACTIVE
CV_PAS SEPARATE ONLYPOOLSUBCOOLED
CV_PTD PVOL 101325.
CV_PAD 289.9405
CV_VAT 2

	1	2.1957	0.	
	2	2.5827	8.5326E-2	

=====

=====
CV_ID CPVLC06B 2252
CV_THR NONEQUILNOFOG ACTIVE
CV_PAS SEPARATE ONLYPOOLSUBCOOLED
CV_PTD PVOL 101325.
CV_PAD 289.9405
CV_VAT 2

	1	2.5827	0.	
	2	2.9697	8.5326E-2	

=====

=====
CV_ID CPVLC07B 2262
CV_THR NONEQUILNOFOG ACTIVE
CV_PAS SEPARATE ONLYPOOLSUBCOOLED
CV_PTD PVOL 101325.
CV_PAD 289.9405
CV_VAT 2

	1	2.9697	0.	
	2	3.3567	8.5326E-2	

=====

=====
CV_ID CPVLC08B 2272
CV_THR NONEQUILNOFOG ACTIVE
CV_PAS SEPARATE ONLYPOOLSUBCOOLED
CV_PTD PVOL 101325.
CV_PAD 289.9405
CV_VAT 2

	1	3.3567	0.	
	2	3.7437	8.5326E-2	

=====

=====
CV_ID CPVLC09B 2282
CV_THR NONEQUILNOFOG ACTIVE
CV_PAS SEPARATE ONLYPOOLSUBCOOLED
CV_PTD PVOL 101325.
CV_PAD 289.9405
CV_VAT 2

	1	3.7437	0.	
	2	4.1307	8.5326E-2	

=====

=====
CV_ID CPVLC10B 2292
CV_THR NONEQUILNOFOG ACTIVE
CV_PAS SEPARATE ONLYPOOLSUBCOOLED
CV_PTD PVOL 101325.
CV_PAD 289.9405
CV_VAT 2

	1	4.1307	0.	
	2	4.5177	8.5326E-2	

=====

=====
!=====ECS=====

=====
CV_ID CPVECS01A 2301
CV_THR NONEQUILNOFOG ACTIVE
CV_PAS SEPARATE ONLYPOOLSUBCOOLED
CV_PTD PVOL 101325.
CV_PAD 289.9405
CV_VAT 2

	1	4.5177	0.	
	2	4.7717	5.60E-2	

=====

=====
CV_ID CPVECS02A 2311
CV_THR NONEQUILNOFOG ACTIVE
CV_PAS SEPARATE ONLYPOOLSUBCOOLED
CV_PTD PVOL 101325.
CV_PAD 289.9405
CV_VAT 2

	1	4.7717	0.	
	2	5.0257	5.60E-2	

=====

=====
CV_ID CPVECS01B 2302
CV_THR NONEQUILNOFOG ACTIVE
CV_PAS SEPARATE ONLYPOOLSUBCOOLED
CV_PTD PVOL 101325.
CV_PAD 289.9405
CV_VAT 2

	1	4.5177	0.	
	2	4.7717	5.60E-2	

=====

=====
CV_ID CPVECS02B 2312
CV_THR NONEQUILNOFOG ACTIVE
CV_PAS SEPARATE ONLYPOOLSUBCOOLED
CV_PTD PVOL 101325.
CV_PAD 289.9405
CV_VAT 2

	1	4.7717	0.	
	2	5.0257	5.60E-2	

=====

=====
!=====UCS=====

=====
CV_ID CPVUCS01A 2401
CV_THR NONEQUILNOFOG ACTIVE
CV_PAS SEPARATE ONLYPOOLSUBCOOLED
CV_PTD PVOL 101325.
CV_PAD 289.9405
CV_VAT 2

	1	5.0257	0.	
	2	5.1467	2.66782E-2	

=====

=====
CV_ID CPVUCS02A 2411
CV_THR NONEQUILNOFOG ACTIVE
CV_PAS SEPARATE ONLYPOOLSUBCOOLED
CV_PTD PVOL 101325.
CV_PAD 289.9405
CV_VAT 2

	1	5.1467	0.	
	2	5.2677	2.66782E-2	

=====

=====
CV_ID CPVUCS3A 2421
CV_THR NONEQUILNOFOG ACTIVE
CV_PAS SEPARATE ONLYPOOLSUBCOOLED

CV_PTD	PVOL	101325.		
CV_PAD	289.9405			
CV_VAT	2			
		1	5.2677	0.
		2	5.3887	2.66782E-2

=====

=====
CV_ID CPVUCS04A 2431
CV_THR NONEQUILNOFOG ACTIVE
CV_PAS SEPARATE ONLYPOOLSUBCOOLED
CV_PTD PVOL 101325.
CV_PAD 289.9405
CV_VAT 2

		1	5.3887	0.
		2	5.5097	2.66782E-2

=====

=====
CV_ID CPVUCS05A 2441
CV_THR NONEQUILNOFOG ACTIVE
CV_PAS SEPARATE ONLYPOOLSUBCOOLED
CV_PTD PVOL 101325.
CV_PAD 289.9405
CV_VAT 2

		1	5.5097	0.
		2	5.6307	2.66782E-2

=====

=====
CV_ID CPVUCS06A 2451
CV_THR NONEQUILNOFOG ACTIVE
CV_PAS SEPARATE ONLYPOOLSUBCOOLED
CV_PTD PVOL 101325.
CV_PAD 289.9405
CV_VAT 2

		1	5.6307	0.
		2	5.7517	2.66782E-2

=====

=====
CV_ID CPVUCS07A 2461
CV_THR NONEQUILNOFOG ACTIVE
CV_PAS SEPARATE ONLYPOOLSUBCOOLED
CV_PTD PVOL 101325.
CV_PAD 289.9405
CV_VAT 2

		1	5.7517	0.
		2	5.8727	2.66782E-2

=====

=====
CV_ID CPVUCS08A 2471
CV_THR NONEQUILNOFOG ACTIVE
CV_PAS SEPARATE ONLYPOOLSUBCOOLED
CV_PTD PVOL 101325.
CV_PAD 289.9405
CV_VAT 2

		1	5.8727	0.
		2	5.9937	2.66782E-2

=====

=====
CV_ID CPVUCS09A 2481
CV_THR NONEQUILNOFOG ACTIVE
CV_PAS SEPARATE ONLYPOOLSUBCOOLED
CV_PTD PVOL 101325.
CV_PAD 289.9405
CV_VAT 2

		1	5.9937	0.
		2	6.1147	2.66782E-2

=====

=====
CV_ID CPVUCS10A 2491
CV_THR NONEQUILNOFOG ACTIVE
CV_PAS SEPARATE ONLYPOOLSUBCOOLED
CV_PTD PVOL 101325.

CV_PAD	289.9405			
CV_VAT	2			
		1	6.1147	0.
		2	6.2357	2.66782E-2

=====

=====
CV_ID CPVUCS01B 2402
CV_THR NONEQUILNOFOG ACTIVE
CV_PAS SEPARATE ONLYPOOLSUBCOOLED
CV_PTD PVOL 101325.
CV_PAD 289.9405
CV_VAT 2

		1	5.0257	0.
		2	5.1467	2.66782E-2

=====

=====
CV_ID CPVUCS02B 2412
CV_THR NONEQUILNOFOG ACTIVE
CV_PAS SEPARATE ONLYPOOLSUBCOOLED
CV_PTD PVOL 101325.
CV_PAD 289.9405
CV_VAT 2

		1	5.1467	0.
		2	5.2677	2.66782E-2

=====

=====
CV_ID CPVUCS3B 2422
CV_THR NONEQUILNOFOG ACTIVE
CV_PAS SEPARATE ONLYPOOLSUBCOOLED
CV_PTD PVOL 101325.
CV_PAD 289.9405
CV_VAT 2

		1	5.2677	0.
		2	5.3887	2.66782E-2

=====

=====
CV_ID CPVUCS04B 2432
CV_THR NONEQUILNOFOG ACTIVE
CV_PAS SEPARATE ONLYPOOLSUBCOOLED
CV_PTD PVOL 101325.
CV_PAD 289.9405
CV_VAT 2

		1	5.3887	0.
		2	5.5097	2.66782E-2

=====

=====
CV_ID CPVUCS05B 2442
CV_THR NONEQUILNOFOG ACTIVE
CV_PAS SEPARATE ONLYPOOLSUBCOOLED
CV_PTD PVOL 101325.
CV_PAD 289.9405
CV_VAT 2

		1	5.5097	0.
		2	5.6307	2.66782E-2

=====

=====
CV_ID CPVUCS06B 2452
CV_THR NONEQUILNOFOG ACTIVE
CV_PAS SEPARATE ONLYPOOLSUBCOOLED
CV_PTD PVOL 101325.
CV_PAD 289.9405
CV_VAT 2

		1	5.6307	0.
		2	5.7517	2.66782E-2

=====

=====
CV_ID CPVUCS07B 2462
CV_THR NONEQUILNOFOG ACTIVE
CV_PAS SEPARATE ONLYPOOLSUBCOOLED
CV_PTD PVOL 101325.
CV_PAD 289.9405


```

CV_VAT 2
          1      5.7517  0.
          2      5.8727  2.66782E-2
=====
=====
CV_ID    CPVUCS08B      2472
CV_THR   NONEQUILNOFOG  ACTIVE
CV_PAS   SEPARATE ONLYPOOLSUBCOOLED
CV_PTD   PVOL    101325.
CV_PAD   289.9405
CV_VAT   2
          1      5.8727  0.
          2      5.9937  2.66782E-2
=====
=====
CV_ID    CPVUCS09B      2482
CV_THR   NONEQUILNOFOG  ACTIVE
CV_PAS   SEPARATE ONLYPOOLSUBCOOLED
CV_PTD   PVOL    101325.
CV_PAD   289.9405
CV_VAT   2
          1      5.9937  0.
          2      6.1147  2.66782E-2
=====
=====
CV_ID    CPVUCS10B      2492
CV_THR   NONEQUILNOFOG  ACTIVE
CV_PAS   SEPARATE ONLYPOOLSUBCOOLED
CV_PTD   PVOL    101325.
CV_PAD   289.9405
CV_VAT   2
          1      6.1147  0.
          2      6.2357  2.66782E-2
=====
=====
=====HEM=====
=====
CV_ID    CPVHEMA 2501
CV_THR   NONEQUILNOFOG  ACTIVE
CV_PAS   SEPARATE ONLYPOOLSUBCOOLED
CV_PTD   PVOL    101325.
CV_PAD   289.9405
CV_VAT   2
          1      6.2357  0.
          2      6.4007  3.63794E-2
=====
=====
CV_ID    CPVHEMB 2502
CV_THR   NONEQUILNOFOG  ACTIVE
CV_PAS   SEPARATE ONLYPOOLSUBCOOLED
CV_PTD   PVOL    101325.
CV_PAD   289.9405
CV_VAT   2
          1      6.2357  0.
          2      6.4007  3.63794E-2
=====
=====
=====TOP=====
=====
CV_ID    CPVTOP01A      2601
CV_THR   NONEQUILNOFOG  ACTIVE
CV_PAS   SEPARATE ONLYPOOLSUBCOOLED
CV_PTD   PVOL    101325.
CV_PAD   289.9405
CV_VAT   2
          1      6.4007  0.
          2      6.7238  7.12374E-2
=====
=====
CV_ID    CPVTOP02A      2611
CV_THR   NONEQUILNOFOG  ACTIVE

```

```

CV_PAS   SEPARATE ONLYPOOLSUBCOOLED
CV_PTD   PVOL    101325.
CV_PAD   289.9405
CV_VAT   2
          1      6.7238  0.
          2      7.0469  7.12374E-2
=====
=====
CV_ID    CPVTOP3A 2621
CV_THR   NONEQUILNOFOG  ACTIVE
CV_PAS   SEPARATE ONLYPOOLSUBCOOLED
CV_PTD   PVOL    101325.
CV_PAD   289.9405
CV_VAT   2
          1      7.0469  0.
          2      7.37    7.12374E-2
=====
=====
CV_ID    CPVTOP01B      2602
CV_THR   NONEQUILNOFOG  ACTIVE
CV_PAS   SEPARATE ONLYPOOLSUBCOOLED
CV_PTD   PVOL    101325.
CV_PAD   289.9405
CV_VAT   2
          1      6.4007  0.
          2      6.7238  7.12374E-2
=====
=====
CV_ID    CPVTOP02B      2612
CV_THR   NONEQUILNOFOG  ACTIVE
CV_PAS   SEPARATE ONLYPOOLSUBCOOLED
CV_PTD   PVOL    101325.
CV_PAD   289.9405
CV_VAT   2
          1      6.7238  0.
          2      7.0469  7.12374E-2
=====
=====
CV_ID    CPVTOP3B 2622
CV_THR   NONEQUILNOFOG  ACTIVE
CV_PAS   SEPARATE ONLYPOOLSUBCOOLED
CV_PTD   PVOL    101325.
CV_PAD   289.9405
CV_VAT   2
          1      7.0469  0.
          2      7.37    7.12374E-2
=====
=====
CV_ID    VERYTOP 3333
CV_THR   NONEQUILNOFOG  ACTIVE
CV_PAS   SEPARATE ONLYATM SUPERHEATED
CV_PTD   PVOL    101325.
CV_AAD   TATM    296.4465
CV_NCG   2      PNCG    101325.
          1      N2      .8
          2      O2      .2
CV_VAT   2
          1      7.37    0.
          2      8.00    .2777806
=====
=====
CV_ID    TOPAMB 4444
CV_THR   NONEQUILNOFOG  TIME-INDEP
CV_PAS   SEPARATE ONLYATM SUPERHEATED
CV_PTD   PVOL    101325.
CV_AAD   TATM    296.4465
CV_NCG   2      PNCG    101325.
          1      N2      .8
          2      O2      .2
CV_VAT   2
          1      8.      0.

```

```

                2          9.          1.
!=====
=====

fl-hpc.h.inp
AllowReplace
FL_INPUT
!=====HORIZONTAL=====
=====
!=====LCS=====
=====
FL_ID      LCS01AB
FL_FT      LCS01A  LCS01B  .8412  .8412
FL_GEO     .1012  .1308  1.
FL_JSW     3      NOBUBBLERISE  NOBUBBLERISE
FL_USL     0.     0.     0.     0.
FL_JLF     .6477  1.0347
FL_JLT     .6477  1.0347
FL_SEG     1
                1          .1012  .1308  .3911
!=====
=====
FL_ID      LCS02AB
FL_FT      LCS02A  LCS02B  1.2282  1.2282
FL_GEO     .1012  .1308  1.
FL_JSW     3      NOBUBBLERISE  NOBUBBLERISE
FL_USL     0.     0.     0.     0.
FL_JLF     1.0347  1.4217
FL_JLT     1.0347  1.4217
FL_SEG     1
                1          .1012  .1308  .5232
!=====
=====
FL_ID      LCS3AB
FL_FT      LCS3A   LCS3B   1.6152  1.6152
FL_GEO     .1012  .1308  1.
FL_JSW     3      NOBUBBLERISE  NOBUBBLERISE
FL_USL     0.     0.     0.     0.
FL_JLF     1.4217  1.8087
FL_JLT     1.4217  1.8087
FL_SEG     1
                1          .1012  .1308  .5232
!=====
=====
FL_ID      LCS4AB
FL_FT      LCS04A  LCS04B  2.0022  2.0022
FL_GEO     .1012  .1308  1.
FL_JSW     3      NOBUBBLERISE  NOBUBBLERISE
FL_USL     0.     0.     0.     0.
FL_JLF     1.8087  2.1957
FL_JLT     1.8087  2.1957
FL_SEG     1
                1          .1012  .1308  .5232
!=====
=====
FL_ID      LCS05AB
FL_FT      LCS05A  LCS05B  2.3892  2.3892
FL_GEO     .1012  .1308  1.
FL_JSW     3      NOBUBBLERISE  NOBUBBLERISE
FL_USL     0.     0.     0.     0.
FL_JLF     2.1957  2.5827
FL_JLT     2.1957  2.5827
FL_SEG     1
                1          .1012  .1308  .5232
!=====
=====
FL_ID      LCS06AB
FL_FT      LCS06A  LCS06B  2.7762  2.7762
FL_GEO     .1012  .1308  1.
FL_JSW     3      NOBUBBLERISE  NOBUBBLERISE
FL_USL     0.     0.     0.     0.

```

```

FL_JLF     2.5827  2.9697
FL_JLT     2.5827  2.9697
FL_SEG     1
                1          .1012  .1308  .5232
!=====
=====
FL_ID      LCS07AB
FL_FT      LCS07A  LCS07B  3.1632  3.1632
FL_GEO     .1012  .1308  1.
FL_JSW     3      NOBUBBLERISE  NOBUBBLERISE
FL_USL     0.     0.     0.     0.
FL_JLF     2.9697  3.3567
FL_JLT     2.9697  3.3567
FL_SEG     1
                1          .1012  .1308  .5232
!=====
=====
FL_ID      LCS08AB
FL_FT      LCS08A  LCS08B  3.5502  3.5502
FL_GEO     .1012  .1308  1.
FL_JSW     3      NOBUBBLERISE  NOBUBBLERISE
FL_USL     0.     0.     0.     0.
FL_JLF     3.3567  3.7437
FL_JLT     3.3567  3.7437
FL_SEG     1
                1          .1012  .1308  .5232
!=====
=====
FL_ID      LCS09AB
FL_FT      LCS09A  LCS09B  3.9372  3.9372
FL_GEO     .1012  .1308  1.
FL_JSW     3      NOBUBBLERISE  NOBUBBLERISE
FL_USL     0.     0.     0.     0.
FL_JLF     3.7437  4.1307
FL_JLT     3.7437  4.1307
FL_SEG     1
                1          .1012  .1308  .5232
!=====
=====
FL_ID      LCS10AB
FL_FT      LCS10A  LCS10B  4.3242  4.3242
FL_GEO     .1012  .1308  1.
FL_JSW     3      NOBUBBLERISE  NOBUBBLERISE
FL_USL     0.     0.     0.     0.
FL_JLF     4.1307  4.5177
FL_JLT     4.1307  4.5177
FL_SEG     1
                1          .1012  .1308  .5232
!=====
=====
!=====ECS=====
=====
FL_ID      ECS01AB
FL_FT      ECS01A  ECS01B  4.6447  4.6447
FL_GEO     9.808E-2 .1931  1.
FL_JSW     3      NOBUBBLERISE  NOBUBBLERISE
FL_USL     0.     0.     0.     0.
FL_JLF     4.5177  4.7717
FL_JLT     4.5177  4.7717
FL_SEG     1
                1          9.808E-2 .1931  .7723
!=====
=====
FL_ID      ECS02AB
FL_FT      ECS02A  ECS02B  4.8987  4.8987
FL_GEO     9.808E-2 .1931  1.
FL_JSW     3      NOBUBBLERISE  NOBUBBLERISE
FL_USL     0.     0.     0.     0.
FL_JLF     4.7717  5.0257
FL_JLT     4.7717  5.0257
FL_SEG     1

```

```

1          9.808E-2 .1931 .7723
=====
=====UCS=====
=====
FL_ID      UCS01AB
FL_FT      UCS01A  UCS01B  5.0862  5.0862
FL_GEO     6.032E-2 .2492  1.
FL_JSW     3        NOBUBBLERISE  NOBUBBLERISE
FL_USL     0.        0.        0.        0.
FL_JLF     5.0257  5.1467
FL_JLT     5.0257  5.1467
FL_SEG     1
1          6.032E-2 .2492 .9970
=====
=====
FL_ID      UCS02AB
FL_FT      UCS02A  UCS02B  5.2072  5.2072
FL_GEO     6.032E-2 .2492  1.
FL_JSW     3        NOBUBBLERISE  NOBUBBLERISE
FL_USL     0.        0.        0.        0.
FL_JLF     5.1467  5.2677
FL_JLT     5.1467  5.2677
FL_SEG     1
1          6.032E-2 .2492 .9970
=====
=====
FL_ID      UCS3AB
FL_FT      UCS3A   UCS3B   5.3282  5.3282
FL_GEO     6.032E-2 .2492  1.
FL_JSW     3        NOBUBBLERISE  NOBUBBLERISE
FL_USL     0.        0.        0.        0.
FL_JLF     5.2677  5.3887
FL_JLT     5.2677  5.3887
FL_SEG     1
1          6.032E-2 .2492 .9970
=====
=====
FL_ID      UCS04AB
FL_FT      UCS04A  UCS04B  5.4492  5.4492
FL_GEO     6.032E-2 .2492  1.
FL_JSW     3        NOBUBBLERISE  NOBUBBLERISE
FL_USL     0.        0.        0.        0.
FL_JLF     5.3887  5.5097
FL_JLT     5.3887  5.5097
FL_SEG     1
1          6.032E-2 .2492 .9970
=====
=====
FL_ID      UCS05AB
FL_FT      UCS05A  UCS05B  5.5702  5.5702
FL_GEO     6.032E-2 .2492  1.
FL_JSW     3        NOBUBBLERISE  NOBUBBLERISE
FL_USL     0.        0.        0.        0.
FL_JLF     5.5097  5.6307
FL_JLT     5.5097  5.6307
FL_SEG     1
1          6.032E-2 .2492 .9970
=====
=====
FL_ID      UCS06AB
FL_FT      UCS06A  UCS06B  5.6912  5.6912
FL_GEO     6.032E-2 .2492  1.
FL_JSW     3        NOBUBBLERISE  NOBUBBLERISE
FL_USL     0.        0.        0.        0.
FL_JLF     5.6307  5.7517
FL_JLT     5.6307  5.7517
FL_SEG     1
1          6.032E-2 .2492 .9970
=====
=====

```

```

FL_ID      UCS07AB
FL_FT      UCS07A  UCS07B  5.8122  5.8122
FL_GEO     6.032E-2 .2492  1.
FL_JSW     3        NOBUBBLERISE  NOBUBBLERISE
FL_USL     0.        0.        0.        0.
FL_JLF     5.7517  5.8727
FL_JLT     5.7517  5.8727
FL_SEG     1
1          6.032E-2 .2492 .9970
=====
=====
FL_ID      UCS08AB
FL_FT      UCS08A  UCS08B  5.9332  5.9332
FL_GEO     6.032E-2 .2492  1.
FL_JSW     3        NOBUBBLERISE  NOBUBBLERISE
FL_USL     0.        0.        0.        0.
FL_JLF     5.8727  5.9937
FL_JLT     5.8727  5.9937
FL_SEG     1
1          6.032E-2 .2492 .9970
=====
=====
FL_ID      UCS09AB
FL_FT      UCS09A  UCS09B  6.0542  6.0542
FL_GEO     6.032E-2 .2492  1.
FL_JSW     3        NOBUBBLERISE  NOBUBBLERISE
FL_USL     0.        0.        0.        0.
FL_JLF     5.9937  6.1147
FL_JLT     5.9937  6.1147
FL_SEG     1
1          6.032E-2 .2492 .9970
=====
=====
FL_ID      UCS10AB
FL_FT      UCS10A  UCS10B  6.1752  6.1752
FL_GEO     6.032E-2 .2492  1.
FL_JSW     3        NOBUBBLERISE  NOBUBBLERISE
FL_USL     0.        0.        0.        0.
FL_JLF     6.1147  6.2357
FL_JLT     6.1147  6.2357
FL_SEG     1
1          6.032E-2 .2492 .9970
=====
=====
=====UCS
HEM=====
FL_ID      UCSHEMAB
FL_FT      HEMA    HEMB    6.3182  6.3182
FL_GEO     5.938E-2 .2492  1.
FL_JSW     3        NOBUBBLERISE  NOBUBBLERISE
FL_USL     0.        0.        0.        0.
FL_JLF     6.2357  6.4007
FL_JLT     6.2357  6.4007
FL_SEG     1
1          5.983E-2 .2492 .375
=====
=====
fl-hpc-v.inp
AllowReplace
FL_INPUT
=====VERTICAL=====
=====
=====LCS
A=====
FL_ID      LCS12A
FL_FT      LCS01A  LCS02A  1.0347  1.0347
FL_GEO     5.376E-2 .387    1.
FL_JSW     0        NOBUBBLERISE  NOBUBBLERISE
FL_USL     0.        0.        0.        0.
FL_SEG     1

```

```

1      5.376E-2 .387 .2616
=====
=====
FL_ID   LCS23A
FL_FT   LCS02A  LCS3A  1.4217  1.4217
FL_GEO  5.376E-2 .387  1.
FL_JSW  0      NOBUBBLERISE  NOBUBBLERISE
FL_USL  0.      0.      0.      0.
FL_SEG  1
1      5.376E-2 .387 .2616
=====
=====
FL_ID   LCS34A
FL_FT   LCS3A  LCS04A  1.8087  1.8087
FL_GEO  5.376E-2 .387  1.
FL_JSW  0      NOBUBBLERISE  NOBUBBLERISE
FL_USL  0.      0.      0.      0.
FL_SEG  1
1      5.376E-2 .387 .2616
=====
=====
FL_ID   LCS45A
FL_FT   LCS04A  LCS05A  2.1957  2.1957
FL_GEO  5.376E-2 .387  1.
FL_JSW  0      NOBUBBLERISE  NOBUBBLERISE
FL_USL  0.      0.      0.      0.
FL_SEG  1
1      5.376E-2 .387 .2616
=====
=====
FL_ID   LCS56A
FL_FT   LCS05A  LCS06A  2.5827  2.5827
FL_GEO  5.376E-2 .387  1.
FL_JSW  0      NOBUBBLERISE  NOBUBBLERISE
FL_USL  0.      0.      0.      0.
FL_SEG  1
1      5.376E-2 .387 .2616
=====
=====
FL_ID   LCS67A
FL_FT   LCS06A  LCS07A  2.9697  2.9697
FL_GEO  5.376E-2 .387  1.
FL_JSW  0      NOBUBBLERISE  NOBUBBLERISE
FL_USL  0.      0.      0.      0.
FL_SEG  1
1      5.376E-2 .387 .2616
=====
=====
FL_ID   LCS78A
FL_FT   LCS07A  LCS08A  3.3567  3.3567
FL_GEO  5.376E-2 .387  1.
FL_JSW  0      NOBUBBLERISE  NOBUBBLERISE
FL_USL  0.      0.      0.      0.
FL_SEG  1
1      5.376E-2 .387 .2616
=====
=====
FL_ID   LCS89A
FL_FT   LCS08A  LCS09A  3.7437  3.7437
FL_GEO  5.376E-2 .387  1.
FL_JSW  0      NOBUBBLERISE  NOBUBBLERISE
FL_USL  0.      0.      0.      0.
FL_SEG  1
1      5.376E-2 .387 .2616
=====
=====
FL_ID   LCS90A
FL_FT   LCS09A  LCS10A  4.1307  4.1307
FL_GEO  5.376E-2 .387  1.
FL_JSW  0      NOBUBBLERISE  NOBUBBLERISE
FL_USL  0.      0.      0.      0.

```

```

FL_SEG  1
1      5.376E-2 .387 .2616
=====
=====
=====LCS
B=====
FL_ID   LCS12B
FL_FT   LCS01B  LCS02B  1.0347  1.0347
FL_GEO  5.376E-2 .387  1.
FL_JSW  0      NOBUBBLERISE  NOBUBBLERISE
FL_USL  0.      0.      0.      0.
FL_SEG  1
1      5.376E-2 .387 .2616
=====
=====
FL_ID   LCS23B
FL_FT   LCS02B  LCS3B  1.4217  1.4217
FL_GEO  5.376E-2 .387  1.
FL_JSW  0      NOBUBBLERISE  NOBUBBLERISE
FL_USL  0.      0.      0.      0.
FL_SEG  1
1      5.376E-2 .387 .2616
=====
=====
FL_ID   LCS34B
FL_FT   LCS3B  LCS04B  1.8087  1.8087
FL_GEO  5.376E-2 .387  1.
FL_JSW  0      NOBUBBLERISE  NOBUBBLERISE
FL_USL  0.      0.      0.      0.
FL_SEG  1
1      5.376E-2 .387 .2616
=====
=====
FL_ID   LCS45B
FL_FT   LCS04B  LCS05B  2.1957  2.1957
FL_GEO  5.376E-2 .387  1.
FL_JSW  0      NOBUBBLERISE  NOBUBBLERISE
FL_USL  0.      0.      0.      0.
FL_SEG  1
1      5.376E-2 .387 .2616
=====
=====
FL_ID   LCS56B
FL_FT   LCS05B  LCS06B  2.5827  2.5827
FL_GEO  5.376E-2 .387  1.
FL_JSW  0      NOBUBBLERISE  NOBUBBLERISE
FL_USL  0.      0.      0.      0.
FL_SEG  1
1      5.376E-2 .387 .2616
=====
=====
FL_ID   LCS67B
FL_FT   LCS06B  LCS07B  2.9697  2.9697
FL_GEO  5.376E-2 .387  1.
FL_JSW  0      NOBUBBLERISE  NOBUBBLERISE
FL_USL  0.      0.      0.      0.
FL_SEG  1
1      5.376E-2 .387 .2616
=====
=====
FL_ID   LCS78B
FL_FT   LCS07B  LCS08B  3.3567  3.3567
FL_GEO  5.376E-2 .387  1.
FL_JSW  0      NOBUBBLERISE  NOBUBBLERISE
FL_USL  0.      0.      0.      0.
FL_SEG  1
1      5.376E-2 .387 .2616
=====
=====
FL_ID   LCS89B
FL_FT   LCS08B  LCS09B  3.7437  3.7437

```

```

FL_GEO 5.376E-2 .387 1.
FL_JSW 0 NOBUBBLERISE NOBUBBLERISE
FL_USL 0. 0. 0. 0.
FL_SEG 1

=====
=====
1 5.376E-2 .387 .2616
=====
=====
FL_ID LCS90B
FL_FT LCS09B LCS10B 4.1307 4.1307
FL_GEO 5.376E-2 .387 1.
FL_JSW 0 NOBUBBLERISE NOBUBBLERISE
FL_USL 0. 0. 0. 0.
FL_SEG 1

=====
=====
1 5.376E-2 .387 .2616
=====
=====
=====LCS TO
ECS=====
FL_ID LCS2ECSA
FL_FT LCS10A ECS01A 4.5177 4.5177
FL_GEO .1171 .3205 1.
FL_JSW 0 NOBUBBLERISE NOBUBBLERISE
FL_USL 0. 0. 0. 0.
FL_SEG 1

=====
=====
1 .1171 .3205 .3862
=====
=====
FL_ID LCS2ECSB
FL_FT LCS10B ECS01B 4.5177 4.5177
FL_GEO .1171 .3205 1.
FL_JSW 0 NOBUBBLERISE NOBUBBLERISE
FL_USL 0. 0. 0. 0.
FL_SEG 1

=====
=====
1 .1171 .3205 .3862
=====
=====
=====ECS=====
=====
FL_ID ECS12A
FL_FT ECS01A ECS02A 4.7717 4.7717
FL_GEO .1171 .254 1.
FL_JSW 0 NOBUBBLERISE NOBUBBLERISE
FL_USL 0. 0. 0. 0.
FL_SEG 1

=====
=====
1 .1171 .254 .3862
=====
=====
FL_ID ECS12B
FL_FT ECS01B ECS02B 4.7717 4.7717
FL_GEO .1171 .254 1.
FL_JSW 0 NOBUBBLERISE NOBUBBLERISE
FL_USL 0. 0. 0. 0.
FL_SEG 1

=====
=====
1 .1171 .254 .3862
=====
=====
=====ECS TO
UCS=====
FL_ID ECS2UCSA
FL_FT ECS02A UCS01A 5.0257 5.0257
FL_GEO .1952 .1875 1.
FL_JSW 0 NOBUBBLERISE NOBUBBLERISE
FL_USL 0. 0. 0. 0.
FL_SEG 1

=====
=====
1 .1952 .1875 .4985
=====
=====
FL_ID ECS2UCSB
FL_FT ECS02B UCS01B 5.0257 5.0257
FL_GEO .1952 .1875 1.
FL_JSW 0 NOBUBBLERISE NOBUBBLERISE

```

```

FL_USL 0. 0. 0. 0.
FL_SEG 1

=====
=====
1 .1952 .1875 .4985
=====
=====
=====UCS
A=====
FL_ID UCS12A
FL_FT UCS01A UCS02A 5.1467 5.1467
FL_GEO .1952 .121 1.
FL_JSW 0 NOBUBBLERISE NOBUBBLERISE
FL_USL 0. 0. 0. 0.
FL_SEG 1

=====
=====
1 .1952 .121 .4985
=====
=====
FL_ID UCS23A
FL_FT UCS02A UCS3A 5.2677 5.2677
FL_GEO .1952 .121 1.
FL_JSW 0 NOBUBBLERISE NOBUBBLERISE
FL_USL 0. 0. 0. 0.
FL_SEG 1

=====
=====
1 .1952 .121 .4985
=====
=====
FL_ID UCS34A
FL_FT UCS3A UCS04A 5.3887 5.3887
FL_GEO .1952 .121 1.
FL_JSW 0 NOBUBBLERISE NOBUBBLERISE
FL_USL 0. 0. 0. 0.
FL_SEG 1

=====
=====
1 .1952 .121 .4985
=====
=====
FL_ID UCS45A
FL_FT UCS04A UCS05A 5.5097 5.5097
FL_GEO .1952 .121 1.
FL_JSW 0 NOBUBBLERISE NOBUBBLERISE
FL_USL 0. 0. 0. 0.
FL_SEG 1

=====
=====
1 .1952 .121 .4985
=====
=====
FL_ID UCS56A
FL_FT UCS05A UCS06A 5.6307 5.6307
FL_GEO .1952 .121 1.
FL_JSW 0 NOBUBBLERISE NOBUBBLERISE
FL_USL 0. 0. 0. 0.
FL_SEG 1

=====
=====
1 .1952 .121 .4985
=====
=====
FL_ID UCS67A
FL_FT UCS06A UCS07A 5.7517 5.7517
FL_GEO .1952 .121 1.
FL_JSW 0 NOBUBBLERISE NOBUBBLERISE
FL_USL 0. 0. 0. 0.
FL_SEG 1

=====
=====
1 .1952 .121 .4985
=====
=====
FL_ID UCS78A
FL_FT UCS07A UCS08A 5.8727 5.8727
FL_GEO .1952 .121 1.
FL_JSW 0 NOBUBBLERISE NOBUBBLERISE
FL_USL 0. 0. 0. 0.
FL_SEG 1

=====
=====
1 .1952 .121 .4985
=====
=====
FL_ID UCS89A

```

```

FL_FT    UCS08A    UCS09A    5.9937    5.9937
FL_GEO    .1952    .121    1.
FL_JSW    0        NOBUBBLERISE    NOBUBBLERISE
FL_USL    0.        0.        0.        0.
FL_SEG    1
                1        .1952    .121    .4985
=====
=====
FL_ID    UCS90A
FL_FT    UCS09A    UCS10A    6.1147    6.1147
FL_GEO    .1952    .121    1.
FL_JSW    0        NOBUBBLERISE    NOBUBBLERISE
FL_USL    0.        0.        0.        0.
FL_SEG    1
                1        .1952    .121    .4985
=====
=====
FL_ID    UCS10HEMA
FL_FT    UCS10A    HEMA    6.2357    6.2357
FL_GEO    .1952    .143    1.
FL_JSW    0        NOBUBBLERISE    NOBUBBLERISE
FL_USL    0.        0.        0.        0.
FL_SEG    1
                1        .1952    .143    .4985
=====
=====
=====UCS
B=====
FL_ID    UCS12B
FL_FT    UCS01B    UCS02B    5.1467    5.1467
FL_GEO    .1952    .121    1.
FL_JSW    0        NOBUBBLERISE    NOBUBBLERISE
FL_USL    0.        0.        0.        0.
FL_SEG    1
                1        .1952    .121    .4985
=====
=====
FL_ID    UCS23B
FL_FT    UCS02B    UCS3B    5.2677    5.2677
FL_GEO    .1952    .121    1.
FL_JSW    0        NOBUBBLERISE    NOBUBBLERISE
FL_USL    0.        0.        0.        0.
FL_SEG    1
                1        .1952    .121    .4985
=====
=====
FL_ID    UCS34B
FL_FT    UCS3B    UCS04B    5.3887    5.3887
FL_GEO    .1952    .121    1.
FL_JSW    0        NOBUBBLERISE    NOBUBBLERISE
FL_USL    0.        0.        0.        0.
FL_SEG    1
                1        .1952    .121    .4985
=====
=====
FL_ID    UCS45B
FL_FT    UCS04B    UCS05B    5.5097    5.5097
FL_GEO    .1952    .121    1.
FL_JSW    0        NOBUBBLERISE    NOBUBBLERISE
FL_USL    0.        0.        0.        0.
FL_SEG    1
                1        .1952    .121    .4985
=====
=====
FL_ID    UCS56B
FL_FT    UCS05B    UCS06B    5.6307    5.6307
FL_GEO    .1952    .121    1.
FL_JSW    0        NOBUBBLERISE    NOBUBBLERISE
FL_USL    0.        0.        0.        0.
FL_SEG    1
                1        .1952    .121    .4985

```

```

=====
=====
FL_ID    UCS67B
FL_FT    UCS06B    UCS07B    5.7517    5.7517
FL_GEO    .1952    .121    1.
FL_JSW    0        NOBUBBLERISE    NOBUBBLERISE
FL_USL    0.        0.        0.        0.
FL_SEG    1
                1        .1952    .121    .4985
=====
=====
FL_ID    UCS78B
FL_FT    UCS07B    UCS08B    5.8727    5.8727
FL_GEO    .1952    .121    1.
FL_JSW    0        NOBUBBLERISE    NOBUBBLERISE
FL_USL    0.        0.        0.        0.
FL_SEG    1
                1        .1952    .121    .4985
=====
=====
FL_ID    UCS89B
FL_FT    UCS08B    UCS09B    5.9937    5.9937
FL_GEO    .1952    .121    1.
FL_JSW    0        NOBUBBLERISE    NOBUBBLERISE
FL_USL    0.        0.        0.        0.
FL_SEG    1
                1        .1952    .121    .4985
=====
=====
FL_ID    UCS90B
FL_FT    UCS09B    UCS10B    6.1147    6.1147
FL_GEO    .1952    .121    1.
FL_JSW    0        NOBUBBLERISE    NOBUBBLERISE
FL_USL    0.        0.        0.        0.
FL_SEG    1
                1        .1952    .121    .4985
=====
=====
FL_ID    UCS10HEMB
FL_FT    UCS10B    HEMB    6.2357    6.2357
FL_GEO    .1952    .143    1.
FL_JSW    0        NOBUBBLERISE    NOBUBBLERISE
FL_USL    0.        0.        0.        0.
FL_SEG    1
                1        .1952    .143    .4985
=====
=====
fl-cpv-h.inp
AllowReplace
FL_INPUT
=====HORIZONTAL=====
=====
=====BOT=====
=====
FL_ID    CPVBOT01AB
FL_FT    CPVBOT01A    CPVBOT01B    .161925
                .161925
FL_GEO    .2427    .3747    1.
FL_JSW    3        NOBUBBLERISE    NOBUBBLERISE
FL_USL    0.        0.        0.        0.
FL_JLF    0.        .32385
FL_JLT    0.        .32385
FL_SEG    1
                1        .2427    .3747    .6948
=====
=====
FL_ID    CPVBOT02AB
FL_FT    CPVBOT02A    CPVBOT02B    .485775
                .485775
FL_GEO    .2427    .3747    1.

```

FL_JSW	3	NOBUBBLERISE	NOBUBBLERISE		
FL_USL	0.	0.	0.	0.	
FL_JLF	.32385	.6477			
FL_JLT	.32385	.6477			
FL_SEG	1				
		1	.2427	.3747	1.499
=====					
=====					
=====LCS=====					
=====					
FL_ID	CPVLC01AB				
FL_FT	CPVLC01A	CPVLC01B		.8412	
	.8412				
FL_GEO	.29	.3747	1.		
FL_JSW	3	NOBUBBLERISE	NOBUBBLERISE		
FL_USL	0.	0.	0.	0.	
FL_JLF	.6477	1.0347			
FL_JLT	.6477	1.0347			
FL_SEG	1				
		1	.29	.3747	1.499
=====					
=====					
FL_ID	CPVLC02AB				
FL_FT	CPVLC02A	CPVLC02B		1.2282	
	1.2282				
FL_GEO	.29	.3747	1.		
FL_JSW	3	NOBUBBLERISE	NOBUBBLERISE		
FL_USL	0.	0.	0.	0.	
FL_JLF	1.0347	1.4217			
FL_JLT	1.0347	1.4217			
FL_SEG	1				
		1	.29	.3747	1.499
=====					
=====					
FL_ID	CPVLC03AB				
FL_FT	CPVLC03A	CPVLC03B	1.6152	1.6152	
FL_GEO	.29	.3747	1.		
FL_JSW	3	NOBUBBLERISE	NOBUBBLERISE		
FL_USL	0.	0.	0.	0.	
FL_JLF	1.4217	1.8087			
FL_JLT	1.4217	1.8087			
FL_SEG	1				
		1	.29	.3747	1.499
=====					
=====					
FL_ID	CPVLC04AB				
FL_FT	CPVLC04A	CPVLC04B		2.0022	
	2.0022				
FL_GEO	.29	.3747	1.		
FL_JSW	3	NOBUBBLERISE	NOBUBBLERISE		
FL_USL	0.	0.	0.	0.	
FL_JLF	1.8087	2.1957			
FL_JLT	1.8087	2.1957			
FL_SEG	1				
		1	.29	.3747	1.499
=====					
=====					
FL_ID	CPVLC05AB				
FL_FT	CPVLC05A	CPVLC05B		2.3892	
	2.3892				
FL_GEO	.29	.3747	1.		
FL_JSW	3	NOBUBBLERISE	NOBUBBLERISE		
FL_USL	0.	0.	0.	0.	
FL_JLF	2.1957	2.5827			
FL_JLT	2.1957	2.5827			
FL_SEG	1				
		1	.29	.3747	1.499
=====					
=====					
FL_ID	CPVLC06AB				

FL_FT	CPVLC06A	CPVLC06B		2.7762	
	2.7762				
FL_GEO	.29	.3747	1.		
FL_JSW	3	NOBUBBLERISE	NOBUBBLERISE		
FL_USL	0.	0.	0.	0.	
FL_JLF	2.5827	2.9697			
FL_JLT	2.5827	2.9697			
FL_SEG	1				
		1	.29	.3747	1.499
=====					
=====					
FL_ID	CPVLC07AB				
FL_FT	CPVLC07A	CPVLC07B		3.1632	
	3.1632				
FL_GEO	.29	.3747	1.		
FL_JSW	3	NOBUBBLERISE	NOBUBBLERISE		
FL_USL	0.	0.	0.	0.	
FL_JLF	2.9697	3.3567			
FL_JLT	2.9697	3.3567			
FL_SEG	1				
		1	.29	.3747	1.499
=====					
=====					
FL_ID	CPVLC08AB				
FL_FT	CPVLC08A	CPVLC08B		3.5502	
	3.5502				
FL_GEO	.29	.3747	1.		
FL_JSW	3	NOBUBBLERISE	NOBUBBLERISE		
FL_USL	0.	0.	0.	0.	
FL_JLF	3.3567	3.7437			
FL_JLT	3.3567	3.7437			
FL_SEG	1				
		1	.29	.3747	1.499
=====					
=====					
FL_ID	CPVLC09AB				
FL_FT	CPVLC09A	CPVLC09B		3.9372	
	3.9372				
FL_GEO	.29	.3747	1.		
FL_JSW	3	NOBUBBLERISE	NOBUBBLERISE		
FL_USL	0.	0.	0.	0.	
FL_JLF	3.7437	4.1307			
FL_JLT	3.7437	4.1307			
FL_SEG	1				
		1	.29	.3747	1.499
=====					
=====					
FL_ID	CPVLC10AB				
FL_FT	CPVLC10A	CPVLC10B		4.3242	
	4.3242				
FL_GEO	.29	.3747	1.		
FL_JSW	3	NOBUBBLERISE	NOBUBBLERISE		
FL_USL	0.	0.	0.	0.	
FL_JLF	4.1307	4.5177			
FL_JLT	4.1307	4.5177			
FL_SEG	1				
		1	.29	.3747	1.499
=====					
=====					
=====ECS=====					
=====					
FL_ID	CPVECS01AB				
FL_FT	CPVECS01A	CPVECS01B		4.6447	
	4.6447				
FL_GEO	190.3E-3	.3747	1.		
FL_JSW	3	NOBUBBLERISE	NOBUBBLERISE		
FL_USL	0.	0.	0.	0.	
FL_JLF	4.5177	4.7717			
FL_JLT	4.5177	4.7717			
FL_SEG	1				
		1	190.3E-3	.3747	.7723

```

=====
=====
FL_ID      CPVECS02AB
FL_FT      CPVECS02A      CPVECS02B      4.8987
4.8987
FL_GEO     190.3E-3 .3747 1.
FL_JSW     3      NOBUBBLERISE      NOBUBBLERISE
FL_USL     0.      0.      0.      0.
FL_JLF     4.7717 5.0257
FL_JLT     4.7717 5.0257
FL_SEG     1
1      190.3E-3 .3747 .7723
=====
=====
=====UCS=====
=====
FL_ID      CPVUCS01AB
FL_FT      CPVUCS01A      CPVUCS01B      5.0862
5.0862
FL_GEO     9.067E-2 .3747 1.
FL_JSW     3      NOBUBBLERISE      NOBUBBLERISE
FL_USL     0.      0.      0.      0.
FL_JLF     5.0257 5.1467
FL_JLT     5.0257 5.1467
FL_SEG     1
1      9.067E-2 .3747 1.499
=====
=====
FL_ID      CPVUCS02AB
FL_FT      CPVUCS02A      CPVUCS02B      5.2072
5.2072
FL_GEO     9.067E-2 .3747 1.
FL_JSW     3      NOBUBBLERISE      NOBUBBLERISE
FL_USL     0.      0.      0.      0.
FL_JLF     5.1467 5.2677
FL_JLT     5.1467 5.2677
FL_SEG     1
1      9.067E-2 .3747 1.499
=====
=====
FL_ID      CPVUCS3AB
FL_FT      CPVUCS3A CPVUCS3B 5.3282 5.3282
FL_GEO     9.067E-2 .3747 1.
FL_JSW     3      NOBUBBLERISE      NOBUBBLERISE
FL_USL     0.      0.      0.      0.
FL_JLF     5.2677 5.3887
FL_JLT     5.2677 5.3887
FL_SEG     1
1      9.067E-2 .3747 1.499
=====
=====
FL_ID      CPVUCS04AB
FL_FT      CPVUCS04A      CPVUCS04B      5.4492
5.4492
FL_GEO     9.067E-2 .3747 1.
FL_JSW     3      NOBUBBLERISE      NOBUBBLERISE
FL_USL     0.      0.      0.      0.
FL_JLF     5.3887 5.5097
FL_JLT     5.3887 5.5097
FL_SEG     1
1      9.067E-2 .3747 1.499
=====
=====
FL_ID      CPVUCS05AB
FL_FT      CPVUCS05A      CPVUCS05B      5.5702
5.5702
FL_GEO     9.067E-2 .3747 1.
FL_JSW     3      NOBUBBLERISE      NOBUBBLERISE
FL_USL     0.      0.      0.      0.
FL_JLF     5.5097 5.6307
FL_JLT     5.5097 5.6307

```

```

FL_SEG     1
1      9.067E-2 .3747 1.499
=====
=====
FL_ID      CPVUCS06AB
FL_FT      CPVUCS06A      CPVUCS06B      5.6912
5.6912
FL_GEO     9.067E-2 .3747 1.
FL_JSW     3      NOBUBBLERISE      NOBUBBLERISE
FL_USL     0.      0.      0.      0.
FL_JLF     5.6307 5.7517
FL_JLT     5.6307 5.7517
FL_SEG     1
1      9.067E-2 .3747 1.499
=====
=====
FL_ID      CPVUCS07AB
FL_FT      CPVUCS07A      CPVUCS07B      5.8122
5.8122
FL_GEO     9.067E-2 .3747 1.
FL_JSW     3      NOBUBBLERISE      NOBUBBLERISE
FL_USL     0.      0.      0.      0.
FL_JLF     5.7517 5.8727
FL_JLT     5.7517 5.8727
FL_SEG     1
1      9.067E-2 .3747 1.499
=====
=====
FL_ID      CPVUCS08AB
FL_FT      CPVUCS08A      CPVUCS08B      5.9332
5.9332
FL_GEO     9.067E-2 .3747 1.
FL_JSW     3      NOBUBBLERISE      NOBUBBLERISE
FL_USL     0.      0.      0.      0.
FL_JLF     5.8727 5.9937
FL_JLT     5.8727 5.9937
FL_SEG     1
1      9.067E-2 .3747 1.499
=====
=====
FL_ID      CPVUCS09AB
FL_FT      CPVUCS09A      CPVUCS09B      6.0542
6.0542
FL_GEO     9.067E-2 .3747 1.
FL_JSW     3      NOBUBBLERISE      NOBUBBLERISE
FL_USL     0.      0.      0.      0.
FL_JLF     5.9937 6.1147
FL_JLT     5.9937 6.1147
FL_SEG     1
1      9.067E-2 .3747 1.499
=====
=====
FL_ID      CPVUCS10AB
FL_FT      CPVUCS10A      CPVUCS10B      6.1752
6.1752
FL_GEO     9.067E-2 .3747 1.
FL_JSW     3      NOBUBBLERISE      NOBUBBLERISE
FL_USL     0.      0.      0.      0.
FL_JLF     6.1147 6.2357
FL_JLT     6.1147 6.2357
FL_SEG     1
1      9.067E-2 .3747 1.499
=====
=====
FL_ID      CPVHEMAB
FL_FT      CPVHEMA CPVHEMB 6.3182 6.3182
FL_GEO     .1236 .3747 1.
FL_JSW     3      NOBUBBLERISE      NOBUBBLERISE
FL_USL     0.      0.      0.      0.
FL_JLF     6.2357 6.4007
FL_JLT     6.2357 6.4007

```



```

FL_SEG 1
1 .1236 .3747 1.499
=====
=====
=====TOP=====
=====
FL_ID CPVTOP01AB
FL_FT CPVTOP01A CPVTOP01B 6.56225
6.56225
FL_GEO .2421 .3747 1.
FL_JSW 3 NOBUBBLERISE NOBUBBLERISE
FL_USL 0. 0. 0. 0.
FL_JLF 6.4007 6.7238
FL_JLT 6.4007 6.7238
FL_SEG 1
1 .2421 .3747 1.499
=====
=====
FL_ID CPVTOP02AB
FL_FT CPVTOP02A CPVTOP02B 6.88535
6.88535
FL_GEO .2421 .3747 1.
FL_JSW 3 NOBUBBLERISE NOBUBBLERISE
FL_USL 0. 0. 0. 0.
FL_JLF 6.7238 7.0469
FL_JLT 6.7238 7.0469
FL_SEG 1
1 .2421 .3747 1.499
=====
=====
FL_ID CPVTOP3AB
FL_FT CPVTOP3A CPVTOP3B 7.20845 7.20845
FL_GEO .2421 .3747 1.
FL_JSW 3 NOBUBBLERISE NOBUBBLERISE
FL_USL 0. 0. 0. 0.
FL_JLF 7.0469 7.37
FL_JLT 7.0469 7.37
FL_SEG 1
1 .2421 .3747 .6948
=====
=====
fl-cpv-v.inp
AllowReplace
FL_INPUT
=====VERTICAL=====
=====
=====BOT=====
=====
FL_ID CPVBOT12A
FL_FT CPVBOT01A CPVBOT02A .32385
.32385
FL_GEO .441 .3239 1.
FL_JSW 0 NOBUBBLERISE NOBUBBLERISE
FL_USL 0. 0. 0. 0.
FL_SEG 1
1 .441 .3239 .7493
=====
=====
FL_ID CPVBOT12B
FL_FT CPVBOT01B CPVBOT02B .32385
.32385
FL_GEO .441 .3239 1.
FL_JSW 0 NOBUBBLERISE NOBUBBLERISE
FL_USL 0. 0. 0. 0.
FL_SEG 1
1 .441 .3239 .7493
=====
=====
=====BOT TO
LCS=====

```

```

FL_ID CPVBOT2LCSA
FL_FT CPVBOT02A CPVLC01A .6477
.6477
FL_GEO .441 .3554 1.
FL_JSW 0 NOBUBBLERISE NOBUBBLERISE
FL_USL 0. 0. 0. 0.
FL_SEG 1
1 .441 .3554 .7493
=====
=====
FL_ID CPVBOT2LCSB
FL_FT CPVBOT02B CPVLC01B .6477
.6477
FL_GEO .441 .3554 1.
FL_JSW 0 NOBUBBLERISE NOBUBBLERISE
FL_USL 0. 0. 0. 0.
FL_SEG 1
1 .441 .3554 .7493
=====
=====
=====LCS
A=====
FL_ID CPVLC012A
FL_FT CPVLC01A CPVLC02A 1.0347
1.0347
FL_GEO .441 .387 1.
FL_JSW 0 NOBUBBLERISE NOBUBBLERISE
FL_USL 0. 0. 0. 0.
FL_SEG 1
1 .441 .387 .7493
=====
=====
FL_ID CPVLC023A
FL_FT CPVLC02A CPVLC03A 1.4217 1.4217
FL_GEO .441 .387 1.
FL_JSW 0 NOBUBBLERISE NOBUBBLERISE
FL_USL 0. 0. 0. 0.
FL_SEG 1
1 .441 .387 .7493
=====
=====
FL_ID CPVLC034A
FL_FT CPVLC03A CPVLC04A 1.8087 1.8087
FL_GEO .441 .387 1.
FL_JSW 0 NOBUBBLERISE NOBUBBLERISE
FL_USL 0. 0. 0. 0.
FL_SEG 1
1 .441 .387 .7493
=====
=====
FL_ID CPVLC045A
FL_FT CPVLC04A CPVLC05A 2.1957
2.1957
FL_GEO .441 .387 1.
FL_JSW 0 NOBUBBLERISE NOBUBBLERISE
FL_USL 0. 0. 0. 0.
FL_SEG 1
1 .441 .387 .7493
=====
=====
FL_ID CPVLC056A
FL_FT CPVLC05A CPVLC06A 2.5827
2.5827
FL_GEO .441 .387 1.
FL_JSW 0 NOBUBBLERISE NOBUBBLERISE
FL_USL 0. 0. 0. 0.
FL_SEG 1
1 .441 .387 .7493
=====
=====
=====CPVLC067A

```

FL_FT	CPVLCS06A	CPVLCS07A	2.9697	
	2.9697			
FL_GEO	.441	.387	1.	
FL_JSW	0	NOBUBBLERISE	NOBUBBLERISE	
FL_USL	0.	0.	0.	
FL_SEG	1			
	1	.441	.387	.7493
=====				
=====				
FL_ID	CPVLCS78A			
FL_FT	CPVLCS07A	CPVLCS08A	3.3567	
	3.3567			
FL_GEO	.441	.387	1.	
FL_JSW	0	NOBUBBLERISE	NOBUBBLERISE	
FL_USL	0.	0.	0.	
FL_SEG	1			
	1	.441	.387	.7493
=====				
=====				
FL_ID	CPVLCS89A			
FL_FT	CPVLCS08A	CPVLCS09A	3.7437	
	3.7437			
FL_GEO	.441	.387	1.	
FL_JSW	0	NOBUBBLERISE	NOBUBBLERISE	
FL_USL	0.	0.	0.	
FL_SEG	1			
	1	.441	.387	.7493
=====				
=====				
FL_ID	CPVLCS90A			
FL_FT	CPVLCS09A	CPVLCS10A	4.1307	
	4.1307			
FL_GEO	.441	.387	1.	
FL_JSW	0	NOBUBBLERISE	NOBUBBLERISE	
FL_USL	0.	0.	0.	
FL_SEG	1			
	1	.441	.387	.7493
=====				
=====				
=====LCS				
B=====				
FL_ID	CPVLCS12B			
FL_FT	CPVLCS01B	CPVLCS02B	1.0347	
	1.0347			
FL_GEO	.441	.387	1.	
FL_JSW	0	NOBUBBLERISE	NOBUBBLERISE	
FL_USL	0.	0.	0.	
FL_SEG	1			
	1	.441	.387	.7493
=====				
=====				
FL_ID	CPVLCS23B			
FL_FT	CPVLCS02B	CPVLCS3B	1.4217	1.4217
FL_GEO	.441	.387	1.	
FL_JSW	0	NOBUBBLERISE	NOBUBBLERISE	
FL_USL	0.	0.	0.	
FL_SEG	1			
	1	.441	.387	.7493
=====				
=====				
FL_ID	CPVLCS34B			
FL_FT	CPVLCS3B	CPVLCS04B	1.8087	1.8087
FL_GEO	.441	.387	1.	
FL_JSW	0	NOBUBBLERISE	NOBUBBLERISE	
FL_USL	0.	0.	0.	
FL_SEG	1			
	1	.441	.387	.7493
=====				
=====				
FL_ID	CPVLCS45B			

FL_FT	CPVLCS04B	CPVLCS05B	2.1957	
	2.1957			
FL_GEO	.441	.387	1.	
FL_JSW	0	NOBUBBLERISE	NOBUBBLERISE	
FL_USL	0.	0.	0.	
FL_SEG	1			
	1	.441	.387	.7493
=====				
=====				
FL_ID	CPVLCS56B			
FL_FT	CPVLCS05B	CPVLCS06B	2.5827	
	2.5827			
FL_GEO	.441	.387	1.	
FL_JSW	0	NOBUBBLERISE	NOBUBBLERISE	
FL_USL	0.	0.	0.	
FL_SEG	1			
	1	.441	.387	.7493
=====				
=====				
FL_ID	CPVLCS67B			
FL_FT	CPVLCS06B	CPVLCS07B	2.9697	
	2.9697			
FL_GEO	.441	.387	1.	
FL_JSW	0	NOBUBBLERISE	NOBUBBLERISE	
FL_USL	0.	0.	0.	
FL_SEG	1			
	1	.441	.387	.7493
=====				
=====				
FL_ID	CPVLCS78B			
FL_FT	CPVLCS07B	CPVLCS08B	3.3567	
	3.3567			
FL_GEO	.441	.387	1.	
FL_JSW	0	NOBUBBLERISE	NOBUBBLERISE	
FL_USL	0.	0.	0.	
FL_SEG	1			
	1	.441	.387	.7493
=====				
=====				
FL_ID	CPVLCS89B			
FL_FT	CPVLCS08B	CPVLCS09B	3.7437	
	3.7437			
FL_GEO	.441	.387	1.	
FL_JSW	0	NOBUBBLERISE	NOBUBBLERISE	
FL_USL	0.	0.	0.	
FL_SEG	1			
	1	.441	.387	.7493
=====				
=====				
FL_ID	CPVLCS90B			
FL_FT	CPVLCS09B	CPVLCS10B	4.1307	
	4.1307			
FL_GEO	.441	.387	1.	
FL_JSW	0	NOBUBBLERISE	NOBUBBLERISE	
FL_USL	0.	0.	0.	
FL_SEG	1			
	1	.441	.387	.7493
=====				
=====				
=====LCS				
ECS=====				
FL_ID	CPVLCS2ECSA			
FL_FT	CPVLCS10A	CPVECS01A	4.5177	
	4.5177			
FL_GEO	.441	.3205	1.	
FL_JSW	0	NOBUBBLERISE	NOBUBBLERISE	
FL_USL	0.	0.	0.	
FL_SEG	1			
	1	.441	.3205	.7493
=====				
=====				

FL_ID	CPVLC2ECSB				
FL_FT	CPVLC210B	CPVECS01B	4.5177		
	4.5177				
FL_GEO	.441	.3205	1.		
FL_JSW	0	NOBUBBLERISE	NOBUBBLERISE		
FL_USL	0.	0.	0.	0.	
FL_SEG	1				
		1	.441	.3205	.7493
!=====					
=====					
!=====ECS=====					
=====					
FL_ID	CPVECS12A				
FL_FT	CPVECS01A	CPVECS02A	4.7717		
	4.7717				
FL_GEO	.441	.254	1.		
FL_JSW	0	NOBUBBLERISE	NOBUBBLERISE		
FL_USL	0.	0.	0.	0.	
FL_SEG	1				
		1	.441	.254	.7493
!=====					
=====					
FL_ID	CPVECS12B				
FL_FT	CPVECS01B	CPVECS02B	4.7717		
	4.7717				
FL_GEO	.441	.254	1.		
FL_JSW	0	NOBUBBLERISE	NOBUBBLERISE		
FL_USL	0.	0.	0.	0.	
FL_SEG	1				
		1	.441	.254	.7493
!=====					
=====					
!=====ECS					
UCS=====					
FL_ID	CPVECS2UCSA				
FL_FT	CPVECS02A	CPVUCS01A	5.0257		
	5.0257				
FL_GEO	.441	.1875	1.		
FL_JSW	0	NOBUBBLERISE	NOBUBBLERISE		
FL_USL	0.	0.	0.	0.	
FL_SEG	1				
		1	.441	.1875	.7493
!=====					
=====					
FL_ID	CPVECS2UCSB				
FL_FT	CPVECS02B	CPVUCS01B	5.0257		
	5.0257				
FL_GEO	.441	.1875	1.		
FL_JSW	0	NOBUBBLERISE	NOBUBBLERISE		
FL_USL	0.	0.	0.	0.	
FL_SEG	1				
		1	.441	.1875	.7493
!=====					
=====					
!=====UCS					
A=====					
FL_ID	CPVUCS12A				
FL_FT	CPVUCS01A	CPVUCS02A	5.1467		
	5.1467				
FL_GEO	.441	.121	1.		
FL_JSW	0	NOBUBBLERISE	NOBUBBLERISE		
FL_USL	0.	0.	0.	0.	
FL_SEG	1				
		1	.441	.121	.7493
!=====					
=====					
FL_ID	CPVUCS23A				
FL_FT	CPVUCS02A	CPVUCS3A	5.2677	5.2677	
FL_GEO	.441	.121	1.		
FL_JSW	0	NOBUBBLERISE	NOBUBBLERISE		
FL_USL	0.	0.	0.	0.	

FL_SEG	1				
		1	.441	.121	.7493
!=====					
=====					
FL_ID	CPVUCS34A				
FL_FT	CPVUCS3A	CPVUCS04A	5.3887	5.3887	
FL_GEO	.441	.121	1.		
FL_JSW	0	NOBUBBLERISE	NOBUBBLERISE		
FL_USL	0.	0.	0.	0.	
FL_SEG	1				
		1	.441	.121	.7493
!=====					
=====					
FL_ID	CPVUCS45A				
FL_FT	CPVUCS04A	CPVUCS05A	5.5097	5.5097	
FL_GEO	.441	.121	1.		
FL_JSW	0	NOBUBBLERISE	NOBUBBLERISE		
FL_USL	0.	0.	0.	0.	
FL_SEG	1				
		1	.441	.121	.7493
!=====					
=====					
FL_ID	CPVUCS56A				
FL_FT	CPVUCS05A	CPVUCS06A	5.6307	5.6307	
FL_GEO	.441	.121	1.		
FL_JSW	0	NOBUBBLERISE	NOBUBBLERISE		
FL_USL	0.	0.	0.	0.	
FL_SEG	1				
		1	.441	.121	.7493
!=====					
=====					
FL_ID	CPVUCS67A				
FL_FT	CPVUCS06A	CPVUCS07A	5.7517	5.7517	
FL_GEO	.441	.121	1.		
FL_JSW	0	NOBUBBLERISE	NOBUBBLERISE		
FL_USL	0.	0.	0.	0.	
FL_SEG	1				
		1	.441	.121	.7493
!=====					
=====					
FL_ID	CPVUCS78A				
FL_FT	CPVUCS07A	CPVUCS08A	5.8727	5.8727	
FL_GEO	.441	.121	1.		
FL_JSW	0	NOBUBBLERISE	NOBUBBLERISE		
FL_USL	0.	0.	0.	0.	
FL_SEG	1				
		1	.441	.121	.7493
!=====					
=====					
FL_ID	CPVUCS89A				
FL_FT	CPVUCS08A	CPVUCS09A	5.9937	5.9937	
FL_GEO	.441	.121	1.		
FL_JSW	0	NOBUBBLERISE	NOBUBBLERISE		
FL_USL	0.	0.	0.	0.	
FL_SEG	1				
		1	.441	.121	.7493
!=====					
=====					
FL_ID	CPVUCS90A				
FL_FT	CPVUCS09A	CPVUCS10A	6.1147	6.1147	
FL_GEO	.441	.121	1.		
FL_JSW	0	NOBUBBLERISE	NOBUBBLERISE		
FL_USL	0.	0.	0.	0.	
FL_SEG	1				
		1	.441	.121	.7493

```

=====
=====
FL_ID    CPVUCS10HEMA
FL_FT    CPVUCS10A          CPVHEMA 6.2357    6.2357
FL_GEO   .441    .143    1.
FL_JSW   0      NOBUBBLERISE    NOBUBBLERISE
FL_USL   0.      0.      0.      0.
FL_SEG   1
                1      .441    .143    .7493
=====
=====
=====UCS
B=====
FL_ID    CPVUCS12B
FL_FT    CPVUCS01B          CPVUCS02B          5.1467
                5.1467
FL_GEO   .441    .121    1.
FL_JSW   0      NOBUBBLERISE    NOBUBBLERISE
FL_USL   0.      0.      0.      0.
FL_SEG   1
                1      .441    .121    .7493
=====
=====
FL_ID    CPVUCS23B
FL_FT    CPVUCS02B          CPVUCS3B 5.2677    5.2677
FL_GEO   .441    .121    1.
FL_JSW   0      NOBUBBLERISE    NOBUBBLERISE
FL_USL   0.      0.      0.      0.
FL_SEG   1
                1      .441    .121    .7493
=====
=====
FL_ID    CPVUCS34B
FL_FT    CPVUCS3B CPVUCS04B          5.3887    5.3887
FL_GEO   .441    .121    1.
FL_JSW   0      NOBUBBLERISE    NOBUBBLERISE
FL_USL   0.      0.      0.      0.
FL_SEG   1
                1      .441    .121    .7493
=====
=====
FL_ID    CPVUCS45B
FL_FT    CPVUCS04B          CPVUCS05B          5.5097
                5.5097
FL_GEO   .441    .121    1.
FL_JSW   0      NOBUBBLERISE    NOBUBBLERISE
FL_USL   0.      0.      0.      0.
FL_SEG   1
                1      .441    .121    .7493
=====
=====
FL_ID    CPVUCS56B
FL_FT    CPVUCS05B          CPVUCS06B          5.6307
                5.6307
FL_GEO   .441    .121    1.
FL_JSW   0      NOBUBBLERISE    NOBUBBLERISE
FL_USL   0.      0.      0.      0.
FL_SEG   1
                1      .441    .121    .7493
=====
=====
FL_ID    CPVUCS67B
FL_FT    CPVUCS06B          CPVUCS07B          5.7517
                5.7517
FL_GEO   .441    .121    1.
FL_JSW   0      NOBUBBLERISE    NOBUBBLERISE
FL_USL   0.      0.      0.      0.
FL_SEG   1
                1      .441    .121    .7493
=====
=====

```

```

FL_ID    CPVUCS78B
FL_FT    CPVUCS07B          CPVUCS08B          5.8727
                5.8727
FL_GEO   .441    .121    1.
FL_JSW   0      NOBUBBLERISE    NOBUBBLERISE
FL_USL   0.      0.      0.      0.
FL_SEG   1
                1      .441    .121    .7493
=====
=====
FL_ID    CPVUCS89B
FL_FT    CPVUCS08B          CPVUCS09B          5.9937
                5.9937
FL_GEO   .441    .121    1.
FL_JSW   0      NOBUBBLERISE    NOBUBBLERISE
FL_USL   0.      0.      0.      0.
FL_SEG   1
                1      .441    .121    .7493
=====
=====
FL_ID    CPVUCS90B
FL_FT    CPVUCS09B          CPVUCS10B          6.1147
                6.1147
FL_GEO   .441    .121    1.
FL_JSW   0      NOBUBBLERISE    NOBUBBLERISE
FL_USL   0.      0.      0.      0.
FL_SEG   1
                1      .441    .121    .7493
=====
=====
FL_ID    CPVUCS10HEMB
FL_FT    CPVUCS10B          CPVHEMB 6.2357    6.2357
FL_GEO   .441    .143    1.
FL_JSW   0      NOBUBBLERISE    NOBUBBLERISE
FL_USL   0.      0.      0.      0.
FL_SEG   1
                1      .441    .143    .7493
=====
=====
=====UCS
TO
TOP=====
FL_ID    CPVUCS2TOPA
FL_FT    CPVHEMA CPVTOP01A          6.4007    6.4007
FL_GEO   .441    .2441    1.
FL_JSW   0      NOBUBBLERISE    NOBUBBLERISE
FL_USL   0.      0.      0.      0.
FL_SEG   1
                1      .441    .2441    .7493
=====
=====
FL_ID    CPVUCS2TOPB
FL_FT    CPVHEMB CPVTOP01B          6.4007    6.4007
FL_GEO   .441    .2441    1.
FL_JSW   0      NOBUBBLERISE    NOBUBBLERISE
FL_USL   0.      0.      0.      0.
FL_SEG   1
                1      .441    .2441    .7493
=====
=====
=====TOP=====
=====
FL_ID    CPVTOP12A
FL_FT    CPVTOP01A          CPVTOP02A          6.7238
                6.7238
FL_GEO   .441    .3231    1.
FL_JSW   0      NOBUBBLERISE    NOBUBBLERISE
FL_USL   0.      0.      0.      0.
FL_SEG   1
                1      .441    .3231    .7493
=====
=====

```

```

FL_ID    CPVTOP23A
FL_FT    CPVTOP02A          CPVTOP3A 7.0469    7.0469
FL_GEO    .441      .3231    1.
FL_JSW    0          NOBUBBLERISE      NOBUBBLERISE
FL_USL    0.        0.        0.        0.
FL_SEG    1
          1          .441      .3231    .7493
=====
=====
FL_ID    CPVTOP12B
FL_FT    CPVTOP01B          CPVTOP02B          6.7238
          6.7238
FL_GEO    .441      .3231    1.
FL_JSW    0          NOBUBBLERISE      NOBUBBLERISE
FL_USL    0.        0.        0.        0.
FL_SEG    1
          1          .441      .3231    .7493
=====
=====
FL_ID    CPVTOP23B
FL_FT    CPVTOP02B          CPVTOP3B 7.0469    7.0469
FL_GEO    .441      .3231    1.
FL_JSW    0          NOBUBBLERISE      NOBUBBLERISE
FL_USL    0.        0.        0.        0.
FL_SEG    1
          1          .441      .3231    .7493
=====
=====

```

```

=====
=====
FL_ID    CPV2VERYA
FL_FT    CPVTOP3A VERYTOP  7.37      7.37
FL_GEO    .441      .47655    1.
FL_JSW    0          NOBUBBLERISE      NOBUBBLERISE
FL_USL    0.        0.        0.        0.
FL_SEG    1
          1          .441      .47655    .7493
=====
=====
FL_ID    CPV2VERYB
FL_FT    CPVTOP3B VERYTOP  7.37      7.37
FL_GEO    .441      .47655    1.
FL_JSW    0          NOBUBBLERISE      NOBUBBLERISE
FL_USL    0.        0.        0.        0.
FL_SEG    1
          1          .441      .47655    .7493
=====
=====
FL_ID    VERYTOP2TOPAMB
FL_FT    VERYTOP          TOPAMB  8.        8.
FL_GEO    .882      .815      1.
FL_JSW    0          NOBUBBLERISE      NOBUBBLERISE
FL_USL    0.        0.        0.        0.
FL_SEG    1
          1          .882      .815      .7493
=====
=====

```

```

hs-hsfon.inp
AllowReplace
HS_INPUT
!=====LCS PORTION=====
HS_ID      HSLCS01  320
HS_GD      RECTANGULAR      YES
HS_EOD     .6477      1.0
HS_SRC     NO
HS_ND      11
           1          1          0.          288.8190 STAINLESS-STEEL-304
           2          2          3.81E-03 288.9311 STAINLESS-STEEL-304
           3          3          7.62E-03 289.0433 STAINLESS-STEEL-304
           4          4          1.14E-02 289.1554 STAINLESS-STEEL-304
           5          5          1.52E-02 289.2676 STAINLESS-STEEL-304
           6          6          1.91E-02 289.3798 STAINLESS-STEEL-304
           7          7          2.29E-02 289.4919 STAINLESS-STEEL-304
           8          8          2.67E-02 289.6041 STAINLESS-STEEL-304
           9          9          3.05E-02 289.7162 STAINLESS-STEEL-304
          10         10          3.43E-02 289.8284 STAINLESS-STEEL-304
          11         11          3.81E-02 289.9405 STAINLESS-STEEL-304
HS_LB      CalcCoefHS      CPVLC01B      NO
HS_LBP     EXT      0.5      0.5      !
HS_LBS     .065016      .387      .387
HS_RB      CalcCoefHS      LCS01A      YES
HS_RBP     EXT      0.5      0.5
HS_RBS     .065016      .387      .387
HS_FT      ON
HS_FTDRN  0
HS_FTLBF  0.
HS_FTLBM  NO
HS_FTLBE  NO
HS_FTRBF  0.
HS_FTRBM  NO
HS_FTRBE  NO
!=====
HS_ID      HSLCS02  321
HS_GD      RECTANGULAR      YES
HS_EOD     1.0347      1.0
HS_SRC     NO
HS_ND      11
           1          1          0.          288.8190 STAINLESS-STEEL-304
           2          2          3.81E-03 288.9311 STAINLESS-STEEL-304
           3          3          7.62E-03 289.0433 STAINLESS-STEEL-304
           4          4          1.14E-02 289.1554 STAINLESS-STEEL-304
           5          5          1.52E-02 289.2676 STAINLESS-STEEL-304
           6          6          1.91E-02 289.3798 STAINLESS-STEEL-304
           7          7          2.29E-02 289.4919 STAINLESS-STEEL-304
           8          8          2.67E-02 289.6041 STAINLESS-STEEL-304
           9          9          3.05E-02 289.7162 STAINLESS-STEEL-304
          10         10          3.43E-02 289.8284 STAINLESS-STEEL-304
          11         11          3.81E-02 289.9405 STAINLESS-STEEL-304
HS_LB      CalcCoefHS      CPVLC02B      NO
HS_LBP     EXT      0.5      0.5      !
HS_LBS     .065016      .387      .387
HS_RB      CalcCoefHS      LCS02A      YES
HS_RBP     EXT      0.5      0.5
HS_RBS     .065016      .387      .387
HS_FT      ON
HS_FTDRN  1
           1          HSLCS01  0.          1.

HS_FTLBF  0.
HS_FTLBM  NO
HS_FTLBE  NO
HS_FTRBF  0.

```

```

HS_FTRBMNO
HS_FTRBE NO
!=====
HS_ID    HSLCS3    322
HS_GD    RECTANGULAR    YES
HS_EOD   1.4217    1.0
HS_SRC   NO
HS_ND    11
          1        1        0.        288.8190 STAINLESS-STEEL-304
          2        2        3.81E-03  288.9311 STAINLESS-STEEL-304
          3        3        7.62E-03  289.0433 STAINLESS-STEEL-304
          4        4        1.14E-02  289.1554 STAINLESS-STEEL-304
          5        5        1.52E-02  289.2676 STAINLESS-STEEL-304
          6        6        1.91E-02  289.3798 STAINLESS-STEEL-304
          7        7        2.29E-02  289.4919 STAINLESS-STEEL-304
          8        8        2.67E-02  289.6041 STAINLESS-STEEL-304
          9        9        3.05E-02  289.7162 STAINLESS-STEEL-304
         10       10       3.43E-02  289.8284 STAINLESS-STEEL-304
         11       11       3.81E-02  289.9405 STAINLESS-STEEL-304
HS_LB    CalcCoefHS    CPVLC3B NO
HS_LBP   EXT    0.5    0.5    !
HS_LBS   .065016    .387    .387
HS_RB    CalcCoefHS    LCS3A    YES
HS_RBP   EXT    0.5    0.5
HS_RBS   .065016    .387    .387
HS_FT    ON
HS_FTDRN 1
          1        HSLCS02    0.        1.

HS_FTLBF 0.
HS_FTLBM NO
HS_FTLBE NO
HS_FTRBF 0.
HS_FTRBMNO
HS_FTRBE NO
!=====
HS_ID    HSLCS04    323
HS_GD    RECTANGULAR    YES
HS_EOD   1.8087    1.0
HS_SRC   NO
HS_ND    11
          1        1        0.        288.8190 STAINLESS-STEEL-304
          2        2        3.81E-03  288.9311 STAINLESS-STEEL-304
          3        3        7.62E-03  289.0433 STAINLESS-STEEL-304
          4        4        1.14E-02  289.1554 STAINLESS-STEEL-304
          5        5        1.52E-02  289.2676 STAINLESS-STEEL-304
          6        6        1.91E-02  289.3798 STAINLESS-STEEL-304
          7        7        2.29E-02  289.4919 STAINLESS-STEEL-304
          8        8        2.67E-02  289.6041 STAINLESS-STEEL-304
          9        9        3.05E-02  289.7162 STAINLESS-STEEL-304
         10       10       3.43E-02  289.8284 STAINLESS-STEEL-304
         11       11       3.81E-02  289.9405 STAINLESS-STEEL-304
HS_LB    CalcCoefHS    CPVLC04B    NO
HS_LBP   EXT    0.5    0.5    !
HS_LBS   .065016    .387    .387
HS_RB    CalcCoefHS    LCS04A    YES
HS_RBP   EXT    0.5    0.5
HS_RBS   .065016    .387    .387
HS_FT    ON
HS_FTDRN 1
          1        HSLCS3    0.        1.

HS_FTLBF 0.
HS_FTLBM NO
HS_FTLBE NO
HS_FTRBF 0.
HS_FTRBMNO
HS_FTRBE NO

```

```

=====
HS_ID    HSLCS05  324
HS_GD    RECTANGULAR      YES
HS_EOD   2.1957    1.0
HS_SRC   NO
HS_ND    11
          1         1         0.         288.8190 STAINLESS-STEEL-304
          2         2         3.81E-03 288.9311 STAINLESS-STEEL-304
          3         3         7.62E-03 289.0433 STAINLESS-STEEL-304
          4         4         1.14E-02 289.1554 STAINLESS-STEEL-304
          5         5         1.52E-02 289.2676 STAINLESS-STEEL-304
          6         6         1.91E-02 289.3798 STAINLESS-STEEL-304
          7         7         2.29E-02 289.4919 STAINLESS-STEEL-304
          8         8         2.67E-02 289.6041 STAINLESS-STEEL-304
          9         9         3.05E-02 289.7162 STAINLESS-STEEL-304
         10        10        3.43E-02 289.8284 STAINLESS-STEEL-304
         11        11        3.81E-02 289.9405 STAINLESS-STEEL-304
HS_LB     CalcCoefHS      CPVLC05B      NO
HS_LBP    EXT      0.5      0.5      !
HS_LBS    .065016 .387      .387
HS_RB     CalcCoefHS      LCS05A      YES
HS_RBP    EXT      0.5      0.5
HS_RBS    .065016 .387      .387
HS_FT     ON
HS_FTDRN 1
          1         HSLCS04 0.         1.

HS_FTLBF 0.
HS_FTLBM NO
HS_FTLBE NO
HS_FTRBF 0.
HS_FTRBM NO
HS_FTRBE NO
=====
HS_ID    HSLCS06  325
HS_GD    RECTANGULAR      YES
HS_EOD   2.5827    1.0
HS_SRC   NO
HS_ND    11
          1         1         0.         288.8190 STAINLESS-STEEL-304
          2         2         3.81E-03 288.9311 STAINLESS-STEEL-304
          3         3         7.62E-03 289.0433 STAINLESS-STEEL-304
          4         4         1.14E-02 289.1554 STAINLESS-STEEL-304
          5         5         1.52E-02 289.2676 STAINLESS-STEEL-304
          6         6         1.91E-02 289.3798 STAINLESS-STEEL-304
          7         7         2.29E-02 289.4919 STAINLESS-STEEL-304
          8         8         2.67E-02 289.6041 STAINLESS-STEEL-304
          9         9         3.05E-02 289.7162 STAINLESS-STEEL-304
         10        10        3.43E-02 289.8284 STAINLESS-STEEL-304
         11        11        3.81E-02 289.9405 STAINLESS-STEEL-304
HS_LB     CalcCoefHS      CPVLC06B      NO
HS_LBP    EXT      0.5      0.5      !
HS_LBS    .065016 .387      .387
HS_RB     CalcCoefHS      LCS06A      YES
HS_RBP    EXT      0.5      0.5
HS_RBS    .065016 .387      .387
HS_FT     ON
HS_FTDRN 1
          1         HSLCS05 0.         1.

HS_FTLBF 0.
HS_FTLBM NO
HS_FTLBE NO
HS_FTRBF 0.
HS_FTRBM NO
HS_FTRBE NO
=====
HS_ID    HSLCS07  326

```


HS_GD	RECTANGULAR	YES			
HS_EOD	2.9697	1.0			
HS_SRC	NO				
HS_ND	11				
	1	1	0.	288.8190	STAINLESS-STEEL-304
	2	2	3.81E-03	288.9311	STAINLESS-STEEL-304
	3	3	7.62E-03	289.0433	STAINLESS-STEEL-304
	4	4	1.14E-02	289.1554	STAINLESS-STEEL-304
	5	5	1.52E-02	289.2676	STAINLESS-STEEL-304
	6	6	1.91E-02	289.3798	STAINLESS-STEEL-304
	7	7	2.29E-02	289.4919	STAINLESS-STEEL-304
	8	8	2.67E-02	289.6041	STAINLESS-STEEL-304
	9	9	3.05E-02	289.7162	STAINLESS-STEEL-304
	10	10	3.43E-02	289.8284	STAINLESS-STEEL-304
	11	11	3.81E-02	289.9405	STAINLESS-STEEL-304
HS_LB	CalcCoefHS	CPVLC07B	NO		
HS_LBP	EXT 0.5	0.5	!		
HS_LBS	.065016 .387	.387			
HS_RB	CalcCoefHS	LCS07A	YES		
HS_RBP	EXT 0.5	0.5			
HS_RBS	.065016 .387	.387			
HS_FT	ON				
HS_FTDRN	1	1	HSLCS06	0.	1.
HS_FTLBF	0.				
HS_FTLBM	NO				
HS_FTLBE	NO				
HS_FTRBF	0.				
HS_FTRBM	NO				
HS_FTRBE	NO				
!=====					
HS_ID	HSLCS08	327			
HS_GD	RECTANGULAR	YES			
HS_EOD	3.3567	1.0			
HS_SRC	NO				
HS_ND	11				
	1	1	0.	288.8190	STAINLESS-STEEL-304
	2	2	3.81E-03	288.9311	STAINLESS-STEEL-304
	3	3	7.62E-03	289.0433	STAINLESS-STEEL-304
	4	4	1.14E-02	289.1554	STAINLESS-STEEL-304
	5	5	1.52E-02	289.2676	STAINLESS-STEEL-304
	6	6	1.91E-02	289.3798	STAINLESS-STEEL-304
	7	7	2.29E-02	289.4919	STAINLESS-STEEL-304
	8	8	2.67E-02	289.6041	STAINLESS-STEEL-304
	9	9	3.05E-02	289.7162	STAINLESS-STEEL-304
	10	10	3.43E-02	289.8284	STAINLESS-STEEL-304
	11	11	3.81E-02	289.9405	STAINLESS-STEEL-304
HS_LB	CalcCoefHS	CPVLC08B	NO		
HS_LBP	EXT 0.5	0.5	!		
HS_LBS	.065016 .387	.387			
HS_RB	CalcCoefHS	LCS08A	YES		
HS_RBP	EXT 0.5	0.5			
HS_RBS	.065016 .387	.387			
HS_FT	ON				
HS_FTDRN	1	1	HSLCS07	0.	1.
HS_FTLBF	0.				
HS_FTLBM	NO				
HS_FTLBE	NO				
HS_FTRBF	0.				
HS_FTRBM	NO				
HS_FTRBE	NO				
!=====					
HS_ID	HSLCS09	328			
HS_GD	RECTANGULAR	YES			
HS_EOD	3.7437	1.0			

HS_SRC	NO					
HS_ND	11					
		1	1	0.	288.8190	STAINLESS-STEEL-304
		2	2	3.81E-03	288.9311	STAINLESS-STEEL-304
		3	3	7.62E-03	289.0433	STAINLESS-STEEL-304
		4	4	1.14E-02	289.1554	STAINLESS-STEEL-304
		5	5	1.52E-02	289.2676	STAINLESS-STEEL-304
		6	6	1.91E-02	289.3798	STAINLESS-STEEL-304
		7	7	2.29E-02	289.4919	STAINLESS-STEEL-304
		8	8	2.67E-02	289.6041	STAINLESS-STEEL-304
		9	9	3.05E-02	289.7162	STAINLESS-STEEL-304
		10	10	3.43E-02	289.8284	STAINLESS-STEEL-304
		11	11	3.81E-02	289.9405	STAINLESS-STEEL-304
HS_LB	CalcCoefHS		CPVLCS09B		NO	
HS_LBP	EXT	0.5	0.5	!		
HS_LBS	.065016	.387	.387			
HS_RB	CalcCoefHS		LCS09A	YES		
HS_RBP	EXT	0.5	0.5			
HS_RBS	.065016	.387	.387			
HS_FT	ON					
HS_FTDRN	1					
			1	HSLCS08	0.	1.
HS_FTLBF	0.					
HS_FTLBM	NO					
HS_FTLBE	NO					
HS_FTRBF	0.					
HS_FTRBM	NO					
HS_FTRBE	NO					
!=====						
HS_ID	HSLCS10	329				
HS_GD	RECTANGULAR		YES			
HS_EOD	4.1307	1.0				
HS_SRC	NO					
HS_ND	11					
		1	1	0.	288.8190	STAINLESS-STEEL-304
		2	2	3.81E-03	288.9311	STAINLESS-STEEL-304
		3	3	7.62E-03	289.0433	STAINLESS-STEEL-304
		4	4	1.14E-02	289.1554	STAINLESS-STEEL-304
		5	5	1.52E-02	289.2676	STAINLESS-STEEL-304
		6	6	1.91E-02	289.3798	STAINLESS-STEEL-304
		7	7	2.29E-02	289.4919	STAINLESS-STEEL-304
		8	8	2.67E-02	289.6041	STAINLESS-STEEL-304
		9	9	3.05E-02	289.7162	STAINLESS-STEEL-304
		10	10	3.43E-02	289.8284	STAINLESS-STEEL-304
		11	11	3.81E-02	289.9405	STAINLESS-STEEL-304
HS_LB	CalcCoefHS		CPVLCS10B		NO	
HS_LBP	EXT	0.5	0.5	!		
HS_LBS	.065016	.387	.387			
HS_RB	CalcCoefHS		LCS10A	YES		
HS_RBP	EXT	0.5	0.5			
HS_RBS	.065016	.387	.387			
HS_FT	ON					
HS_FTDRN	1					
			1	HSLCS09	0.	1.
HS_FTLBF	0.					
HS_FTLBM	NO					
HS_FTLBE	NO					
HS_FTRBF	0.					
HS_FTRBM	NO					
HS_FTRBE	NO					
!=====						
!=====ECS PORTION=====						
HS_ID	HSECS01	330				
HS_GD	RECTANGULAR		YES			
HS_EOD	4.5177	1.0				
HS_SRC	NO					

HS_ND	11					
	1	1	0.	288.8190	STAINLESS-STEEL-304	
	2	2	3.81E-03	288.9311	STAINLESS-STEEL-304	
	3	3	7.62E-03	289.0433	STAINLESS-STEEL-304	
	4	4	1.14E-02	289.1554	STAINLESS-STEEL-304	
	5	5	1.52E-02	289.2676	STAINLESS-STEEL-304	
	6	6	1.91E-02	289.3798	STAINLESS-STEEL-304	
	7	7	2.29E-02	289.4919	STAINLESS-STEEL-304	
	8	8	2.67E-02	289.6041	STAINLESS-STEEL-304	
	9	9	3.05E-02	289.7162	STAINLESS-STEEL-304	
	10	10	3.43E-02	289.8284	STAINLESS-STEEL-304	
	11	11	3.81E-02	289.9405	STAINLESS-STEEL-304	
HS_LB	CalcCoefHS	CPVECS01B	NO			
HS_LBP	EXT 0.5	0.5	!			
HS_LBS	.042672 .254	.254				
HS_RB	CalcCoefHS	ECS01A	YES			
HS_RBP	EXT 0.5	0.5				
HS_RBS	.042672 .254	.254				
HS_FT	ON					
HS_FTDRN	1					
		1	HSLCS10	0.	1.	
HS_FTLBF	0.					
HS_FTLBM	NO					
HS_FTLBE	NO					
HS_FTRBF	0.					
HS_FTRBMNO						
HS_FTRBE	NO					
!=====						
HS_ID	HSECS02 331					
HS_GD	RECTANGULAR	YES				
HS_EOD	4.7717 1.0					
HS_SRC	NO					
HS_ND	11					
	1	1	0.	288.8190	STAINLESS-STEEL-304	
	2	2	3.81E-03	288.9311	STAINLESS-STEEL-304	
	3	3	7.62E-03	289.0433	STAINLESS-STEEL-304	
	4	4	1.14E-02	289.1554	STAINLESS-STEEL-304	
	5	5	1.52E-02	289.2676	STAINLESS-STEEL-304	
	6	6	1.91E-02	289.3798	STAINLESS-STEEL-304	
	7	7	2.29E-02	289.4919	STAINLESS-STEEL-304	
	8	8	2.67E-02	289.6041	STAINLESS-STEEL-304	
	9	9	3.05E-02	289.7162	STAINLESS-STEEL-304	
	10	10	3.43E-02	289.8284	STAINLESS-STEEL-304	
	11	11	3.81E-02	289.9405	STAINLESS-STEEL-304	
HS_LB	CalcCoefHS	CPVECS02B	NO			
HS_LBP	EXT 0.5	0.5	!			
HS_LBS	.042672 .254	.254				
HS_RB	CalcCoefHS	ECS02A	YES			
HS_RBP	EXT 0.5	0.5				
HS_RBS	.042672 .254	.254				
HS_FT	ON					
HS_FTDRN	1					
		1	HSECS01	0.	1.	
HS_FTLBF	0.					
HS_FTLBM	NO					
HS_FTLBE	NO					
HS_FTRBF	0.					
HS_FTRBMNO						
HS_FTRBE	NO					
!=====						
!=====UCS PORTION=====						
HS_ID	HSUCS01 340					
HS_GD	RECTANGULAR	YES				
HS_EOD	5.0257 1.0					
HS_SRC	NO					
HS_ND	11					

		1	1	0.	288.8190	STAINLESS-STEEL-304
		2	2	3.81E-03	288.9311	STAINLESS-STEEL-304
		3	3	7.62E-03	289.0433	STAINLESS-STEEL-304
		4	4	1.14E-02	289.1554	STAINLESS-STEEL-304
		5	5	1.52E-02	289.2676	STAINLESS-STEEL-304
		6	6	1.91E-02	289.3798	STAINLESS-STEEL-304
		7	7	2.29E-02	289.4919	STAINLESS-STEEL-304
		8	8	2.67E-02	289.6041	STAINLESS-STEEL-304
		9	9	3.05E-02	289.7162	STAINLESS-STEEL-304
		10	10	3.43E-02	289.8284	STAINLESS-STEEL-304
		11	11	3.81E-02	289.9405	STAINLESS-STEEL-304
HS_LB	CalcCoefHS		CPVUCS01B	NO		
HS_LBP	EXT	0.5	0.5	!		
HS_LBS	20.328E-3	.121	.121			
HS_RB	CalcCoefHS		UCS01A	YES		
HS_RBP	EXT	0.5	0.5			
HS_RBS	20.328E-3	.121	.121			
HS_FT	ON					
HS_FTDRN	1					
			1	HSECS02	0.	1.
HS_FTLBF	0.					
HS_FTLBM	NO					
HS_FTLBE	NO					
HS_FTRBF	0.					
HS_FTRBM	NO					
HS_FTRBE	NO					
!=====						
HS_ID	HSUCS02	341				
HS_GD	RECTANGULAR		YES			
HS_EOD	5.1467	1.0				
HS_SRC	NO					
HS_ND	11					
		1	1	0.	288.8190	STAINLESS-STEEL-304
		2	2	3.81E-03	288.9311	STAINLESS-STEEL-304
		3	3	7.62E-03	289.0433	STAINLESS-STEEL-304
		4	4	1.14E-02	289.1554	STAINLESS-STEEL-304
		5	5	1.52E-02	289.2676	STAINLESS-STEEL-304
		6	6	1.91E-02	289.3798	STAINLESS-STEEL-304
		7	7	2.29E-02	289.4919	STAINLESS-STEEL-304
		8	8	2.67E-02	289.6041	STAINLESS-STEEL-304
		9	9	3.05E-02	289.7162	STAINLESS-STEEL-304
		10	10	3.43E-02	289.8284	STAINLESS-STEEL-304
		11	11	3.81E-02	289.9405	STAINLESS-STEEL-304
HS_LB	CalcCoefHS		CPVUCS02B	NO		
HS_LBP	EXT	0.5	0.5	!		
HS_LBS	20.328E-3	.121	.121			
HS_RB	CalcCoefHS		UCS02A	YES		
HS_RBP	EXT	0.5	0.5			
HS_RBS	20.328E-3	.121	.121			
HS_FT	ON					
HS_FTDRN	1					
			1	HSUCS01	0.	1.
HS_FTLBF	0.					
HS_FTLBM	NO					
HS_FTLBE	NO					
HS_FTRBF	0.					
HS_FTRBM	NO					
HS_FTRBE	NO					
!=====						
HS_ID	HSUCS3	342				
HS_GD	RECTANGULAR		YES			
HS_EOD	5.2677	1.0				
HS_SRC	NO					
HS_ND	11					
		1	1	0.	288.8190	STAINLESS-STEEL-304
		2	2	3.81E-03	288.9311	STAINLESS-STEEL-304

		3	3	7.62E-03	289.0433	STAINLESS-STEEL-304
		4	4	1.14E-02	289.1554	STAINLESS-STEEL-304
		5	5	1.52E-02	289.2676	STAINLESS-STEEL-304
		6	6	1.91E-02	289.3798	STAINLESS-STEEL-304
		7	7	2.29E-02	289.4919	STAINLESS-STEEL-304
		8	8	2.67E-02	289.6041	STAINLESS-STEEL-304
		9	9	3.05E-02	289.7162	STAINLESS-STEEL-304
		10	10	3.43E-02	289.8284	STAINLESS-STEEL-304
		11	11	3.81E-02	289.9405	STAINLESS-STEEL-304
HS_LB	CalcCofHS		CPVUCS3B	NO		
HS_LBP	EXT	0.5	0.5	!		
HS_LBS	20.328E-3	.121	.121			
HS_RB	CalcCofHS		UCS3A	YES		
HS_RBP	EXT	0.5	0.5			
HS_RBS	20.328E-3	.121	.121			
HS_FT	ON					
HS_FTDRN	1		1	HSUCS02	0.	1.
HS_FTLBF	0.					
HS_FTLBM	NO					
HS_FTLBE	NO					
HS_FTRBF	0.					
HS_FTRBM	NO					
HS_FTRBE	NO					
!=====						
HS_ID	HSUCS04	343				
HS_GD	RECTANGULAR		YES			
HS_EOD	5.3887	1.0				
HS_SRC	NO					
HS_ND	11					
		1	1	0.	288.8190	STAINLESS-STEEL-304
		2	2	3.81E-03	288.9311	STAINLESS-STEEL-304
		3	3	7.62E-03	289.0433	STAINLESS-STEEL-304
		4	4	1.14E-02	289.1554	STAINLESS-STEEL-304
		5	5	1.52E-02	289.2676	STAINLESS-STEEL-304
		6	6	1.91E-02	289.3798	STAINLESS-STEEL-304
		7	7	2.29E-02	289.4919	STAINLESS-STEEL-304
		8	8	2.67E-02	289.6041	STAINLESS-STEEL-304
		9	9	3.05E-02	289.7162	STAINLESS-STEEL-304
		10	10	3.43E-02	289.8284	STAINLESS-STEEL-304
		11	11	3.81E-02	289.9405	STAINLESS-STEEL-304
HS_LB	CalcCofHS		CPVUCS04B	NO		
HS_LBP	EXT	0.5	0.5	!		
HS_LBS	20.328E-3	.121	.121			
HS_RB	CalcCofHS		UCS04A	YES		
HS_RBP	EXT	0.5	0.5			
HS_RBS	20.328E-3	.121	.121			
HS_FT	ON					
HS_FTDRN	1		1	HSUCS3	0.	1.
HS_FTLBF	0.					
HS_FTLBM	NO					
HS_FTLBE	NO					
HS_FTRBF	0.					
HS_FTRBM	NO					
HS_FTRBE	NO					
!=====						
HS_ID	HSUCS05	344				
HS_GD	RECTANGULAR		YES			
HS_EOD	5.5097	1.0				
HS_SRC	NO					
HS_ND	11					
		1	1	0.	288.8190	STAINLESS-STEEL-304
		2	2	3.81E-03	288.9311	STAINLESS-STEEL-304
		3	3	7.62E-03	289.0433	STAINLESS-STEEL-304
		4	4	1.14E-02	289.1554	STAINLESS-STEEL-304

		5	5	1.52E-02	289.2676	STAINLESS-STEEL-304
		6	6	1.91E-02	289.3798	STAINLESS-STEEL-304
		7	7	2.29E-02	289.4919	STAINLESS-STEEL-304
		8	8	2.67E-02	289.6041	STAINLESS-STEEL-304
		9	9	3.05E-02	289.7162	STAINLESS-STEEL-304
		10	10	3.43E-02	289.8284	STAINLESS-STEEL-304
		11	11	3.81E-02	289.9405	STAINLESS-STEEL-304
HS_LB	CalcCoefHS		CPVUCS05B		NO	
HS_LBP	EXT	0.5	0.5	!		
HS_LBS	20.328E-3	.121	.121			
HS_RB	CalcCoefHS		UCS05A	YES		
HS_RBP	EXT	0.5	0.5			
HS_RBS	20.328E-3	.121	.121			
HS_FT	ON					
HS_FTDRN	1					
			1	HSUCS04	0.	1.
HS_FTLBF	0.					
HS_FTLBM	NO					
HS_FTLBE	NO					
HS_FTRBF	0.					
HS_FTRBM	NO					
HS_FTRBE	NO					
!=====						
HS_ID	HSUCS06	345				
HS_GD	RECTANGULAR		YES			
HS_EOD	5.6307	1.0				
HS_SRC	NO					
HS_ND	11					
		1	1	0.	288.8190	STAINLESS-STEEL-304
		2	2	3.81E-03	288.9311	STAINLESS-STEEL-304
		3	3	7.62E-03	289.0433	STAINLESS-STEEL-304
		4	4	1.14E-02	289.1554	STAINLESS-STEEL-304
		5	5	1.52E-02	289.2676	STAINLESS-STEEL-304
		6	6	1.91E-02	289.3798	STAINLESS-STEEL-304
		7	7	2.29E-02	289.4919	STAINLESS-STEEL-304
		8	8	2.67E-02	289.6041	STAINLESS-STEEL-304
		9	9	3.05E-02	289.7162	STAINLESS-STEEL-304
		10	10	3.43E-02	289.8284	STAINLESS-STEEL-304
		11	11	3.81E-02	289.9405	STAINLESS-STEEL-304
HS_LB	CalcCoefHS		CPVUCS06B		NO	
HS_LBP	EXT	0.5	0.5	!		
HS_LBS	20.328E-3	.121	.121			
HS_RB	CalcCoefHS		UCS06A	YES		
HS_RBP	EXT	0.5	0.5			
HS_RBS	20.328E-3	.121	.121			
HS_FT	ON					
HS_FTDRN	1					
			1	HSUCS05	0.	1.
HS_FTLBF	0.					
HS_FTLBM	NO					
HS_FTLBE	NO					
HS_FTRBF	0.					
HS_FTRBM	NO					
HS_FTRBE	NO					
!=====						
HS_ID	HSUCS07	346				
HS_GD	RECTANGULAR		YES			
HS_EOD	5.7517	1.0				
HS_SRC	NO					
HS_ND	11					
		1	1	0.	288.8190	STAINLESS-STEEL-304
		2	2	3.81E-03	288.9311	STAINLESS-STEEL-304
		3	3	7.62E-03	289.0433	STAINLESS-STEEL-304
		4	4	1.14E-02	289.1554	STAINLESS-STEEL-304
		5	5	1.52E-02	289.2676	STAINLESS-STEEL-304
		6	6	1.91E-02	289.3798	STAINLESS-STEEL-304

		7	7	2.29E-02	289.4919	STAINLESS-STEEL-304
		8	8	2.67E-02	289.6041	STAINLESS-STEEL-304
		9	9	3.05E-02	289.7162	STAINLESS-STEEL-304
		10	10	3.43E-02	289.8284	STAINLESS-STEEL-304
		11	11	3.81E-02	289.9405	STAINLESS-STEEL-304
HS_LB	CalcCoefHS		CPVUCS07B		NO	
HS_LBP	EXT	0.5	0.5	!		
HS_LBS	20.328E-3	.121	.121			
HS_RB	CalcCoefHS		UCS07A	YES		
HS_RBP	EXT	0.5	0.5			
HS_RBS	20.328E-3	.121	.121			
HS_FT	ON					
HS_FTDRN	1					
			1	HSUCS06	0.	1.
HS_FTLBF	0.					
HS_FTLBM	NO					
HS_FTLBE	NO					
HS_FTRBF	0.					
HS_FTRBM	NO					
HS_FTRBE	NO					
!=====						
HS_ID	HSUCS08	347				
HS_GD	RECTANGULAR		YES			
HS_EOD	5.8727	1.0				
HS_SRC	NO					
HS_ND	11					
		1	1	0.	288.8190	STAINLESS-STEEL-304
		2	2	3.81E-03	288.9311	STAINLESS-STEEL-304
		3	3	7.62E-03	289.0433	STAINLESS-STEEL-304
		4	4	1.14E-02	289.1554	STAINLESS-STEEL-304
		5	5	1.52E-02	289.2676	STAINLESS-STEEL-304
		6	6	1.91E-02	289.3798	STAINLESS-STEEL-304
		7	7	2.29E-02	289.4919	STAINLESS-STEEL-304
		8	8	2.67E-02	289.6041	STAINLESS-STEEL-304
		9	9	3.05E-02	289.7162	STAINLESS-STEEL-304
		10	10	3.43E-02	289.8284	STAINLESS-STEEL-304
		11	11	3.81E-02	289.9405	STAINLESS-STEEL-304
HS_LB	CalcCoefHS		CPVUCS08B		NO	
HS_LBP	EXT	0.5	0.5	!		
HS_LBS	20.328E-3	.121	.121			
HS_RB	CalcCoefHS		UCS08A	YES		
HS_RBP	EXT	0.5	0.5			
HS_RBS	20.328E-3	.121	.121			
HS_FT	ON					
HS_FTDRN	1					
			1	HSUCS07	0.	1.
HS_FTLBF	0.					
HS_FTLBM	NO					
HS_FTLBE	NO					
HS_FTRBF	0.					
HS_FTRBM	NO					
HS_FTRBE	NO					
!=====						
HS_ID	HSUCS09	348				
HS_GD	RECTANGULAR		YES			
HS_EOD	5.9937	1.0				
HS_SRC	NO					
HS_ND	11					
		1	1	0.	288.8190	STAINLESS-STEEL-304
		2	2	3.81E-03	288.9311	STAINLESS-STEEL-304
		3	3	7.62E-03	289.0433	STAINLESS-STEEL-304
		4	4	1.14E-02	289.1554	STAINLESS-STEEL-304
		5	5	1.52E-02	289.2676	STAINLESS-STEEL-304
		6	6	1.91E-02	289.3798	STAINLESS-STEEL-304
		7	7	2.29E-02	289.4919	STAINLESS-STEEL-304
		8	8	2.67E-02	289.6041	STAINLESS-STEEL-304

		9	9	3.05E-02	289.7162	STAINLESS-STEEL-304
		10	10	3.43E-02	289.8284	STAINLESS-STEEL-304
		11	11	3.81E-02	289.9405	STAINLESS-STEEL-304
HS_LB	CalcCoefHS		CPVUCS09B		NO	
HS_LBP	EXT	0.5	0.5	!		
HS_LBS	20.328E-3	.121	.121			
HS_RB	CalcCoefHS		UCS09A	YES		
HS_RBP	EXT	0.5	0.5			
HS_RBS	20.328E-3	.121	.121			
HS_FT	ON					
HS_FTDRN	1					

1	HSUCS08	0.	1.
---	---------	----	----

HS_FTLBF 0.
HS_FTLBM NO
HS_FTLBE NO
HS_FTRBF 0.
HS_FTRBMNO
HS_FTRBE NO

!=====

HS_ID	HSUCS10	349	
HS_GD	RECTANGULAR		YES
HS_EOD	6.1147	1.0	
HS_SRC	NO		
HS_ND	11		

1	1	0.	288.8190	STAINLESS-STEEL-304
2	2	3.81E-03	288.9311	STAINLESS-STEEL-304
3	3	7.62E-03	289.0433	STAINLESS-STEEL-304
4	4	1.14E-02	289.1554	STAINLESS-STEEL-304
5	5	1.52E-02	289.2676	STAINLESS-STEEL-304
6	6	1.91E-02	289.3798	STAINLESS-STEEL-304
7	7	2.29E-02	289.4919	STAINLESS-STEEL-304
8	8	2.67E-02	289.6041	STAINLESS-STEEL-304
9	9	3.05E-02	289.7162	STAINLESS-STEEL-304
10	10	3.43E-02	289.8284	STAINLESS-STEEL-304
11	11	3.81E-02	289.9405	STAINLESS-STEEL-304

HS_LB	CalcCoefHS		CPVUCS10B		NO
HS_LBP	EXT	0.5	0.5	!	
HS_LBS	20.328E-3	.121	.121		
HS_RB	CalcCoefHS		UCS10A	YES	
HS_RBP	EXT	0.5	0.5		
HS_RBS	20.328E-3	.121	.121		
HS_FT	ON				
HS_FTDRN	1				

1	HSUCS09	0.	1.
---	---------	----	----

HS_FTLBF 0.
HS_FTLBM NO
HS_FTLBE NO
HS_FTRBF 0.
HS_FTRBMNO
HS_FTRBE NO

!=====

hs-tankfon.inp

AllowReplace

HS_INPUT

!=====

HS_ID	HSTLCS01	3200	
HS_GD	CYLINDRICAL		YES
HS_EOD	.6477	1.0	
HS_SRC	NO		
HS_ND	11		

1	1	0.13081	288.8189817	STAINLESS-STEEL-304
2	2	0.131229	289.5817312	STAINLESS-STEEL-304
3	3	0.131648	290.3444808	STAINLESS-STEEL-304
4	4	0.132067	291.1072303	STAINLESS-STEEL-304
5	5	0.132486	291.8699799	STAINLESS-STEEL-304

		6	6	0.132905	292.6327294	STAINLESS-STEEL-304
		7	7	0.133324	293.395479	STAINLESS-STEEL-304
		8	8	0.133743	294.1582286	STAINLESS-STEEL-304
		9	9	0.134162	294.9209781	STAINLESS-STEEL-304
		10	10	0.134581	295.6837277	STAINLESS-STEEL-304
		11	11	0.135	296.4464772	STAINLESS-STEEL-304
HS_LB	CalcCoefHS		LCS01B	YES		
HS_LBP	EXT	0.5	0.5	!		
HS_LBS	.318077	.387	.387			
HS_RB	SYMMETRY					
HS_RBP	EXT	0.5	0.5			
HS_FT	ON					
HS_FTDRN	2					
			1	HSBOTCAP01	.5	0.
			2	HSBOTCAP02	.5	0.
HS_FTLBF	0.					
HS_FTLBM	NO					
HS_FTLBE	NO					
HS_FTRBF	0.					
HS_FTRBM	NO					
HS_FTRBE	NO					
!=====						
HS_ID	HSTLCS02	3210				
HS_GD	CYLINDRICAL		YES			
HS_EOD	1.0347	1.0				
HS_SRC	NO					
HS_ND	11					
		1	1	0.13081	288.8189817	STAINLESS-STEEL-304
		2	2	0.131229	289.5817312	STAINLESS-STEEL-304
		3	3	0.131648	290.3444808	STAINLESS-STEEL-304
		4	4	0.132067	291.1072303	STAINLESS-STEEL-304
		5	5	0.132486	291.8699799	STAINLESS-STEEL-304
		6	6	0.132905	292.6327294	STAINLESS-STEEL-304
		7	7	0.133324	293.395479	STAINLESS-STEEL-304
		8	8	0.133743	294.1582286	STAINLESS-STEEL-304
		9	9	0.134162	294.9209781	STAINLESS-STEEL-304
		10	10	0.134581	295.6837277	STAINLESS-STEEL-304
		11	11	0.135	296.4464772	STAINLESS-STEEL-304
HS_LB	CalcCoefHS		LCS02B	YES		
HS_LBP	EXT	0.5	0.5	!		
HS_LBS	.318077	.387	.387			
HS_RB	SYMMETRY					
HS_RBP	EXT	0.5	0.5			
HS_FT	ON					
HS_FTDRN	1					
			1	HSTLCS01	1.	0.
HS_FTLBF	0.					
HS_FTLBM	NO					
HS_FTLBE	NO					
HS_FTRBF	0.					
HS_FTRBM	NO					
HS_FTRBE	NO					
!=====						
HS_ID	HSTLCS3	3220				
HS_GD	CYLINDRICAL		YES			
HS_EOD	1.4217	1.0				
HS_SRC	NO					
HS_ND	11					
		1	1	0.13081	288.8189817	STAINLESS-STEEL-304
		2	2	0.131229	289.5817312	STAINLESS-STEEL-304
		3	3	0.131648	290.3444808	STAINLESS-STEEL-304
		4	4	0.132067	291.1072303	STAINLESS-STEEL-304
		5	5	0.132486	291.8699799	STAINLESS-STEEL-304
		6	6	0.132905	292.6327294	STAINLESS-STEEL-304
		7	7	0.133324	293.395479	STAINLESS-STEEL-304
		8	8	0.133743	294.1582286	STAINLESS-STEEL-304

		9	9	0.134162	294.9209781	STAINLESS-STEEL-304
		10	10	0.134581	295.6837277	STAINLESS-STEEL-304
		11	11	0.135	296.4464772	STAINLESS-STEEL-304
HS_LB	CalcCoefHS		LCS3B	YES		
HS_LBP	EXT	0.5	0.5	!		
HS_LBS	.318077	.387	.387			
HS_RB	SYMMETRY					
HS_RBP	EXT	0.5	0.5			
HS_FT	ON					
HS_FTDRN	1					
			1	HSTLCS02	1.	0.
HS_FTLBF	0.					
HS_FTLBM	NO					
HS_FTLBE	NO					
HS_FTRBF	0.					
HS_FTRBM	NO					
HS_FTRBE	NO					
!=====						
HS_ID	HSTLCS04	3230				
HS_GD	CYLINDRICAL		YES			
HS_EOD	1.8087	1.0				
HS_SRC	NO					
HS_ND	11					
		1	1	0.13081	288.8189817	STAINLESS-STEEL-304
		2	2	0.131229	289.5817312	STAINLESS-STEEL-304
		3	3	0.131648	290.3444808	STAINLESS-STEEL-304
		4	4	0.132067	291.1072303	STAINLESS-STEEL-304
		5	5	0.132486	291.8699799	STAINLESS-STEEL-304
		6	6	0.132905	292.6327294	STAINLESS-STEEL-304
		7	7	0.133324	293.395479	STAINLESS-STEEL-304
		8	8	0.133743	294.1582286	STAINLESS-STEEL-304
		9	9	0.134162	294.9209781	STAINLESS-STEEL-304
		10	10	0.134581	295.6837277	STAINLESS-STEEL-304
		11	11	0.135	296.4464772	STAINLESS-STEEL-304
HS_LB	CalcCoefHS		LCS04B	YES		
HS_LBP	EXT	0.5	0.5	!		
HS_LBS	.318077	.387	.387			
HS_RB	SYMMETRY					
HS_RBP	EXT	0.5	0.5			
HS_FT	ON					
HS_FTDRN	1					
			1	HSTLCS3	1.	0.
HS_FTLBF	0.					
HS_FTLBM	NO					
HS_FTLBE	NO					
HS_FTRBF	0.					
HS_FTRBM	NO					
HS_FTRBE	NO					
!=====						
HS_ID	HSTLCS05	3240				
HS_GD	CYLINDRICAL		YES			
HS_EOD	2.1957	1.0				
HS_SRC	NO					
HS_ND	11					
		1	1	0.13081	288.8189817	STAINLESS-STEEL-304
		2	2	0.131229	289.5817312	STAINLESS-STEEL-304
		3	3	0.131648	290.3444808	STAINLESS-STEEL-304
		4	4	0.132067	291.1072303	STAINLESS-STEEL-304
		5	5	0.132486	291.8699799	STAINLESS-STEEL-304
		6	6	0.132905	292.6327294	STAINLESS-STEEL-304
		7	7	0.133324	293.395479	STAINLESS-STEEL-304
		8	8	0.133743	294.1582286	STAINLESS-STEEL-304
		9	9	0.134162	294.9209781	STAINLESS-STEEL-304
		10	10	0.134581	295.6837277	STAINLESS-STEEL-304
		11	11	0.135	296.4464772	STAINLESS-STEEL-304
HS_LB	CalcCoefHS		LCS05B	YES		

HS_LBP	EXT	0.5	0.5	!		
HS_LBS	.318077	.387	.387			
HS_RB	SYMMETRY					
HS_RBP	EXT	0.5	0.5			
HS_FT	ON					
HS_FTDRN	1					
			1	HSTLCS04	1.	0.
HS_FTLBF	0.					
HS_FTLBM	NO					
HS_FTLBE	NO					
HS_FTRBF	0.					
HS_FTRBM	NO					
HS_FTRBE	NO					
!=====						
HS_ID	HSTLCS06	3250				
HS_GD	CYLINDRICAL		YES			
HS_EOD	2.5827	1.0				
HS_SRC	NO					
HS_ND	11					
		1	1	0.13081	288.8189817	STAINLESS-STEEL-304
		2	2	0.131229	289.5817312	STAINLESS-STEEL-304
		3	3	0.131648	290.3444808	STAINLESS-STEEL-304
		4	4	0.132067	291.1072303	STAINLESS-STEEL-304
		5	5	0.132486	291.8699799	STAINLESS-STEEL-304
		6	6	0.132905	292.6327294	STAINLESS-STEEL-304
		7	7	0.133324	293.395479	STAINLESS-STEEL-304
		8	8	0.133743	294.1582286	STAINLESS-STEEL-304
		9	9	0.134162	294.9209781	STAINLESS-STEEL-304
		10	10	0.134581	295.6837277	STAINLESS-STEEL-304
		11	11	0.135	296.4464772	STAINLESS-STEEL-304
HS_LB	CalcCoefHS		LCS06B	YES		
HS_LBP	EXT	0.5	0.5	!		
HS_LBS	.318077	.387	.387			
HS_RB	SYMMETRY					
HS_RBP	EXT	0.5	0.5			
HS_FT	ON					
HS_FTDRN	1					
			1	HSTLCS05	1.	0.
HS_FTLBF	0.					
HS_FTLBM	NO					
HS_FTLBE	NO					
HS_FTRBF	0.					
HS_FTRBM	NO					
HS_FTRBE	NO					
!=====						
HS_ID	HSTLCS07	3260				
HS_GD	CYLINDRICAL		YES			
HS_EOD	2.9697	1.0				
HS_SRC	NO					
HS_ND	11					
		1	1	0.13081	288.8189817	STAINLESS-STEEL-304
		2	2	0.131229	289.5817312	STAINLESS-STEEL-304
		3	3	0.131648	290.3444808	STAINLESS-STEEL-304
		4	4	0.132067	291.1072303	STAINLESS-STEEL-304
		5	5	0.132486	291.8699799	STAINLESS-STEEL-304
		6	6	0.132905	292.6327294	STAINLESS-STEEL-304
		7	7	0.133324	293.395479	STAINLESS-STEEL-304
		8	8	0.133743	294.1582286	STAINLESS-STEEL-304
		9	9	0.134162	294.9209781	STAINLESS-STEEL-304
		10	10	0.134581	295.6837277	STAINLESS-STEEL-304
		11	11	0.135	296.4464772	STAINLESS-STEEL-304
HS_LB	CalcCoefHS		LCS07B	YES		
HS_LBP	EXT	0.5	0.5	!		
HS_LBS	.318077	.387	.387			
HS_RB	SYMMETRY					
HS_RBP	EXT	0.5	0.5			

```

HS_FT      ON
HS_FTDRN 1

                                1          HSTLCS06 1.          0.

HS_FTLBF 0.
HS_FTLBM NO
HS_FTLBE NO
HS_FTRBF 0.
HS_FTRBM NO
HS_FTRBE NO
=====
HS_ID      HSTLCS08 3270
HS_GD      CYLINDRICAL      YES
HS_EOD     3.3567      1.0
HS_SRC     NO
HS_ND      11

                                1          1          0.13081  288.8189817      STAINLESS-STEEL-304
                                2          2          0.131229  289.5817312      STAINLESS-STEEL-304
                                3          3          0.131648  290.3444808      STAINLESS-STEEL-304
                                4          4          0.132067  291.1072303      STAINLESS-STEEL-304
                                5          5          0.132486  291.8699799      STAINLESS-STEEL-304
                                6          6          0.132905  292.6327294      STAINLESS-STEEL-304
                                7          7          0.133324  293.395479      STAINLESS-STEEL-304
                                8          8          0.133743  294.1582286      STAINLESS-STEEL-304
                                9          9          0.134162  294.9209781      STAINLESS-STEEL-304
                                10         10         0.134581  295.6837277      STAINLESS-STEEL-304
                                11         11         0.135      296.4464772      STAINLESS-STEEL-304
HS_LB      CalcCoefHS      LCS08B  YES
HS_LBP     EXT      0.5      0.5      !
HS_LBS     .318077      .387      .387
HS_RB      SYMMETRY
HS_RBP     EXT      0.5      0.5
HS_FT      ON
HS_FTDRN 1

                                1          HSTLCS07 1.          0.

HS_FTLBF 0.
HS_FTLBM NO
HS_FTLBE NO
HS_FTRBF 0.
HS_FTRBM NO
HS_FTRBE NO
=====
HS_ID      HSTLCS09 3280
HS_GD      CYLINDRICAL      YES
HS_EOD     3.7437      1.0
HS_SRC     NO
HS_ND      11

                                1          1          0.13081  288.8189817      STAINLESS-STEEL-304
                                2          2          0.131229  289.5817312      STAINLESS-STEEL-304
                                3          3          0.131648  290.3444808      STAINLESS-STEEL-304
                                4          4          0.132067  291.1072303      STAINLESS-STEEL-304
                                5          5          0.132486  291.8699799      STAINLESS-STEEL-304
                                6          6          0.132905  292.6327294      STAINLESS-STEEL-304
                                7          7          0.133324  293.395479      STAINLESS-STEEL-304
                                8          8          0.133743  294.1582286      STAINLESS-STEEL-304
                                9          9          0.134162  294.9209781      STAINLESS-STEEL-304
                                10         10         0.134581  295.6837277      STAINLESS-STEEL-304
                                11         11         0.135      296.4464772      STAINLESS-STEEL-304
HS_LB      CalcCoefHS      LCS09B  YES
HS_LBP     EXT      0.5      0.5      !
HS_LBS     .318077      .387      .387
HS_RB      SYMMETRY
HS_RBP     EXT      0.5      0.5
HS_FT      ON
HS_FTDRN 1

                                1          HSTLCS08 1.          0.

HS_FTLBF 0.

```

```

HS_FTLBM NO
HS_FTLBE NO
HS_FTRBF 0.
HS_FTRBMNO
HS_FTRBE NO
=====
HS_ID      HSTLCS10 3290
HS_GD      CYLINDRICAL      YES
HS_EOD     4.1307      1.0
HS_SRC     NO
HS_ND      11
          1      1      0.13081 288.8189817 STAINLESS-STEEL-304
          2      2      0.131229 289.5817312 STAINLESS-STEEL-304
          3      3      0.131648 290.3444808 STAINLESS-STEEL-304
          4      4      0.132067 291.1072303 STAINLESS-STEEL-304
          5      5      0.132486 291.8699799 STAINLESS-STEEL-304
          6      6      0.132905 292.6327294 STAINLESS-STEEL-304
          7      7      0.133324 293.395479 STAINLESS-STEEL-304
          8      8      0.133743 294.1582286 STAINLESS-STEEL-304
          9      9      0.134162 294.9209781 STAINLESS-STEEL-304
         10     10      0.134581 295.6837277 STAINLESS-STEEL-304
         11     11      0.135      296.4464772 STAINLESS-STEEL-304
HS_LB      CalcCoefHS      LCS10B YES
HS_LBP     EXT      0.5      0.5      !
HS_LBS     .318077 .387      .387
HS_RB      SYMMETRY
HS_RBP     EXT      0.5      0.5
HS_FT      ON
HS_FTDRN 1
          1      HSTLCS09 1.      0.
HS_FTLBF 0.
HS_FTLBM NO
HS_FTLBE NO
HS_FTRBF 0.
HS_FTRBMNO
HS_FTRBE NO
=====
=====ECS PORTION=====
HS_ID      HSTECS01 3300
HS_GD      CYLINDRICAL      YES
HS_EOD     4.5177      1.0
HS_SRC     NO
HS_ND      11
          1      1      0.246060 288.8189817 STAINLESS-STEEL-304
          2      2      0.246854 289.5817312 STAINLESS-STEEL-304
          3      3      0.247648 290.3444808 STAINLESS-STEEL-304
          4      4      0.248442 291.1072303 STAINLESS-STEEL-304
          5      5      0.249236 291.8699799 STAINLESS-STEEL-304
          6      6      0.250030 292.6327294 STAINLESS-STEEL-304
          7      7      0.250824 293.395479 STAINLESS-STEEL-304
          8      8      0.251618 294.1582286 STAINLESS-STEEL-304
          9      9      0.252412 294.9209781 STAINLESS-STEEL-304
         10     10      0.253206 295.6837277 STAINLESS-STEEL-304
         11     11      0.254      296.4464772 STAINLESS-STEEL-304
HS_LB      CalcCoefHS      ECS01B YES
HS_LBP     EXT      0.5      0.5      !
HS_LBS     .202779 .254      .254
HS_RB      SYMMETRY
HS_RBP     EXT      0.5      0.5
HS_FT      ON
HS_FTDRN 1
          1      HSTLCS10 1.      0.
HS_FTLBF 0.
HS_FTLBM NO
HS_FTLBE NO
HS_FTRBF 0.

```

```

HS_FTRBMNO
HS_FTRBE NO
!=====
HS_ID    HSTEC02 3310
HS_GD    CYLINDRICAL      YES
HS_EOD   4.7717    1.0
HS_SRC   NO
HS_ND    11
          1      1      0.246060 288.8189817    STAINLESS-STEEL-304
          2      2      0.246854 289.5817312    STAINLESS-STEEL-304
          3      3      0.247648 290.3444808    STAINLESS-STEEL-304
          4      4      0.248442 291.1072303    STAINLESS-STEEL-304
          5      5      0.249236 291.8699799    STAINLESS-STEEL-304
          6      6      0.250030 292.6327294    STAINLESS-STEEL-304
          7      7      0.250824 293.395479    STAINLESS-STEEL-304
          8      8      0.251618 294.1582286    STAINLESS-STEEL-304
          9      9      0.252412 294.9209781    STAINLESS-STEEL-304
         10     10      0.253206 295.6837277    STAINLESS-STEEL-304
         11     11      0.254    296.4464772    STAINLESS-STEEL-304
HS_LB     CalcCoefHS      ECS02B  YES
HS_LBP    EXT      0.5      0.5      !
HS_LBS    .392694 .254    .254
HS_RB     SYMMETRY
HS_RBP    EXT      0.5      0.5
HS_FT     ON
HS_FTDRN 1
          1      HSTEC01 1.      0.

HS_FTLBF 0.
HS_FTLBMNO
HS_FTLBE NO
HS_FTRBF 0.
HS_FTRBMNO
HS_FTRBE NO
!=====
!=====UCS PORTION=====
HS_ID    HSTUC01 3400
HS_GD    CYLINDRICAL      YES
HS_EOD   5.0257    1.0
HS_SRC   NO
HS_ND    11
          1      1      0.24924 288.8189817    STAINLESS-STEEL-304
          2      2      0.249716 289.5817312    STAINLESS-STEEL-304
          3      3      0.250192 290.3444808    STAINLESS-STEEL-304
          4      4      0.250668 291.1072303    STAINLESS-STEEL-304
          5      5      0.251144 291.8699799    STAINLESS-STEEL-304
          6      6      0.251620 292.6327294    STAINLESS-STEEL-304
          7      7      0.252096 293.395479    STAINLESS-STEEL-304
          8      8      0.252572 294.1582286    STAINLESS-STEEL-304
          9      9      0.253048 294.9209781    STAINLESS-STEEL-304
         10     10      0.253524 295.6837277    STAINLESS-STEEL-304
         11     11      0.254    296.4464772    STAINLESS-STEEL-304
HS_LB     CalcCoefHS      UCS01B  YES
HS_LBP    EXT      0.5      0.5      !
HS_LBS    .189489 .121    .121
HS_RB     SYMMETRY
HS_RBP    EXT      0.5      0.5
HS_FT     ON
HS_FTDRN 1
          1      HSTEC02 1.      0.

HS_FTLBF 0.
HS_FTLBMNO
HS_FTLBE NO
HS_FTRBF 0.
HS_FTRBMNO
HS_FTRBE NO
!=====

```

HS_ID	HSTUCS02	3410				
HS_GD	CYLINDRICAL		YES			
HS_EOD	5.1467	1.0				
HS_SRC	NO					
HS_ND	11					
	1	1	0.24924	288.8189817	STAINLESS-STEEL-304	
	2	2	0.249716	289.5817312	STAINLESS-STEEL-304	
	3	3	0.250192	290.3444808	STAINLESS-STEEL-304	
	4	4	0.250668	291.1072303	STAINLESS-STEEL-304	
	5	5	0.251144	291.8699799	STAINLESS-STEEL-304	
	6	6	0.251620	292.6327294	STAINLESS-STEEL-304	
	7	7	0.252096	293.395479	STAINLESS-STEEL-304	
	8	8	0.252572	294.1582286	STAINLESS-STEEL-304	
	9	9	0.253048	294.9209781	STAINLESS-STEEL-304	
	10	10	0.253524	295.6837277	STAINLESS-STEEL-304	
	11	11	0.254	296.4464772	STAINLESS-STEEL-304	
HS_LB	CalcCoefHS	UCS02B	YES			
HS_LBP	EXT	0.5	0.5	!		
HS_LBS	.189489	.121	.121			
HS_RB	SYMMETRY					
HS_RBP	EXT	0.5	0.5			
HS_FT	ON					
HS_FTDRN	1					
		1	HSTUCS01	1.	0.	
HS_FTLBF	0.					
HS_FTLBM	NO					
HS_FTLBE	NO					
HS_FTRBF	0.					
HS_FTRBM	NO					
HS_FTRBE	NO					
!=====						
HS_ID	HSTUCS3	3420				
HS_GD	CYLINDRICAL		YES			
HS_EOD	5.2677	1.0				
HS_SRC	NO					
HS_ND	11					
	1	1	0.24924	288.8189817	STAINLESS-STEEL-304	
	2	2	0.249716	289.5817312	STAINLESS-STEEL-304	
	3	3	0.250192	290.3444808	STAINLESS-STEEL-304	
	4	4	0.250668	291.1072303	STAINLESS-STEEL-304	
	5	5	0.251144	291.8699799	STAINLESS-STEEL-304	
	6	6	0.251620	292.6327294	STAINLESS-STEEL-304	
	7	7	0.252096	293.395479	STAINLESS-STEEL-304	
	8	8	0.252572	294.1582286	STAINLESS-STEEL-304	
	9	9	0.253048	294.9209781	STAINLESS-STEEL-304	
	10	10	0.253524	295.6837277	STAINLESS-STEEL-304	
	11	11	0.254	296.4464772	STAINLESS-STEEL-304	
HS_LB	CalcCoefHS	UCS3B	YES			
HS_LBP	EXT	0.5	0.5	!		
HS_LBS	.189489	.121	.121			
HS_RB	SYMMETRY					
HS_RBP	EXT	0.5	0.5			
HS_FT	ON					
HS_FTDRN	1					
		1	HSTUCS02	1.	0.	
HS_FTLBF	0.					
HS_FTLBM	NO					
HS_FTLBE	NO					
HS_FTRBF	0.					
HS_FTRBM	NO					
HS_FTRBE	NO					
!=====						
HS_ID	HSTUCS04	3430				
HS_GD	CYLINDRICAL		YES			
HS_EOD	5.3887	1.0				
HS_SRC	NO					

HS_ND	11					
	1	1	0.24924	288.8189817	STAINLESS-STEEL-304	
	2	2	0.249716	289.5817312	STAINLESS-STEEL-304	
	3	3	0.250192	290.3444808	STAINLESS-STEEL-304	
	4	4	0.250668	291.1072303	STAINLESS-STEEL-304	
	5	5	0.251144	291.8699799	STAINLESS-STEEL-304	
	6	6	0.251620	292.6327294	STAINLESS-STEEL-304	
	7	7	0.252096	293.395479	STAINLESS-STEEL-304	
	8	8	0.252572	294.1582286	STAINLESS-STEEL-304	
	9	9	0.253048	294.9209781	STAINLESS-STEEL-304	
	10	10	0.253524	295.6837277	STAINLESS-STEEL-304	
	11	11	0.254	296.4464772	STAINLESS-STEEL-304	
HS_LB	CalcCofHS	UCS04B	YES			
HS_LBP	EXT	0.5	0.5	!		
HS_LBS	.189489	.121	.121			
HS_RB	SYMMETRY					
HS_RBP	EXT	0.5	0.5			
HS_FT	ON					
HS_FTDRN	1					
		1	HSTUCS3	1.	0.	
HS_FTLBF	0.					
HS_FTLBM	NO					
HS_FTLBE	NO					
HS_FTRBF	0.					
HS_FTRBM	NO					
HS_FTRBE	NO					
!=====						
HS_ID	HSTUCS05	3440				
HS_GD	CYLINDRICAL		YES			
HS_EOD	5.5097	1.0				
HS_SRC	NO					
HS_ND	11					
	1	1	0.24924	288.8189817	STAINLESS-STEEL-304	
	2	2	0.249716	289.5817312	STAINLESS-STEEL-304	
	3	3	0.250192	290.3444808	STAINLESS-STEEL-304	
	4	4	0.250668	291.1072303	STAINLESS-STEEL-304	
	5	5	0.251144	291.8699799	STAINLESS-STEEL-304	
	6	6	0.251620	292.6327294	STAINLESS-STEEL-304	
	7	7	0.252096	293.395479	STAINLESS-STEEL-304	
	8	8	0.252572	294.1582286	STAINLESS-STEEL-304	
	9	9	0.253048	294.9209781	STAINLESS-STEEL-304	
	10	10	0.253524	295.6837277	STAINLESS-STEEL-304	
	11	11	0.254	296.4464772	STAINLESS-STEEL-304	
HS_LB	CalcCofHS	UCS05B	YES			
HS_LBP	EXT	0.5	0.5	!		
HS_LBS	.189489	.121	.121			
HS_RB	SYMMETRY					
HS_RBP	EXT	0.5	0.5			
HS_FT	ON					
HS_FTDRN	1					
		1	HSTUCS04	1.	0.	
HS_FTLBF	0.					
HS_FTLBM	NO					
HS_FTLBE	NO					
HS_FTRBF	0.					
HS_FTRBM	NO					
HS_FTRBE	NO					
!=====						
HS_ID	HSTUCS06	3450				
HS_GD	CYLINDRICAL		YES			
HS_EOD	5.6307	1.0				
HS_SRC	NO					
HS_ND	11					
	1	1	0.24924	288.8189817	STAINLESS-STEEL-304	
	2	2	0.249716	289.5817312	STAINLESS-STEEL-304	
	3	3	0.250192	290.3444808	STAINLESS-STEEL-304	

		4	4	0.250668	291.1072303	STAINLESS-STEEL-304
		5	5	0.251144	291.8699799	STAINLESS-STEEL-304
		6	6	0.251620	292.6327294	STAINLESS-STEEL-304
		7	7	0.252096	293.395479	STAINLESS-STEEL-304
		8	8	0.252572	294.1582286	STAINLESS-STEEL-304
		9	9	0.253048	294.9209781	STAINLESS-STEEL-304
		10	10	0.253524	295.6837277	STAINLESS-STEEL-304
		11	11	0.254	296.4464772	STAINLESS-STEEL-304
HS_LB	CalcCoefHS		UCS06B	YES		
HS_LBP	EXT	0.5	0.5	!		
HS_LBS	.189489	.121	.121			
HS_RB	SYMMETRY					
HS_RBP	EXT	0.5	0.5			
HS_FT	ON					
HS_FTDRN	1					
			1	HSTUCS05	1.	0.
HS_FTLBF	0.					
HS_FTLBM	NO					
HS_FTLBE	NO					
HS_FTRBF	0.					
HS_FTRBM	NO					
HS_FTRBE	NO					
!=====						
HS_ID	HSTUCS07	3460				
HS_GD	CYLINDRICAL		YES			
HS_EOD	5.7517	1.0				
HS_SRC	NO					
HS_ND	11					
		1	1	0.24924	288.8189817	STAINLESS-STEEL-304
		2	2	0.249716	289.5817312	STAINLESS-STEEL-304
		3	3	0.250192	290.3444808	STAINLESS-STEEL-304
		4	4	0.250668	291.1072303	STAINLESS-STEEL-304
		5	5	0.251144	291.8699799	STAINLESS-STEEL-304
		6	6	0.251620	292.6327294	STAINLESS-STEEL-304
		7	7	0.252096	293.395479	STAINLESS-STEEL-304
		8	8	0.252572	294.1582286	STAINLESS-STEEL-304
		9	9	0.253048	294.9209781	STAINLESS-STEEL-304
		10	10	0.253524	295.6837277	STAINLESS-STEEL-304
		11	11	0.254	296.4464772	STAINLESS-STEEL-304
HS_LB	CalcCoefHS		UCS07B	YES		
HS_LBP	EXT	0.5	0.5	!		
HS_LBS	.189489	.121	.121			
HS_RB	SYMMETRY					
HS_RBP	EXT	0.5	0.5			
HS_FT	ON					
HS_FTDRN	1					
			1	HSTUCS06	1.	0.
HS_FTLBF	0.					
HS_FTLBM	NO					
HS_FTLBE	NO					
HS_FTRBF	0.					
HS_FTRBM	NO					
HS_FTRBE	NO					
!=====						
HS_ID	HSTUCS08	3470				
HS_GD	CYLINDRICAL		YES			
HS_EOD	5.8727	1.0				
HS_SRC	NO					
HS_ND	11					
		1	1	0.24924	288.8189817	STAINLESS-STEEL-304
		2	2	0.249716	289.5817312	STAINLESS-STEEL-304
		3	3	0.250192	290.3444808	STAINLESS-STEEL-304
		4	4	0.250668	291.1072303	STAINLESS-STEEL-304
		5	5	0.251144	291.8699799	STAINLESS-STEEL-304
		6	6	0.251620	292.6327294	STAINLESS-STEEL-304
		7	7	0.252096	293.395479	STAINLESS-STEEL-304

		8	8	0.252572	294.1582286	STAINLESS-STEEL-304
		9	9	0.253048	294.9209781	STAINLESS-STEEL-304
		10	10	0.253524	295.6837277	STAINLESS-STEEL-304
		11	11	0.254	296.4464772	STAINLESS-STEEL-304
HS_LB	CalcCoefHS		UCS08B	YES		
HS_LBP	EXT	0.5	0.5	!		
HS_LBS	.189489	.121	.121			
HS_RB	SYMMETRY					
HS_RBP	EXT	0.5	0.5			
HS_FT	ON					
HS_FTDRN	1					
			1	HSTUCS07	1.	0.
HS_FTLBF	0.					
HS_FTLBM	NO					
HS_FTLBE	NO					
HS_FTRBF	0.					
HS_FTRBMNO						
HS_FTRBE	NO					
!=====						
HS_ID	HSTUCS09	3480				
HS_GD	CYLINDRICAL		YES			
HS_EOD	5.9937	1.0				
HS_SRC	NO					
HS_ND	11					
		1	1	0.24924	288.8189817	STAINLESS-STEEL-304
		2	2	0.249716	289.5817312	STAINLESS-STEEL-304
		3	3	0.250192	290.3444808	STAINLESS-STEEL-304
		4	4	0.250668	291.1072303	STAINLESS-STEEL-304
		5	5	0.251144	291.8699799	STAINLESS-STEEL-304
		6	6	0.251620	292.6327294	STAINLESS-STEEL-304
		7	7	0.252096	293.395479	STAINLESS-STEEL-304
		8	8	0.252572	294.1582286	STAINLESS-STEEL-304
		9	9	0.253048	294.9209781	STAINLESS-STEEL-304
		10	10	0.253524	295.6837277	STAINLESS-STEEL-304
		11	11	0.254	296.4464772	STAINLESS-STEEL-304
HS_LB	CalcCoefHS		UCS09B	YES		
HS_LBP	EXT	0.5	0.5	!		
HS_LBS	.189489	.121	.121			
HS_RB	SYMMETRY					
HS_RBP	EXT	0.5	0.5			
HS_FT	ON					
HS_FTDRN	1					
			1	HSTUCS08	1.	0.
HS_FTLBF	0.					
HS_FTLBM	NO					
HS_FTLBE	NO					
HS_FTRBF	0.					
HS_FTRBMNO						
HS_FTRBE	NO					
!=====						
HS_ID	HSTUCS10	3490				
HS_GD	CYLINDRICAL		YES			
HS_EOD	6.1147	1.0				
HS_SRC	NO					
HS_ND	11					
		1	1	0.24924	288.8189817	STAINLESS-STEEL-304
		2	2	0.249716	289.5817312	STAINLESS-STEEL-304
		3	3	0.250192	290.3444808	STAINLESS-STEEL-304
		4	4	0.250668	291.1072303	STAINLESS-STEEL-304
		5	5	0.251144	291.8699799	STAINLESS-STEEL-304
		6	6	0.251620	292.6327294	STAINLESS-STEEL-304
		7	7	0.252096	293.395479	STAINLESS-STEEL-304
		8	8	0.252572	294.1582286	STAINLESS-STEEL-304
		9	9	0.253048	294.9209781	STAINLESS-STEEL-304
		10	10	0.253524	295.6837277	STAINLESS-STEEL-304
		11	11	0.254	296.4464772	STAINLESS-STEEL-304

HS_LB	CalcCoefHS	UCS10B	YES	
HS_LBP	EXT 0.5	0.5	!	
HS_LBS	.189489 .121	.121		
HS_RB	SYMMETRY			
HS_RBP	EXT 0.5	0.5		
HS_FT	ON			
HS_FTDRN	1			
		1	HSTUCS09 1.	0.
HS_FTLBF	0.			
HS_FTLBM	NO			
HS_FTLBE	NO			
HS_FTRBF	0.			
HS_FTRBM	NO			
HS_FTRBE	NO			
!=====				
HS_ID	HSTOPCAP01	3511		
HS_GD	RECTANGULAR	YES		
HS_EOD	6.4007 0.			
HS_SRC	NO			
HS_ND	11			
	1	1	0.000E+00 288.8189817	STAINLESS-STEEL-304
	2	2	6.305E-04 289.5817312	STAINLESS-STEEL-304
	3	3	1.270E-03 290.3444808	STAINLESS-STEEL-304
	4	4	1.905E-03 291.1072303	STAINLESS-STEEL-304
	5	5	2.540E-03 291.8699799	STAINLESS-STEEL-304
	6	6	3.175E-03 292.6327294	STAINLESS-STEEL-304
	7	7	3.810E-03 293.395479	STAINLESS-STEEL-304
	8	8	4.445E-03 294.1582286	STAINLESS-STEEL-304
	9	9	5.080E-03 294.9209781	STAINLESS-STEEL-304
	10	10	5.715E-03 295.6837277	STAINLESS-STEEL-304
	11	11	6.350E-03 296.4464772	STAINLESS-STEEL-304
HS_LB	CalcCoefHS	HEMA	YES	
HS_LBP	EXT 0.5	0.5	!	
HS_LBS	9.76E-2 .24924	.24924		
HS_RB	SYMMETRY			
HS_RBP	EXT 0.5	0.5		
HS_FT	ON			
HS_FTDRN	1			
		1	HSTUCS10 1.	0.
HS_FTLBF	0.			
HS_FTLBM	NO			
HS_FTLBE	NO			
HS_FTRBF	0.			
HS_FTRBM	NO			
HS_FTRBE	NO			
!=====				
HS_ID	HSTOPCAP02	3512		
HS_GD	RECTANGULAR	YES		
HS_EOD	6.4007 0.			
HS_SRC	NO			
HS_ND	11			
	1	1	0.000E+00 288.8189817	STAINLESS-STEEL-304
	2	2	6.305E-04 289.5817312	STAINLESS-STEEL-304
	3	3	1.270E-03 290.3444808	STAINLESS-STEEL-304
	4	4	1.905E-03 291.1072303	STAINLESS-STEEL-304
	5	5	2.540E-03 291.8699799	STAINLESS-STEEL-304
	6	6	3.175E-03 292.6327294	STAINLESS-STEEL-304
	7	7	3.810E-03 293.395479	STAINLESS-STEEL-304
	8	8	4.445E-03 294.1582286	STAINLESS-STEEL-304
	9	9	5.080E-03 294.9209781	STAINLESS-STEEL-304
	10	10	5.715E-03 295.6837277	STAINLESS-STEEL-304
	11	11	6.350E-03 296.4464772	STAINLESS-STEEL-304
HS_LB	CalcCoefHS	HEMB	YES	
HS_LBP	EXT 0.5	0.5	!	
HS_LBS	9.76E-2 .24924	.24924		

```

HS_RB    SYMMETRY
HS_RBP   EXT      0.5      0.5
HS_FT    ON
HS_FTDRN 1
                                     1      HSTUCS10 1.      0.

HS_FTLBF 0.
HS_FTLBM NO
HS_FTLBE NO
HS_FTRBF 0.
HS_FTRBM NO
HS_FTRBE NO
=====
HS_ID     HSBOTCAP01      3521
HS_GD     RECTANGULAR    YES
HS_EOD    .6223      -1.E-7
HS_SRC    NO
HS_ND     11
                                     1      1      0.000E+00 288.8189817      STAINLESS-STEEL-304
                                     2      2      2.540E-04 289.5817312      STAINLESS-STEEL-304
                                     3      3      5.080E-03 290.3444808      STAINLESS-STEEL-304
                                     4      4      7.620E-03 291.1072303      STAINLESS-STEEL-304
                                     5      5      1.016E-02 291.8699799      STAINLESS-STEEL-304
                                     6      6      1.270E-02 292.6327294      STAINLESS-STEEL-304
                                     7      7      1.524E-02 293.395479      STAINLESS-STEEL-304
                                     8      8      1.778E-02 294.1582286      STAINLESS-STEEL-304
                                     9      9      2.032E-02 294.9209781      STAINLESS-STEEL-304
                                    10     10     2.286E-02 295.6837277      STAINLESS-STEEL-304
                                    11     11     2.540E-02 296.4464772      STAINLESS-STEEL-304
HS_LB     CalcCoefHS      LCS01A  YES
HS_LBP    EXT      0.5      0.5      !
HS_LBS    2.69E-2      .13081      .13081
HS_RB     SYMMETRY
HS_RBP    EXT      0.5      0.5
HS_FT     ON
HS_FTDRN 0
HS_FTLBF 0.
HS_FTLBM NO
HS_FTLBE NO
HS_FTRBF 0.
HS_FTRBM NO
HS_FTRBE NO
=====
HS_ID     HSBOTCAP02      3522
HS_GD     RECTANGULAR    YES
HS_EOD    .6223      -1.E-7
HS_SRC    NO
HS_ND     11
                                     1      1      0.000E+00 288.8189817      STAINLESS-STEEL-304
                                     2      2      2.540E-04 289.5817312      STAINLESS-STEEL-304
                                     3      3      5.080E-03 290.3444808      STAINLESS-STEEL-304
                                     4      4      7.620E-03 291.1072303      STAINLESS-STEEL-304
                                     5      5      1.016E-02 291.8699799      STAINLESS-STEEL-304
                                     6      6      1.270E-02 292.6327294      STAINLESS-STEEL-304
                                     7      7      1.524E-02 293.395479      STAINLESS-STEEL-304
                                     8      8      1.778E-02 294.1582286      STAINLESS-STEEL-304
                                     9      9      2.032E-02 294.9209781      STAINLESS-STEEL-304
                                    10     10     2.286E-02 295.6837277      STAINLESS-STEEL-304
                                    11     11     2.540E-02 296.4464772      STAINLESS-STEEL-304
HS_LB     CalcCoefHS      LCS01B  YES
HS_LBP    EXT      0.5      0.5      !
HS_LBS    2.69E-2      .13081      .13081
HS_RB     SYMMETRY
HS_RBP    EXT      0.5      0.5
HS_FT     ON
HS_FTDRN 0
HS_FTLBF 0.

```

HS_FTLBM NO
 HS_FTLBE NO
 HS_FTRBF 0.
 HS_FTRBMNO
 HS_FTRBE NO

mp.inp

AllowReplace

MP_INPUT

```

!=====
!           Material Specifications Below           !
!=====
!-----!
!           Default Property Loads                 !
!-----!
IMP_ID  ZIRCALOY                ! default
IMP_ID  ZIRCONIUM-OXIDE         ! default
IMP_ID  URANIUM-DIOXIDE         ! default
MP_ID   STAINLESS-STEEL         ! default
IMP_ID  STAINLESS-STEEL-OXIDE   ! default
IMP_ID  BORON-CARBIDE           ! default
IMP_ID  SILVER-INDIUM-CADMIUM   ! default
IMP_ID  URANIUM-METAL           ! default
IMP_ID  CONCRETE                ! default
MP_ID   ALUMINUM                ! default
IMP_ID  ALUMINUM-OXIDE          ! default
IMP_ID  CADMIUM                 ! default
MP_ID   STAINLESS-STEEL-304     ! default
IMP_ID  LITHIUM-ALUMINUM        ! default
IMP_ID  URANIUM-ALUMINUM        ! default
IMP_ID  CARBON-STEEL            ! default
IMP_ID  B4C-INT                 ! default
IMP_ID  ZRO2-INT                ! default
IMP_ID  UO2-INT                 ! default
!=====

```